



Politecnico  
di Bari

Repository Istituzionale dei Prodotti della Ricerca del Politecnico di Bari

## Robust optimization of ORC turbine expanders

This is a PhD Thesis

*Original Citation:*

Robust optimization of ORC turbine expanders / Bufi, Elio Antonio. - (2017). [10.60576/poliba/iris/bufi-elio-antonio\_phd2017]

*Availability:*

This version is available at <http://hdl.handle.net/11589/103442> since: 2017-05-03

*Published version*

Politecnico di Bari  
[10.60576/poliba/iris/bufi-elio-antonio\\_phd2017](http://10.60576/poliba/iris/bufi-elio-antonio_phd2017)

*Terms of use:*

Altro tipo di accesso

(Article begins on next page)



Politecnico  
di Bari

Department of Mechanics, Mathematics and Management  
MECHANICAL AND MANAGEMENT ENGINEERING

Ph.D. Program

SSD: ING-IND/08–FLUID MACHINERY

**Final Dissertation**

---

# Robust optimization of ORC turbine expanders

---

by

Elio Antonio BUFI

Supervisors:

Prof. Paola CINNELLA

Prof. Sergio M. CAMPOREALE

Prof. Bernardo FORTUNATO

M.CF. Xavier MERLE

*Coordinator of Ph.D Program:*

*Prof. Giuseppe DEMELIO*

---



*XXIX cycle, 2014-2016*



**Politecnico  
di Bari**

Department of Mechanics, Mathematics and Management  
**MECHANICAL AND MANAGEMENT ENGINEERING**

**Ph.D. Program**

**SSD: ING-IND/08–FLUID MACHINERY**

**Final Dissertation**

---

# **Robust optimization of ORC turbine expanders**

---

by

**Elio Antonio BUFI :**

---

Referees:

Prof. Pietro M. CONGEDO

Prof. Giacomo B. A. PERSICO

Supervisors:

Prof. Sergio M. CAMPOREALE

---

Prof. Bernardo FORTUNATO

---

Prof. Paola CINNELLA

---

M.CF. Xavier MERLE

*Coordinator of Ph.D Program:*

*Prof. Giuseppe DEMELIO*

---



École doctorale n° 432 : Science des Métiers de l'ingénieur

**Doctorat ParisTech**

**T H È S E**

pour obtenir le grade de docteur délivré par

**l'École Nationale Supérieure d'Arts et Métiers**

**Spécialité “ Mécanique des fluides ”**

*présentée et soutenue publiquement par*

**Elio Antonio BUFI**

14/12/2016

**Robust optimization of ORC turbine expanders**

Directeur de thèse : **Paola CINNELLA**

Co-Directeurs : **Sergio M. CAMPOREALE**  
**Bernardo FORTUNATO**

Co-encadrant : **Xavier MERLE**

**Jury**

**M. Stéphan AUBERT**, Professeur, Ecole Centrale Lyon  
**M. Pietro M. CONGEDO**, Chargé de Recherche INRIA (CR1, HDR)  
**M. Giacomo B. A. PERSICO**, Professeur, Politecnico di Milano  
**M. Sergio M. CAMPOREALE**, Professeur, Politecnico di Bari  
**Mme Paola CINNELLA**, Professeur, DynFluid, ENSAM  
**M. Xavier MERLE**, Maître de Conférences, DynFluid, ENSAM  
**M. Benoit OBERT**, ENERTIME

Président  
Rapporteur  
Rapporteur  
Examineur  
Examineur  
Examineur  
Invité

**T  
H  
È  
S  
E**



# SUMMARY

## Sommario esteso

In questa tesi è proposta una metodologia di progettazione e ottimizzazione 2-D per turbine ORC supersoniche con basso grado di reazione. Sia lo statore che il rotore sono progettati mediante un metodo delle caratteristiche (MOC) adattato a equazioni di stato complesse per tener accuratamente conto degli effetti di gas denso, legati alla complessità molecolare del fluido di lavoro. Per la progettazione del rotore è stato implementato un approccio a vortice libero e il problema dell'incidenza unica è stato risolto in modo originale nel regime di gas denso. Inoltre, i profili statorici e rotorici non viscosi, ottenuti con i metodi precedenti, sono stati corretti tenendo conto della presenza dello spessore dello strato limite. Gli effetti del modello termodinamico sulla progettazione sono stati studiati e confrontati con quelli forniti dal modello di gas perfetto. Le prestazioni di statore e rotore sono state valutate tramite simulazioni numeriche con l'ausilio di codici fluidodinamici ai volumi finiti.

La caratteristica fondamentale della tecnologia ORC è quella di sfruttare fonti di calore a bassa temperatura con fluidi organici che lavorano in stati termodinamici vicino alla curva di saturazione e la regione critica, dove gli effetti di gas reale sono dominanti. La corretta descrizione del comportamento del fluido in queste condizioni può essere fatto introducendo un parametro indicatore della influenza della fase gassosa ad alta densità sulla valutazione dei parametri termodinamici. Questa proprietà è nota come *derivata fondamentale* (Thompson, 1971):

$$\Gamma = \frac{a^4}{2v^3} \left( \frac{\partial^2 v}{\partial p^2} \right)_s = 1 + \frac{\rho}{a} \left( \frac{\partial a}{\partial \rho} \right)_s \quad (1)$$

dove  $a$  è la velocità del suono definita come  $\left[ -v^2 \left( \frac{\partial p}{\partial v} \right)_s \right]^{0.5}$ , mentre  $s$  è l'entropia specifica. Lo studio di Eqn. (2.1) fornisce informazioni circa il comportamento delle proprietà termodinamiche e rappresenta una misura della velocità di variazione locale della velocità del suono. Il valore di  $\Gamma$  e il suo segno sono indicatori della presenza di fenomeni di gas denso. Nelle regioni di flusso in cui  $\Gamma > 1$ , il gas mostra un comportamento classico: la velocità del suono diminuisce nelle espansioni isentropiche, aumenta nelle compressioni isentropiche e solo onde d'urto di compressione sono ammesse. Questo è il caso dei gas perfetti, aventi un valore costante  $\Gamma = (\gamma + 1)/2 > 1$ . Se  $0 < \Gamma < 1$ , è possibile osservare un comportamento opposto rispetto al precedente, e solo onde d'urto di compressione sono consentite anche se le relative perdite d'urto sono inferiori. In questo lavoro, una metodologia completa di progettazione per turbine ad azione ORC supersoniche ed assiali è stata sviluppata al fine di tenere adeguatamente conto degli effetti di gas denso. Come è stato esaminato in passato da Guardone et al. (2013) e Wheeler and Ong (2013), un ugello supersonico progettato mediante la legge dei gas perfetti non è in grado di fornire le corrette geometrie e prestazioni attese utilizzando un modello di gas denso e, quindi, è necessaria un'analisi più accurata. Qui è proposto un design semi-analitico.

---

La procedura si basa su un *metodo delle caratteristiche* (MOC) generalizzato per statori, insieme a un approccio di progettazione a vortice libero per rotori. Il MOC è uno strumento classico per risolvere sistemi iperbolici di equazioni differenziali alle derivate parziali e, nel design inverso, può essere vantaggiosamente utilizzato per progettare la parte supersonica di ugelli (Zucrow and Hoffman, 1976; Ali et al., 2006; Détery, 2010). Il MOC è stato ampiamente studiato in gasdinamica classica, ma solo negli ultimi anni è aumentato l'interesse per problemi di gas reale grazie ai grandi passi avanti nella modellazione termodinamica. Un primo esempio di progettazione di ugelli supersonici mediante il MOC per gas reali è stato fornito da Cramer and Crickenberger (1992), che ha fornito una breve descrizione del comportamento non classico della funzione di Prandtl-Meyer, che è di grande importanza per la teoria caratteristica, nel regime di gas denso. La funzione di Prandtl-Meyer, infatti, diminuisce anziché aumentare, con il numero di Mach a densità, temperatura, e numeri di Mach tali che  $\Gamma < 1$ . Aldo and Argrow (1993), per la prima volta, hanno sviluppato un MOC per ugelli bidimensionali e assialsimmetrici con gas di van der Waals. Più recentemente, Guardone et al. (2013) ha implementato un MOC accoppiato con modelli termodinamici di gas reale per valutare l'influenza della complessità molecolare del fluido di lavoro sul disegno della parte supersonica dell'ugello, considerando fluidi diversi per le stesse condizioni operative, mentre Wheeler and Ong (2013) hanno studiato i flussi di gas reale che si sviluppano in turbine radiali ORC. Un nuovo metodo, basato su un'estensione del MOC per gas perfetto ai gas densi per la progettazione di ugelli supersonici, è stato discusso e applicato al caso di palette di turbina con un alto rapporto di espansione.

Al fine di tenere conto degli effetti di gas denso durante la progettazione degli ugelli statorici, il MOC classico per i gas perfetti è stato esteso ad una generica equazione di stato (EOS). Qui, le equazioni multi-parametro fornite da REFPROP (REF per brevità) sono state implementate. Il metodo di Carrière per gas perfetti è stato modificato considerando un rapporto equivalente dei calori specifici  $\gamma_{eq}$ , calcolato come coefficiente di regressione lineare di un processo politropico, a entropia costante, per un determinato intervallo di pressioni e densità.

Considerando EOS complesse non lineari per modellare il comportamento del gas, le equazioni di governo del flusso non possono essere più integrate in modo analitico. Nel seguito, una procedura numerica è invece presentata seguendo una metodologia simile a quella proposta da Zucrow and Hoffman (1976). La portata  $G$  e la distribuzione di pressione  $p(x)/p_0$  lungo l'asse dell'ugello, sono noti. Anche la pressione e la temperatura nel plenum,  $p_0$  e  $T_0$ , sono conosciute. Ciò permette di calcolare le condizioni termodinamiche soniche in gola per l'ugello (flusso strozzato).

Per calcolare i punti a valle della caratteristica iniziale, viene eseguito un calcolo preliminare tenendo conto degli effetti di gas denso. I passaggi sono i seguenti:

1. Sono noti i dati iniziali  $(p_0, T_0)$ ,  $p(x)/p_0$  e  $G$ , e considerando il flusso strozzato, le condizioni statiche in gola sono calcolate.
2. Viene calcolata la velocità sui punti all'asse dell'ugello come  $V = \sqrt{2(h_0 - h)}$ . L'entalpia statica  $h(x)$  lungo l'asse viene calcolata come  $h(x) = h(p(x), s)$ , dove l'entropia è costante per definizione e  $s = s(p_0, T_0)$ . Anche l'entalpia totale  $h_0$  è costante, essendo l'ugello adiabatico, ed è data da  $h_0 = h(p_0, T_0)$ .
3. La velocità del suono sull'asse dell'ugello  $a(x)$  è calcolata come  $a = a(p(x), s)$  e, quindi, la distribuzione del numero di Mach  $M(x)$  è calcolata.
4. La prima caratteristica  $\xi_0$  è calcolata applicando il metodo di Carrière (Détery, 2010), modificato usando il valore di gas reale  $\gamma_{eq}$  per il rapporto dei gas specifici.

Le fasi di inizializzazione precedenti permettono di iniziare il calcolo delle proprietà cinematiche e termodinamiche per punti lungo le caratteristiche a valle della gola. Il sistema delle equazioni

---

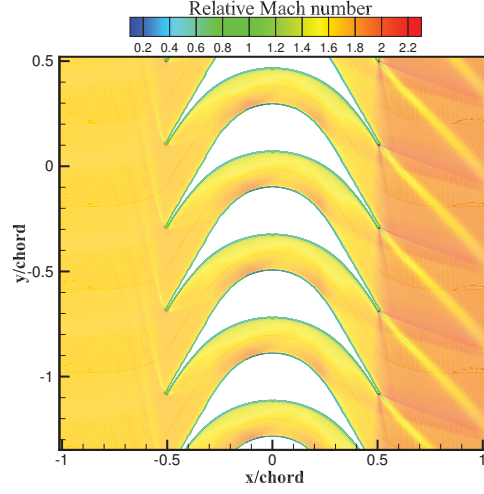
di governo del flusso è numericamente integrato con un metodo di Eulero accurato al secondo ordine.

La procedura iterativa è applicata per ogni punto lungo le caratteristiche fino a quando la convergenza sulla portata non viene raggiunta. In questo modo la forma dell'ugello è determinata. Il MOC è stato implementato nel codice FORTRAN NODEC. Il codice NODEC è stato verificato confrontando i risultati MOC con quelli forniti da un solutore CFD dotato di EOS per gas reale (i risultati sono omessi per brevità e sono mostrati nel manoscritto completo). Sebbene i calcoli necessari con EOS per gas reale sono più complessi di quelli basati sul modello ideale, questo algoritmo è molto veloce e pochi secondi sono necessari per l'ottenimento di forme di ugelli accurate su una macchina a singolo processore.

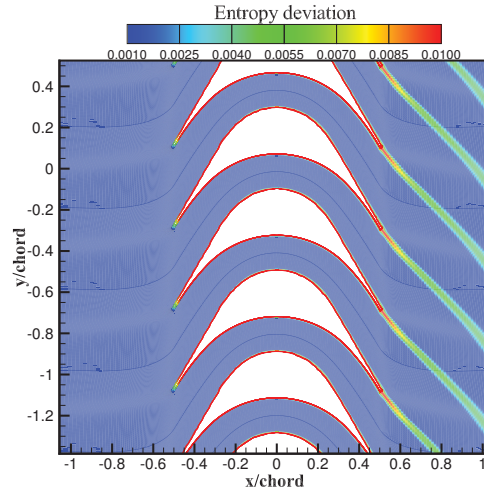
Un contributo originale di questo lavoro di tesi riguarda la metodologia di progettazione di rotori supersonici con effetti di gas reale. Calcoli viscosi sono stati effettuati per il rotore isolato progettato con il MOC per verificare l'accuratezza della metodologia di progettazione. Il problema di periodicità legato all'incidenza unica è stato preso in considerazione ed è stato quindi imposto in ingresso l'angolo relativo di flusso corretto.

Le condizioni termodinamiche sono leggermente supercritiche, in modo da lavorare in una regione termodinamica ove gli effetti non ideali sono massimizzati e il fluido di lavoro è R245fa. I risultati sono mostrati nelle Figg. 1 in termini di numero di Mach relativo e deviazione di entropia, quest'ultima definita come la variazione di entropia relativa  $(S - S_{in})/S_{in}$  rispetto all'entropia in ingresso  $S_{in}$ . In Fig. 1a si può notare come il design con il RODEC fornisca un rotore avviato con un bow-shock sul bordo d'attacco che conferma la presenza del problema di incidenza unica. All'interno dei vani rotorici, il flusso è caratterizzato da riflessioni delle onde d'urto oblique. Lo strato limite modifica l'effettiva area di passaggio del flusso e influisce sulle prestazioni della schiera rotorica, che possono essere valutate in termini di grado di reazione  $\Lambda$  e deviazione di entropia. Il calcolo di  $\Lambda$  si basa sulle entalpie statiche medie in ingresso e uscita rotore,  $\Lambda = \frac{\Delta h_{rotore}}{\Delta h_{totale}}$ . Dal momento che il rotore è isolato, un valore costante di riferimento è stato assegnato a  $\Delta h_{totale}$  al fine di calcolare  $\Lambda$ . Il design MOC fornisce  $\Lambda = -0.034$ , che è leggermente diverso dal valore nominale (grado di reazione nullo). Il valore negativo implica che vi è una nuova compressione del flusso supersonico, a causa dello sviluppo dello strato limite, portando ad una distribuzione non simmetrica dell'area effettiva. La correzione con strato limite della geometria del rotore potrebbe attenuare questo effetto.

L'analisi della deviazione di entropia, riportato nella Fig. 1b, mostra che le perdite sono localizzate nello strato limite turbolento e vicino al bordo di uscita. Una simulazione CFD viscosa è stata effettuata per il rotore modificato dalla correzione con strato limite ed i risultati sono stati confrontati con quelli precedentemente ottenuti per un disegno puramente inviscido. Il numero di Mach e deviazione entropia per il rotore corretto sono riportati in Fig. 2. Il numero di Mach mostra un modello di shock simile con diverse riflessioni nel vano rotorico fino all'uscita. Il rotore è di nuovo completamente avviato. Si osserva che il profilo "viscoso" comporta minori perdite, in termini di deviazione di entropia, poiché lo strato limite è più sottile (senza compressione in questo caso), e lo stesso vale per la scia (Fig. 2b). La correzione di strato limite ha un effetto benefico anche sul grado di reazione ( $\Lambda = -0,011$ ), riducendo in modo significativo gli effetti di ricompressione dovuta alla variazione della effettiva area di passaggio del flusso. Una valutazione dei vantaggi della metodologia di progettazione proposta rispetto a disegni classici basati su semplici considerazioni geometriche derivate dai triangoli di velocità del flusso, è stata effettuata. Questi disegni sono generalmente basati sulla concatenazione di archi di cerchio, senza ulteriori considerazioni termodinamiche o aerodinamiche. Il design classico basato su archi di cerchio e triangoli di velocità non fornisce risultati soddisfacenti (Fig. 3a). La soluzione è caratterizzata da una forte interazione tra il ramo inferiore dell'urto e il lato in depressione della pala adiacente, oltre ad un'ampia regione subsonica sul lato in pressione. Sulla parte posteriore della paletta, lo



(a)

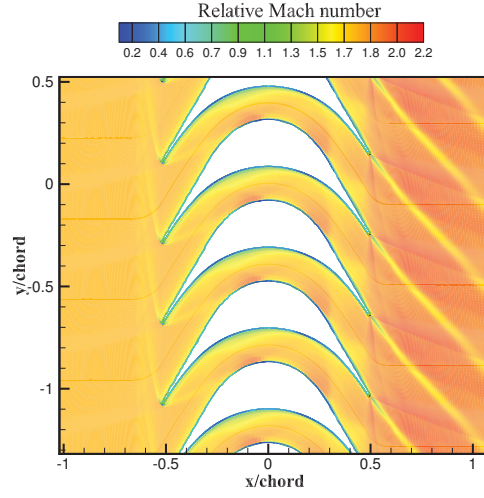


(b)

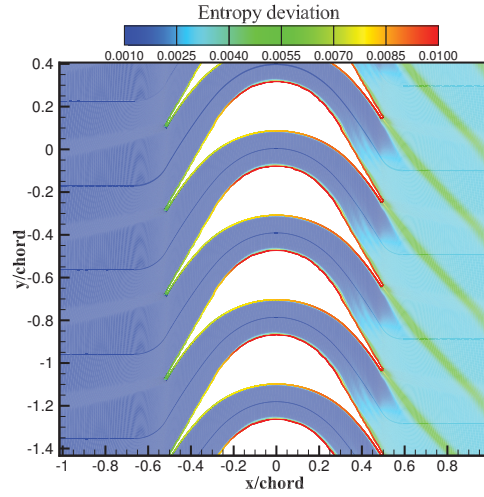
**Figure 1:** Contour del numero di Mach per RODEC (a) e deviazione di entropia (b).

strato limite si separa dalla parete. Questi fenomeni influiscono sulle prestazioni della schiera, valutate in termini di grado di reazione e deviazione di entropia. Il disegno ad arco di cerchio fornisce  $\Lambda = -0.12$ , che è un ordine di grandezza inferiore rispetto al disegno MOC. L'analisi della deviazione di entropia, riportata in Fig. 3b, mostra perdite di entropia molto più elevate per il design ad arco circolare, in particolare sul lato in depressione posteriore e sulla scia viscosa. L'analisi della distribuzione di pressione sulla pala rotorica (vedi Fig. 4) conferma che la distribuzione di riferimento, fornita dalla soluzione MOC non viscoso, è ben approssimata dalla progettazione MOC, eccetto per alcune oscillazioni sui lati in pressione e depressione dovuti a riflessioni delle onde d'urto. D'altra parte, il design ad arco circolare non garantisce di poter





(a)

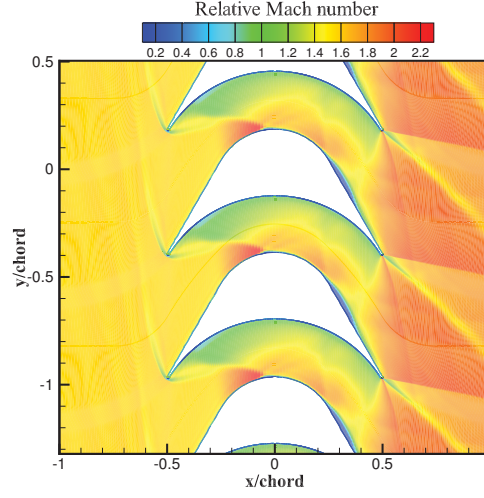


(b)

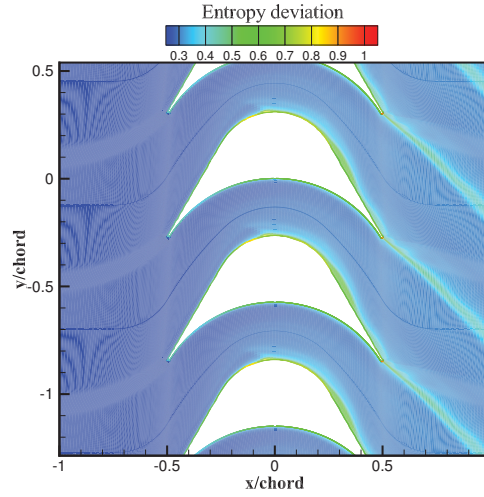
**Figure 2:** Mach number contour plot (a) and entropy deviation (b) for RODEC rotors with boundary layer correction.

realizzare la distribuzione di pressione target e, quindi, le prestazioni desiderate.

Un secondo contributo originale di questo lavoro di tesi è stato lo sviluppo di una metodologia efficiente per l'ottimizzazione robusta di turbine supersoniche. L'ottimizzazione robusta (RDO) per configurazioni di flusso complesse per mezzo di modelli avanzati CFD si basa spesso su modelli surrogati per approssimare la risposta della funzione di costo e ridurre il costo computazionale. La costruzione di surrogati affidabili è un compito difficile, vale a dire per gli spazi di progettazione con un grande numero di dimensioni. In questa tesi è stata sviluppata una strategia RDO efficiente per la progettazione di espansori ORC 2-D supersonici. Il flusso è caratterizzato da forti effetti di gas denso, e richiede la soluzione delle equazioni di Navier-Stokes mediate alla



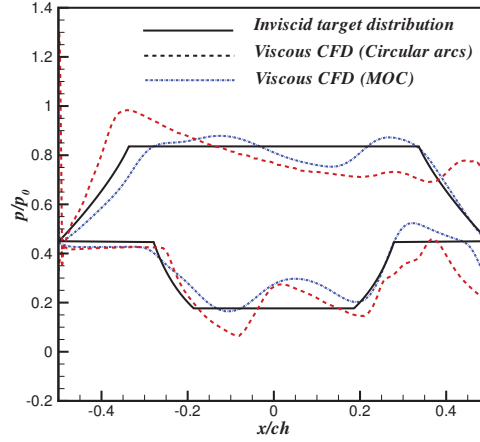
(a)



(b)

**Figure 3:** Contour del numero di Mach per RODEC (a) and archi di cerchio (b).

Reynolds, integrate dalle EOS avanzate. La metodologia di progettazione si basa su due livelli di surrogati Kriging Bayesiano: il surrogato di primo livello dipende solo dai parametri incerti, e viene utilizzato per approssimare le statistiche necessarie (media e varianza) della funzione di costo; il modello surrogato di secondo livello nello spazio di progettazione è accoppiato con un algoritmo genetico multi-obiettivo (NSGA). Una strategia di allenamento adattativa della superficie di risposta viene utilizzata per arricchire il surrogato durante la convergenza NSGA. Pochi step di arricchimento sono sufficienti per migliorare la precisione del fronte di Pareto finale in modo notevole, in modo che l'algoritmo adattativo RDO conservi una prestazione soddisfacente in parallelo. La strategia proposta è stata prima verificata per un problema modello e quindi applicata alla progettazione dello statore di una turbina supersonica ORC.

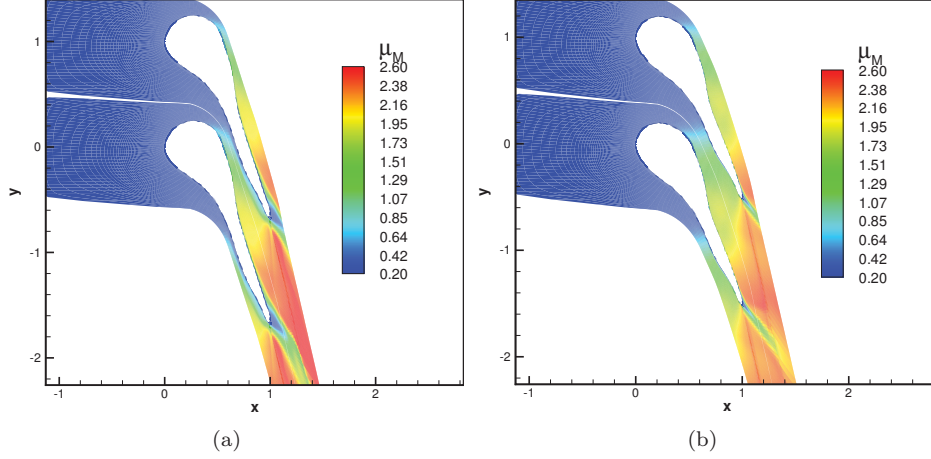


**Figure 4:** Distribuzione di pressione a parete sul rotore per simulazione viscosa con correzione di strato limite e confronto con la distribuzione di riferimento.

Per questa applicazione, possono essere considerate tre principali fonti di incertezza: il modello termodinamico, la geometria e le condizioni operative. Il numero di parametri in ogni categoria ha una forte influenza sulla fattibilità dell’analisi UQ e, conseguentemente, del processo RDO. Per ridurre la dimensione dello spazio parametrico, un’analisi preliminare di sensibilità viene effettuata, dimostrando che i parametri più influenti sono due parametri operativi (pressione totale e temperatura) e un parametro geometrico (spessore della paletta). La paletta è parametrizzata mediante un approccio a deformazione libera (FFD), che consente di gestire facilmente qualsiasi tipo di forma indipendentemente dalla complessità geometrica. La parametrizzazione risultante della paletta dipende da un numero relativamente basso di parametri. In questo studio, le deformazioni massime consentite con l’FFD sono impostate a 20% nel sistema di riferimento del reticolo, e 8 punti di controllo sono usati per descrivere la geometria. Il rendimento isoentropico è calcolato risolvendo le equazioni RANS sulla base di uno schema ai volumi finiti accurato al terzo ordine e il modello di turbolenza Spalart-Allmaras. I calcoli CFD sono effettuati su una griglia strutturata  $384 \times 128$ , tale che  $y^+ < 1$ . Una ottimizzazione deterministica viene prima applicata alla geometria di base. I parametri di progetto nominali sono definiti in termini di pressione totale e temperatura ridotti ( $p_{0_r} = 1,1$ ,  $T_{0_r} = 0,98$ ) normalizzate rispetto alle condizioni critiche, e rapporto di espansione ( $\beta = 5$ ) per il fluido R245fa.

L’ottimizzazione deterministica migliora l’efficienza isoentropica da 0.879 fino a 0,962 (8,6 %), abbassando le perdite viscose e dell’urto, situate sulla scia e vicino al bordo di uscita, rispettivamente (osservare 5a e 5b). Successivamente, è stata eseguita una ottimizzazione robusta massimizzando la media  $\mu_{\eta_s}$  e minimizzando la varianza  $\sigma_{\eta_s}^2$  del rendimento isoentropico. Le condizioni totali ridotte in ingresso ( $p_{0_r}$ ,  $T_{0_r}$ ) e lo spessore della paletta  $\varepsilon$  sono impostate come variabili incerte, con la distribuzione mostrata in 5.3. La scelta di una pdfs di tipo beta, con un calcolo dei parametri di forma basati sulla media e deviazione standard assegnati, permette di evitare espansioni nella regione liquido-vapore. Le funzioni obiettivo sono valutate mediante un’analisi di incertezza tramite Kriging con 24 campioni. Il surrogato multi-obiettivo Kriging con campionamento adattativo è attivato per accelerare l’NSGA. Il ciclo di ottimizzazione è eseguito sino a 60 generazioni e con 3 campioni aggiuntivi (uno ogni 20 generazioni).

Per valutare l’effetto della ottimizzazione robusta, la variazione delle prestazioni rispetto ai val-



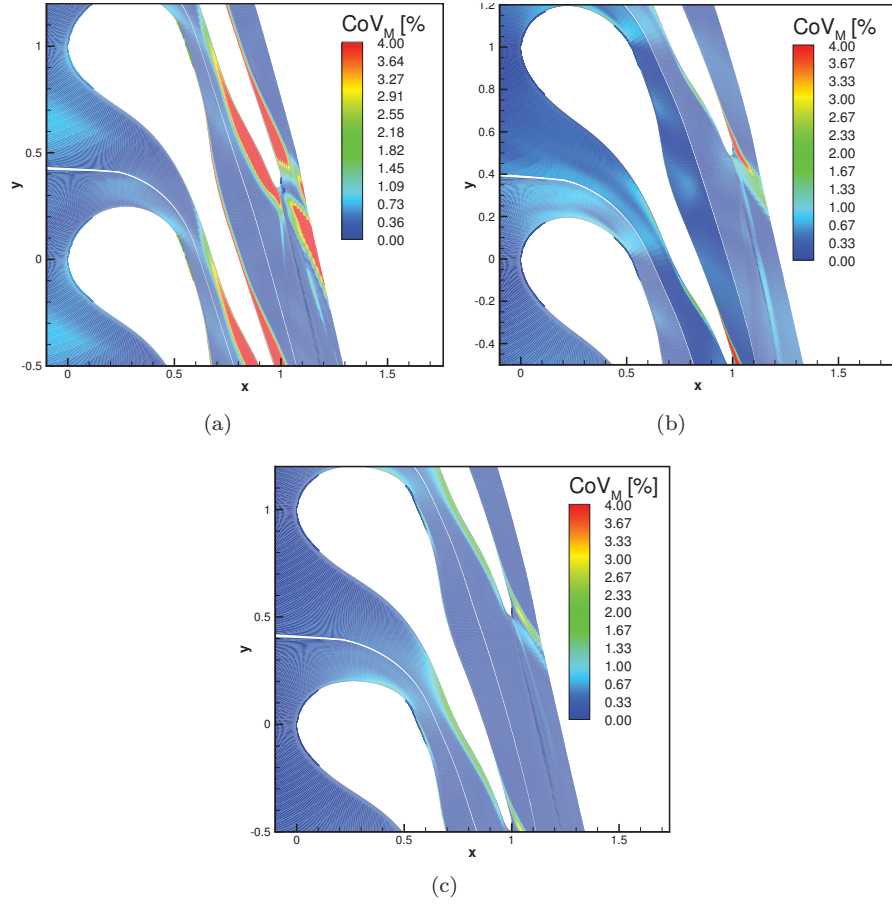
**Figure 5:** Contour plots del numero di Mach per la baseline (a); Contour plots del numero di Mach per il profilo ottimizzato deterministicamente (b).

ori medi viene analizzato e confrontato con gli altri disegni. In 6 il coefficiente di variazione (in percentuale) del numero di Mach è indicato per il profilo base (6a), deterministico (6b) e robusto (6c). Il profilo di base è caratterizzato da elevati livelli di incertezza localizzati all'interno dello strato limite turbolento e sulla scia viscosa, con variazioni massime di 8 %. L'ottimizzazione deterministica fornisce una forma con alte prestazioni medie, grazie alla minimizzazione degli strati viscosi, ma i risultati sono caratterizzati da bassa robustezza e varianza elevata in prossimità del bordo di uscita, corrispondente ad una variazione massima di 7.4 %. Il design robusto riduce la variazione massima del numero di Mach del 2 %.

Le prestazioni dei diversi design sono state confrontate. L'ottimizzazione deterministica fornisce un valore medio dell'efficienza isoentropica pari a  $\mu_{\eta_{is,det}} = 0,946$ , vale a dire leggermente inferiore rispetto al valore deterministico  $\eta_{is,det} = 0.962$ , con una variazione di 1,5%. La soluzione deterministica ha una varianza del 50% superiore per gli individui robusti, fornendo così una geometria meno robusta, pur con prestazioni medie più elevate. L'ottimizzazione robusta mostra un rendimento isoentropico medio dall'1% al 7% più alto del disegno di base, mentre la deviazione standard è da 4% a 45% inferiore.

**Table 1:** Variabili incerte. Pressione e temperatura totali ridotte ( $p_{0r}$ ,  $T_{0r}$ ), spessore della pala  $\varepsilon$ .

| Parameter     | Mean | CoV% | pdf     |
|---------------|------|------|---------|
| $p_{0r}$      | 0.98 | 8%   | BETA    |
| $T_{0r}$      | 1.13 | 8%   | BETA    |
| $\varepsilon$ | 1    | 1%   | UNIFORM |



**Figure 6:** Variazione del numero di Mach per: Baseline (a); profilo ottimizzato deterministico (b); profilo ottimizzato robusto (c).

---

## Résumé étendu

Dans cette thèse, nous avons proposé une méthodologie pour la conception et l'optimisation 2-D des turbines ORC (Organic Rankine Cycle) supersoniques avec degré de réaction faible. Le stator et le rotor sont conçus à l'aide d'une méthode des caractéristiques (MOC) étendu aux équations d'état complexes pour prendre en compte attentivement les effets de gaz dense, liés à la complexité moléculaire du fluide de travail. La conception du rotor est basée sur une modèle de vortex libre et le problème d'incidence unique a été résolu d'une manière originale dans le régime de gaz dense. En outre, les profils des aubes de stator et de rotor obtenus par les modèles non visqueux ci-dessus, ont été corrigés en tenant compte de l'épaisseur de la couche limite. Les effets du modèle thermodynamique ont été étudiés et les résultats ont été comparés à celles fournis par le modèle de gaz idéal. Les performances du stator et rotor ont été évaluées au moyen de simulations numériques. La fonction principale des machines ORC est l'exploitation des sources de chaleur à basse . Dans ces conditions, les fluides de travail choisis sont des fluides organiques travaillent dans des états thermodynamiques proches de la courbe de saturation et de la région critique, où les effets de gaz réels sont dominants. La description du comportement du fluide dans ces conditions peut être effectué en introduisant un paramètre connu sous le nom *dérivée fondamentale* (Thompson, 1971):

$$\Gamma = \frac{a^4}{2v^3} \left( \frac{\partial^2 v}{\partial p^2} \right)_s = 1 + \frac{\rho}{a} \left( \frac{\partial a}{\partial \rho} \right)_s \quad (2)$$

où  $a$  est la vitesse du son définie comme  $\left[ -v^2 \left( \frac{\partial p}{\partial v} \right)_s \right]^{0.5}$  et  $s$  est l'entropie spécifique. L'équation. (2) fournit des informations sur le comportement des propriétés thermodynamiques et représente une mesure de la vitesse locale du changement de la vitesse du son. La valeur de  $\Gamma$  et son signe sont des indicateurs de la présence de phénomènes de gaz denses. Dans les régions d'écoulement où  $\Gamma > 1$ , le gaz se comporte de manière classique: la vitesse du son diminue dans l'expansion isentropique, et augmente lors d'une compression isentropiques. Tel est le cas des gaz parfaits, ayant une valeur constante de  $\Gamma = (\gamma + 1)/2 > 1$ . Si  $0 < \Gamma < 1$ , la vitesse du son se comporte de manière opposée et augmente lors d'une détente isentropique. Ceci tend à réduire le nombre de Mach maximal atteint par l'écoulement et, par conséquent, donne lieu à des ondes de choc plus faibles que celles qui peuvent apparaître dans les écoulements supersoniques de gaz parfait. Par ailleurs, pour un même nombre de Mach amont, un choc dans des conditions où  $\Gamma$  est proche de zéro induit moins de pertes. Dans cette thèse, une méthodologie de conception complète pour turbines ORC axiale supersonique a été développé afin de tenir compte des effets de gaz denses. Comme cela a été discuté dans le passé par Guardone et al. (2013) et Wheeler and Ong (2013), une tuyère supersonique conçue en utilisant la loi des gaz parfaits ne donne pas de performances satisfaisantes en régime de gaz dense. Pour pallier à cet inconvénient, nous proposons ici une méthode de design semi-analytique basée sur des modèles de gaz dense avancés.

La procédure est basée sur un *méthode des caractéristiques* (MOC) étendue à des gaz régis par une loi d'état quelconque. Nous utilisons notamment les lois d'état de référence disponibles dans la bibliothèque de modèles thermodynamiques REFPROP du NIST. Le MOC est un outil classique pour résoudre des systèmes hyperboliques d'équations différentielles partielles et, dans la conception inverse, peut être avantageusement utilisée pour concevoir la partie supersonique de la tuyère (Zucrow and Hoffman, 1976; Ali et al., 2006; Détery, 2010). Le MOC a été largement étudié dans la dynamique des gaz classiques, mais seulement au cours des dernières années a augmenté l'intérêt en problèmes des gaz réel grâce à de grands progrès dans la modélisation thermodynamique. Un excellent exemple de la conception des avions supersoniques en utilisant la MOC pour les gaz réels a été fourni par Cramer and Crickenberger (1992), qui ont fourni une

brève description du comportement non-classique de la fonction Prandtl-Meyer, qui est d'une grande importance pour la théorie des caractéristiques, dans le régime de gaz dense. La fonction Prandtl-Meyer, en effet, diminue au lieu d'augmenter, avec le nombre de Mach, de la densité, de la température, pour un nombre de Mach tels que  $\Gamma < 1$ . Aldo and Argrow (1993), pour la première fois, ont mis au point un MOC pour les tuyères à deux dimensions et axisymétriques pour un gaz de van der Waals. Plus récemment, Guardone et al. (2013) a mis en place une MOC couplée avec des modèles thermodynamiques de gaz réel pour évaluer l'influence de la complexité moléculaire du fluide de travail sur la conception de la partie supersonique de la tuyère, avec différents fluides pour les mêmes conditions de fonctionnement, alors que Wheeler and Ong (2013) ont étudié les flux de gaz réels qui se développent dans les turbines radiales ORC. Une nouvelle méthode, basée sur une extension de la MOC pour le gaz parfait a été discutée et appliquée au cas des aubes de turbine avec un taux d'expansion élevé.

Afin de tenir compte des effets de gaz denses lors de la conception des tuyères de stator, le MOC classique des gaz parfaits a été étendue à une équation d'état générique (EOS). Ici, les équations multi-paramètres fournis par REFPROP ont été mises en œuvre. La méthode du Carrière pour gaz parfaits a été modifiée avec un rapport équivalent des chaleurs spécifiques  $\gamma_{eq}$ , calculé comme un coefficient de régression linéaire d'un processus polytropique, à entropie constante, pour une gamme donnée de pressions et de densités.

Considérant EOS complexe pour modéliser le comportement non-linéaire du gaz, les équations régissant le flux ne peut pas être intégré analytiquement. Dans ce qui suit, une procédure numérique est présentée suivant une méthode similaire à celle proposée par Zucrow and Hoffman (1976). Le débit de masse  $G$  et la distribution de la pression  $p(x)/p_0$  le long de l'axe de tuyère, sont connus. En outre, la pression et la température totale,  $p_0$  et  $T_0$ , sont connus. Ceci permet de calculer les conditions thermodynamiques de la gol sonique à la tuyère.

Pour calculer les points aval de la première caractéristique, il effectue un calcul préliminaire en tenant compte des effets du gaz dense. Les étapes sont les suivantes:

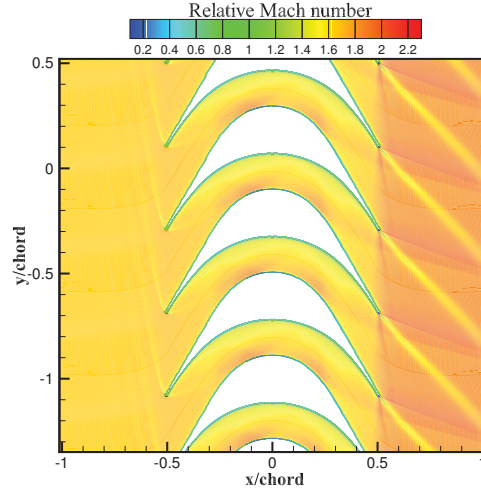
1. sont connus les données initiales  $(p_0, T_0)$ ,  $p(x)/p_0$  et  $G$ , et compte tenu du débit, les conditions statiques dans la gol sont calculées .
2. Il est calculé la vitesse sur la tuyère de points d'axe  $V = \sqrt{2(h_0 - h)}$ . L'enthalpie static  $h(x)$  le long de l'axe est calculé comme  $h(x) = h(p(x), s)$ , où l'entropie est constante et. Même l'enthalpie total  $h_0$  est constante, étant la tuyère adiabatique, et est donné par  $h_0 = h(p_0, T_0)$ .
3. La vitesse du son dans l'axe de la tuyère  $a(x)$  est calculée comme  $a = a(p(x), s)$  et, par conséquent, la distribution du nombre de Mach  $M(x)$  est calculé.
4. La première caractéristique  $\xi_0$  et calculée en appliquant le méthode Carrière (Délerly, 2010), modifié en utilisant la valeur de gaz réelle  $\gamma_{eq}$  pour le ratio de gaz spécifique.

Les étapes d'initialisation précédentes permettent de démarrer le calcul des propriétés cinématiques et thermodynamiques pour les points le long des caractéristiques en aval de la gol. Les équations du système d'écoulement est numériquement intégrée avec une méthode d'Euler précise au second ordre.

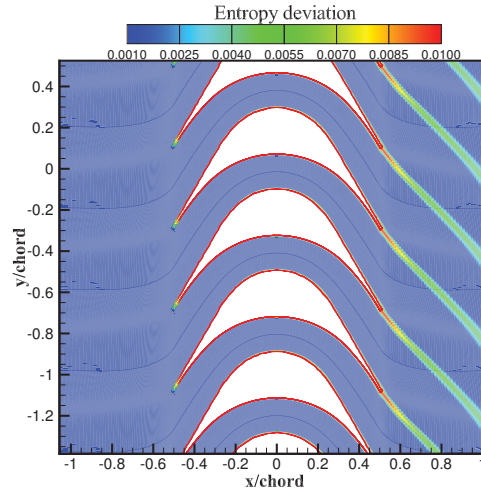
La procédure itérative est appliquée à chaque point le long des caractéristiques jusqu'à atteindre la convergence sur la débit massique. De cette manière, la forme de la tuyère est déterminée. Le MOC a été mis en œuvre dans une code FORTRAN NODEC. Le code NODEC a été vérifiée en comparant les résultats avec ceux MOC fournies par un solveur CFD équipée avec EOS pour le gaz réel. Bien que les calculs nécessaires avec EOS pour les gaz réels sont plus complexes que celles fondées sur le modèle idéal, cet algorithme est très rapide et quelques secondes sont



nécessaires pour obtenir des formes précises de tuyères sur une PC mono-processeur. Une contribution originale de cette thèse porte sur la méthodologie de conception du rotor supersonique avec des effets de gaz réel. Des calculs visqueux ont été faites pour le rotor isolé conçu avec le MOC pour vérifier l'exactitude de la méthodologie de conception. L'incidence du problème de la périodicité a été pris en compte.



(a)



(b)

**Figure 7:** Contour du nombre de Mach pour RODEC (a) et deviation d'entropie (b).

Les conditions thermodynamiques sont légèrement supercritique dans une région thermodynamique où les effets non idéales sont maximisés et le fluide de travail est R245fa. Les résultats sont présentés sur les Fig. 7 en termes de nombre de Mach et écart relatif de l'entropie, cette dernière étant définie comme le changement de rapport entropie  $(S - S_{in})/S_{in}$  par rapport à

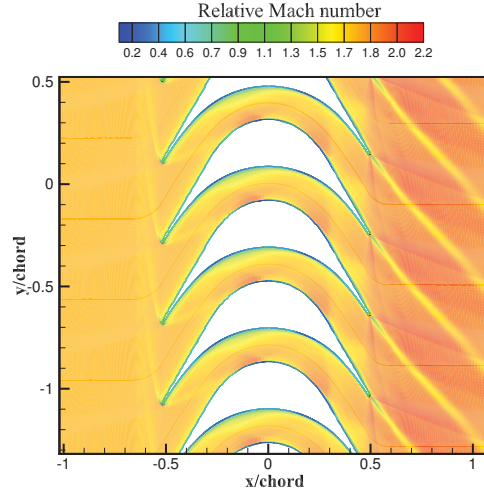


l'entropie d'entrée  $S_{in}$ . Dans la Fig. 7 on peut noter comment la conception avec le RODEC fournir un rotor avec un bow-shock sur le bord d'attaque qui confirme la présence du problème d'incidence unique. A l'intérieur du rotor, le flux est caractérisée par des réflexions des ondes de choc obliques. La couche limite modifier la zone de passage efficace de l'écoulement et affecte les performances du rotor, qui peut être évaluée en termes de degré de réaction  $\Lambda$  et la déviation de l'entropie. Le calcul est basé sur l'enthalpie statique moyenne à l'entrée et la sortie du rotor,  $\Lambda = \frac{\Delta h_{rotore}}{\Delta h_{totale}}$ . Le design MOC fournit  $\Lambda = -0.034$ , ce qui est légèrement différente de la valeur nominale (degré de réaction zéro). La valeur négative implique qu'il y a une nouvelle compression de l'écoulement supersonique, en raison du développement de la couche limite, ce qui conduit à une distribution non symétrique de la surface réelle. La correction de la couche limite de la géométrie du rotor pourrait atténuer cet effet.

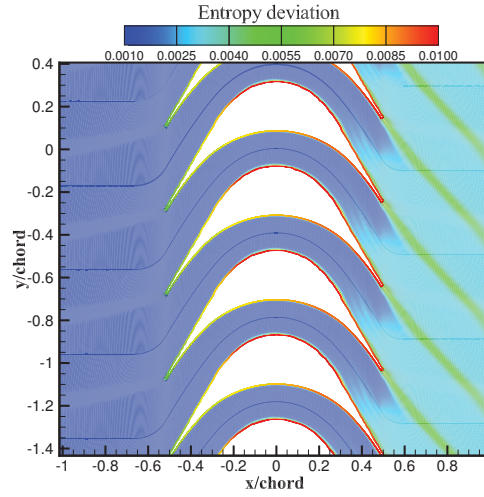
L'analyse de l'écart de l'entropie, représentée sur la Fig. 7b, montre que les pertes sont localisée dans la couche limite turbulente et à proximité du bord de fuite. Une simulation CFD visqueuse a été réalisée pour le rotor modifié par correction avec la couche limite et les résultats ont été comparés avec ceux obtenus précédemment pour une méthodes purement non-visqueux. Le nombre de Mach et l'écart d'entropie pour le rotor sont présentés sur la Fig. 8. Le nombre de Mach montre une situation similaire avec différentes réflexions dans le rotor à la sortie. Le rotor est entièrement démarré. La correction de la couche limite a un effet bénéfique également sur le degré de réaction ( $\Lambda = -0.011$ ), ce qui réduit considérablement les effets de recompression en raison de la variation de la surface effective du passage d'écoulement. Une évaluation des avantages de la méthodologie proposée par rapport aux conceptions classiques basées sur des considérations géométriques simples dérivées des triangles de vitesse d'écoulement, a été réalisée. Ces modèles sont généralement basées sur la concaténation des arcs de cercle, sans autres considérations thermodynamiques ou aérodynamiques. La conception classique basé sur des arcs de cercle et des triangles de vitesse ne fournit pas de résultats satisfaisants (Fig. 9a). La solution est caractérisée par une forte interaction entre la bosse de branche inférieure et le côté aspiration de l'aube adjacente, et aussi d'une grande région subsonique sur le côté en pression. Sur le dos de la palette, la couche limite se sépare de la paroi. Ces phénomènes affectent la performance, mesurée en termes de degré de réaction et de déviation de l'entropie. L'arc de cercle fournit  $\Lambda = -0.12$ , ce qui est un ordre de grandeur inférieur à la conception MOC. L'analyse de l'écart d'entropie, représentée sur la Fig. 9b, présentent des pertes de l'entropie beaucoup plus élevé pour la conception d'arc de cercle, en particulier sur le côté en dépression arrière et le sillage visqueux.

L'analyse de la répartition de la pression sur la pale de rotor (voir Fig. 10) confirme que la distribution de référence, fourni par la solution MOC, est bien approchée par la conception MOC, à l'exception de certaines oscillations de pression sur les côtés en dépression due à des réflexions des ondes de choc. D'autre part, le design en arc de cercle ne permet pas de vérifier la distribution de la pression cible et, par conséquent, la performance souhaitée.

Une deuxième contribution originale de cette thèse est le développement d'une méthodologie efficace pour l'optimisation robuste des turbines supersonique. L'optimisation robuste (RDO) pour les configurations d'écoulement complexes au moyen de modèles CFD avancés est souvent basée sur des modèles de substitution pour l'approximation de la réponse de la fonction de coût et de réduire le coût de calcul. La construction de surfaces précises est une tâche difficile, à savoir pour des espaces de design avec un grand nombre de dimensions. Dans cette thèse nous avons développé une stratégie efficace pour la conception de expandeurs ORC 2-D supersonique robustes. L'écoulement se caractérise par de forts effets de gaz denses et nécessite la solution des equations RANS, complétées par une loi d'état avancée. La méthodologie de conception est basée sur deux niveaux de krigeage bayésien : le krigeage de haut niveau ne dépend que des paramètres incertains, et est utilisé pour rapprocher les statistiques requises (moyenne et vari-



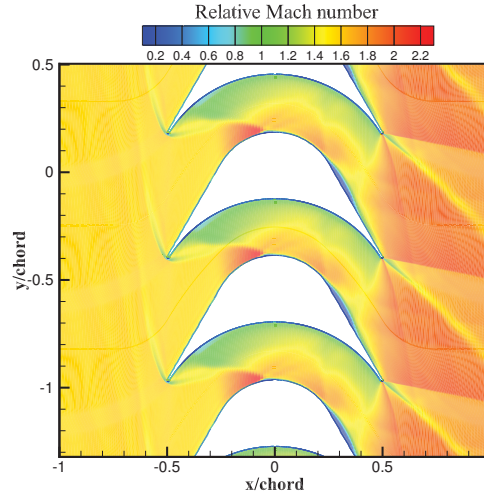
(a)



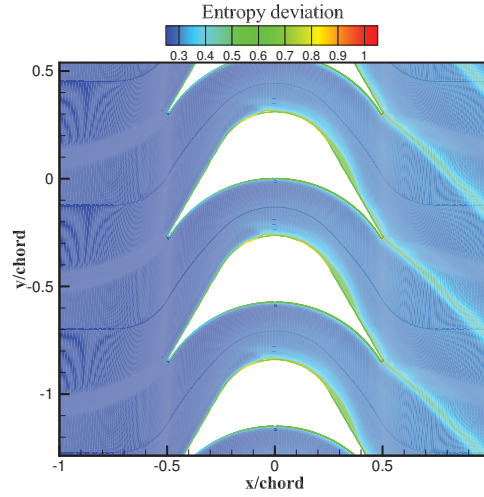
(b)

**Figure 8:** Contour du nombre de Mach contour (a) et deviation de l'entropie (b) pour les rotors RODEC avec correction de la couche limite.

ance) de la fonction de coût; le modèle de substitution de second niveau dans l'espace de design est couplé avec un algorithme génétique multi-objectif (NSGA). Une surface de réponse adaptative de la stratégie de formation est utilisée pour enrichir le krigeage pendant la convergence NSGA. Quelques étapes d'enrichissement sont suffisantes pour améliorer la précision du front final de Pareto d'une manière remarquable, de sorte que l'algorithme adaptatif RDO conserve une performance satisfaisante en parallèle. La stratégie proposée a été testée pour un problème modèle, puis appliqué à la conception de stator d'une turbine ORC supersonique. Pour cette application, il peut être considéré comme trois principales sources d'incertitude: le modèle thermodynamique, les conditions de géométrie et de fonctionnement. Le nombre de



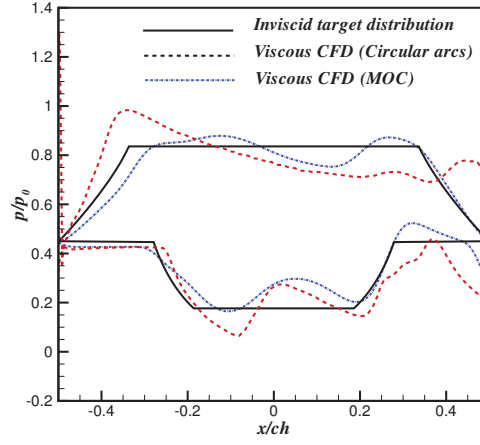
(a)



(b)

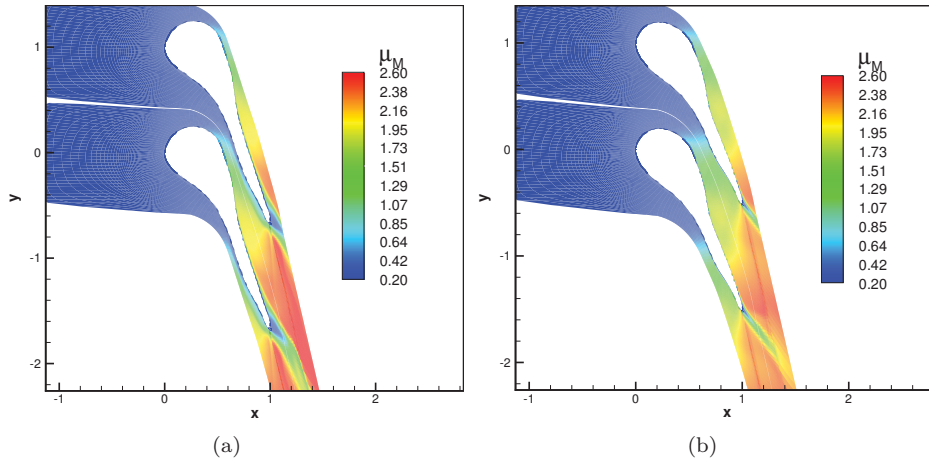
**Figure 9:** Contour du nombre de Mach pour RODEC (a) et des arcs de cercle (b).

paramètres dans chaque catégorie a une forte influence sur la faisabilité d'analyse UQ et, par conséquent, sur le processus RDO. Pour réduire la taille de l'espace des paramètres, une analyse préliminaire de la sensibilité est réalisée, montrant que les paramètres les plus influents sont deux paramètres de fonctionnement (pression totale et température) et un paramètre géométrique (l'épaisseur de l'aube). L'aube est paramétrisée par une approche FFD (Free Form Deformation), qui permet de gérer facilement tout type de forme indépendamment de la complexité géométrique. Le paramétrage de la pale résultant dépend d'un nombre relativement restreint de paramètres. Dans cette étude, les déformations maximales autorisées par le FFD sont fixées à 20 % du réseau dans le système de référence, et 8 points de contrôle sont utilisés pour décrire la géométrie. Le rendement isentropique est calculé en résolvant les équations RANS sur la



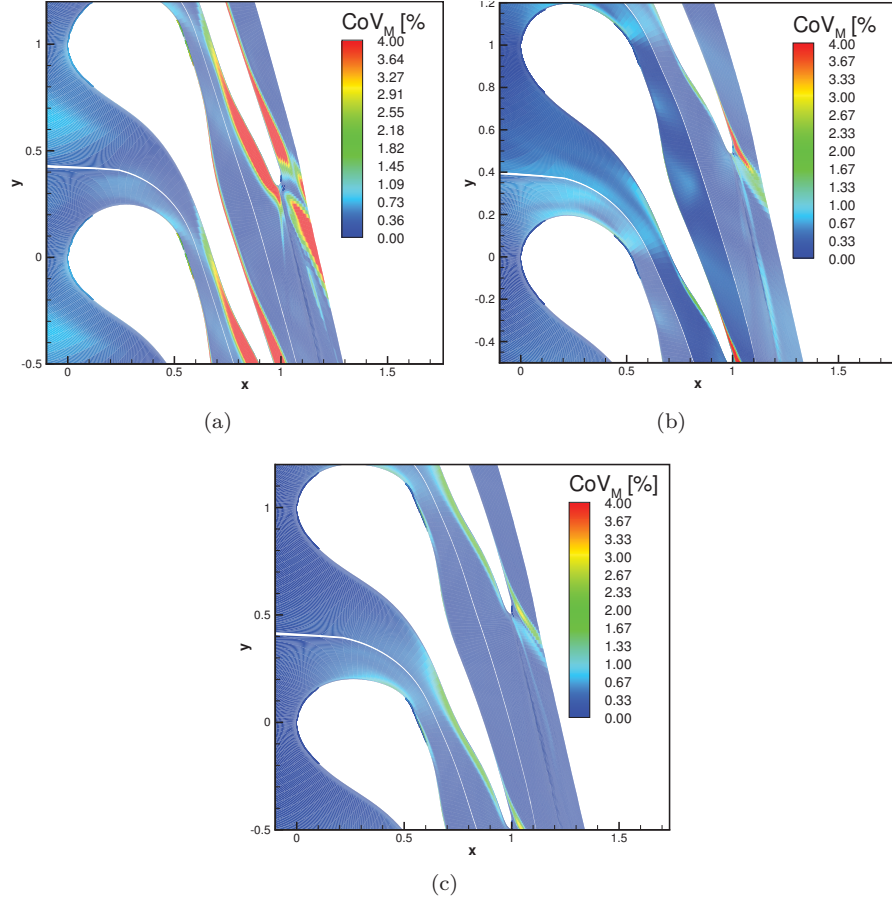
**Figure 10:** Répartition de la pression de la paroi sur le rotor pour la simulation visqueuse avec une correction du couche limite et comparaison avec la distribution de référence.

base d'un système à volume fini précis au troisième ordre avec le modèle de turbulence Spalart-Allmaras. Les calculs CFD sont effectués sur une grille structurée  $384 \times 128$ , tel que  $y^+ < 1$ . Une optimisation déterministe est d'abord appliquée à la géométrie de base. Les paramètres de conception nominaux sont définis en termes de pression totale et température ( $p_{0r}$ ,  $T_{0r}$ ) normalisées par rapport à des conditions critique, et le rapport d'expansion ( $\beta = 5$ ) pour le fluide R245fa.



**Figure 11:** Contour du nombre de Mach pour la ligne de base (a); Contour du nombre de Mach pour le profil optimisé déterministe (b).

L'optimisation déterministe améliore l'efficacité isentropique de 0.879 à 0.962 (8.6%), en abaissant les pertes visqueuses et bosse, situées à l'arrière et à proximité du bord de fuite, respectivement



**Figure 12:** Variation du nombre de Mach pour: Baseline (a); profil déterministe optimisé (b); profil robuste optimisé (c).

(note Figg. 11a et 11b). Par la suite, une optimisation robuste a été réalisée en maximisant la moyenne  $\mu_{\eta_{is}}$  et en minimisant la variance  $\sigma_{\eta_{is}}^2$  de l'efficacité isentropique. Les conditions totales en entrée, normalisées par les valeurs au point critique ( $p_{0r}$ ,  $T_{0r}$ ) et l'épaisseur de l'aube  $\varepsilon$  sont traitées comme des variables incertaines, avec la distribution indiquée dans 2. Le choix d'un type pdfs bêta permet d'éviter l'expansion dans la région liquide-vapeur. Les fonctions objectif sont évaluées par une analyse de l'incertitude en utilisant le krigeage avec 24 échantillons. Le krigeage avec échantillonnage adaptatif est activé pour accélérer la NSGA. La boucle d'optimisation est exécutée jusqu'à 60 générations avec 3 échantillons supplémentaires (un toutes les 20 générations). Pour évaluer l'effet de l'optimisation robuste, la variation du rendement par rapport aux valeurs moyennes sont analysées et comparées avec d'autres conceptions. Dans 12 le coefficient de variation (en pourcentage) du nombre de Mach est indiqué pour le profil de base (12a) déterministe (12b) et robuste (12c). Le profil de base est caractérisée par des niveaux élevés d'incertitude localisée dans la couche limite turbulente et sillage visqueux, avec des variations maximales de 8 %. L'optimisation déterministe fournit une forme avec des performances moyennes élevées, grâce à la minimisation des couches visqueuses, mais les résultats sont caractérisés par une faible résistance et une forte variance dans le voisinage du bord de fuite, ce qui correspond à une vari-

---

ation maximale de 7.4 %. La conception robuste réduit la variation maximale du nombre de Mach de 2 %.

La performances ont été comparés. L'optimisation déterministe donne une valeur moyenne de l'efficacité isentropique de  $\mu_{\eta_{is,det}} = 0.946$ , ce qui est légèrement inférieur à la valeur déterministe de  $\eta_{is,det} = 0.962$ , avec une variation de 1.5 %. La solution déterministe a une variance de 50 % plus haut pour les individus robustes, offrant ainsi une géométrie moins robuste, bien que la performance moyenne plus élevée. L'optimisation robuste permet d'obtenir une efficacité isentropique moyenne de 1 % à 7% de plus que la conception de base, tandis que l'écart type est 4% à 45 % de moins.

**Table 2:** Variables incertaine: pression et température réduite totale ( $p_{0_r}$ ,  $T_{0_r}$ ), épaisseur de la lame  $\varepsilon$ .

| Parameter     | Mean | CoV% | pdf     |
|---------------|------|------|---------|
| $p_{0_r}$     | 0.98 | 8%   | BETA    |
| $T_{0_r}$     | 1.13 | 8%   | BETA    |
| $\varepsilon$ | 1    | 1%   | UNIFORM |

# Contents

|          |   |           |
|----------|---|-----------|
| <b>1</b> | <b>INTRODUCTION</b>   | <b>28</b> |
| 1.1      | General overview . . . . .  | 28        |
| 1.2      | Thesis outline . . . . .  | 33        |
| <b>2</b> | <b>GOVERNING EQUATIONS AND NUMERICAL MODELS</b>                                     | <b>35</b> |
| 2.1      | Dense gas dynamics . . . . .  | 35        |
| 2.2      | Governing equations and numerical solver . . . . .                                  | 37        |
| 2.2.1    | Spatial discretisation . . . . .  | 38        |
| 2.2.2    | Time discretisation . . . . .   | 41        |
| 2.2.3    | Boundary Conditions . . . . .   | 41        |
| 2.3      | Thermodynamic models . . . . .  | 41        |
| 2.3.1    | The Peng-Robinson-Stryjek-Vera EOS . . . . .  | 42        |
| 2.3.2    | Helmholtz free-energy multi-parameter EOS . . . . .                                 | 43        |
| 2.4      | Conclusions . . . . .   | 46        |
| <b>3</b> | <b>FAST DESIGN METHODOLOGY FOR SUPERSONIC TURBINES WITH STRONG REAL GAS EFFECTS</b> | <b>47</b> |
| 3.1      | Introduction . . . . .  | 47        |
| 3.2      | Method of characteristics for supersonic stator design . . . . .                    | 48        |
| 3.2.1    | MOC for real gases . . . . .  | 52        |
| 3.2.2    | Nozzle guide vane design . . . . .  | 55        |
| 3.2.3    | Numerical implementation of the MOC . . . . .                                       | 56        |
| 3.2.4    | Nozzle guide vane performance . . . . .   | 59        |
| 3.3      | Method of characteristics for rotor design . . . . .                                | 68        |
| 3.3.1    | Design of dense gas supersonic rotor blades . . . . .                               | 69        |
| 3.3.2    | Examples of rotor blade designs . . . . .   | 71        |
| 3.3.3    | Started and unstarted supersonic rotors . . . . .                                   | 74        |
| 3.3.4    | The unique incidence problem in dense gas regime . . . . .                          | 79        |
| 3.3.5    | RODEC: code verification . . . . .  | 86        |
| 3.4      | Full stage design and simulation . . . . .  | 88        |
| 3.4.1    | ORC turbine stage design methodology . . . . .                                      | 88        |
| 3.4.2    | Full stage numerical simulations . . . . .  | 89        |
| 3.5      | Boundary layer correction . . . . .   | 93        |
| 3.5.1    | Boundary layer integral equations . . . . .   | 94        |
| 3.5.2    | Numerical solution of the boundary layer integral equations . . . . .               | 95        |
| 3.5.3    | Application to supersonic nozzles . . . . .   | 96        |
| 3.5.4    | Application to supersonic rotors . . . . .  | 97        |

|          |   |            |
|----------|---|------------|
| 3.6      | Conclusions . . . . .   | 102        |
| <b>4</b> | <b>UNCERTAINTY QUANTIFICATION</b>   | <b>103</b> |
| 4.1      | Introduction . . . . .  | 103        |
| 4.2      | UQ methodologies . . . . .  | 104        |
| 4.2.1    | Probabilistic Collocation Method . . . . .  | 104        |
| 4.2.2    | Simplex Stochastic Collocation . . . . .  | 105        |
| 4.2.3    | Bayesian-Kriging . . . . .  | 107        |
| 4.2.4    | Mean Value Second Order Second Moment . . . . .   | 108        |
| 4.3      | Sensitivity of supersonic ORC nozzle guide vane designs to fluctuating operating conditions . . . . . | 110        |
| 4.3.1    | Sensitivity of supersonic convergent-divergent nozzle designs . . . . .                               | 110        |
| 4.3.2    | Sensitivity of supersonic nozzle guide vane designs . . . . .   | 113        |
| 4.4      | Selection of an efficient uncertainty quantification method for ORC applications .                    | 117        |
| 4.5      | Conclusions . . . . .   | 120        |
| <b>5</b> | <b>ROBUST OPTIMIZATION OF SUPERSONIC ORC NOZZLE GUIDE VANES</b>                                       | <b>122</b> |
| 5.1      | Introduction . . . . .  | 122        |
| 5.2      | Shape parametrization: FFD method . . . . .   | 124        |
| 5.3      | Robust Optimization strategy . . . . .  | 127        |
| 5.3.1    | Adaptive sample infill strategy . . . . .   | 128        |
| 5.3.2    | Parallelisation of the RO on cluster . . . . .  | 131        |
| 5.4      | Numerical verifications . . . . .   | 131        |
| 5.4.1    | Surrogate-based optimization of the multi-dimensional Kursawe function .                              | 132        |
| 5.4.2    | RO of a quasi-1D supersonic nozzle . . . . .  | 132        |
| 5.5      | Application: RO of ORC nozzle guide vanes . . . . .   | 135        |
| 5.6      | Conclusions . . . . .   | 141        |
|          | <b>CONCLUSIONS AND PERSPECTIVES</b>   | <b>142</b> |
| <b>I</b> | <b>Appendix</b>   | <b>147</b> |
| I.1      | Spatial grid convergence study . . . . .  | 147        |
| I.1.1    | Nozzle guide vane . . . . .   | 148        |
| I.1.2    | Isolated rotor . . . . .  | 149        |



# List of Figures

|     |  |    |
|-----|--|----|
| 1   | Contour del numero di Mach per RODEC (a) e deviazione di entropia (b). . . . .   | 4  |
| 2   | Mach number contour plot (a) and entropy deviation (b) for RODEC rotors with boundary layer correction. . . . .  | 5  |
| 3   | Contour del numero di Mach per RODEC (a) and archi di cerchio (b). . . . .   | 6  |
| 4   | Distribuzione di pressione a parete sul rotore per simulazione viscosa con correzione di strato limite e confronto con la distribuzione di riferimento. . . . .  | 7  |
| 5   | Contour plots del numero di Mach per la baseline (a); Contour plots del numero di Mach per il profilo ottimizzato deterministicamente (b). . . . .   | 8  |
| 6   | Variazione del numero di Mach per: Baseline (a); profilo ottimizzato deterministico (b); profilo ottimizzato robusto (c). . . . .  | 9  |
| 7   | Contour du nombre de Mach pour RODEC (a) et deviation d'entropie (b). . . .  | 12 |
| 8   | Contour du nombre de Mach contour (a) et deviation de l'entropie (b) pour les rotors RODEC avec correction de la couche limite. . . . .  | 14 |
| 9   | Contour du nombre de Mach pour RODEC (a) et des arcs de cercle (b). . . . .  | 15 |
| 10  | Répartition de la pression de la paroi sur le rotor pour la simulation viscosse avec une correction du couche limite et comparaison avec la distribution de référence. . . . .   | 16 |
| 11  | Contour du nombre de Mach pour la ligne de base (a); Contour du nombre de Mach pour le profil optimisé déterministe (b). . . . .   | 16 |
| 12  | Variation du nombre de Mach pour: Baseline (a); profil déterministe optimisé (b); profil robuste optimisé (c). . . . .   | 17 |
| 1.1 | (a) Scheme of an Organic Rankine Cycle. (b) Comparison between steam and generic organic working fluid saturation curves. Figures extracted from (Karellas and Schuster, 2008). . . . .  | 29 |
| 1.2 | Energy balance of a 1.4 l spark ignition engine. Figures extracted from (El Chammas and Clodic, 2005). . . . .   | 30 |
| 1.3 | Enthalpy diagram showing thermal match in a supercritical ORC. (a) Heating R152a in a subcritical ORC at 20 bar from 31.16 °C to 100 °C. (b) Heating R143a in a supercritical ORC at 40 bar from 33.93 °C to 100 °C. Figures extracted from (Saleh et al., 2007). . . . .  | 31 |
| 1.4 | Schematic sketch of the Organic Rankine Cycle used to recover the heat discharged by the exhaust gases of the Diesel power pack in the project TREENERGY. . . .  | 33 |
| 2.1 | Clapeyron diagram in terms of reduced variables for the R245fa fluid, ruled by the Peng-Robinson-Stryjek-Vera EOS. The grey area represents the dense-gas region, delimited by the unit iso- $\Gamma$ line. The dotted line represents the critical isotherm, whereas the black dot a typical ORC turbine start condition. . . . . | 36 |

|      |   |    |
|------|---|----|
| 3.1  | Characteristic line patterns and nozzle divergent shape design. . . . .   | 49 |
| 3.2  | Pressure-density plots along isentropes for four organic fluids at total reduced conditions $p_r=1.28$ , $T_r=1.05$ . . . . .   | 53 |
| 3.3  | Schematic geometrical post-processing for the ORC turbine blade vane generation. . . . .  | 56 |
| 3.4  | Flow-chart of the MOC algorithm for stator designs. . . . .   | 57 |
| 3.5  | Nozzle divergent shape calculated for the three gas models and R245fa fluid. The axis are normalized respect to the nozzle throat half-height $H_t$ . . . . .   | 58 |
| 3.6  | (a) Sketch of the nozzle convergent design procedure (b) Computational grid used for the calculations. . . . .  | 59 |
| 3.7  | Comparison among the Euler calculations and NODEC results: (a) Reduced pressure evolution along the nozzle axis. (b) Reduced pressure evolution along the nozzle wall. (c) Mach number evolution along the nozzle axis. (d) Mach number evolution along the nozzle wall. . . . .  | 60 |
| 3.8  | Results for the inviscid simulation for fluid R245fa: (a) Mach number contour plot. (b) Speed of sound contour plot. (c) Fundamental Derivative $\Gamma$ . The nozzle geometry is normalised with respect to the throat height. (d) Mach number contour plot provided by the NODEC algorithm. Only the divergent part of the nozzle has been computed with the MOC. . . . . | 61 |
| 3.9  | REF Vs PRSV model results for inviscid simulations: (a) Nozzle axis Mach number distribution. (b) Wall nozzle Mach number distribution. . . . .   | 62 |
| 3.10 | Numerical results for inviscid calculations with fluid R245fa: (a) Mach number contour plot. (b) Reduced static pressure $p/p_c$ contour plot. (c) Fundamental Derivative $\Gamma$ contour plot. (d) Stream traces on the trailing edge with Mach number contour plot. . . . .  | 64 |
| 3.11 | Clapeyron diagram with iso- $\Gamma$ and nominal isentrope lines for: (a) R245FA (b) NOVEC649 (c) R449 (d) RE347MCC; fundamental derivative profiles along the blade vane centerline for fluids R245fa and R449 (e). . . . .  | 66 |
| 3.12 | Viscous results for R245fa: (a) Mach number contour plot. (b) Stream traces underlining the presence of a recirculation bubble. . . . .   | 67 |
| 3.13 | Example of impulse blade geometry and velocity triangles . . . . .  | 68 |
| 3.14 | Scheme of the system of characteristic lines in the rotor vane. (Goldman, 1968) . . . . .   | 69 |
| 3.15 | Schematic description of the rotor blade design. . . . .  | 70 |
| 3.16 | Lower transition arc design. . . . .  | 70 |
| 3.17 | Blade designs for R245FA at operating conditions ( $p_r^0 = 1.05$ , $T_r^0 = 1.05$ , $M_{in} = M_{out} = 1.5$ ) (a) and at dilute conditions ( $p_r^0 = 0.055$ , $T_r^0 = 1.15$ , $M_{in} = M_{out} = 1.5$ )(b). Dashed lines represent designs obtained under the perfect gas model. . . . .   | 72 |
| 3.18 | Examples of blade design for R245FA at operating conditions ( $p_r^0 = 1.05$ , $T_r^0 = 1.05$ ) for different inlet and outlet Mach numbers and flow turning angles. . . . .  | 73 |
| 3.19 | Bow-shocks pattern for a supersonic rotor row. . . . .  | 74 |
| 3.20 | Total pressure losses across a shock as function of the wall deflection $\delta$ for a perfect gas. Figure extracted from (Paniagua et al., 2014). . . . .  | 75 |
| 3.21 | Unstarted configuration for a supersonic rotor blade row. . . . .   | 76 |
| 3.22 | Started configuration for a supersonic rotor blade row. . . . .   | 76 |
| 3.23 | Bow shock schematic representation on the leading edge of a supersonic rotor. . . . .   | 77 |
| 3.24 | Definition of the area sections for a supersonic rotor. . . . .   | 79 |
| 3.25 | Kantrowitz contraction factor as function of the inlet Mach number for the R245fa fluid. . . . .  | 79 |
| 3.26 | Comparison of the Kantrowitz contraction factor as function of the inlet Mach number for the R245fa fluid in dense and dilute gas conditions. . . . .   | 80 |

|      |  |     |
|------|--|-----|
| 3.27 | Flow patterns and related boundary conditions of possible cascade flow configurations, where $\beta_1$ and $\beta_2$ are the inlet and outlet relative flow angles, respectively. Figure extracted from (Starken, 1993).   | 81  |
| 3.28 | Characteristics pattern and expansion fan lines for a supersonic rotor (a); definition of the control volume upstream and downstream of the bow-shock (b).   | 82  |
| 3.29 | Geometric scheme of the bow-shock and sonic line (Moeckel, 1949) (a); oblique shock geometric scheme and reference system (b).   | 83  |
| 3.30 | Main characteristic lines on the rotor leading edge.   | 84  |
| 3.31 | Unique incidence solution and comparison of the inlet and incidence flow angles, $\phi_1$ and $\beta_{i,1}$ respectively, as functions of the inlet Mach number $M_1$ for the R245fa fluid in dense ( $p_r^0 = 0.1$ , $T_r^0 = 0.95$ ) and dilute ( $p_r^0 = 0.01$ , $T_r^0 = 1.18$ ) gas conditions. The solution is evaluated for a $r/s$ ratio of 0.05 (with $r$ the leading edge radius and $s$ the cascade pitch) and a stagger angle $\beta_s = \pi/3$ . | 85  |
| 3.32 | Mach number contour plot for RODEC (a) and circular arcs (b) designs.  | 86  |
| 3.33 | Entropy deviation $(S - S_{in})/S_{in}$ (with $S$ the specific entropy and $S_{in}$ an inlet entropy reference) contour plot for RODEC (a) and circular arcs (b) designs.  | 87  |
| 3.34 | Typical velocity triangles for an axial turbine stage. Figure extracted from (Cohen et al., 1987).   | 88  |
| 3.35 | Isentropic turbine expansion on the R245FA T-S diagram (a); Fundamental Derivative of gas dynamics $\Gamma$ evaluated along the turbine expansion (b).   | 91  |
| 3.36 | Computational block structured grid for full turbine stage (330066 elements) (a); relative Mach number distribution for R245FA fluid (b).  | 92  |
| 3.37 | Entropy deviation contour plot for the isolated rotor (R245FA fluid) (a); Mach number distribution for the isolated rotor (R245FA fluid) (b).  | 93  |
| 3.38 | Comparison between inviscid (red) and viscous (green) shape for nozzle calculation with R245FA fluid.  | 96  |
| 3.39 | Comparison between inviscid and viscous nozzle guide vane shapes with view enlargement of the exit section.  | 97  |
| 3.40 | Comparison between inviscid (a) and viscous (b) nozzle blade shapes Mach number contour plot.  | 98  |
| 3.41 | Integral boundary layer parameters (a); Compressible Ludwig-Tillmann skin friction coefficient (b).  | 99  |
| 3.42 | Comparison between inviscid and viscous nozzle shape of the static enthalpy evolution along the guide vane center-line.  | 100 |
| 3.43 | Comparison between inviscid and viscous impulse rotor blade shapes.  | 100 |
| 3.44 | Mach number contour plot (a) and entropy deviation (b) for RODEC rotors with boundary layer correction.  | 101 |
| 4.1  | Delaunay triangulation of randomized sampling points in a two-dimensional parameter space $\Xi$ with $n_\xi = 2$ before (a) and after (b) refinement.  | 106 |
| 4.2  | Bayesian-Kriging algorithm test for the 2-D Rosenbrock function. (a) True function; (b) surrogate function with 20 samples; (c) surrogate error in terms of Kriging variance.  | 109 |
| 4.3  | Coefficient of Variation (a) and mean value (b) of the Mach number for uniformly distributed input parameters ( $\pm 3\%$ of variation around the nominal point).  | 111 |
| 4.4  | Variability of the nozzle shape geometry for uniformly distributed input parameters ( $\pm 3\%$ of variation around the mean value).   | 111 |
| 4.5  | Variability of the nozzle shape geometry for beta distributed input parameters (8% Coefficient of Variation).  | 112 |

|      |  |     |
|------|--|-----|
| 4.6  | Coefficient of Variation of the nozzle Mach number for beta distributed input parameters (8% Coefficient of Variation). . . . .  | 112 |
| 4.7  | Coefficient of Variation of Mach number for beta distributed input parameters (8% Coefficient of Variation) for an inviscid stochastic calculation (a); mean Mach number contour plot for beta distributed input parameters ((8% Coefficient of Variation) for an inviscid stochastic calculation. . . . .   | 113 |
| 4.8  | Coefficient of Variation (a) and mean (b) of Mach number contour plot for five uniformly distributed input parameters for an inviscid stochastic calculation (a). . . . .  | 115 |
| 4.9  | ANOVA of the contribution of the five input parameters to the variance of the Mach number along the vane axis (a) and of the nozzle blade performances in terms of efficiency and power output (b). . . . .  | 116 |
| 4.10 | Mean (a) and Coefficient of Variation (b) of the Mach number for a viscous supersonic nozzle blade vane evaluated by means of the full-factorial PCM with five uncertainties. The wake is visible at the vane exit, which is source of high levels of uncertainty. . . . .   | 118 |
| 4.11 | Mean and Coefficient of Variation of the blade vane isentropic efficiency for the four UQ models. . . . .  | 119 |
| 4.12 | Comparison of the different UQ models sampling strategy in terms of maximum Kriging error. . . . .   | 119 |
| 5.1  | Application of FFD to a supersonic nozzle blade for a $l \times m$ lattice ( $l = 6, m = 1$ ) with 8 control parameters. (a); classical parametrization by means of Bezier's curves of the nozzle blade pressure side (b). . . . .   | 126 |
| 5.2  | Flow chart of the RO algorithm. . . . .  | 127 |
| 5.3  | Probability of improvement and expected improvement for one-dimensional test function: solid line, true function $f_e(x)$ ; x , sample points; dashed line, Kriging surrogate. Figure extracted from (Keane, 2006). . . . .  | 128 |
| 5.4  | Example of Pareto fronts of a two-objective optimization process. (a) Pareto front with augmenting (shaded area) and dominating (hatched area) designs; (b) possibilities of improvement during optimization; (c) centroid of probability integral and moment arm used for calculating the multi-objective expected improvement. Figures extracted from (Keane, 2006). . . . . | 130 |
| 5.5  | Pareto fronts comparison among exact 2-D Kursawe function and Kriging surrogates with and without MOEI (a); exact Pareto front and comparison with the Kriging surrogate best individuals recalculated with the exact 2-D Kursawe function (b). . . . .  | 133 |
| 5.6  | Exact Pareto front and comparison with the Kriging surrogate best individuals recalculated with the exact 8-D Kursawe function. . . . .  | 133 |
| 5.7  | Scheme of the quasi-1D nozzle optimization problem. . . . .  | 134 |
| 5.8  | Maximum Kriging error estimate convergence plot as function of the number of samples. (a); Variance and mean convergence plot as function of the number of samples (b). . . . .  | 135 |
| 5.9  | Pareto fronts comparison between high-fidelity CFD RO and Kriging surrogate (with and without MOEI) RO. (a); Pareto individuals recalculation for the Kriging surrogate with MOEI and comparison with CFD (b). . . . .   | 135 |
| 5.10 | Mach contour plots for the baseline design (a); the deterministically optimized blade (b); and the robustly optimized blade (individual #A, from Fig. 5.12) (c). . . . .   | 136 |
| 5.11 | Convergence of the UQ Kriging surrogate statistics for the nozzle guide vane baseline. . . . .   | 137 |

|      |  |     |
|------|--|-----|
| 5.12 | Pareto front of the ORC nozzle RO. Horizontal arrow: design compared with the deterministic optimization. (a); Comparison among baseline and deterministically and robustly optimized shapes. The robust shape is selected from the center zone of the Pareto front (horizontal arrow in (a)) (b); Pareto front comparison between full CFD (red points) and Kriging-surrogate with MOEI (blue squares) RO. The green diamonds corresponds to the Kriging-MOEI Pareto individuals (marked with green square) recomputed with Kriging UQ. The individual marked with #A is used for further comparisons with the other designs (c). . . . . | 139 |
| 5.13 | Mach percent variation contour plots of: Baseline (a); Deterministically optimized shape (b); Robustly optimized shape (individual #A, see Fig. 5.12) (c). . . . .   | 140 |
| I.1  | Computational domain of the nozzle guide vane and boundary conditions. . . .   | 148 |
| I.2  | Computational mesh details of the nozzle guide vane leading and trailing edge, for viscous ((a)-(b), medium mesh with 384· 128 cells), and inviscid ((c)-(d), medium mesh with 384· 64 cells) calculations. . . . .  | 149 |
| I.3  | Nozzle guide vane wall pressure distributions for the inviscid (a) and viscous (b) grids. . . . .  | 150 |
| I.4  | Computational domain of the isolated rotor and multi-block split strategy (a); leading edge detail of the medium computational viscous mesh of the rotor (98304 cells) (b); wall rotor pressure distributions for the three computational grids (c). . . . .   | 151 |

# List of Tables

|      |  |     |
|------|--|-----|
| 1    | Variabili incerte. Pressione e temperatura totali ridotte ( $p_{0_r}$ , $T_{0_r}$ ), spessore della pala $\varepsilon$ . . . . .   | 8   |
| 2    | Variables incertaine: pression et température réduite totale ( $p_{mathit{0_r}}$ , $mathit{0_r}T$ ), épaisseur de la lame <i>varepsilon</i> . . . . .  | 18  |
| 2.1  | Thermophysical properties for different organic substances, based on reference EOS (from REFPROP ver. 9.1). . . . .  | 44  |
| 2.2  | R245fa coefficients for the technical EOS, Eq. (2.47). . . . .   | 45  |
| 2.3  | R245fa coefficients for the ideal-gas state reduced Helmholtz free-energy, Eq. (2.44), with $M_1 = 2$ and $M_2 = 3$ . . . . .  | 45  |
| 2.4  | Coefficient for the calculation of the ideal heat capacity, Eq. (2.49). . . . .  | 45  |
| 2.5  | Number of elements in the sums of Eq. (2.45) for the three working fluids. . . . .   | 45  |
| 3.1  | $\gamma$ for the four organic substances used in this Section. . . . .   | 52  |
| 3.2  | Polytropic coefficient $\gamma_{eq}$ for different organic substances at total reduced conditions $p_r=1.28$ , $T_r=1.05$ . . . . .  | 52  |
| 3.3  | Test case reduced operating conditions and design parameters . . . . .   | 57  |
| 3.4  | Expansion pressure ratio $\beta = p_t/p_{out}$ results for $M_e = 2.06$ and $G = 20kg/s \cdot m$ . . . . .   | 58  |
| 3.5  | Main settings for the computational simulations and the nozzle blade vane design. . . . .  | 60  |
| 3.6  | Summary of the guide vane performances for different working fluids and blade designs based on various gas models. . . . .   | 63  |
| 3.7  | Summary of the guide vane performances for R245fa fluid, viscous calculations and blade shape calculated with REF model. . . . .   | 64  |
| 3.8  | Operating and design conditions for the rotor design. . . . .  | 72  |
| 3.9  | Geometrical output parameters for four different organic fluids under the same operating condition ( $p_r^0 = 1.05$ , $T_r^0 = 1.05$ , $M_{in} = M_{out} = 1.5$ , $M_l = 1$ , $M_u = 2$ , $\beta_{in} = \beta_{out} = 65^\circ$ ). . . . . | 72  |
| 3.10 | Rotor blade design parameters for R245fa fluid. . . . .  | 86  |
| 3.11 | Rotor blade design parameters. . . . .   | 90  |
| 3.12 | Main turbine full stage working parameters. . . . .  | 91  |
| 3.13 | Main turbine working parameters. . . . .   | 96  |
| 3.14 | Main nozzle performances with and without boundary layer correction. . . . .   | 97  |
| 4.1  | Nominal nozzle operating conditions. . . . .   | 113 |
| 4.2  | Means and variations of nozzle guide vane performances (two uncertainties case). . . . .   | 113 |
| 4.3  | Means and variations of nozzle guide vane performances (five uncertainties case). . . . .  | 115 |
| 4.4  | Nozzle main design parameters. . . . .   | 118 |
| 4.5  | Input uncertain parameters and their distributions. . . . .  | 118 |

|     |   |     |
|-----|---|-----|
| 4.6 | Performance analysis of the UQ models. . . . .  | 119 |
| 5.1 | Uncertain variables for the 1D supersonic nozzle. Total pressure and temperature are normalised respect to the critical values, $\varepsilon$ is the wall nozzle displacement. . .  | 134 |
| 5.2 | Nominal nozzle parameters. Total pressure and temperature are normalised with respect to the critical values whereas $\beta$ is the throat-to-exit static pressure ratio. . .   | 136 |
| 5.3 | Uncertain variables for the ORC supersonic nozzle. Total pressure and temperature are normalised respect to the critical values, $\varepsilon$ is the blade thickness. . . .  | 140 |
| 5.4 | Computational costs comparison between the full CFD-based and the surrogate-based with MOEI RO. . . . .   | 141 |
| 5.5 | Summary of means and variances for the blade vane performances, Carnot factor $\Theta_C$ , specific power per depth unit and massflow per depth unit for the three nozzle guide vane shapes: baseline, deterministically optimized and robustly optimized (individual #A of Fig. 5.12). . . . . | 141 |

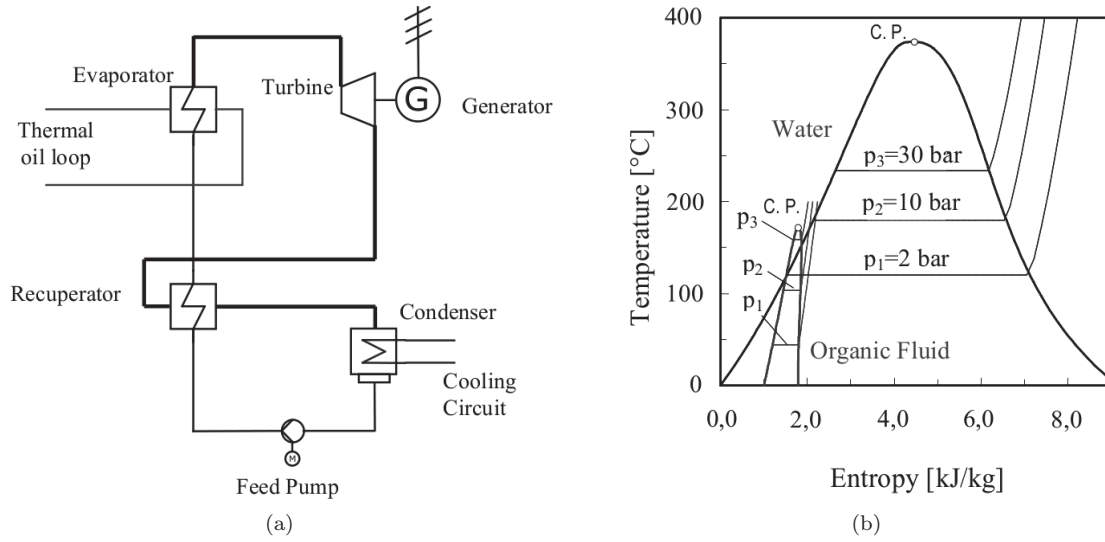
# Chapter 1

## INTRODUCTION

### 1.1 General overview

In recent years, the Organic Rankine Cycle (ORC) technology has received great interest from the scientific and technical community because of its capability to recover energy from low-grade heat sources. ORC is similar to a Rankine steam cycle, but uses an organic working fluid instead of water. A sketch of an ORC layout is shown in 1.1a. The working fluid is compressed and pumped in the evaporator by the feed pump. Before evaporation it is also pre-heated by the recuperator which exploits the heat of the expanded fluid. After evaporation, the enthalpy drop is converted into electric energy by means of a turbine expander coupled with a generator. In co-generation applications this energy can be converted also into thermal power output. The fluid is then cooled in the condenser in order to close the thermodynamic cycle. The thermal oil loop represents here the low-grade heat-transfer fluid which extracts energy from different sources. The most widespread and promising fields of application of ORC are: waste heat recovery (WHR), biomass power plant, geothermal plants and solar thermal power (Quoilin et al., 2013). The working fluid is usually a low boiling organic fluid, e.g. a refrigerant, a hydrocarbon or a silicon oil, which allows exploiting lower-temperature heat sources (Lemort et al., 2012). Indeed, due to its thermodynamic and physical properties, steam is not suitable for these applications (Colonna et al., 2015). Specifically, the low specific heat of water, if compared with an organic working fluid at the same power input, would provide smaller massflows and higher enthalpy drops, leading to a larger number of expansion stages and to small flow passages. Besides, steam does not provide lubrication of the expander inner contact surfaces implying the use of external lubricants with loss of overall efficiency. Finally, the steam expander design becomes challenging in this conditions and the efficiency improvement margins are very narrow. On the other hand, the use of a fluid with high molecular mass and a lower boiling point than water can provide lower enthalpy drops, higher expander flow passages and the friction losses minimized by the intrinsic lubricating properties of some organic working fluids. Other advantages of organic fluids commonly used in ORC applications are their lower critical temperatures and pressures, high thermal conductivity, high thermal stability, low corrosivity and toxicity, and compatibility with cycle component materials (Kandathil, 2015). As it has been widely investigated (Yamamoto et al., 2001; Karellas and Schuster, 2008), thermo-physical properties of the organic fluid play a fundamental role for system efficiency. Specifically, low boiling point, high density in gas phase, low critical temperature and low latent heat are the main characteristics required for an optimal usage of the low-grade heat sources. Efficiency improvement techniques like the introduction of superheaters, are not always profitable for these high specific heat fluids, because of the huge

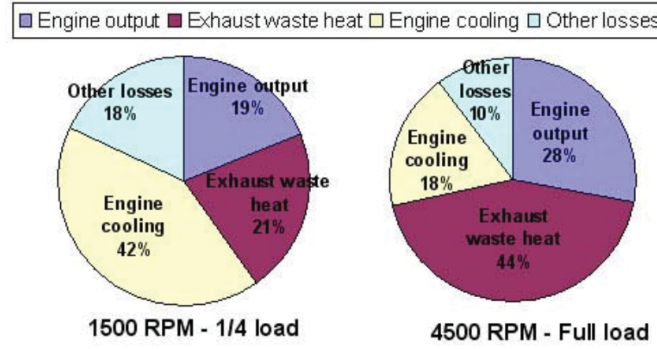




**Figure 1.1:** (a) Scheme of an Organic Rankine Cycle. (b) Comparison between steam and generic organic working fluid saturation curves. Figures extracted from (Karellas and Schuster, 2008).

exchange surfaces that would be required (Chen et al., 2010). However, superheating is generally not necessary for working fluids of the "retrograde" or "dry" type (i.e. with a positive slope of the liquid/vapor coexistence curve, see Fig.1.1b). Indeed the expansion, starting from saturated vapor conditions, leads to dry final conditions and does not produce any liquid phase. For these reasons, most working fluids used in ORC, such as R245fa, R134a, R227ea (refrigerants) or MM, MDM, MD2M (silicon oils) are dry fluids (Maizza and Maizza, 1996; Saleh et al., 2007; Mago et al., 2007; Schuster et al., 2010; Hung et al., 2010).

In some applications, as WHR, ORC plants need to be as compact as possible because of geometrical and weight constraints. Recently, these issues have been studied in order to promote the ORC technology for Internal Combustion Engine (ICE) applications. It has been estimated that only about one-third of the fuel energy is converted into mechanical power on typical driving cycles at full load (El Chammas and Clodic, 2005; Quoilin et al., 2013), see Fig. 1.2. For example, a typical 1.4 l spark ignition ICE, with a thermal efficiency ranging from 15% to 32%, releases 1.7–45 kW of heat through the radiator (at a temperature close to 80–100 °C) and 4.6–120 kW via the exhaust gas (400–900 °C). The idea to recover this residual energy is not new and the 1970s energy crisis encouraged the development of feasible ORC small-scale plants (1-10 kWe) (Platell, 1976; Doyle et al., 1979). A practical solution was found for the first time by Mack Trucks (Patel and Doyle, 1976) for a 288 HP truck engine by using a fluorinol mixture as working fluid. In recent years other more effective solutions have been proposed by Honda (Strobl et al., 2008) and BMW (Ibaraki et al., 2007) for passenger cars and Cummins (Nelson, 2008) for long-haul trucks. Even if the performances of recently developed prototypes of ORC for automotive applications seem promising (El Chammas and Clodic, 2005; Endo et al., 2007; Teng and Regner, 2009), with reduction of fuel consumption up to 12% and engine thermal efficiency improvements of 10%, currently no commercial ORC solutions in the automotive field are available. This is mainly due to the low robustness of the present technology to the large range of operational conditions on



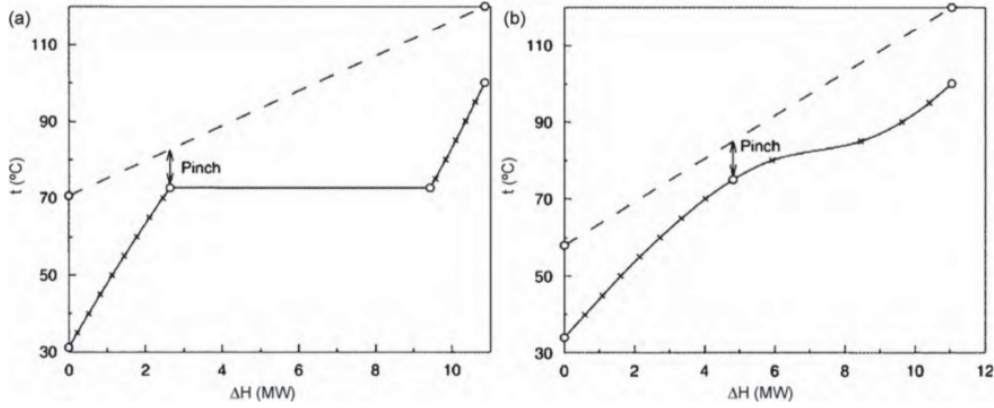
**Figure 1.2:** Energy balance of a 1.4 l spark ignition engine. Figures extracted from (El Chammas and Clodic, 2005).

typical duty driving cycles and the subsequent low improvements of engine global performances compared to the economic effort to realize the ORC components. On the other hand, the research in this field remains fertile and the challenge of a cost-effective WHR for automotive applications implies the development of contributions on many other subjects. In this sense, a key component of the ORC is the working fluid which have to satisfy engineering, legislations and, where applicable, health and safety requirements. Depending on the application, a widespread set of organic fluids is available. A comprehensive analysis on the most suitable fluid for solar plant applications is provided by Rayegan and Tao (2011) who experimentally compare the performances of 115 fluids of the REFPROP 8.0 library, while Jing et al. (2010) focus the attention on the R123 refrigerant. Borsukiewicz-Gozdur and Nowak (2007) found the R236ea to be the best choice for a geothermal application in the 80-120 °C temperature range. For WHR, Glover et al. (2015) provide a rational selection of 16 suitable fluids among 105 candidates, focusing attention on R144a and R245fa. They show the importance of shape and slope of the isothermal curves close and away from the wet region to WHR ORC performance. Dai et al. (2009) carry out a parametric study of ORC performances under different working fluids, whose thermodynamic properties are optimized with exergy efficiency as an objective function by means of a genetic algorithm, leading to the selection of R236ea as the best candidate for this application. In many other studies (Maizza and Maizza, 1996, 2001; Gu et al., 2009) a thorough selection of working fluids for WHR, made both with experimental and numerical techniques, can be found.

Supercritical and transcritical ORC cycles, i.e. cycles for which the expander inlet conditions are characterized by pressures and temperatures beyond the liquid/vapour critical point, have also been studied extensively. In this way, the low-grade heat source is better exploited thanks to a better thermal matching (see Fig. 1.3), improving the heat exchange efficiency and avoiding the use of regeneration, simplifying the plant layout (Saleh et al., 2007).

Most organic fluids of interest for ORC are characterized by a complex thermodynamics behaviour and exhibit considerable deviations from perfect gases. Specifically, several ORC working fluids fall within the category of so-called *dense gases*.

This may lead to uncommon fluid dynamic behaviours, namely in transonic and supersonic regimes, as discussed, e.g., by Thompson (1971). Further developments of dense gas dynamics have been made in the years (see (Aldo and Argrow, 1995; Monaco et al., 1997; Brown and Argrow, 2000; Guardone et al., 2004) for a review). Especially, the role of dense gas dynamics in transonic internal flows has been widely studied (Kluwick, 2004; Cinnella and Congedo, 2005b; Wheeler and Ong, 2013; Guardone et al., 2013; Guardone and Vimercati, 2016), due to its im-



**Figure 1.3:** Enthalpy diagram showing thermal match in a supercritical ORC. (a) Heating R152a in a subcritical ORC at 20 bar from  $31.16^{\circ}\text{C}$  to  $100^{\circ}\text{C}$ . (b) Heating R143a in a supercritical ORC at 40 bar from  $33.93^{\circ}\text{C}$  to  $100^{\circ}\text{C}$ . Figures extracted from (Saleh et al., 2007).

portance for turbomachinery applications involved in low-grade energy exploitation, such as the ORC. The peculiar behaviour of dense gases observed in transonic and supersonic regimes, needs to be taken accurately into account when designing ORC components, as namely the expander, whose performance strongly influences that of the global cycle. Depending on the operating conditions and the size of the system, a turbine or a volumetric expander can be used. Historically, the positive-displacement expanders have found a widespread diffusion for ORC applications thanks to their low cost and manufacturing simplicity due to their conversion from volumetric compressors (e.g. scroll, screw, piston, vane expanders) (Song et al., 2015; Potenza et al., 2014). They assure low flow rates, high pressure ratios and low rotational speeds which allow to avoid the use of gear-boxes, reducing weight and mechanical complexity. However, for small-scale applications as automotive WHR, they do not show high performances due to volumetric expander intrinsic problems as low adaptivity to volumetric ratios different from the nominal ones, resulting in losses for under- or over-expansions, internal leakages and lubricating issues (Quoilin et al., 2013). On the other hand, turbo-expanders could provide higher performances in a wide range of operating conditions, but the high rotational velocities, high pressure ratios, complexity of the working fluids and the need for a compact geometry make the design of an efficient ORC turbine challenging. The mean-line preliminary design by means of 1-D analysis has been carried out for centrifugal expanders (Pini et al., 2013; Casati et al., 2014). On the base of these results, Persico et al. (2015) has investigated the aerodynamic performance of a fixed and a rotating cascade of centrifugal turbine by applying a three-dimensional CFD model.

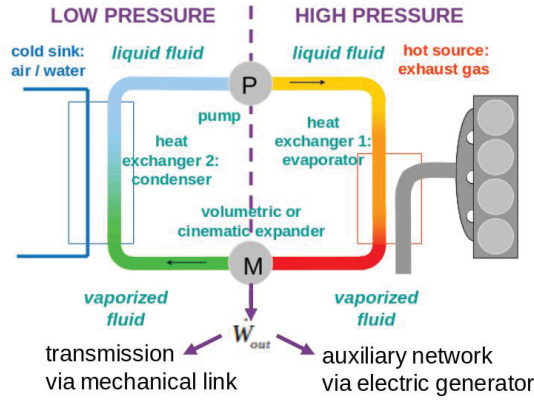
Few authors have proposed more accurate 2-D mean-line design solutions, by focusing attention on radial expanders (Wheeler and Ong, 2013; Rinaldi et al., 2015), which allow to develop higher enthalpy drops than axial expander. However, for WHR with ORC, the attention has been recently focused on axial turbines, which reduce the average system size, if compared with radial solutions at the same pressure ratios and enthalpy drops. Especially, the axial configuration with low degree of reaction is well known to be able, for steam turbine applications, to elaborate high pressure ratios in a minimum number of stages (generally one or two, see e.g. the Curtis turbine wheels) ensuring high performances and high specific work at the nominal point. Unfortunately, these characteristics are challenging to realize for an organic working fluid, due to its thermo-

physical properties and operating conditions. Indeed, the pressure ratios, combined with the low speed of sound, leads the flow to be transonic or supersonic resulting in strong shock waves.

In this thesis work, a novel design methodology for supersonic ORC axial impulse turbine stages is proposed. It consists in a fast, accurate two-dimensional design which is carried out for the mean-line stator and rotor blade rows of a turbine stage by means of a method of characteristic (MOC) extended to a generic equation of state. The viscous effects are taken into account by introducing a proper turbulent compressible boundary layer correction to the inviscid design obtained with MOC. A first study of the influence of dense gas effects on the design of nozzles by means of MOC was provided by Aldo and Argrow (1995), who implemented the Van der Waals equation of state into the design process of minimum length nozzles. To the authors knowledge, only recently a MOC equipped with complex equations of state has been proposed to study the influence of the molecular complexity of the working fluid on planar supersonic nozzles (Guardone, 2010; Guardone et al., 2013), while a MOC with a Prandtl-Meyer function modified for real gases has been proposed to design supersonic radial nozzle guide vanes (Wheeler and Ong, 2013). For the first time, a thorough approach for axial supersonic ORC turbine stages is described and tested.

The design methodology mentioned above, however, is insufficient to design efficient turbines if other aspects are not taken into account. Proposed heat sources for ORC turbines typically include variable energy sources such as WHR from industrial processes or automotive applications. As a result, to improve the feasibility of this technology, the resistance to variable input conditions must be taken into account at an early stage of the development process. Robust design has been developed to improve the product quality and reliability in industrial Engineering. The concept of robust design had been introduced by Taguchi in the late 1940s and his technique has become commonly known as the Taguchi method or robust design (Fowlkes and Creveling, 1995; Park et al., 2004). Since 1980s, the Taguchi method has been applied to numerical optimization under uncertainties. This newly developed method is often called robust optimization and it overcomes the limitation of deterministic optimization that neglects the effect of uncertainties in design variables and design parameters. The robustness is determined by a measure of insensitivity of the design with respect to variations of the design parameters, like geometrical tolerances or fluctuations of the operating conditions. To measure the robustness of a new design, statistics such as mean and variance (or standard deviation) of a response are calculated in the robust optimization process. Currently, there are significant difficulties associated with calculation of statistics of the objective function, especially in fluid dynamics, where each evaluation of the cost functions requires solving a complex non-linear problem with many degrees of freedom. In recent years, several robust optimization techniques for aerodynamic problems have been proposed (Duvigneau, 2007; Cinnella and Hercus, 2010; Tang and P riaux, 2012). In most cases, applications have been limited to problems like flow around isolated airfoils. Some applications to 2D compressor blades have also been investigated (Kumar et al., 2008; Hercus and Cinnella, 2011). Additionally, the computational cost of robust optimizations needs to be drastically reduced to make it feasible for configurations of practical interest.

This work is a contribution to the development of an efficient methodology for the design and the robust optimization of ORC turbine blades. It is part of the project TREENERGY (TRain ENergy Efficiency via Rankine-cycle exhaust Gas heat recoverY), funded by the French Agence Nationale de la Recherche, and involving partners as IFPEN (Institut Fran ais du P trole Energies Nouvelles), ALSTOM, and ENOGIA (French constructor for ORC engines). In this context, the project aims at evaluating the interest of using a Rankine Cycle in order to recover some lost heat and to increase the efficiency of the Diesel power packs used as engine of a new concept train, namely the *Regiolis*, built by ALSTOM. In Fig. 1.4 a scheme of the ORC system is shown. The use of Rankine cycle systems has already been investigated in the past for transportation



**Figure 1.4:** Schematic sketch of the Organic Rankine Cycle used to recover the heat discharged by the exhaust gases of the Diesel power pack in the project TREN-ERGY.

means (train, trucks and more recently cars), but the fact is that up to now they are mainly used for stationary equipments (power plants, heat recovery for boilers, furnaces and ovens etc.) or for heavy ships. For lighter transportations, several scientific and technical bottlenecks still have to be addressed before Rankine cycles may represent profitable devices for increasing energy efficiency. This is especially due to the highly variable behaviour of the heat source that characterizes this kind of applications.

In this framework, the collaboration with the DynFluid Laboratory ParisTECH has aimed to develop the tools for the design of a compact high efficient low-power turbine and the contribution is reported in this thesis work.

## 1.2 Thesis outline

This work aims at providing a complete description of the turbine design process, starting from the definition of the baseline geometry up to the robust optimization step.

The manuscript is organised as follows:

- **Chapter 2:**

- **Governing equations and numerical models** provides a description of the equations of state for real gases and the numerical methods used to evaluate the thermodynamic properties of the organic working fluids and to solve the turbulent flow governing equations, respectively;

- **Chapter 3:**

- **Fast design methodology for supersonic turbines with strong real gas effects** describes the design methodology for the ORC nozzle guide vane and supersonic rotor at mean-line. A ORC turbine stage 2-D steady simulation is provided in order to evaluate the main performances for operating conditions in the dense gas region.

- **Chapter 4:**

- **Uncertainty Quantification** describes some state-of-the-art tools for the non-intrusive uncertainty quantification (UQ) and assesses their performance for ORC nozzle blade design. A sensitivity analysis of the nozzle design to fluctuating operating conditions is carried out and efficient comparison of the different UQ methodologies is provided.
- **Chapter 5:**
  - **Robust Optimization of supersonic ORC nozzle guide vanes** discusses the Robust Optimization (RO) strategy for ORC nozzle guide vanes. The nozzle mean-line design is used as baseline whereas the UQ tool selected in the previous section is implemented during the optimization process to evaluate the statistics of the quantity of interest. A comparison of the robust shape with a deterministically optimized one is carried out in terms of performances and geometric differences.
- **Conclusions and perspectives:** the conclusions about the thesis work are drawn and the future perspectives are provided.

## Chapter 2

# GOVERNING EQUATIONS AND NUMERICAL MODELS

### 2.1 Dense gas dynamics

The key feature of the ORC technology is to exploit low-temperature heat sources with organic fluids which work in thermodynamic states close to the saturation curve and the critical region, where the real gas effects are dominant. The proper description of the fluid behaviour in these conditions can be done by introducing a parameter as indicator of the influence of the high density gas phase on the thermodynamic parameters evaluation. The dynamics of dense gases can be described through the thermodynamic property known as the *fundamental derivative* (Thompson, 1971):

$$\Gamma = \frac{a^4}{2v^3} \left( \frac{\partial^2 v}{\partial p^2} \right)_s = 1 + \frac{\rho}{a} \left( \frac{\partial a}{\partial \rho} \right)_s \quad (2.1)$$

where  $a$  is the speed of sound defined as  $\left[ -v^2 \left( \frac{\partial p}{\partial v} \right)_s \right]^{0.5}$ , whereas  $s$  is the specific entropy. The study of Eq. (2.1) provides informations about the behaviour of thermodynamic properties and represents a measure of the rate of change for the local speed of sound. The value of  $\Gamma$  and its sign are good revealers of local dense gas phenomena. In flow regions where  $\Gamma > 1$ , the gas shows a classical behaviour: the speed of sound drops in isentropic expansions, rises in isentropic compressions and only compression shock waves are allowed. This is the case of ideal gases, having a constant  $\Gamma = (\gamma + 1)/2 > 1$ . If  $0 < \Gamma < 1$ , it is possible to observe a reverse behaviour with respect to the previous one, but still only compression shock waves are allowed although the related shock losses are lower.

To better understand this point, it is useful to write the entropy variation across a discontinuity as series development. As shown in (Bethe, 1998), the latter can be written in the form below:

$$\Delta s = - \left( \frac{\partial^2 p}{\partial v^2} \right)_s \frac{(\Delta v)^3}{12T} + O((\Delta v)^4) \quad (2.2)$$

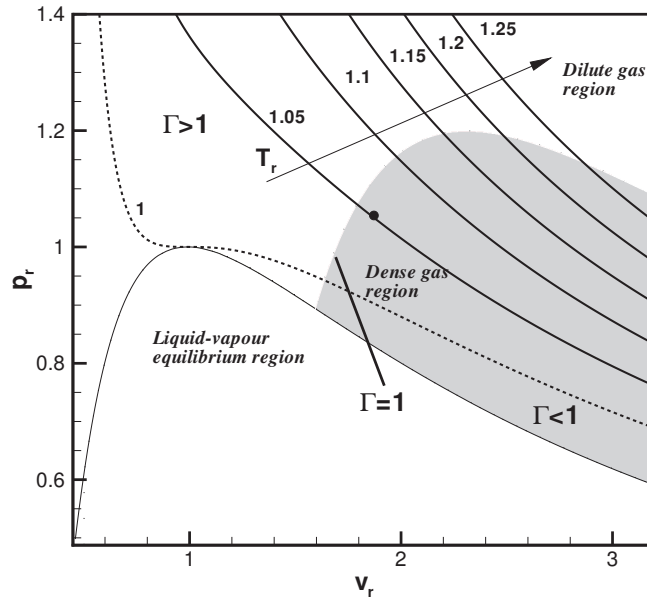
where  $\Delta v$  is the specific volume variation across the shock. The above equation shows that for positive values of  $\left( \frac{\partial^2 p}{\partial v^2} \right)_s$  only negative volume variations, i.e. compression shocks, are allowed in order to not violate the entropy condition  $\Delta s > 0$ . This behaviour is typical of fluids in dilute gas conditions, characterized by isentropes with a positive concavity shape, far from the



critical region, which are well described by the ideal gas law. By reformulating the Eq. (2.2) in function of  $\Gamma$  it is possible to get a deeper insight into the role of the dense gas dynamics for ORC turbines:

$$\Delta s = -\frac{a^2}{6v^3T}\Gamma(\Delta v)^3 + O((\Delta v)^4) \quad (2.3)$$

For  $\Gamma > 1$ , as for ideal gases, the entropy variation is of order  $O((\Delta v)^3)$ , but in the dense gas region, close to the critical point and the saturation curve, is  $\Gamma < 1$  which implies  $\Delta s \sim O((\Delta v)^4)$ . Then, in dense gas conditions the shocks are one order less dissipative than in dilute conditions, which is an advantage for ORC turbomachinery applications thanks to the minimization of the shock-wave drag losses. In Fig. 2.1 a typical ORC turbine start condition is shown by the black



**Figure 2.1:** Clapeyron diagram in terms of reduced variables for the R245fa fluid, ruled by the Peng-Robinson-Stryjek-Vera EOS. The grey area represents the dense-gas region, delimited by the unit iso- $\Gamma$  line. The dotted line represents the critical isotherm, whereas the black dot a typical ORC turbine start condition.

dot in the Clapeyron diagram in terms of reduced variables for the R245fa fluid described by the Peng-Robinson-Stryjek-Vera EOS. It is possible to see that the expansion would occur entirely in the dense gas region and, even though higher performances with respect to the dilute gas conditions are achieved, the thermodynamic modelling is much more complex and expensive in terms of computational costs.

For some fluids exists a region of negative  $\Gamma$  values in the vapor phase and they are called Bethe-Zel'dovich-Thompson (BZT) fluids which show strongly non-linear behaviour close to the critical conditions and the saturation curves. When  $\Gamma < 0$ , compression shock waves are forbidden and only expansion shock waves are physically possible (Cramer and Tarkenton, 1992). This phenomenon is theoretically predicted for a small amount of organic fluids (siloxanes, heavy



hydrocarbons, heavy fluorocarbon such as PP10, PP11, PP25 etc.) in particular thermodynamic conditions and it will not be investigated here.

Another important feature of dense gases resides in the viscous behaviour, that is very different from the light gases one. Indeed, this is intermediate between that of liquids, for which viscosity tends to decrease with increasing temperature, and that of gases, with an opposite variation. The dynamic viscosity  $\mu$  and the thermal conductivity  $\kappa$  cannot be considered independent from temperature and pressure in the real gas regions. In a similar way, the approximation of a constant Prandtl number  $Pr$  does not hold any more. Its behaviour tends to be controlled by variations of the specific heat  $c_p$ , the thermal conductivity showing variations with temperature and pressure similar to viscosity. In the supercritical regime, where  $c_p$  becomes large, strong variations of  $Pr$  can be observed, in contrast with the behaviour of perfect gases. The fluid viscosity and thermal conductivity are evaluated using the method proposed by [Chung et al. \(1984\)](#), who provided equations based on kinetic gas theories and correlated with experimental data. The viscosity (measured in  $\mu Poise$ ) is related to the absolute temperature as follows:

$$\mu = 40.785 \frac{F_c M_w^{1/2} T^{1/2}}{V^{2/3} \Omega_v} \quad (2.4)$$

where  $M_w$  ( $g/mol$ ) is the fluid molecular weight and  $V_c$  ( $cm^3/mol$ ) the critical volume. The coefficient  $F_c$  is calculated as  $F_c = 1 - 0.2756\omega + 0.059035\delta_r^4 + \xi$ , where  $\omega$  is the acentric factor,  $\delta_r$  a dimensionless dipole moment  $\delta_r = 131.3\delta/(V_c T_c)^{1/2}$  and  $\xi$  a correction for polar fluids.

In Eq. (2.4), the term  $\Omega_v$  represents the viscosity collision integral, evaluated as:

$$\Omega_v = A(T^*)^{-B} + C \exp(-DT^*) + E \exp(-FT^*) \quad (2.5)$$

where  $T^* = 1.2593(T/T_c)$ ,  $A = 1.16145$ ,  $B = 0.14874$ ,  $C = 0.52487$ ,  $D = 0.77320$ ,  $E = 2.16178$  and  $F = 2.43787$ .

The thermal conductivity  $\kappa$  is calculated with the following formula:

$$\kappa = \frac{\mu C_v}{M_w} \cdot \frac{3.75\Psi}{C_v/R} \quad (2.6)$$

where now  $M_w$  is in  $kg/mol$ ,  $c_v$  is the constant specific volume heat in  $J/(mol \cdot K)$ ,  $R$  the universal gas constant and  $\Psi$  a coefficient given by  $\Psi = 1 + \alpha_1 \frac{0.215 + 0.28288\alpha_1 - 1.061\beta + 0.26665\Xi}{0.6366 + \beta \cdot \Xi + 1.061\alpha_1\beta}$ , with  $\alpha_1 = (C_v/R) - 3/2$ ,  $\beta = 0.7862 - 1.7109\omega + 1.3168\omega^2$  and  $\Xi = 2.0 + 10.5(T/T_c)^2$ .

The viscous behaviour of dense gas flows has been discussed in ([Cinnella and Congedo, 2007](#)).

## 2.2 Governing equations and numerical solver

Here the conservation equations for single-phase, viscous, non reacting flow, written in integral form for a control volume  $\Omega$  with boundary  $\partial\Omega$  are considered:

$$\frac{d}{dt} \int_{\Omega} \mathbf{w} d\Omega + \int_{\partial\Omega} (\mathbf{f} - \mathbf{f}_v) \cdot \mathbf{n} dS = 0 \quad (2.7)$$

In Eq. (2.7),  $\mathbf{w}$  is the conservative variable vector:

$$\mathbf{w} = (\rho, \rho\mathbf{v}, \rho E)^T \quad (2.8)$$

where  $\mathbf{n}$  is the outer normal to  $\partial\Omega$ ,  $\mathbf{f}$  the inviscid flux density:

$$\mathbf{f} = (\rho\mathbf{v}, -p\mathbf{I} + \rho\mathbf{v}\mathbf{v}, \rho\mathbf{v}H)^T \quad (2.9)$$

and  $\mathbf{f}_v$  the viscous fluxes:

$$\mathbf{f}_v = \left( 0, \bar{\bar{\tau}}, \bar{\bar{\tau}} \cdot \mathbf{v} - \mathbf{q} \right)^T \quad (2.10)$$

In Eq. (2.10),  $\bar{\bar{\tau}} = 2\mu(\nabla \mathbf{v} + \nabla \mathbf{v}^T) - \frac{2}{3}\mu(\nabla \cdot \mathbf{v})\mathbf{I}$  is the stress tensor and  $\mathbf{q} = -\kappa \nabla T$  the heat flux vector, with  $\kappa$  the thermal conductivity and  $\mu$  the dynamic viscosity. If  $\mathbf{f}_v = 0$ , the Euler equations are obtained.

In the above equations,  $\mathbf{v}$  is the velocity vector,  $E$  the specific total energy,  $H = E + p/\rho$  the specific total enthalpy,  $p$  is the pressure,  $\rho$  is the density and  $\mathbf{I}$  is the unit tensor.

The Eq. (2.7) are completed by a thermal EOS:

$$p = p(\rho(\mathbf{w}), T(\mathbf{w})) \quad (2.11)$$

In Eq. (2.11),  $T$  is the absolute temperature, and a caloric EOS for the specific internal energy  $e$  is also derived in order to satisfy the compatibility relation:

$$\begin{aligned} e &= e(\rho(\mathbf{w}), T(\mathbf{w})) \\ &= e_r + \int_{T_r}^T c_{v,\infty}(T') dT' - \int_{\rho_r}^{\rho} \left[ T \left( \frac{\partial p}{\partial T} \right)_{\rho} - p \right] \frac{d\rho'}{\rho'^2} \end{aligned} \quad (2.12)$$

In equation ((2.12)),  $c_{v,\infty}$  is the ideal gas specific heat at constant volume, quantities with a prime superscript are auxiliary integration variables, and subscript  $r$  indicates a reference state. The caloric equation of state is completely determined once a variation law for  $c_{v,\infty}$  has been specified.

### 2.2.1 Spatial discretisation

The governing equations above are discretized using a cell-centred finite volume scheme for structured multi-block meshes of third-order accuracy, which allows the computation of flows governed by arbitrary EOS (Cinnella and Congedo, 2005b). The scheme is obtained by correcting the dispersive error of the classical second-order-accurate Jameson's scheme (Jameson et al., 1981). To preserve the high accuracy on non-Cartesian grids, the numerical fluxes are constructed by using weighted discretization formulas, which take into account the mesh deformations (Rezgui et al., 2001). This ensures to achieve third-order accuracy on moderately distorted meshes and second-order accuracy at least on highly deformed mesh. The equations are then integrated in time using a four-stage Runge-Kutta scheme. Local time stepping, implicit residual smoothing and multi-grid acceleration are used in order to drive the solution to the steady state. The accuracy of the numerical solver has been already demonstrated in previous works (Cinnella and Congedo, 2005a,b). Further details about the numerical method are provided below.

If the viscous fluxes  $\mathbf{f}_v$  are neglected and a one-dimensional problem is considered for simplicity, the flow is governed by the Euler equation, which can be written in the conservative form as:

$$\frac{\partial \omega}{\partial t} + \frac{\partial f(\omega)}{\partial x} = 0, \quad (2.13)$$

where:

$$\begin{cases} \omega = (\rho, \rho u, \rho E)^T & \text{is the vector of the conservative variables,} \\ f(\omega) = (\rho u, \rho u^2 + p, \rho H)^T & \text{is the flux function.} \end{cases} \quad (2.14)$$

The equation (2.13) can be rewritten as:

$$\frac{\partial \omega}{\partial t} + \frac{\partial f}{\partial \omega} \frac{\partial \omega}{\partial x} = 0. \quad (2.15)$$

We define thus the *Jacobian matrix* of the flux:

$$A(\omega) := \frac{\partial f(\omega)}{\partial \omega}. \quad (2.16)$$

Considering the fundamental equation of state  $p = p(e(w), \rho(w))$ , the Jacobian matrix can be written in the matricial form:

$$A = \begin{bmatrix} 0 & 1 & 1 \\ a^2 - u^2 - \frac{p_c}{\rho} (H - u^2) & 2u - \frac{up_c}{\rho} & \frac{p_c}{\rho} \\ u(a^2 - H) - \frac{up_c}{\rho} (H - u^2) & h - \frac{u^2 p_c}{\rho} & u + \frac{up_c}{\rho} \end{bmatrix}. \quad (2.17)$$

The eigenvalues of the flux Jacobian matrix are the characteristic velocities of the fluid, i.e.:

$$\begin{cases} \lambda_1 = u - a \\ \lambda_2 = u \\ \lambda_3 = u + a. \end{cases} \quad (2.18)$$

In order to solve the hyperbolic system (2.13), the scheme proposed in (Huang et al., 1998) has been used. The differential operator  $\delta$  upon one cell is defined:

$$(\delta \cdot)_{j+\frac{1}{2}} = (\cdot)_{j+1} - (\cdot)_j, \quad (2.19)$$

where  $j$  is a given mesh point, and the average operator upon one cell:

$$(\mu \cdot)_{j+\frac{1}{2}} = \frac{(\cdot)_j + (\cdot)_{j+1}}{2}. \quad (2.20)$$

At the interface of adjacent cells, the flux function is initially approximated with a second-order classical centered numerical flux:

$$h_{j+\frac{1}{2}} = (\mu f)_{j+\frac{1}{2}}, \quad (2.21)$$

where  $h$  is the numerical flux. In this way a second-order semi-discrete scheme is obtained:

$$\left. \frac{\partial \omega}{\partial t} \right|_j + \frac{1}{\delta x} \delta \mu f|_j = 0. \quad (2.22)$$

The fourth-order equivalent equation of (2.22) is given by:

$$\frac{\partial \omega}{\partial t} + \frac{\partial f(\omega)}{\partial x} + \frac{\delta x^2}{6} \frac{\partial^3 f(\omega)}{\partial x^3} = 0. \quad (2.23)$$

The last term represents a phase error (dispersion) which has to be removed in order to increase the accuracy order of the scheme. It is possible to replace the third-order derivative with a second-order centered approximation, so that we have a fourth-order, centered, non dissipative scheme, whose numerical flux is represented by:

$$h_j = \mu f|_j - \frac{1}{6} \delta^2 \mu f|_j; \quad (2.24)$$

hence, one has:

$$\left. \frac{\partial \omega}{\partial t} \right|_j + \frac{1}{\delta x} \delta \mu f|_j - \frac{1}{6 \delta x} \delta^3 \mu f|_j = 0. \quad (2.25)$$

In order to ensure stability and avoid oscillations of the solution, a numerical dissipation term has to be included. A possible choice is to use the "artificial viscosity" term of the Jameson scheme (Jameson et al., 1981), indicated with  $\mathcal{D}$ :

$$\mathcal{D}\omega = \frac{1}{\delta x}[\delta(\varepsilon_2\rho(A)\delta\omega)] - \frac{1}{\delta x}[\delta(\varepsilon_4\rho(A)\delta^3\omega)], \quad (2.26)$$

with

$$\rho(A) = |u| + a, \quad (2.27)$$

$$a = \left( \frac{p}{\rho^2} \frac{\partial p}{\partial e} + \frac{\partial p}{\partial \rho} \right)^{\frac{1}{2}}, \quad (2.28)$$

$$(\varepsilon_2)_{j+\frac{1}{2}} = k_2 \max[v_j, v_{j+1}], \quad (\varepsilon_4)_{j+\frac{1}{2}} = \max[0, k_4 - (\varepsilon_2)_{j+\frac{1}{2}}], \quad (2.29)$$

$$v_j = \left| \frac{p_{j+1} - 2p_j + p_{j-1}}{p_{j+1} + 2p_j + p_{j-1}} \right|, \quad (2.30)$$

and the numerical flux equal to:

$$h_{j+\frac{1}{2}} = (\mu f)_{j+\frac{1}{2}} - \frac{1}{6} (\partial^2 \mu f)_{j+\frac{1}{2}} - (\varepsilon_2 \rho(A) (\partial \omega) - \varepsilon_4 \rho(A) (\partial^3 \omega))_{j+\frac{1}{2}}. \quad (2.31)$$

where  $k_2$  and  $k_4$  are constant parameters, considered equal to 0.5 and 0.032 for all the executed computations,  $\rho(A)$  the spectral radius of the Jacobian matrix,  $p$  is the pressure and  $a$  the speed of sound.

In smooth flow regions,  $\varepsilon_2 = O(\delta x^2)$  and  $\varepsilon_4 = O(1)$ , so that the dissipative numerical flux is  $\mathcal{D}\omega = O(\delta x^3)$  and the scheme

$$\left. \frac{\partial \omega}{\partial t} \right|_j + \frac{1}{\delta x} \delta \mu f|_j - \frac{1}{6\delta x} \delta^3 \mu f|_j = \mathcal{D}\omega|_j \quad (2.32)$$

is globally third-order accurate. This scheme can be applied to any fluid: it is sufficient to calculate pressure and speed of sound from the conservative variables.

If the fluid examined has a constitutive law which links directly pressure and internal energy, the application of this scheme is immediate: the pressure is calculated with  $p = p(e(w), \rho(w))$  and the sound speed with (2.28). Then from (2.27) the spectral radius and all the parameters are known.

With more complex EoS the use of iterative techniques is required: for fixed values of the conservative variables, the temperature is given by the caloric EoS (2.12) using a Newton-Raphson algorithm. Once obtained, the pressure can be calculated from the thermic EoS (2.11). Then, the sound speed and the spectral radius are calculated in the same way as the previous case.

The scalar dissipation term simplifies the implementation of the scheme when complex EoS are used and reduces heavily the total calculation time. This scheme could be seen as a third-order extension of the classical Jameson scheme (Jameson et al., 1981). Specifically, the high-order scheme can be derived by correcting the truncation error leading term of the Jameson scheme (which represents a dispersive error). This correction reduces the tendency of the scheme to produce spurious oscillations in proximity of the flux discontinuities. Furthermore, also the dispersion error is reduced: if the scheme gives less oscillating solutions, the second-order non-linear dispersive term of (2.26) will remain small. The very low intrinsic dissipation of the third-order centered scheme has been confirmed by numerical results (Huang et al., 1998; Napolitano et al., 2002; Cinnella and Congedo, 2004).

### 2.2.2 Time discretisation

For steady flows calculations, the time integration is realized through a classical fourth-step Runge-Kutta method (Jameson et al., 1981) with implicit redistribution of the residuals (Lerat et al., 1982; Jameson and Baker, 1983). The Runge-Kutta scheme is written as:

$$\begin{cases} \omega_j^{(0)} = \omega_j^n \\ \mathcal{I}(\omega_j^{(n)} - \omega_j^{(0)}) = -a_k \Delta t \mathcal{R} \omega_j^{(k-1)}, \quad k = 1, \dots, 4 \\ \omega_j^{(n+1)} = \omega_j^{(4)} \end{cases} \quad (2.33)$$

where  $\omega^n$  is the numerical solution at the time  $n\Delta t$ ,  $j$  indicates the grid point of coordinates  $x_j = j\delta x$ ,  $\mathcal{R} = \mathcal{L} - \mathcal{D}$  is the discretization of the spatial derivatives and  $a_1 = 1/4, a_2 = 1/3, a_3 = 1/2, a_4 = 1$  are fixed coefficients. The implicit operator for a one-dimensional problem containing the Euler and viscous terms contributions, is written:

$$\mathcal{I} = 1 - \beta^e \left( \frac{\Delta t}{\delta x} \right)^2 \delta(\lambda^e \delta) - \beta^v \frac{\Delta t}{\delta x^2} \delta(\lambda^v \delta), \quad (2.34)$$

where  $\lambda^e$  and  $\lambda^v$  are respectively the spectral radius of the Euler flux and the viscous flux and the quantities  $\beta^e$  and  $\beta^v$  are positive parameters. It is possible to show that, for a pure advection problem the scheme (2.33) coupled to the spatial discretization (2.32) with  $\mathcal{D} = 0$  is unconditionally stable for  $\beta^e \geq 1/8$ . Besides, for a pure diffusion problem, the scheme (2.33) coupled with a second-order centered discretization for the viscous terms is unconditionally stable for  $\beta^v \geq \frac{2}{\Omega^v}$ , with  $\Omega^v \approx 2.785$ . The convergence to the steady state is usually accelerated by means of a variable time integration step from cell to cell (i.e., *local time stepping*) and a *multigrid* algorithm (Collercandy, 1998).

### 2.2.3 Boundary Conditions

The boundary conditions used for the CFD simulations of the ORC turbine nozzle guide vanes and rotors are:

- A condition of non-permeability on each wall;
- Periodic conditions on the upper and lower side of the computational domains in order to limit the study to a single blade;
- Total thermodynamic conditions applied at flow inlet for the nozzle guide vanes, along with a non-reflecting condition for isolated supersonic rotors;
- Static pressure imposed as outlet condition;
- Non coincident joints are imposed in the ORC nozzleguide vane in order to use a single block C-type mesh: the conservative variables are averaged at the interface so that information can pass through the joint; for the rotor an H-type multi-block mesh with a O-block around the blade to build the boundary layer is used without the need to define no-match joints.

## 2.3 Thermodynamic models

In thermodynamic conditions close to the saturation curve or of the same order of the critical parameters, the validity of the ideal gas equation, which is suitable for low-density states, does not

hold anymore. In order to take into account the complex behaviour of the working fluids analysed in this thesis work, more accurate EOS than the perfect gas law have been considered: the Peng-Robinson equation with the Stryjek-Vera correction and the multi-parameter equations available through the NIST-REFPROP library ver. 9.1. More details about these thermodynamic models are provided below.

### 2.3.1 The Peng-Robinson-Stryjek-Vera EOS

The PRSV EOS (Stryjek and Vera, 1986) is a cubic EOS (CEOS) developed as an improvement of the well known Peng-Robinson equation (Peng and Robinson, 1976). The CEOS are written as a cubic function of the volume  $V$  and different models have been proposed in the years. The first, simplest cubic model was presented by Van der Waals in his doctoral dissertation (Van der Waals, 1873) on 1873, where two fluid-dependent constants were introduced as modification of the ideal gas law. These constants, known as repulsive or co-volume  $b$  and attraction term  $a$ , take into account the real gas effects by considering the molecular interactions which occur at high pressures and low temperatures. However, it fails to describe the fluid properties in the vicinity of the liquid-vapor equilibrium (VLE) or the critical point. A substantial improvement was provided by the Redlich-Kwong (RK) (Redlich and Kwong, 1949) and the further correction Soave-Redlich-Kwong (SRK) (Soave, 1972) CEOS, which provided higher accuracy in the critical region and introduced the *acentric factor*  $\omega$  as representative of the deviation of the fluid molecule structure from a spheric one, typical of polar fluids. Nevertheless, the SRK model still suffered of low accuracy in the VLE region, which was improved by the PRSV CEOS. In this model, the thermal EOS is given by:

$$p = \frac{RT}{v-b} - \frac{a}{v^2 + 2bv - b^2}. \quad (2.35)$$

where  $p$  and  $v$  denote respectively the fluid pressure and its specific volume,  $a$  and  $b$  are substance specific parameters related to the fluid critical-point properties  $p_c$  and  $T_c$ . To achieve high accuracy for saturation pressure estimates of pure fluids, the temperature-dependent parameter  $a$  in Eq. (2.35) is expressed as:

$$a = (0.457235R^2T_c^2/p_c^2) \cdot \alpha(T) \quad (2.36)$$

while

$$b = 0.077796RT_c/p_c. \quad (2.37)$$

These properties are not completely independent, since the EOS should satisfy the conditions of zero curvature and zero slope at the critical point. Such conditions allow computing the critical compressibility factor  $Z_c = (p_cv_c)/(RT_c)$  as the solution of a cubic equation. The correction factor  $\alpha$  is given by:

$$\alpha(T_r) = [1 + K(1 - T_r^{0.5})]^2 \quad (2.38)$$

with

$$K = 0.378893 + 1.4897153\omega - 0.1713848\omega^2 + 0.0196554\omega^3. \quad (2.39)$$

The caloric behaviour of the fluid is approximated through a power law for the isochoric specific heat in the ideal gas limit:

$$c_{v,\infty}(T) = c_{v,\infty}(T_c) \left( \frac{T}{T_c} \right)^n \quad (2.40)$$

with  $n$  a fluid-dependent parameter.

### 2.3.2 Helmholtz free-energy multi-parameter EOS

The thermodynamic models based on the Helmholtz free energy  $A$  are the most accurate to describe the fluid behaviour close to the critical point and the saturation curves. They are developed starting from the relationship:

$$p = \left( \frac{\partial A}{\partial V} \right)_T \quad (2.41)$$

The previous equation can be integrated between the actual volume  $V$  and the ideal gas state  $\infty$  in order to get an explicit relationship in term of the *residual property*  $A^r$ , as follows:

$$A^r = A - A^0 = - \int_V^\infty (p - \rho RT) dV \quad (2.42)$$

where  $A^0$  is the ideal part of the Helmholtz free-energy, whereas  $A^r$  can be intended as the residual part representative of the real gas effects. By differentiation of Eq. (2.42) it is possible to evaluate all the thermodynamic properties. Usually this equation is rewritten in terms of the reduced Helmholtz free-energy  $\Phi(\delta, \tau) = \frac{A(\rho, T)}{RT}$ , with  $\delta = \rho/\rho^*$  and  $\tau = T^*/T$  being the reduced density and temperature with respect to the critical parameters  $\rho^* = \rho_c$  e  $T^* = T_c$ . Wagner (Setzmann and Wagner, 1989) proposed the following form:

$$\Phi(\delta, \tau) = \Phi^r(\delta, \tau) + \Phi^0(\delta, \tau) \quad (2.43)$$

where the ideal and residual parts are expressed as:

$$\Phi^0(\delta, \tau) = \ln \delta + a_1 \ln \tau + \sum_{m=1}^{M_1} a_m \tau^{j_m} + \sum_{m=M_1+1}^{M_2} a_m \ln[1 - e^{(-u_m \tau)}] \quad (2.44)$$

$$\begin{aligned} \Phi^r(\delta, \tau) = & \sum_{m=M_2+1}^{M_3} a_m \delta^{i_m} \tau^{j_m} + \sum_{m=M_3+1}^{M_4} a_m \delta^{i_m} \tau^{j_m} e^{(-\delta^{k_m})} + \\ & + \sum_{m=M_4+1}^{M_5} a_m \delta^{i_m} \tau^{j_m} e^{[-\alpha_m(\delta - \varepsilon_m)^2 - \beta_m(\tau - \gamma_m)^2]} \end{aligned} \quad (2.45)$$

The last term of Eq. (2.45) expresses the real-gas effects close to the critical point region. All the coefficients and exponents in the Eqs. (2.44),(2.45) are fluid-dependent and are fitted on experimental data by means of an optimization algorithm, as explained in (Setzmann and Wagner, 1989).

For some fluids, as R245fa, no data are available to fit the previous coefficients, then Lemmon and Span proposed a short technical multiparameter EOS (Lemmon and Span, 2006), where the residual part is written as:

$$\begin{aligned} \Phi^r(\delta, \tau) = & n_1 \delta \tau^{0.25} + n_2 \delta \tau^{1.25} + \\ & + n_3 \delta \tau^{1.5} + n_4 \delta^3 \tau^{0.25} + \\ & + n_5 \delta^7 \tau^{0.875} + n_6 \delta \tau^{2.375} e^{-\delta} + \\ & + n_7 \delta^2 \tau^{2.0} e^{-\delta} + n_8 \delta^5 \tau^{2.125} e^{-\delta} + \\ & + n_9 \delta \tau^{3.5} e^{-\delta^2} + n_{10} \delta \tau^{6.5} e^{-\delta^2} + \\ & + n_{11} \delta^4 \tau^{4.75} e^{-\delta^2} + n_{12} \delta^2 \tau^{12.5} e^{-\delta^3} \end{aligned} \quad (2.46)$$

The coefficients  $n_i$  are fluid-dependent and fitted on a wide set of polar and non-polar fluids simultaneously. Since the bell-shape terms for the description of the critic region are not present, this equation is not so accurate as the reference EOS, however it provides higher accuracy and stability than the CEOS. In order to evaluate the caloric properties, the Helmholtz free energy based models need an ancillary equation to evaluate the isobaric specific heat. The latter consists of an ideal part that is usually written in a cubic form in function of the temperature, as follows:

$$c_{p,\infty} = c_{v,\infty} + R = A + B \cdot T + C \cdot T^2 + D \cdot T^3 \quad (2.47)$$

where  $A, B, C, D$  are fluid-dependent coefficients.

The working fluids of interest used in this thesis work are listed in Tab. 2.1, where the thermophysical properties are shown in terms of critical pressure, temperature and density ( $p_c, T_c, \rho_c$ ), molecular weight ( $M_w$ ), acentric factor ( $\omega$ ) and ideal specific heat ratio ( $\gamma$ ), the latter calculated in the dilute gas region along the critical isotherm curve, as:

$$\gamma = \left( \lim_{\rho \rightarrow 0} \frac{c_p}{c_v} \right)_{T_c} \quad (2.48)$$

A fluid for ORC applications is the R245FA, namely pentafluoropropane, which is a hydrofluorocarbon used primarily for closed-cell spray foam insulation. It has no ozone depletion potential and is nearly non-toxic. The ORC nozzle guide vane performances obtained with this fluid have been compared with those provided by other three engineered fluids: NOVEC649, RE347mcc and R449. These are effective heat transfer fluids with a very low boiling point and are useful in heat transfer particularly where non-flammability or environmental factors are a consideration.

**Table 2.1:** Thermophysical properties for different organic substances, based on reference EOS (from REFPROP ver. 9.1).

|                  | <b>R245fa</b> | <b>Novec649</b> | <b>RE347mcc</b> | <b>R449</b> |
|------------------|---------------|-----------------|-----------------|-------------|
| $p_c[MPa]$       | 3.651         | 1.869           | 2.476           | 2.225       |
| $T_c[K]$         | 427.16        | 441.81          | 437.7           | 466.15      |
| $\rho_c[kg/m^3]$ | 516.08        | 606.80          | 524.14          | 555.00      |
| $M_w[g/mol]$     | 134.05        | 316.04          | 200.05          | 250.00      |
| $\omega$         | 0.378         | 0.471           | 0.403           | 0.444       |
| $\gamma$         | 1.061         | 1.027           | 1.039           | 1.030       |

For the R245fa, the technical EOS, Eq. (2.47), holds and the 12 parameters are listed in Tab. 2.2. The coefficients used in Eq. (2.44) are given in Tab. 2.3.

For the other three fluids, a specific reference multi-parameter EOS has been developed by fitting the coefficients on experimental data. The ideal contribution to the gas heat capacity is provided by the following equation:

$$\frac{c_p^0}{R} = c_0 + \sum_{i=1}^j v_i \left( \frac{u_i}{T} \right)^2 \frac{\exp(u_i/T)}{[\exp(u_i/T) - 1]^2} \quad (2.49)$$

where  $j = 1$  for NOVEC649 and R449, and  $j = 2$  for RE347mcc,  $R$  is the universal gas constant in  $J/mol \cdot K$ . The values of coefficients  $c_0, u_i$  and  $v_i$  are reported in Tab. 2.4.

The residual part of the Helmholtz free energy is evaluated by means of Eq. (2.45), and the number of terms for the three fluids are shown in Tab. 2.5. The coefficients in Eq. (2.45) are fluid dependent and are provided by the NIST-REFPROP library, ver. 9.1. As references, full



**Table 2.2:** R245fa coefficients for the technical EOS, Eq. (2.47).

|          |            |
|----------|------------|
| $n_1$    | 1.2904     |
| $n_2$    | -3.2154    |
| $n_3$    | 0.50693    |
| $n_4$    | 0.093148   |
| $n_5$    | 0.00027638 |
| $n_6$    | 0.71458    |
| $n_7$    | 0.87252    |
| $n_8$    | -0.015077  |
| $n_9$    | -0.40645   |
| $n_{10}$ | -0.11701   |
| $n_{11}$ | -0.13062   |
| $n_{12}$ | -0.022952  |

**Table 2.3:** R245fa coefficients for the ideal-gas state reduced Helmholtz free-energy, Eq. (2.44), with  $M_1 = 2$  and  $M_2 = 3$ .

|       |         |
|-------|---------|
| $a_1$ | 3.00    |
| $a_2$ | -13.438 |
| $a_3$ | 9.8724  |
| $a_4$ | 5.5728  |
| $a_5$ | 10.385  |
| $a_6$ | 12.554  |

**Table 2.4:** Coefficient for the calculation of the ideal heat capacity, Eq. (2.49).

|           | <b>Novec649</b> | <b>R449</b> | <b>RE347mcc</b> |
|-----------|-----------------|-------------|-----------------|
| $c_0$     | 30.8            | 17.8        | 13.09           |
| $u_i$ [K] | 1940.00         | 1013.26     | 2045.00/850.00  |
| $v_i$     | 29.80           | 23.76       | 13.78/14.21     |

**Table 2.5:** Number of elements in the sums of Eq. (2.45) for the three working fluids.

|       | <b>Novec649</b> | <b>R449</b> | <b>RE347mcc</b> |
|-------|-----------------|-------------|-----------------|
| $M_3$ | 7               | 4           | 7               |
| $M_4$ | 10              | 10          | 10              |
| $M_5$ | 17              | 14          | 17              |

details about the reference EOS and the data fitting are provided only for the NOVEC649 fluid in (McLinden et al., 2015), whereas for the R449 and RE347mcc results have not been published yet.

## 2.4 Conclusions

In this section, the thermodynamic and numerical methods used in the following of this thesis have been described. A focus has been put on the dense gas effects which are present in ORC turbomachinery applications, and on the needs for an accurate description of the fluid thermodynamic behaviour by means of more complex EOS with respect to the ideal gas law. Finally, the numerical methodology used to discretise the flow governing equations has been shown. The accuracy preserved on deformed computational meshes is a feature useful for the simulation of highly staggered turbine blades, such as those designed and tested in this work.

## Chapter 3

# FAST DESIGN METHODOLOGY FOR SUPERSONIC TURBINES WITH STRONG REAL GAS EFFECTS

### 3.1 Introduction

In this thesis work, a complete methodology to get a fast and as accurate as design of axial supersonic ORC impulse turbines has been developed, in order to take properly into account the dense gas effects. The aim is to design a proper mean-line shape of the turbine blades in order to obtain a baseline suitable for optimization purposes. Indeed, as previously investigated by [Guardone et al. \(2013\)](#) and [Wheeler and Ong \(2013\)](#), a supersonic nozzle designed by means of the perfect gas law is not able to provide the proper geometries and performances expected by using a dense gas model and, then, a more accurate analysis is required. In the optimization framework, the design of a more accurate baseline geometry provides a reduction of the design parameter space size and allows to consider a shorter range of variations for the design parameters, thus improving the convergence of the optimization towards a proper optimized shape in dense gas conditions. Here a semi-analytic design is proposed.

The procedure is based on a generalized *method of characteristics* (MOC) for stators, along with a free-vortex design approach for the rotors. The MOC is a classical tool to solve hyperbolic partial differential equations system and, in inverse design, can be advantageously used to design the supersonic portion of nozzle shapes ([Zucrow and Hoffman, 1976](#); [Ali et al., 2006](#); [D  lery, 2010](#)). The MOC has been widely studied in classical gasdynamics, however only in recent years it has gained interest for real gas problems due to the great improvements in the dense gases thermodynamic modelling. A first insight into the dense gas design of supersonic nozzles by means of the MOC was provided by [Cramer and Crickenberger \(1992\)](#) who gave a brief description of the non-classical behavior of the Prandtl-Meyer function, which is of importance for the characteristics theory, in the dense gas regime. The Prandtl-Meyer function was seen to decrease, rather than increase, with Mach number at densities, temperatures, and Mach numbers

such that  $\Gamma < 1$  (see Eq. (2.1)). Aldo and Argrow (1993), for the first time, developed a MOC for two-dimensional (planar) and axisymmetric flow of a van der Waals gas into minimum length nozzles. Using a straight sonic line assumption, a centered expansion was used to generate an inviscid wall contour. More recently, Guardone et al. (2013) implemented a MOC coupled with the state-of-the-art thermodynamic models to assess the influence of the molecular complexity of the working fluid on the design of the supersonic portion of the nozzle by considering different fluids at the same real-gas operating conditions, Uusitalo et al. (2014) carried out the design and flow analysis of a small scale ORC turbine stator adopting high molecular complexity fluid, namely siloxane MDM, characterized by dry expansion, high pressure ratio over the stator and low speed of sound, resulting into a highly supersonic flow, whereas Wheeler and Ong (2013) studied the real gas flows which occur within radial ORC turbines. A new method, based on an extension of the perfect gas MOC to dense gases, for the design of nozzles was discussed and applied to the case of a high pressure ratio radial turbine vanes.

In this framework, the MOC generalised to dense gases described by the state-of-the-art thermodynamic models is implemented in this thesis work to design, for the first time to the author knowledge, axial supersonic nozzle guide vanes. Besides, a new methodology to design supersonic rotor blade vanes by taking into account the dense gas effects has been developed and tested. It is based on a generalised MOC along with a free-vortex design criterion.

In the following, the theory of the MOC is presented and the analytical generalisation to dense gases is shown. Then, the MOC algorithm is tested and validated by comparison of the results obtained with the finite volume solver equipped with complex multi-parameter EOS (see Eq. (2.41)). The performances of the nozzle guide vane shapes obtained with the MOC are then assessed by using the dense gas numerical solver for different gas models and fluids.

## 3.2 Method of characteristics for supersonic stator design

The MOC is classically employed for the design of the divergent part of supersonic nozzles under the hypotheses of 2D, steady and homentropic flow (Zucrow and Hoffman, 1976; Délerly, 2010). Such a flow is governed by the 2D isentropic Euler equations, which represent an hyperbolic system of conservation laws characterized by two families of characteristic lines. These are described by equations of the form:

$$\frac{dy}{dx} = \tan(\varphi \pm \alpha) \quad (3.1)$$

where  $\varphi$  is the local flow angle and  $\alpha = \arcsin(M^{-1})$  is the Mach angle (see Fig. 3.1). Rewriting the governing equations in the characteristic reference frame, the so-called compatibility equations are obtained, which are just ordinary differential equations, of the form:

$$d\varphi \pm \sqrt{M^2 - 1} \frac{dV}{V} = 0 \quad (3.2)$$

where  $V$  is the velocity magnitude and the sign  $+$  or  $-$  denotes a left-running or  $-$  a right-running characteristic line, respectively. For a perfect gas, the Eq. (3.2) can be integrated analytically after rewriting  $dV/V$  in terms of the Mach number and by using the equation of state, leading to the well-known Prandtl-Meyer relations (Délerly, 2010):

$$\varphi \pm \nu(M, \gamma) = \text{constant} \quad (\text{along a characteristic}) \quad (3.3)$$

$$\nu(M, \gamma) = \frac{1}{\lambda} \tan^{-1}(\lambda\beta) - \tan^{-1} \beta \quad (3.4)$$

where  $\lambda = \sqrt{\frac{\gamma-1}{\gamma+1}}$  and  $\beta = \sqrt{M^2-1}$ . The previous equations, along with the equations of the characteristic lines, Eq. (3.1), are then used as described by Détery (2010) to design the nozzle wall contour.

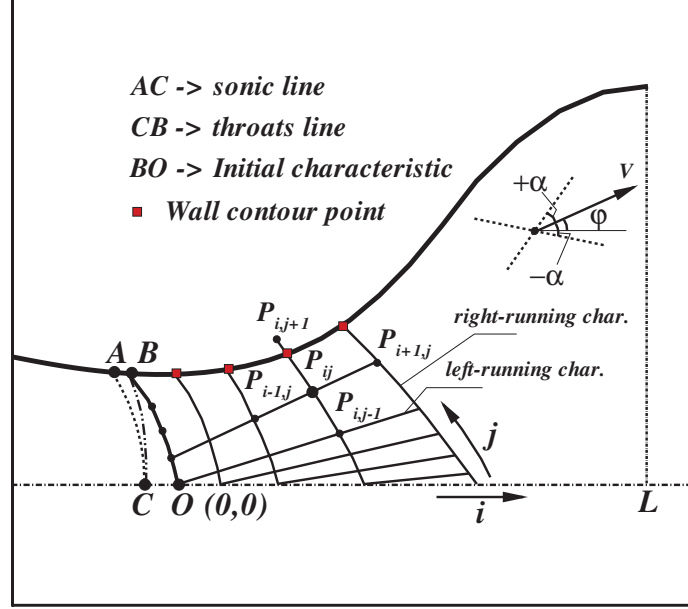


Figure 3.1: Characteristic line patterns and nozzle divergent shape design.

The pattern of characteristic lines in the supersonic part of an adapted nozzle is depicted in Fig. 3.1. Given the inlet massflow rate  $G$  ( $kg/s$ ), the upstream total pressure  $p_0$  ( $Pa$ ) and temperature  $T_0$  ( $K$ ), and the pressure (or Mach number) distribution along the nozzle axis  $p(x)/p_0$ , the MOC allows to perform an inverse design and calculate, in a quasi-analytic way for ideal gases, the inviscid wall contour that realizes the desired operating conditions.

The first step of the design procedure is the treatment of the throat region. Here the flow is transonic and it is governed by an elliptic equation, namely the compressible transonic potential equation for 2-D flows:

$$\left[ a^2 - \left( \frac{\partial \Phi_t}{\partial x} \right)^2 \right] \frac{\partial^2 \Phi_t}{\partial x^2} + \left[ a^2 - \left( \frac{\partial \Phi_t}{\partial y} \right)^2 \right] \frac{\partial^2 \Phi_t}{\partial y^2} - 2 \left( \frac{\partial \Phi_t}{\partial x} \right) \left( \frac{\partial \Phi_t}{\partial y} \right) \left( \frac{\partial^2 \Phi_t}{\partial x \partial y} \right) = 0 \quad (3.5)$$

where  $a$  is the speed of sound,  $x$  and  $y$  the spatial coordinate,  $\Phi_t$  the potential function such that the relations  $u = \partial \Phi_t / \partial x$  and  $v = \partial \Phi_t / \partial y$  (with  $u$  and  $v$  the velocity components in the physical reference system) are verified. The Eq. (3.5) is a strongly non-linear partial differential equation which is difficult to solve analytically.

Different methodologies have been proposed in the years to solve Eq. (3.5). The Sauer's method (Sauer, 1947) is based on the theory of small disturbances. It solves the equation of the small disturbances for a compressible flow for a two-dimensional as well as an axially symmetric flow. Hall (1962) developed a transonic solution based on the small perturbation theory applying it to an irrotational, perfect gas. The velocity components were expressed in cylindrical coordinates in terms of inverse powers of the normalized throat wall radius of curvature. Kliegel and Levine

(1969) proposed a correction to the Hall's method by developing a solution in a system of toroidal coordinates, in which both nozzle axis and wall were coordinate lines.

In this thesis work, the Carriere's method (Délery, 2010) is implemented. It is based on the solution of Eq. (3.5) in the form of a limited expansion in the vicinity of the sonic point on the nozzle axis. Firstly, the variables are normalised with respect to the critical speed of sound,  $a_c$ , such that  $\bar{a} = a/a_c$ ,  $\bar{u} = u/a_c$ ,  $\bar{v} = v/a_c$ . Then, by writing the energy equation in the well-known form:

$$\frac{2}{\gamma-1}\bar{a}^2 + \bar{u}^2 + \bar{v}^2 = \frac{\gamma+1}{\gamma-1} \quad (3.6)$$

the Eq. (3.5) can be rewritten in dimensionless form as:

$$(\bar{u}^2 - \bar{a}^2) \frac{\partial^2 \bar{\Phi}_t}{\partial \bar{x}^2} + 2\bar{u}\bar{v} \frac{\partial^2 \bar{\Phi}_t}{\partial \bar{x} \partial \bar{y}} + (\bar{v}^2 - \bar{a}^2) \frac{\partial^2 \bar{\Phi}_t}{\partial \bar{y}^2} = 0 \quad (3.7)$$

The geometric coordinates  $\bar{x}$  and  $\bar{y}$  are evaluated in a reference system with origin in the sonic point on the axis, point  $C$  in Fig. 3.1, where  $M = 1$ . They are scaled such that  $\bar{x} = \beta x$  and  $\bar{y} = \beta y$ , whit  $\beta$  a scale factor which can be defined in a successive step.

On the nozzle axis a solution in the form  $\bar{u}(\bar{x}, 0) = 1 + \bar{x}$  is imposed, and the dimensionless potential function is considered to have the form of the expansion close to the sonic point, as:

$$\bar{\Phi}_t(\bar{x}, \bar{y}) = \sum_{m,n} \varepsilon_{m,n} \bar{x}^m \bar{y}^n \quad (3.8)$$

By differentiating the preceding equation, the dimensionless solutions of the potential equation, Eq. (3.7), are evaluated, as  $\bar{u} = \partial \bar{\Phi}_t / \partial \bar{x} = \sum_{m,n} m \cdot \varepsilon_{m,n} \bar{x}^{m-1} \bar{y}^n$  and  $\bar{v} = \partial \bar{\Phi}_t / \partial \bar{y} = \sum_{m,n} n \cdot \varepsilon_{m,n} \bar{x}^m \bar{y}^{n-1}$ , where  $\varepsilon_{m,n}$  are expansion coefficient to calculate. Given the symmetry condition with respect to the nozzle axis, such that to a sign variation of  $\bar{y}$  corresponds the same change for  $\bar{v}$ , all coefficients  $\varepsilon_{m,n}$  are zero if  $n$  is odd. Besides, on the axis the conditions:  $\varepsilon_{1,0} = 1$ ,  $2\varepsilon_{2,0} = 1$ ,  $\varepsilon_{3,0}, \varepsilon_{4,0} = \dots = 0$ , hold and, by substituting them into Eq. (3.7), the other unknown coefficients can be calculated and, finally, the form of the dimensionless flow variables can be found as function of the coordinates  $(\bar{x}, \bar{y})$ , as:

$$\begin{aligned} \bar{u} = & 1 + \bar{x} + \frac{\gamma+1}{2} \bar{y}^2 [1 + (2\gamma-1)\bar{x} + 3\gamma(\gamma-1)\bar{x}^2 + (\gamma-1)(4\gamma^2-2\gamma-1)\bar{x}^3] + \\ & + \frac{(\gamma+1)^2}{64} \bar{y}^4 [3.387(6\gamma-1) + 3.788(36\gamma^2-19\gamma-4)\bar{x}] \end{aligned} \quad (3.9)$$

$$\begin{aligned} \bar{v} = & (\gamma+1)\bar{y} \left[ \bar{x} + \frac{2\gamma-1}{2} \bar{x}^2 + \gamma(\gamma-1)\bar{x}^3 + \frac{(\gamma-1)(4\gamma^2-2\gamma-1)}{4} \bar{x}^4 \right] + \\ & + \frac{(\gamma+1)^2}{16} \bar{y}^3 \left[ 2.667 + 3.468(6\gamma-1)\bar{x} + 3.788 \frac{36\gamma^2-19\gamma-4}{2} \bar{x}^2 \right] + \\ & + 4.844 \frac{(\gamma-1)^3(6\gamma-1)}{128} \bar{y}^5 \end{aligned} \quad (3.10)$$

Thanks to these equations, it is possible to determine all the flow properties as function of the geometric position in the dimensionless plane. For a two-dimensional transonic flow, two curves can be defined: the *sonic* and *throat* lines, which are the locus of points where  $M = 1$  or, by definition of Mach number,  $\bar{u}^2 + \bar{v}^2 = 1$ , and  $\bar{v} = 0$  (flow parallel to the nozzle axis), respectively. These two curves are represented in Fig. 3.1.

The equation of the throat line,  $\bar{v} = 0$ , is a quadratic function of the type  $\bar{y} = f(\bar{x})$ , that can be easily handle in an analytic way. Especially, since it represents the condition of parallel flow,

which is proper of the wall nozzle throat point, and depends only by the dimensionless variables, it is possible to choose a suitable point for the throat location in the plane  $(\bar{x}, \bar{y})$ . Here, the location  $(\bar{x} = -0.1, \bar{y}(-0.1))$  is chosen such that the wall throat point lies between  $\bar{x} = 0$  and the throat line maximum  $\bar{x}_{\bar{y}_{max}} = -0.25$ .

By knowing the massflow  $G$  and the upstream total conditions, which allow to calculate the throat critical parameters  $\rho_c$  and  $a_c$ , the nozzle throat semi-height is calculated as  $h_t = G/(2 \cdot \rho_c \cdot a_c)$ . In this way, a metric for the length scale factor  $\beta$  is defined. Indeed, by knowing the dimensionless nozzle throat semi-height  $h_{t,adim} = \bar{y}(-0.1)$ , the scale factor is evaluated as  $\beta = h_{t,adim}/h_t$ . Hence, the coordinates of the first point of the *initial characteristic*  $\xi_0$  on the nozzle wall (point  $B$  in Fig. 3.1) are calculated in the physical plane as  $(x_B = \bar{x}_B/\beta, y_B = h_t)$ , with  $\bar{x}_B = -0.1$ . Besides, all the flow properties can be calculated in the throat region by means of the Eq. (3.9) and (3.10). Especially, the Mach number is evaluated as:

$$M = \sqrt{\frac{(\bar{u}^2 + \bar{v}^2)}{\left(\frac{\gamma+1}{2} - \frac{\gamma-1}{2}(\bar{u}^2 + \bar{v}^2)\right)}} \quad (3.11)$$

By starting from the point  $B$ , the initial characteristic  $\xi_0$  is then reconstructed as a piecewise line by calculating the potential flow solution step-by-step. All the flow properties are evaluated and renormalized in the physical plane. On the nozzle axis, a smooth cubic distribution is prescribed for the normalised static pressure,  $p(x)/p_0$ , evaluated on 100 points, in order to reach the desired exit conditions without discontinuities or too rapid accelerations, which could cause disturbances or shock waves. Besides, the characteristic  $\xi_0$  is discretised in 50 intervals. Given all the previous elements, the MOC procedure is started to calculate the supersonic flow inside the nozzle.

The procedure to calculate the solution, for perfect gases, on the generic point  $P_{ij}$  (see Fig. 3.1), is shown below:

1. The Eq. (3.3), is used to evaluate the flow properties by solving the system equation provided by the right- and left-running characteristic lines:

$$\nu_{ij} + \varphi_{ij} = \nu_{i,j-1} + \varphi_{i,j-1} = k_1 \quad (3.12)$$

$$\nu_{ij} - \varphi_{ij} = \nu_{i-1,j} - \varphi_{i-1,j} = k_2 \quad (3.13)$$

The  $k_1$  and  $k_2$  are integration constants depending on the initial data;

2. Eqs. 3.12, 3.13 have to be both satisfied. Then, they are simultaneously solved as an algebraic system providing the unknowns flow angle  $\varphi_{ij}$  and  $\nu_{ij}(M, \gamma)$  on the point  $P_{ij}$ ;
3. The datum  $\nu_{ij}(M, \gamma)$  is used to invert the non-linear Eq. (3.4) and find  $M_{ij}$ . Then all the thermodynamic properties are determined in  $P_{ij}$  by means of the isentropic relations.

The procedure described above is carried out along a characteristic line  $\xi_i$  until the massflow exceeds the assigned value  $G$ . Then, an interpolation for the calculation of the wall points (the red squares in Fig. 3.1) is carried out, in order to account for the imposed massflow, by solving the continuity equation written on a characteristic:

$$G = \int_{P_{i,0}}^{P_{i,j}} \rho \cdot a \cdot d\xi \quad (3.14)$$

In this work, the nozzle design has been carried out for four different organic working fluids, as explained in Section 2.3.2. Here, the ideal specific heat ratio is recalled in Tab. 3.1 for each of them.

**Table 3.1:**  $\gamma$  for the four organic substances used in this Section.

|        |          |          |       |
|--------|----------|----------|-------|
| R245fa | Novec649 | RE347mcc | R449  |
| 1.061  | 1.027    | 1.039    | 1.030 |

### 3.2.1 MOC for real gases

In order to account for dense gas effects during the nozzle design, the classic MOC for perfect gases showed previously, has been extended to a generic EOS. Here, two real gas models have been implemented. The first one relies on an equivalent- $\gamma$  model (Wheeler and Ong, 2013) and the multi-parameter equations provided by REFPROP (REF for brevity). The second one makes no assumptions on the specific form of the EOS and is applicable to any thermodynamic model.

#### Equivalent- $\gamma$ gas model

A non-expensive and easy way to account for dense gas effects is the equivalent- $\gamma$  model. This model is quite similar to the ideal one, with the difference that the organic gas is supposed to go through a polytropic transformation along the nozzle, obeying to the polytropic relationship:

$$\frac{p}{\rho^{\gamma_{eq}}} = \frac{p_0}{\rho_0^{\gamma_{eq}}} \quad (3.15)$$

In this way it is possible to take into account the real gas effects with small variations on the ideal gas model algorithm. The accuracy of such a model has been already evaluated in (Wheeler and Ong, 2013). The polytropic exponent  $\gamma_{eq}$ , that can be less than 1 and reduces approaching the critical conditions, is held constant and can be evaluated exploiting the linearity of Eq. (3.15) passing to the logarithmic relationship  $\log \frac{p}{p_0} = \gamma_{eq} \cdot \log \frac{\rho}{\rho_0}$  and treating it as the slope of the best fit straight line of a linear regression over an isentropic expansion process. The isentropes evolve over a pressure ratio of 10 for reduced stagnation conditions near the critical point, in order to maximize real gas effects,  $p_r=1.28$  and  $T_r=1.05$  for four different organic fluids (Fig. 3.2), and the data fitting is performed on the REFPROP model using the least squares regression:

$$\gamma_{eq} = \frac{\sum xy - \frac{\sum x \sum y}{n}}{\sum x^2 - \frac{(\sum x)^2}{n}} \quad (3.16)$$

In Eq. 3.16 is  $n=1000$ ,  $x = \log(\rho/\rho_0)$  and  $y = \log(p/p_0)$ . The results are shown in Tab. 3.2.

**Table 3.2:** Polytropic coefficient  $\gamma_{eq}$  for different organic substances at total reduced conditions  $p_r=1.28$ ,  $T_r=1.05$ .

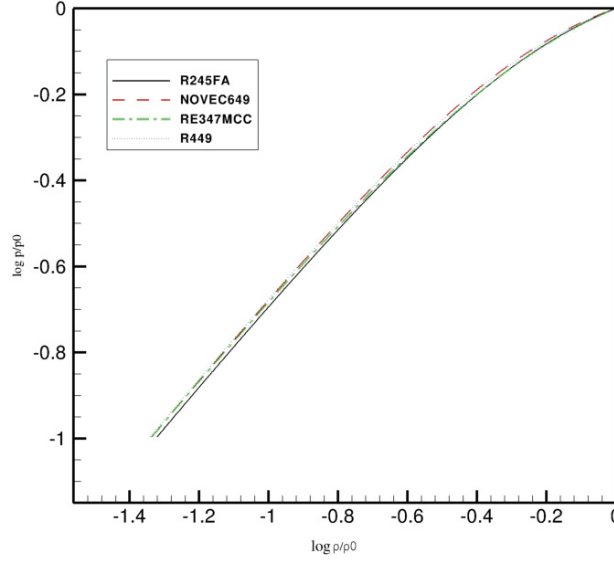
|        |          |          |       |
|--------|----------|----------|-------|
| R245fa | Novec649 | RE347mcc | R449  |
| 0.748  | 0.753    | 0.744    | 0.742 |

When  $\gamma_{eq}$  is less than 1, Eq. (3.4) can not be used anymore, due to the appearance of complex solutions. The analytical integration of Eqs. (3.1), (3.2) results in a modified Prandtl-Meyer function:

$$\nu = \frac{1}{z} \tanh^{-1}(z\beta) - \tan^{-1}\beta \quad (3.17)$$

where  $z$  is the complex part of  $\lambda = iz$ ,  $i$  being the imaginary unit. Then, the ideal gas model





**Figure 3.2:** Pressure-density plots along isentropes for four organic fluids at total reduced conditions  $p_r=1.28$ ,  $T_r=1.05$ .

algorithm can be applied by using 3.17 instead of (3.4). The solution algorithm is the same as described for the ideal gas.

The consequences of having  $\gamma_{eq} < 1$  can be directly observed on thermodynamic properties, as the speed of sound. Combining Eq. 3.17 with the energy equation, it can be shown that  $a^2 = \gamma_{eq} p / \rho = \gamma_{eq} p_0 / \rho_0 \frac{1}{\frac{\gamma_{eq}-1}{2} M^2 + 1}$ . Then, a polytropic exponent less than 1 implies the speed of sound to reduce across compression waves (i.e.  $M$  reduces) and rise for expansion fans, which is typical of the dense gas behaviour.

### Advanced gas models

When complex non-linear EOS are used to model the gas behaviour, Eqs. (3.1), (3.2) cannot be integrated analytically. In the following, a numerical procedure is instead presented by following a methodology similar to the one in [Zucrow and Hoffman \(1976\)](#).

As in the standard MOC, the target massflow  $G$  and the target pressure distribution  $p(x)$  along the nozzle axis, are known data. In addition, the plenum pressure and temperature,  $p_0$  and  $T_0$ , are also given. This allows to calculate the sonic state thermodynamic conditions at the nozzle throat (choked flow). The transonic flow in the throat region is solved by means of the Carriere's method presented in the previous Section and the initial characteristic  $\xi_0$  is then obtained. In order to account for the real gas effects, the ideal heat specific ratio  $\gamma$  in Eq. (3.9) and (3.10) is replaced by the equivalent real gas value  $\gamma_{eq}$ , evaluated for the selected total conditions and working fluid.

In order to compute for points downstream of the initial characteristic, preliminary calculations are performed for the definition of the initial data in the dense gas framework. These steps are given below:

1. Given the initial data  $(p_0, T_0)$ ,  $p(x)/p_0$  and  $G$ , and considering a choked nozzle flow, the sonic static thermodynamic conditions in the nozzle throat are evaluated, ;
2. The velocity magnitude on the points of the nozzle axis is then calculated as  $V = \sqrt{2(h_0 - h)}$ . The static enthalpy  $h(x)$  along the axis is calculated as  $h(x) = h(p(x), s)$ , where the entropy is constant by definition and given by  $s = s(p_0, T_0)$ . Also the total enthalpy  $h_0$  is constant, being the nozzle adiabatic, and it is given by  $h_0 = h(p_0, T_0)$ .
3. The speed of sound on the nozzle axis  $a(x)$  is calculated as  $a = a(p(x), s)$  and, then, the Mach number distribution  $M(x)$  is determined.
4. The initial characteristic  $\xi_0$  is calculated applying the Carrière's method (Déleroy, 2010), modified by replacing the real gas  $\gamma_{eq}$  in Eq. (3.9) and (3.10).

The preceding initialization steps allow to start the calculation of the kinematic and thermodynamic properties for points along the characteristics downstream of the throat. The system of Eqs. (3.1), (3.2) is numerically integrated by an *Euler corrector algorithm with iteration* (Zucrow and Hoffman, 1976) algorithm, which assures a second order accuracy. By considering a generic point  $P_{ij}$  in the supersonic nozzle flow (see Fig. 3.1), the discretised form of the compatibility equation along a characteristic line  $\xi_i$ , Eq. (3.2), is carried out by means of a finite-difference scheme, as:

$$\bar{A}(V_{ij} - V_{i,j-1}) \pm (\varphi_{ij} - \varphi_{i,j-1}) = 0 \quad (3.18)$$

where  $\bar{A} = (A_{ij} - A_{i,j-1})/2$ , with  $A = \sqrt{M^2 - 1}/V$ . The solution of Eq. (3.18) coupled with Eq. (3.1), results in an iterative procedure that provides the variables  $(V_{ij}, \varphi_{ij})$  and the coordinates  $(x_{ij}, y_{ij})$  of subsequent points on the same characteristic line. Given the point  $P_{ij}$  in Fig. 3.1, the  $n_{th}$  iteration of the algorithm to calculate the flow and thermodynamic properties is performed as follows:

1. Predictor step:  $V_{ij}^{(n)} = V_{i,j-1}$ ,  $\varphi_{ij}^{(n)} = \varphi_{i,j-1}$

- Calculation of the static quantities:

$$h_{ij}^{(n)} = h_0 - \frac{(V_{ij}^{(n)})^2}{2} \Rightarrow a_{ij}^{(n)} = a(h, s) \Rightarrow M_{ij}^{(n)}, \alpha_{ij}^{(n)}, A_{ij}^{(n)}$$

The total enthalpy  $h_0$  and the entropy  $s$  are constant flow properties.

- Calculation of the  $P_{ij}^{(n)}$  coordinate  $(x_{ij}, y_{ij})$  as intersection of the two characteristics, which are locally considered as simple-waves and, then, straight lines:

$$(y_{ij} - y_{i,j-1}) = \lambda_r(x_{ij} - x_{i,j-1}) \quad (3.19)$$

$$(y_{ij} - y_{i-1,j}) = \lambda_l(x_{ij} - x_{i-1,j}) \quad (3.20)$$

where  $\lambda_r$  and  $\lambda_l$  are the local slope of the right- and left-running lines, calculated as:

$$\lambda_r = \tan \frac{\varphi_{i,j-1} - \alpha_{i,j-1} + \varphi_{ij}^{(n)} - \alpha_{ij}^{(n)}}{2}$$

$$\lambda_l = \tan \frac{\varphi_{i-1,j} + \alpha_{i-1,j} + \varphi_{ij}^{(n)} + \alpha_{ij}^{(n)}}{2}$$

2. Corrector step:

- The coefficients  $\bar{A}_{ij}$  along the right- ( $r$ ) and left-running ( $l$ ) lines are estimated, as:

$$(\bar{A}_{ij})_r = \frac{A_{i,j-1} + A_{ij}^{(n)}}{2}$$

$$(\bar{A}_{ij})_l = \frac{A_{i-1,j} + A_{ij}^{(n)}}{2}$$

- Solution of the algebraic system in the two unknowns  $(V_{ij}^{(n+1)}, \varphi_{ij}^{(n+1)})$  by means of the Cramer method:

$$(\bar{A}_{ij})_r (V_{ij}^{(n+1)} - V_{i,j-1}) - (\varphi_{ij}^{(n+1)} - \varphi_{i,j-1}) = 0 \quad (3.21)$$

$$(\bar{A}_{ij})_l (V_{ij}^{(n+1)} - V_{i-1,j}) + (\varphi_{ij}^{(n+1)} - \varphi_{i-1,j}) = 0 \quad (3.22)$$

3. Check for convergence, such that:

$$|V_{ij}^{(n+1)} - V_{ij}^{(n)}| < \varepsilon$$

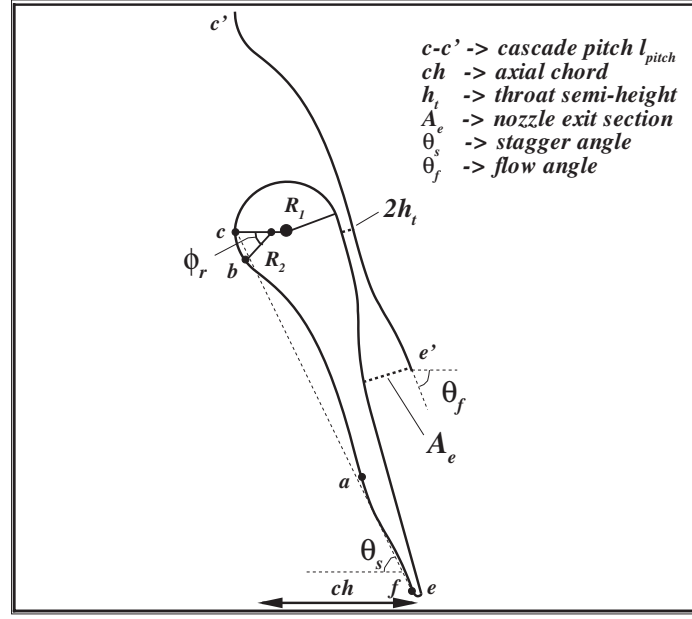
$$|\varphi_{ij}^{(n+1)} - \varphi_{ij}^{(n)}| < \varepsilon$$

where  $\varepsilon$  is a pre-set accuracy threshold. If no convergence is reached, the iterative process restarts from point 1 by using the new values as initial conditions.

The procedure described above is applied for each point along the characteristics until the convergence on the massflow is checked for each curve. In this way the nozzle shape is determined. Although the calculations required for the advanced EOS are more complex than those based on the ideal and equivalent- $\gamma$  models, this algorithm is very fast and only few seconds are required for obtaining accurate nozzle shapes on a single-processor machine.

### 3.2.2 Nozzle guide vane design

The nozzle geometry generated by the MOC is geometrically post-processed to obtain the supersonic guide vane of an axial ORC turbine. The guide vanes are designed as a two dimensional linear cascade. Given the main turbine geometrical characteristics, such as the axial chord  $ch$ , the flow angle  $\Theta_f$  and the blade pitch  $l_{pitch}$  (see Fig. 3.3), the blade vane is designed in the following way: the suction side (d-e) is obtained by rotating the MOC nozzle geometry by the angle  $\Theta_f$  in clockwise direction. Then, given  $ch$  and the coordinates of point (c), the leading edge (d-b) is designed as a circular arc with radius  $R_1$ . The latter is chosen such that  $R_1/2h_t > 6$ , as proposed by [D  lery \(2010\)](#), in order to avoid high flow deflections which could induce separation. The pressure side part of leading edge (c-b) is a circular arc of radius  $R_2$ , whose angular extension  $\phi_r$  is a free parameter. The pressure side (b-a) is designed as a third order polynomial verifying the constraints given by the end-points coordinates (a)-(b) and the angles  $\phi$  and  $\Theta$ . The aft part (a-f) is determined by translating and cutting the nozzle profile by a distance equal to the pitch  $l_{pitch}$ . Finally, a third order polynomial fits the points (f)-(e) in order to obtain the trailing edge.



**Figure 3.3:** Schematic geometrical post-processing for the ORC turbine blade vane generation.

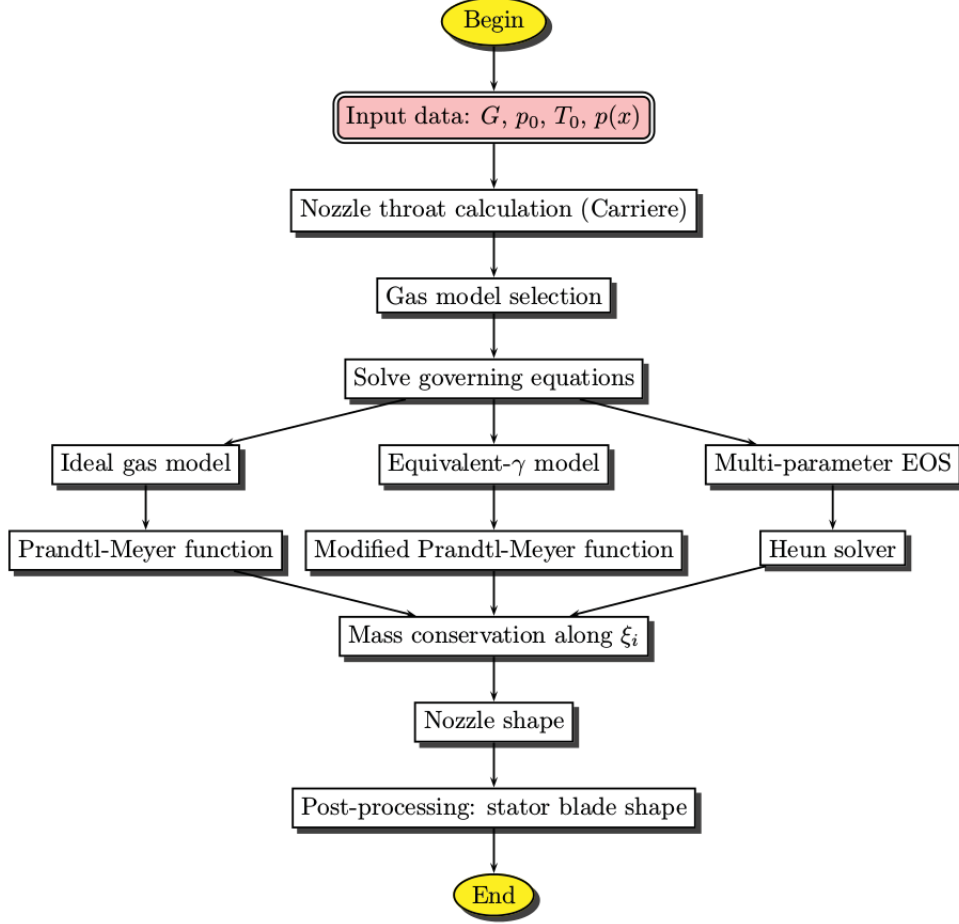
### 3.2.3 Numerical implementation of the MOC

In this work, the MOC presented in the previous Sections has been fully implemented in the FORTRAN code NODEC (acronym of "NOzzle Design with method of Characteristics"). The structure of the algorithm is shown in Fig. 3.4 as flow-chart. In order to start the MOC, the following initial design parameters need to be defined: the gas model; upstream total conditions ( $p_0$  (Pa),  $T_0$  (K)); pressure target distribution on the nozzle axis  $p(x)/p_0$  (see Fig. 3.1); design massflow rate  $G$  (kg/s). The NODEC code is validated by comparison of MOC results with those provided by the in-house CFD solver equipped with a set of EOS suitable for real gas calculations (see Section 2). Hereafter, the REF and the PRSV models are considered. Calculations are carried out for the hypotheses of 2-D, inviscid flow in order to allow direct comparison with the MOC results. A slip condition is imposed at the nozzle wall and a symmetry condition on the nozzle axis. At the subsonic inlet the total pressure, the total temperature and the flow direction are prescribed. At the supersonic outlet, the conservative variables are extrapolated from the inner cells.

### Verification results

The flow conditions considered for the verification test case are representative of a typical small scale axial ORC impulse turbine, where the entire enthalpy jump is elaborated in one single stage. As a consequence, the turbine is heavily loaded and strongly supersonic flow develops in the nozzle blade vanes. Besides, the inlet conditions are chosen above the critical point, so that strong real gas effects are present. These choices aim to better highlight the differences among the different gas models implemented in the NODEC.

The reduced (i.e. normalised with the critical-point values) operating conditions are reported



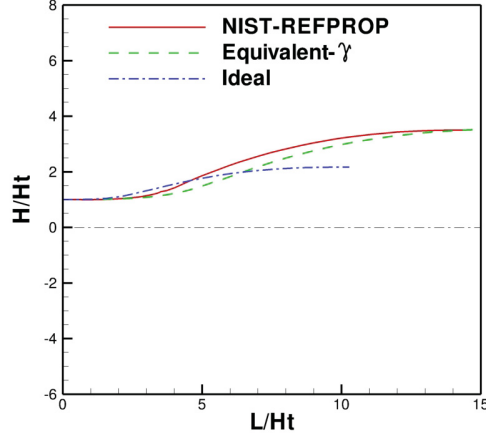
**Figure 3.4:** Flow-chart of the MOC algorithm for stator designs.

in Tab. 3.3, along with the massflow, defined per unit of length in the spanwise direction, and the design exit Mach number. The calculations are carried out for a typical ORC working fluid, namely, the R245fa. The nozzle shapes calculated by using the three different thermodynamic

**Table 3.3:** Test case reduced operating conditions and design parameters

| $p_r^0$ | $T_r^0$ | $G$ [kg/s · m] | $M_e$ | Fluid  |
|---------|---------|----------------|-------|--------|
| 1.24    | 1.05    | 20.0           | 2.06  | R245fa |

models are reported in Fig. 3.5. The geometries are normalized with respect to the nozzle throat half-height  $h_t$  in order to highlight the differences in terms of exit-to-throat area ratios, which has a direct impact on the resulting expansion pressure ratio. For a given exit Mach number and massflow rate, the ideal gas model provides a smaller nozzle, compared to REF and equivalent- $\gamma$  models. Especially, the nozzle is shorter and characterised by a smaller exit-to-throat area ratio. The need for a longer nozzle when real gas effects are considered can be explained analysing the quasi-one-dimensional relations, rewritten in a general form valid for dense gases by introducing



**Figure 3.5:** Nozzle divergent shape calculated for the three gas models and R245fa fluid. The axis are normalized respect to the nozzle throat half-height  $H_t$ .

**Table 3.4:** Expansion pressure ratio  $\beta = p_t/p_{out}$  results for  $M_e = 2.06$  and  $G = 20 \text{ kg/s} \cdot \text{m}$ .

|         | Ideal | Equivalent- $\gamma$ | REF  |
|---------|-------|----------------------|------|
| $\beta$ | 4.23  | 5.19                 | 7.32 |

the fundamental derivative  $\Gamma$  (Guardone et al., 2013):

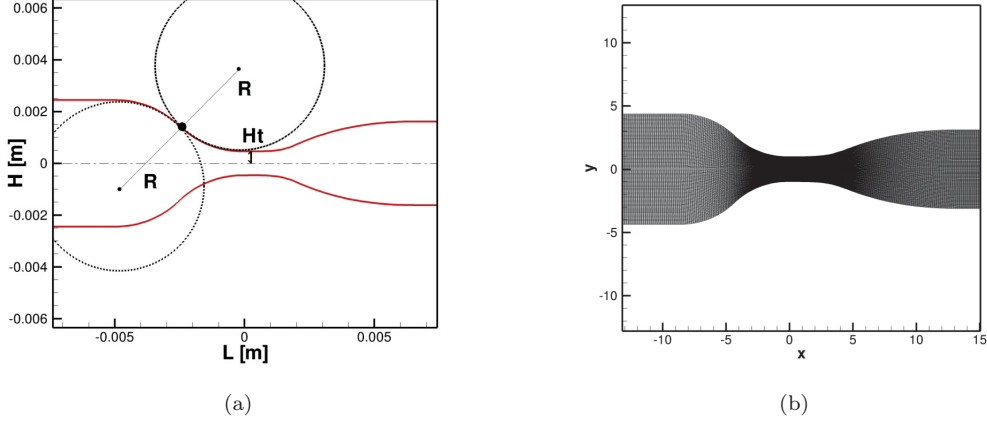
$$\frac{dp}{dx} = \frac{\rho u^2}{P} \frac{1}{1 - M^2} \frac{p}{H} \frac{dH}{dx} \quad (3.23)$$

$$\frac{dM}{dx} = - \frac{1 + (\Gamma - 1) M^2}{1 - M^2} \frac{M}{H} \frac{dH}{dx} \quad (3.24)$$

Since, for a dense gas,  $\Gamma$  is less than 1 in some flow regions, close to the saturation curve, then  $\frac{dM}{dx}$  (and  $\frac{dp}{dx}$ ), are lower than in the perfect-gas case, for which  $\Gamma$  is constant and always greater than 1 and, when  $\Gamma < 1$ , the speed of sound increases during the expansion thus counteracting the Mach number growth. Then, given the exit Mach number, the dense gas requires longer nozzles to reach the same target Mach number. The equivalent- $\gamma$  model gives a more accurate evaluation of the nozzle geometry with respect to the ideal gas model, leading to an exit-to-throat area ratio similar to that provided by REF. However, considerable differences can still be noticed in the resulting expansion ratio  $\beta$  (see Tab. 3.4). This demonstrates that care must be taken in the gas model choice, depending on the considered operating conditions.

In order to compare the NODEC results with the CFD dense gas solver, the nozzle design is completed by adding the convergent part. By considering that the supersonic flow in the divergent is not influenced by the upstream nozzle geometry, the convergent is designed by means of circular arcs (see Fig. 3.3). With this choice the flow is almost uniform in the throat region and the Carriere's method constraints are verified for the throat transonic region design. The resulting geometry for the REF model is shown in Fig. 3.6a. The computational domain is then discretised by a structured mesh of  $196 \cdot 128$  cells. The inviscid simulations are carried on

until a convergence level of  $10^{-8}$  is reached for all the conservative variables.



**Figure 3.6:** (a) Sketch of the nozzle convergent design procedure (b) Computational grid used for the calculations.

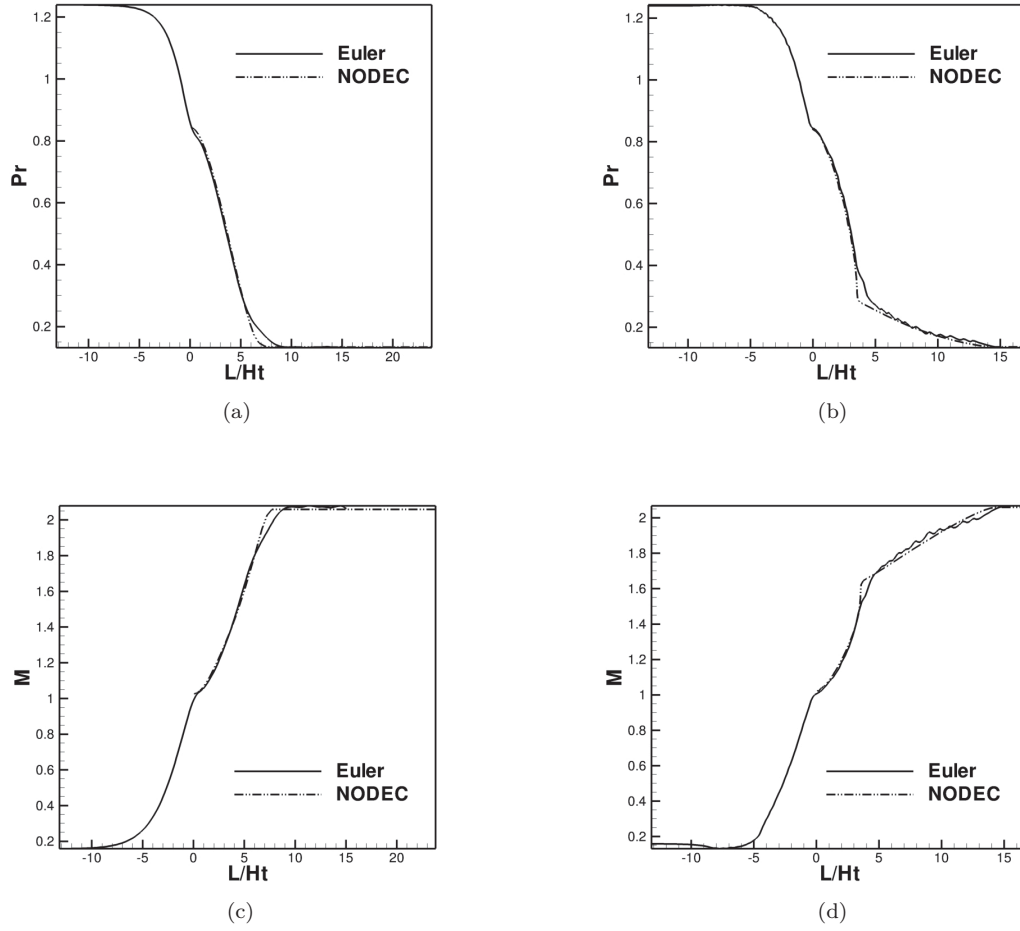
The CFD results are compared to the MOC distribution of the reduced pressure  $p_r$  and Mach number  $M$  along the nozzle center-line in Fig. 3.7. A very good agreement is observed, except for some slight differences in the initial straightening part of the nozzle. The maximum difference for the Mach number is below 1%.

The presence of dense gas effects can be recognised from the plot of the fundamental derivative  $\Gamma$  and the speed of sound (Figs. 3.8b, 3.8c, respectively). For the chosen inlet thermodynamic conditions,  $\Gamma$  has initially values slightly greater than 1 in the convergent and the speed of sound  $a$  decreases as in classical gas dynamics; however, as the expansion continues through the divergent, the Fundamental Derivative falls below 1 and the speed of sound rises, leading to non-classical behaviour.

The use of complex EOS during the CFD inviscid calculations, leads to higher computational costs (up to 10 ten times) than the ideal gas law or cubic EOS, such as the PRSV equation. Besides, no multi-processor calculations can be performed with the present dense gas solver. Because of the high number of simulations performed in this work, the PRSV model is adopted in order to save calculation time. A comparison between complex multi-parameter EOS and the PRSV results has been carried out. The maximum error is approximately 2% with a slight under-estimation of the exit Mach number, as shown in Fig. 3.9.

### 3.2.4 Nozzle guide vane performance

Computational inviscid simulations have been carried out with the dense gas solver equipped with the PRSV EOS. In this work a small scale action axial ORC turbine is investigated. Four alternative organic working fluids suitable for ORC applications have been considered. For each fluid, three nozzle guide vanes geometries (based on the perfect, equivalent- $\gamma$  and REF gas models) have been designed. The performance of the different designs is then investigated by means of inviscid CFD calculations. For one of the geometries designed for the R245fa working fluid, a viscous calculation has been carried out. The designs have been carried out using the



**Figure 3.7:** Comparison among the Euler calculations and NODEC results: (a) Reduced pressure evolution along the nozzle axis. (b) Reduced pressure evolution along the nozzle wall. (c) Mach number evolution along the nozzle axis. (d) Mach number evolution along the nozzle wall.

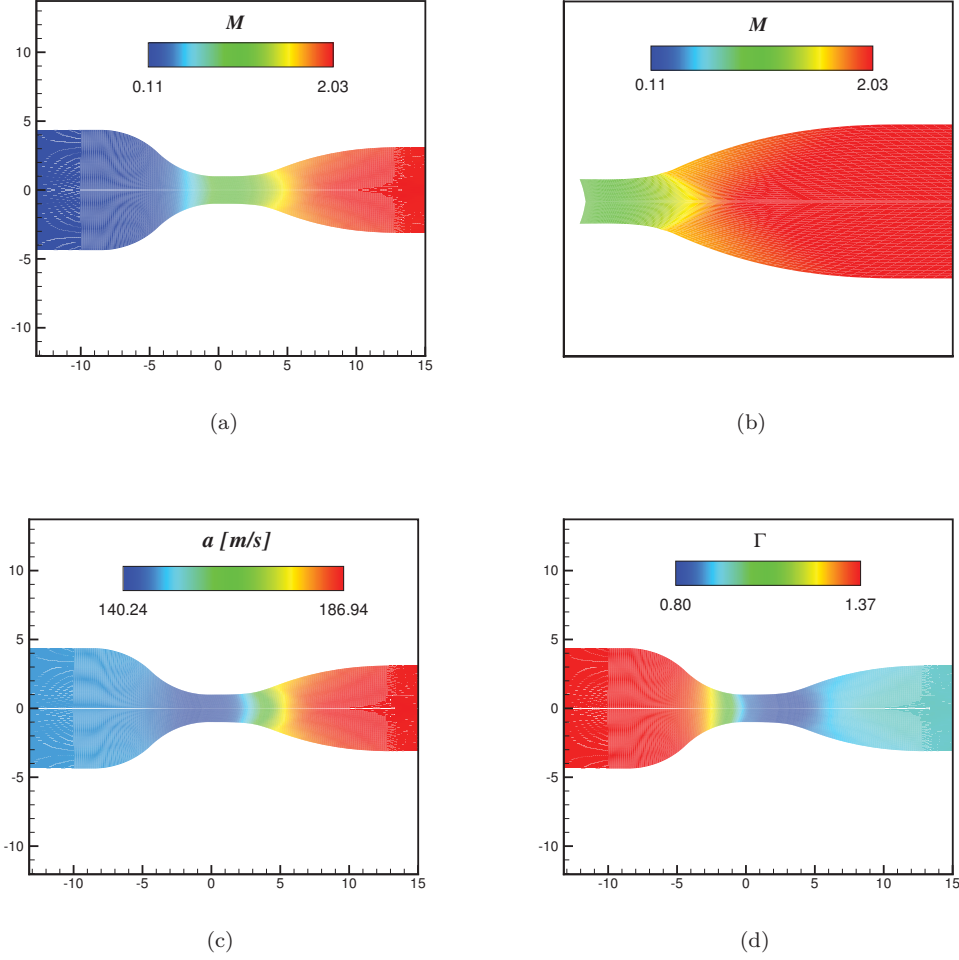
**Table 3.5:** Main settings for the computational simulations and the nozzle blade vane design.

| $p_r^0$ | $T_r^0$ | $\Theta$     | $R/(2h_t)$ | $M_e$ | $G[kg/s \cdot m]$ |
|---------|---------|--------------|------------|-------|-------------------|
| 1.28    | 1.05    | $77.8^\circ$ | 7.5        | 2.0   | 20.0              |

geometrical and operational parameters of Tab. 3.5. The same inlet total reduced conditions are imposed in order to conserve the relative position of the expansion starting point with respect to the saturation curves.

The simulations have been performed on structured single-block C-type grids, created by means of an in-house elliptic grid generator, composed by  $384 \times 64$  cells for the inviscid calculations and

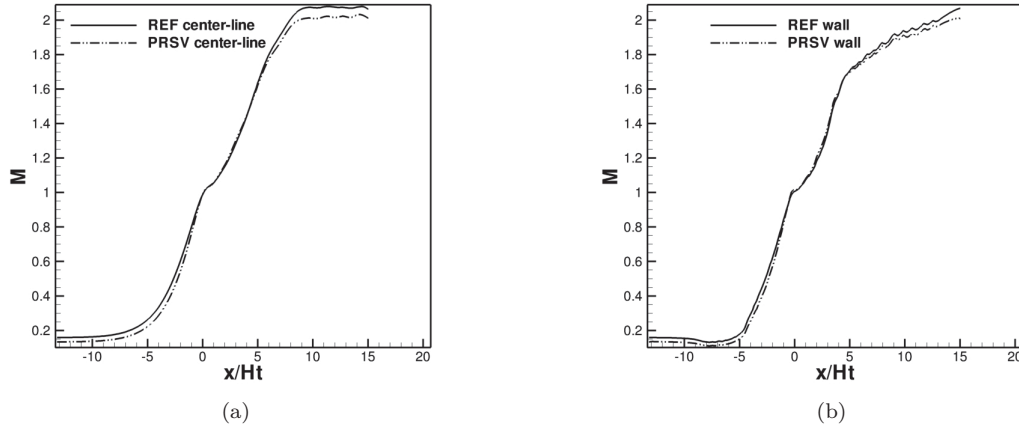




**Figure 3.8:** Results for the inviscid simulation for fluid R245fa: (a) Mach number contour plot. (b) Speed of sound contour plot. (c) Fundamental Derivative  $\Gamma$ . The nozzle geometry is normalised with respect to the throat height. (d) Mach number contour plot provided by the NODEC algorithm. Only the divergent part of the nozzle has been computed with the MOC.

by  $384 \times 128$  cells for the viscous calculations. In the latter case, the grid has been clustered close to the blade wall, in order to get a first cell height such that  $y^+ \approx 1$ . The inviscid simulations have been performed by imposing the nominal inlet reduced total pressure and temperature, and an azimuthal periodicity at inter-blades boundaries. A no-match joint condition is applied to the branch-cut behind the trailing edge, whereas an extrapolation condition is used at the supersonic outlet.

In addition to the inviscid calculations, viscous simulations have been also carried out by assuming an adiabatic wall condition. The flow is highly turbulent with a Reynolds number equal to  $5.3 \cdot 10^7$  referred to the chord and exit conditions, a typical value for small scale ORC axial



**Figure 3.9:** REF Vs PRSV model results for inviscid simulations: (a) Nozzle axis Mach number distribution. (b) Wall nozzle Mach number distribution.

turbines. The Spalart-Allmaras one-equation turbulence model is used to model the turbulent stresses.

In the following we analyse the numerical results obtained for the different nozzle designs in terms of the following quantities of interest:

- the isentropic efficiency  $\eta_{is}$  (computed as the real-to-ideal static enthalpy drop ratio);
- the Carnot factor  $\Theta_C = 1 - T_0/T$ , defined as the Carnot efficiency of a thermal machine operating between the total temperature  $T_0$  and the local static temperature  $T$ ;
- the static enthalpy drop between the outlet and the inlet of the nozzle guide vane;
- the expansion pressure ratio  $\beta = p_e/p_t$ , evaluated between the nozzle throat  $A_t$  and the nozzle exit area  $A_e$ .

All the simulations have been performed for the design conditions listed in Tab. 3.5 and used also for the nozzle guide vane design with NODEC.

The overall flow field obtained for the various working fluids are qualitatively similar. In Fig. 3.10 the results obtained for R245fa are showed. The main performance results for all the fluids are summarized in Tab. 3.6.

The flow in the divergent is, as expected, supersonic and a weak oblique shock wave departs from the trailing edge. No shock waves are present in the divergent part of the vane, confirming that the nozzle design with NODEC is respectful of the adaptation conditions.

In the inviscid calculations the main losses are associated with the oblique shocks and, to a lesser extent, with numerical dissipation errors due to the CFD solver.

The flow accelerates up to  $M = 2$  in the nozzle exit section  $A_e$ , which is close to the design exit Mach number. Then, the flow expands guided by the suction side wall on the bottom and from a free stream surface on the top. This leads to exit Mach numbers higher than expected (maximum  $M \approx 2.7$  for R245fa). The flow is then weakly decelerated across the oblique shock. The latter introduces a significant flow deviation, leading to an exit flow angle (see Fig. 3.10d),

which differs of about  $7.32^\circ$  from the geometrical one. These phenomena needs to be taken carefully into account during the design stage of the complete turbine stage, because a design based on the theoretical velocity triangles could lead to misleading results and to overestimation of the performances.

Dense gas effect have a considerable influence on system performances. As shown in Fig. 3.11, the flow starts to expand from a supercritical condition, subsequently it crosses a region characterised by values of  $\Gamma < 1$ .

The presence of dense gas effects has a strong influence on the blade vane performances (as reported in Tab. 3.6), and specifically in the resulting pressure ratio (and subsequently the massflow per unit span).

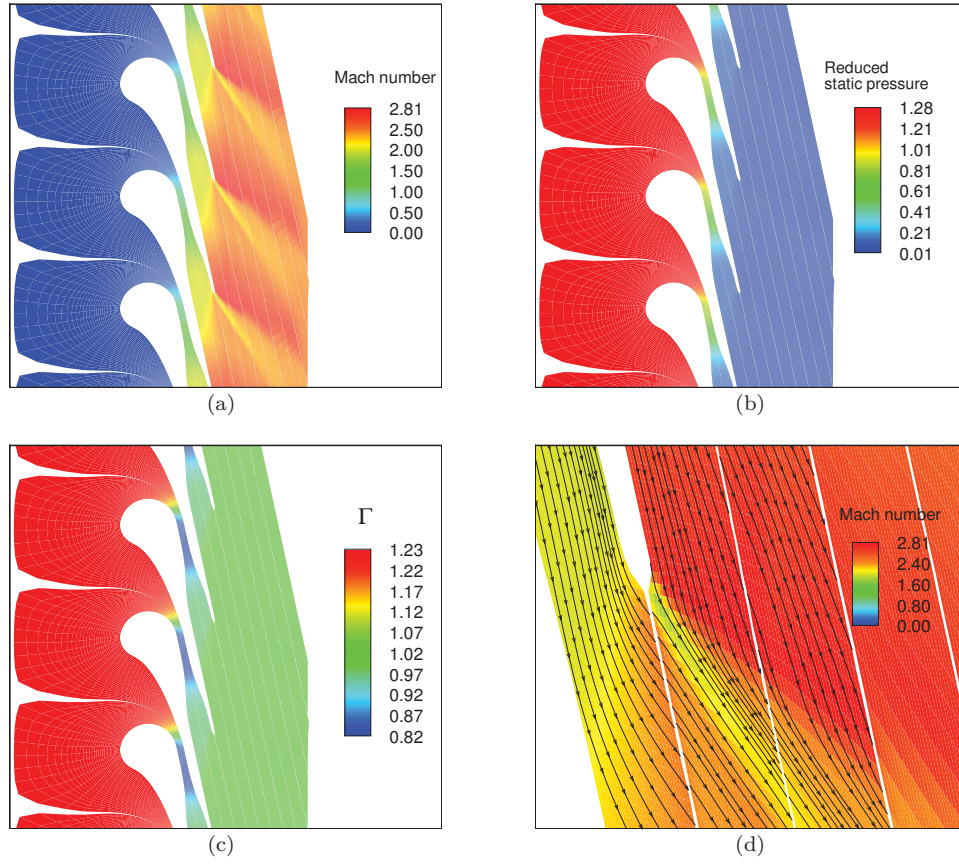
It is observed that, independently on the considered working fluid, the guide vane performance (and namely the isentropic efficiency and the enthalpy drop) improve considerably for blades designed by using a more realistic gas model. In particular, the ideal gas model is shown to be inadequate for the design of ORC nozzle guide vanes. The equivalent- $\gamma$  model provides a reasonably accurate design for Novec649 and the RE347mcc fluids, whereas for R245fa and R449 the design made with the simplified model results in lower efficiency.

Considering only the REF blade shapes, the best performances (for the present choice of the reduced inlet conditions) in terms of isentropic efficiency are shown by the R449 fluid with  $\eta_{is} = 0.984$  that, compared to the R245fa (classically used in ORC applications), provides an increase of 4%. Fig. 3.11e shows the  $\Gamma$  profile along the nozzle blade vane centerline both for R449 and R245fa. The R449 molecular complexity, greater than R245fa, results in lower  $\Gamma$ , implying stronger dense gas effects. Especially, it exhibits lower shock losses and, as a consequence, greater isentropic efficiencies.

For all of the fluids the Carnot factor  $\Theta_C$  and the enthalpy drop increase for designs based on more advanced gas models. Greater  $\Theta_C$  results in better exploitation of heat source. Under this point of view, the R245fa provides the best results compared to all other fluids. However, the higher enthalpy drop and, then, the higher power output (for the same massflow) is provided by R449, which definitely remains the best candidate for this application.

**Table 3.6:** Summary of the guide vane performances for different working fluids and blade designs based on various gas models.

| <i>Fluid</i>    | $\eta_{is}$ | $\Theta_C$ | $\Delta H[kJ/mol \cdot K]$ | $\beta (M_{e,design} = 2)$    | $G [kg/s]$ |
|-----------------|-------------|------------|----------------------------|-------------------------------|------------|
| <b>R245FA</b>   |             |            |                            |                               |            |
| <i>Ideal</i>    | 0.931       | 0.230      | 23.6                       | 5.2 ( $\beta_{des} = 7.5$ )   | 10.2       |
| $\gamma_{eq}$   | 0.938       | 0.242      | 25.6                       | 9.5 ( $\beta_{des} = 10.1$ )  | 18.6       |
| <i>REF</i>      | 0.947       | 0.246      | 26.3                       | 10.2 ( $\beta_{des} = 10.5$ ) | 19.8       |
| <b>NOVEC649</b> |             |            |                            |                               |            |
| <i>Ideal</i>    | 0.926       | 0.100      | 28.2                       | 6.3 ( $\beta_{des} = 7.3$ )   | 12.8       |
| $\gamma_{eq}$   | 0.952       | 0.120      | 31.7                       | 9.8 ( $\beta_{des} = 10.1$ )  | 19.2       |
| <i>REF</i>      | 0.953       | 0.123      | 32.6                       | 9.9 ( $\beta_{des} = 10.3$ )  | 19.7       |
| <b>R449</b>     |             |            |                            |                               |            |
| <i>Ideal</i>    | 0.927       | 0.125      | 29.2                       | 5.6 ( $\beta_{des} = 8.1$ )   | 10.6       |
| $\gamma_{eq}$   | 0.968       | 0.133      | 32.2                       | 10.5 ( $\beta_{des} = 10.9$ ) | 18.8       |
| <i>REF</i>      | 0.984       | 0.132      | 32.5                       | 11.2 ( $\beta_{des} = 11.3$ ) | 20.1       |
| <b>RE347MCC</b> |             |            |                            |                               |            |
| <i>Ideal</i>    | 0.926       | 0.160      | 26.5                       | 5.5 ( $\beta_{des} = 7.9$ )   | 9.9        |
| $\gamma_{eq}$   | 0.941       | 0.166      | 28.4                       | 10.4 ( $\beta_{des} = 10.8$ ) | 18.6       |
| <i>REF</i>      | 0.943       | 0.169      | 29.1                       | 11.2 ( $\beta_{des} = 11.1$ ) | 20.2       |



**Figure 3.10:** Numerical results for inviscid calculations with fluid R245fa: (a) Mach number contour plot. (b) Reduced static pressure  $p/p_c$  contour plot. (c) Fundamental Derivative  $\Gamma$  contour plot. (d) Stream traces on the trailing edge with Mach number contour plot.

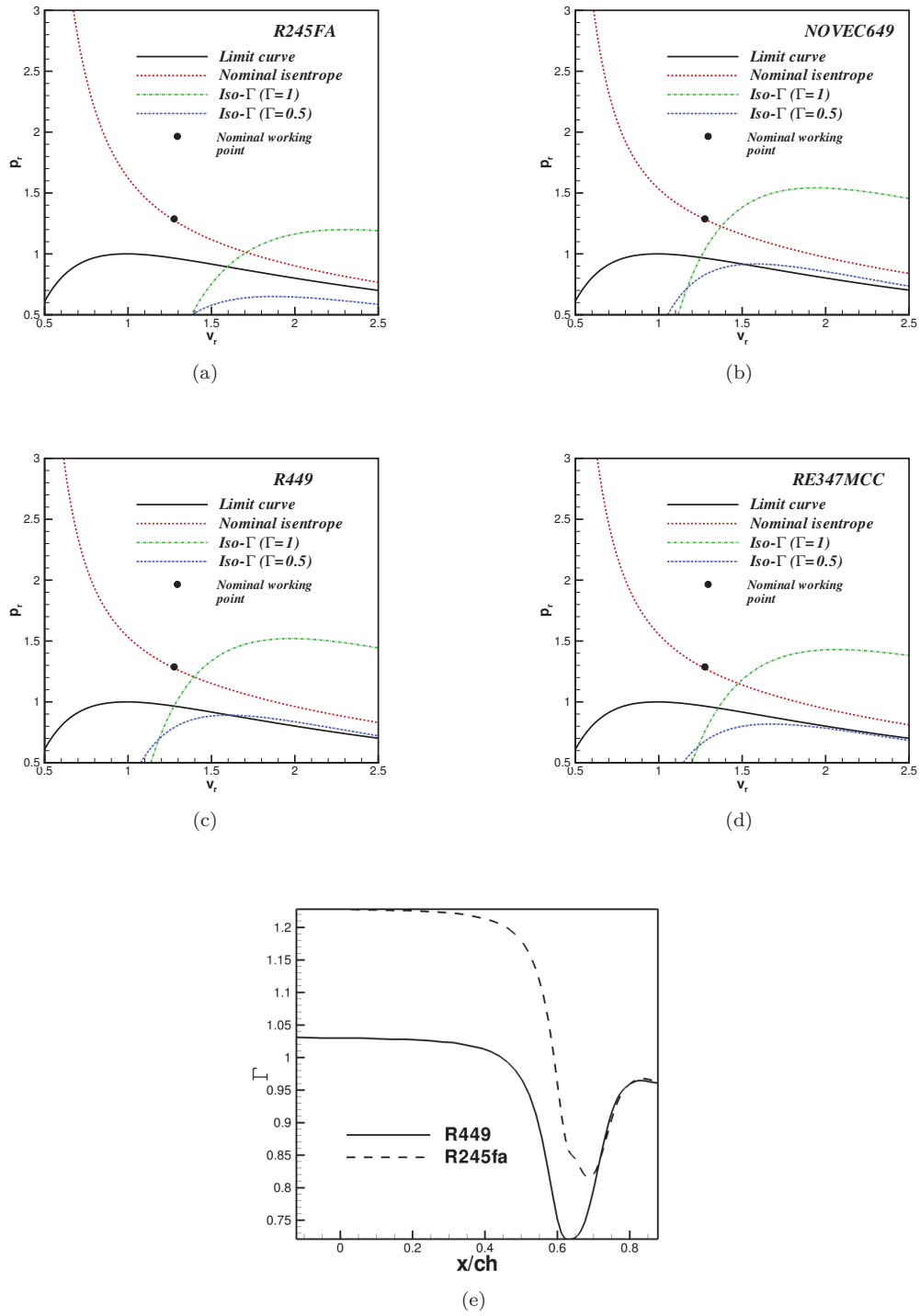
Fig. 3.12 shows the overall solution for R245fa, based on a viscous simulation. The operating condition are the same used for the inviscid calculations (see Tab. 3.5). The attention is focused on nozzle guide vanes designed with the REF model. The performances are summarised in Tab. 3.7.

The isentropic efficiency drops by 10% with respect to the inviscid simulation. Besides, the enthalpy drop is 6% lower. This effect can be explained by viscous losses in the attached boundary layer and in the wake, as well as to the formation of a separation bubble at the suction side, close to trailing edge, leading to a significant reduction of the effective exit-to-throat area ratio.

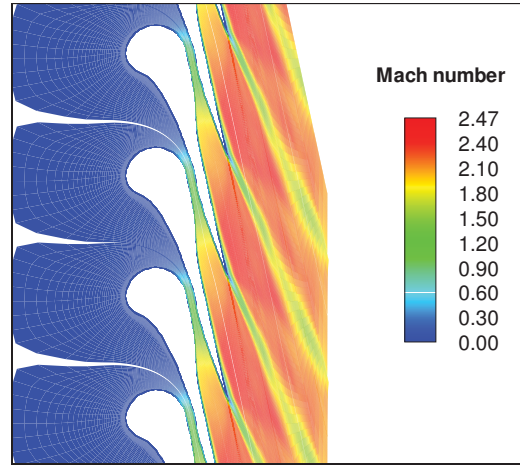
**Table 3.7:** Summary of the guide vane performances for R245fa fluid, viscous calculations and blade shape calculated with REF model.

| Fluid         | $\eta_{is}$ | $\Theta_C$ | $\Delta H[kJ/mol \cdot K]$ | $\beta$ |
|---------------|-------------|------------|----------------------------|---------|
| <b>R245FA</b> | 0.843       | 0.237      | 24.7                       | 5.2     |

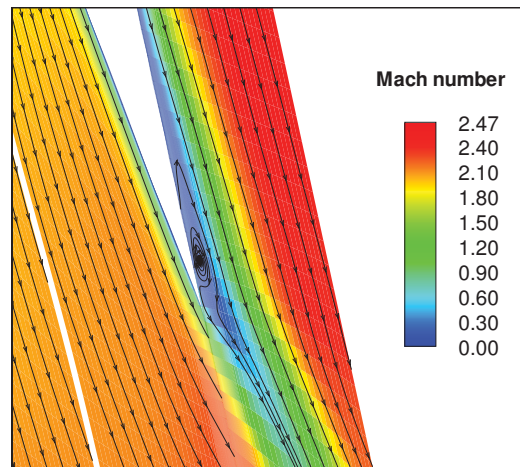
The trailing-edge oblique shock is also present in the viscous simulation, but it is weaker than in the inviscid case. As a consequence, the increased losses are essentially due to the viscous phenomena.



**Figure 3.11:** Clapeyron diagram with iso- $\Gamma$  and nominal isentrope lines for: (a) R245FA (b) NOVEC649 (c) R449 (d) RE347MCC; fundamental derivative profiles along the blade vane centerline for fluids R245fa and R449 (e).



(a)

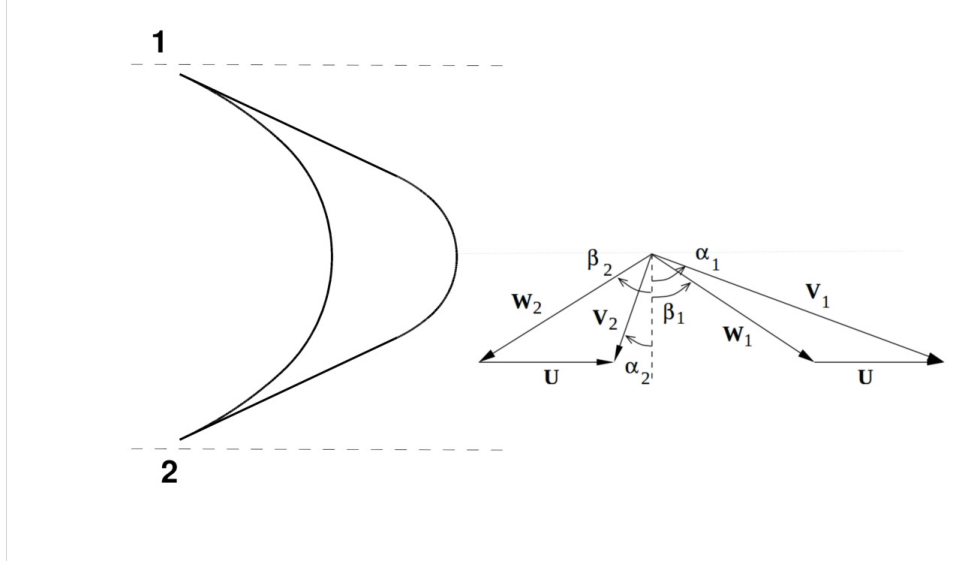


(b)

**Figure 3.12:** Viscous results for R245fa: (a) Mach number contour plot. (b) Stream traces underlining the presence of a recirculation bubble.

### 3.3 Method of characteristics for rotor design

The need for a compact turbine working with high pressure ratios implies the choice of an impulse turbine architecture (see e.g. (Kunte and Seume, 2015)). This can be justified by considering a typical impulse rotor blade and its velocity triangles (Fig. 3.15). By imposing an axial outlet



**Figure 3.13:** Example of impulse blade geometry and velocity triangles

flow for the impeller ( $\alpha_2 = 0$ ), with the axial absolute velocity component kept constant, the work coefficient can be expressed as:

$$\psi = \frac{\Delta H_0}{U^2} = 2(1 - \Lambda) \quad (3.25)$$

In equation ((3.25)),  $U$  represents the peripheral velocity at a specified radius,  $\Delta H_0$  the total enthalpy drop per unit mass across the turbine stage and  $\Lambda$  the degree of reaction. For an impulse turbine ( $\Lambda = 0$ ) and a given  $U$ , the total enthalpy drop is two times greater than for a 0.5 reaction degree turbine. This property allows extracting a large amount of work from a single stage, with a maximum for a vane outlet swirl equal to  $67^\circ$  and rotor turning to  $116^\circ$  ( $\beta_1 = \beta_2 = 58^\circ$ ) (Paniagua et al., 2014). However, particular care must be addressed to the rotor and stator blades aerodynamic design because both behave as supersonic nozzles. Moreover, the typical operating conditions for an ORC turbine are in the proximity of the working fluid saturation curve or sometimes supercritical. Due to the presence of strong dense gas effects, models used to design the blade shapes have to be modified accordingly. Several authors in the past have addressed the design of dense gas nozzles and stator blades (Cramer and Fry, 1993; Guardone et al., 2013; Wheeler and Ong, 2013; Bufi et al., 2015). All of them generally rely on extended version of the Method of Characteristics (MOC) for 2D supersonic flows, as seen in the previous Section. The aim of this Section is to develop a methodology for the design of rotor blades of an axial supersonic ORC impulse turbine which takes properly into account dense gas effects. The procedure is also based on the MOC, along with a vortex flow field approach, and was previously introduced for perfect gas flows by Goldman (1968) and Paniagua et al. (2014). Here, the approach is extended, for the first time to the author's knowledge, to the dense gas case.

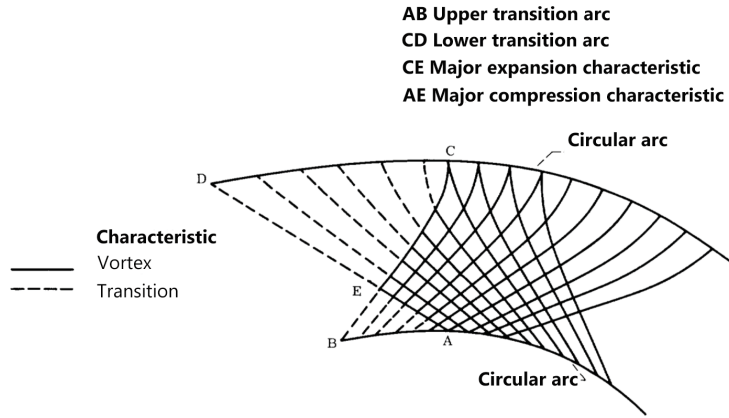


The performances of the rotor blade shapes obtained with MOC using different organic working fluids have been evaluated by means of numerical simulations carried out using the dense gas solver equipped with the PRSV EOS described in Section 2.2.

### 3.3.1 Design of dense gas supersonic rotor blades

For the design of supersonic rotor blades the procedure described in (Paniagua et al., 2014; Goldman, 1968) for perfect gas flows has been followed and extended to dense gases.

The flow at the rotor inlet is assumed to be an uniform one that is simply deflected by the rotor blades. To achieve this deflection, the flow passes through a transition region delimited by upper and lower transition arcs and by characteristic lines. For clarity, the transition region is



**Figure 3.14:** Scheme of the system of characteristic lines in the rotor vane. (Goldman, 1968)

sketched in figure 3.14, where AB and CD are transition arcs and the dashed lines are used to represent the characteristics. Through this region, the uniform inlet flow is converted into a free vortex flow, for which  $V \cdot R = \text{constant}$ , with  $R$  the radius of curvature of a streamline and  $V$  the (constant) velocity magnitude, following an isentropic transformation.

Figure 3.15 shows a schematic description of the rotor blade geometry designed with MOC. The same notation of the MOC for perfect gases reported in Paniagua et al. (2014) and Goldman (1968) has been used. The reader may refer to those references for more details.

In order to start with the new design procedure for dense gases, the following input parameters are defined: inlet relative total pressure and temperature; inlet/outlet relative flow angle  $\beta_i/\beta_o$ ; inlet/outlet relative Mach number  $M_i/M_o$ ; the lower arc Mach number  $M_l$ , assigned on the lower circular arc b-b'; the upper arc Mach number  $M_u$ , assigned on the upper circular arc d-d'. As for the perfect gas model, the lower and upper transition arcs (a-b/a'-b' and d-e/d'-e' for inlet and outlet, respectively) are determined in the unrotated lower/upper reference systems (denoted with subscripts  $l$  and  $u$ ).

For the sake of brevity, the design procedure is sketched in Fig. 3.16 only for the lower transition arc. The same procedure can be applied to the upper arc. The arcs are designed by starting from the vortex region up to the uniform region, in order to match the input inlet conditions.

The vortex flow is described by the general equation  $V \cdot R = \text{cost}$ , with  $V$  the velocity magnitude and  $R$  the curvature radius of the relative streamline, but it can be re-written in non-dimensional form by normalizing with respect to the product  $a^* \cdot r^* = \text{cost}$ , where the super-script \* denotes critical (sonic) parameters. Specifically,  $a^*$  represents the critical speed of sound and  $r^*$  the

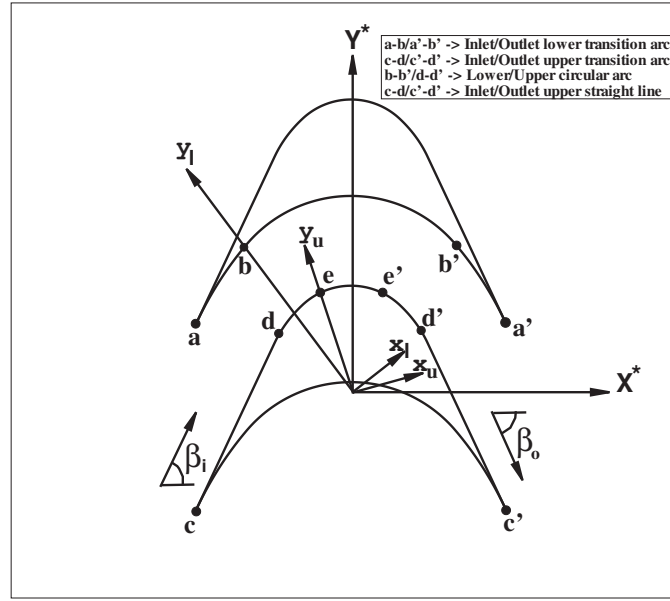


Figure 3.15: Schematic description of the rotor blade design.

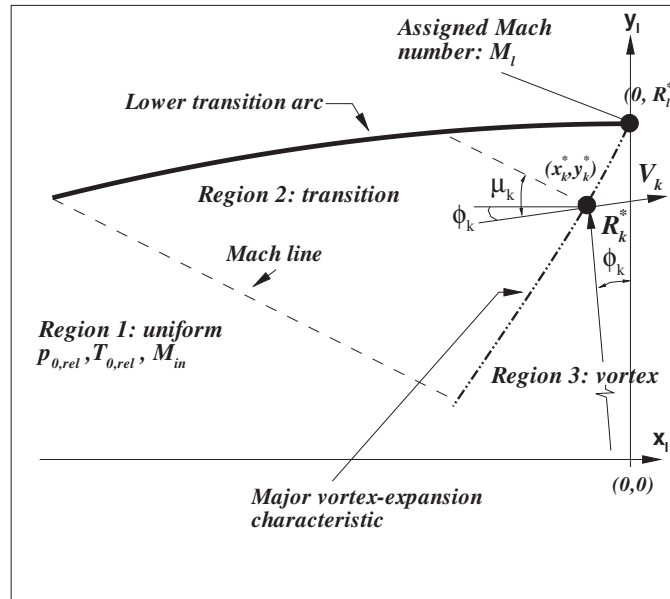


Figure 3.16: Lower transition arc design.

radius of the sonic streamline. The vortex equation becomes:  $M^* \cdot R^* = 1$ , with  $M^* = V/a^*$  and  $R^* = R/r^*$ .

While the MOC for perfect gas provides the analytical Prandtl-Meyer function  $\nu = \nu(M)$  and the critical Mach number  $M^* = M^*(M)$  (with  $M^* = V/a^*$ ), for a dense gas no such analytical expressions are available.

Then, the calculation of the critical Mach number is replaced by the following iterative procedure:

1. The critical speed of sound is first computed from the known values of the total pressure  $p_0$  and temperature  $T_0$  (for a constant height blade) by using the EOS
2. A tentative value  $M^{*(0)}$  for the critical Mach number is prescribed
3. At each iteration of the method, an updated value of the velocity magnitude is computed as  $V^{(m)} = M^{*(m-1)} a^*$
4. The latter is used to compute an updated value of the specific static enthalpy  $h^{(m)}$ , given the total enthalpy  $h_0 = h_0(p_0, T_0)$ .
5. The speed of sound is then updated by using the thermodynamic relation  $a^{(m)} = f(h^{(m)}, s)$ , where the entropy  $s$  is constant everywhere and is known from the prescribed inlet conditions.
6. Finally, an updated value of the Mach number  $M^{(m)} = V^{(m)}/a^{(m)}$  is obtained.
7. If  $M^{(m)} - M^{(m-1)}$  is below a given tolerance (here taken equal to 0.001%), the procedure is stopped. Otherwise, a new value is assigned for  $M^{*(m+1)}$  (by using a bisection procedure) and the iteration is started again.

By applying the procedure above to calculate  $M_l^*$  knowing  $M_l$ , the position of the first point on the lower arc in the reference frame  $(x_l, y_l)$  is  $(0, R_l^*)$ , where  $R_l^* = 1/M_l^*$ . The flow is horizontal at location  $l$ , then  $\varphi_l = 0$  and the flow angle at the new point  $(x_k^*, y_k^*)$  is obtained by adding a small step  $\Delta\varphi$  to the preceding location.

Also, knowing  $M_l$ , the local slope of the left-running characteristic line is  $\mu_l = \arcsin(1/M_l)$ . The coordinates of location  $k$  on the major vortex characteristic are then calculated as intersection between the straight lines of slopes  $\tan(\varphi_k)$  and  $\tan(\mu_l)$ , respectively.

By knowing the coordinates of location  $k$ , the new radius  $R_k^*$  is evaluated and  $M_k^* = 1/R_k^*$ . Then, the Mach number at location  $k$ ,  $M_k$ , can be calculated by means of an iterative procedure similar to the one previously used to calculate  $M^*$ .

In a similar manner, all the other points of the major vortex-expansion characteristic are calculated until the condition  $M_{k+1} = M_{in}$  is verified with an assigned tolerance.

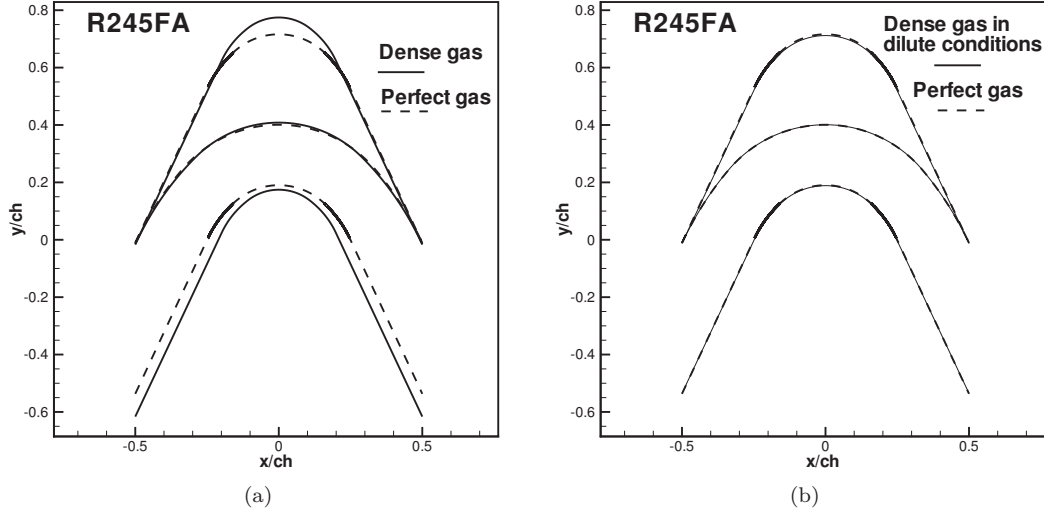
The geometry is afterwards rotated in the  $X^* - Y^*$  reference system and completed with the straight line parts c-d/c'-d' and the circular arcs b-b'/d-d' (see Fig. 3.15). Finally, a finite leading-edge/trailing-edge thickness is added. Besides, non-symmetrical blades with various degrees of reaction can be designed if different inlet/outlet input parameters are imposed.

The preceding design procedure has been implemented is a FORTRAN code named RODEC (ROtor DDesign with method of Characteristics).

In this thesis work, typical phenomena of supersonic rotor cascades have been investigated and analysed. Specifically, the unique incidence problem, related to the supersonic relative flow at the rotor inlet and extended for the first time to the dense gas regime, has been taken into account in a second design step. Further details are provided in Section 3.3.4.

### 3.3.2 Examples of rotor blade designs

The RODEC algorithm has been run for different fluids and design conditions to investigate the impact of real gas effects on the resulting geometry. The degree of reaction is set to zero so that the resulting blade is always symmetric. Figs. 3.17a-b show a comparison of geometries calculated for R245fa (see Tab. 2.1 for properties) with different operating conditions and gas models. The



**Figure 3.17:** Blade designs for R245FA at operating conditions ( $p_r^0 = 1.05, T_r^0 = 1.05, M_{in} = M_{out} = 1.5$ ) (a) and at dilute conditions ( $p_r^0 = 0.055, T_r^0 = 1.15, M_{in} = M_{out} = 1.5$ ) (b). Dashed lines represent designs obtained under the perfect gas model.

operating conditions considered for the design, are given in Tab. 3.8. The first operation point is very close to the R245fa upper saturation curve and this affects the rotor geometry leading to larger cross section variations with respect to perfect gas. Specifically, the dense gas design is characterised by a greater exit-to-throat area ratio. This is a typical behaviour observed for supersonic stators (see Section 3.2.3).

In figure 3.17b the test is repeated by lowering the total pressure and increasing the total temperature in order to reach the dilute dense gas region. In this region, the blade designed with a dense gas EOS is very similar to that obtained with the perfect gas model. Indeed, the two blade geometries are practically overlapped. Then, a parametric study for several working fluids

**Table 3.8:** Operating and design conditions for the rotor design.

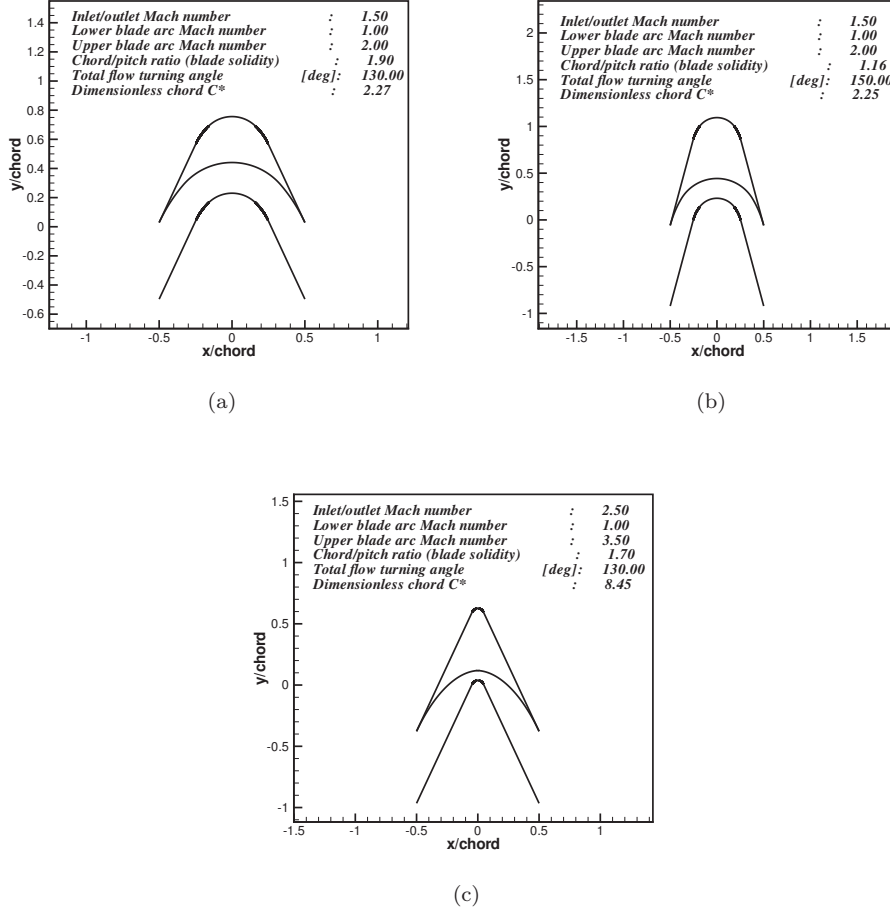
| $p_r^0$ | $T_r^0$ | $M_{in}$ | $M_{out}$ | $M_l$ | $M_u$ | $\beta_{in}$ | $\beta_{out}$ |
|---------|---------|----------|-----------|-------|-------|--------------|---------------|
| 1.05    | 1.05    | 1.5      | 1.5       | 1.0   | 2.0   | 65°          | 65°           |

**Table 3.9:** Geometrical output parameters for four different organic fluids under the same operating condition ( $p_r^0 = 1.05, T_r^0 = 1.05, M_{in} = M_{out} = 1.5, M_l = 1, M_u = 2, \beta_{in} = \beta_{out} = 65^\circ$ ).

|          | R245fa | Novec649 | RE347mcc | R449 |
|----------|--------|----------|----------|------|
| $\sigma$ | 1.67   | 1.61     | 1.62     | 1.60 |
| $ch^*$   | 2.45   | 2.51     | 2.50     | 2.53 |
| $ph^*$   | 1.47   | 1.56     | 1.54     | 1.58 |

suitable for ORC applications at the same reduced input conditions has been carried out. In Tab. 3.9 the following output geometrical parameters are shown: blade solidity  $\sigma$ , defined as the

axial chord to pitch ratio; the axial chord  $ch^*$  and pitch  $ph^*$  normalized respect to the critical radius  $r^*$ , the latter defined as the radius of the sonic streamline in the vortex flow field. It can be noticed that the lower is the fluid molecular complexity (as for the R245FA fluid) the higher is the solidity.

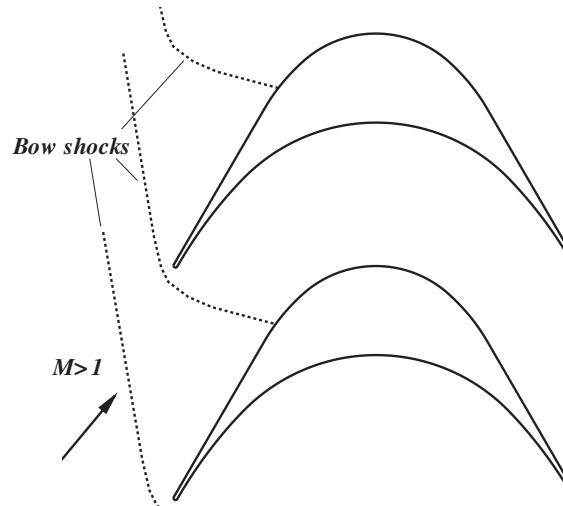


**Figure 3.18:** Examples of blade design for R245FA at operating conditions ( $p_r^0 = 1.05$ ,  $T_r^0 = 1.05$ ) for different inlet and outlet Mach numbers and flow turning angles.

Finally, three blade shapes have been designed for R245fa fluid using different inlet/outlet Mach numbers (precisely, 1.5 and 2.5) and flow turning angles in order to show the variety of the cascade geometries provided by the RODEC algorithm. The resulting geometries are reported in Fig. 3.18. It can be noticed that the higher is Mach number imposed on the suction side the lower is the extension of the upper transition arc, resulting in very narrowed rotor blades. In this way, the expansion required to reach the desired Mach number in the vortex region, can be realised by means of the higher inlet-to-throat area ratio.

### 3.3.3 Started and unstarted supersonic rotors

The ideal design provided by the procedure described in the previous Section is corrected in order to provide a feasible leading-trailing edge thickness by means of circular arcs. Since the inlet flow is fully supersonic, the rounded leading edge behaves as a bluff body immersed in a supersonic flow. This leads to the formation of a bow-shock upstream of the leading edge. The strength and the stand-off distance of the shock from leading edge are function of the inlet Mach number and the leading edge radius. In the case of the supersonic rotor row designed by means of the RODEC algorithm, the shocks pattern is similar to that provided by Fig. 3.19.



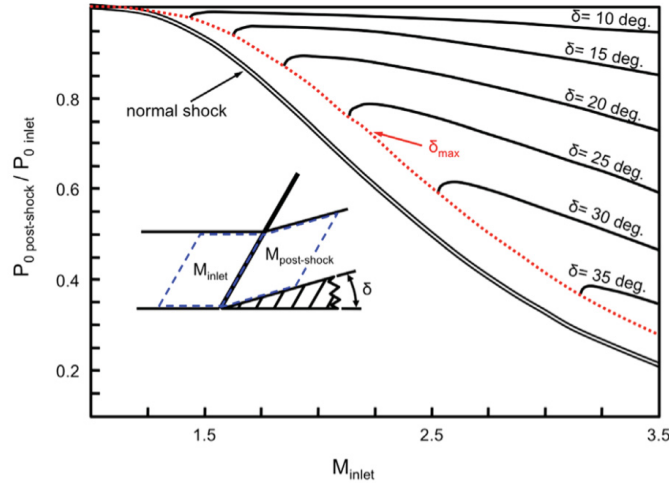
**Figure 3.19:** Bow-shocks pattern for a supersonic rotor row.

Under the hypotheses of steady, two-dimensional flow, after a short transient due to the start of the turbine, different steady shock configurations can be considered. In order to analyse them, it is possible to assume that a rotor blade vane behaves as a supersonic diffuser with respect to the relative inlet flow.

As well known, in a Laval nozzle the gases can be accelerated isentropically up to the supersonic condition in the divergent through the sonic throat. An inversion of the process, i.e. a shock-free deceleration of a supersonic flow up to the subsonic condition, could be possible in principle but unattainable in practice for stability reasons (Kantrowitz and Donaldson, 1948). This point can be understood by considering a supersonic flow initially decelerated through a convergent-divergent diffuser by means of an ideal smooth isentropic process. In this configuration, no information can travel from the sonic throat up to the inlet, however disturbances can be transmitted in the divergent, where the flow is subsonic, up to the throat. Because of this, a disturbance in the sonic region causes a temporary reduction of the massflow but, since the diffuser elaborates the maximum allowable massflow for the given upstream conditions, an accumulation of mass is settled ahead of the throat. This phenomenon is unstable and leads the flow to adapt to the new condition by means of a shock ahead of the diffuser. Then, it can be concluded that a supersonic flow can not be isentropically decelerated up to the subsonic condition in a diffuser designed to produce it.

As shown by Kantrowitz and Donaldson, the strength of the shock in the divergent, its position and, subsequently, the flow properties downstream of it depend on the diffuser geometry and Mach number upstream. By enlarging the throat-to-inlet area ratio, which defines the contraction ratio  $C_R$ , it can be seen that the shock jumps from ahead the diffuser up to the divergent part. For a given limit of  $C_R$ , the shock could be totally swallowed from the diffuser and the flow would be supersonic without shocks. In these conditions the supersonic diffuser is said to be *started*, *unstarted* otherwise.

In the supersonic rotor framework, a started conditions is strongly desirable. Indeed, a dramatic abatement of the dynamic pressure in turbine cascades is provided by normal shock-waves standing ahead the row, and the higher is the inlet Mach number the higher are the losses, see Fig. 3.20. Then, the ideal working condition would be to have a started solution with oblique shock



**Figure 3.20:** Total pressure losses across a shock as function of the wall deflection  $\delta$  for a perfect gas. Figure extracted from (Paniagua et al., 2014).

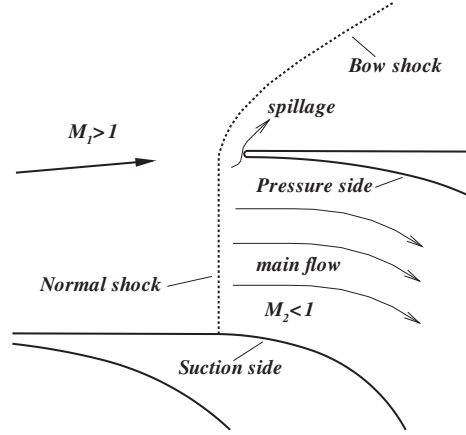
waves originated at the leading edge, and the normal shocks swallowed by the blade vanes. In this configuration, not only the total pressure losses would be minimized, but also the effects of the shock-boundary layer interactions (e.g. boundary layer separation) on the suction side would be reduced thanks to the weaker shocks impinging on the adjacent blade surface.

In order to better visualize the starting problem for the rotor, it is useful to analyse the relative flow in the reference frame rotated by the relative inlet flow angle. For an unstarted turbine the flow configuration is depicted in Fig. 3.21.

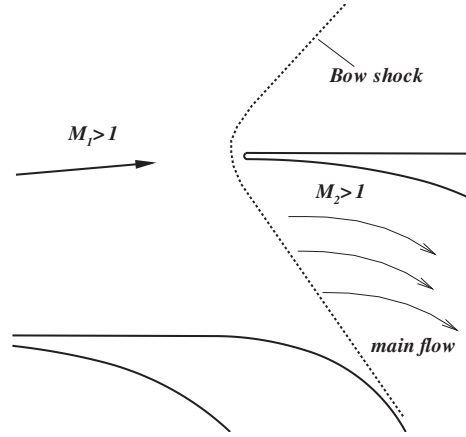
The inlet Mach number  $M_1$  and the contraction factor of the rotor blade vane are such that the normal shock ahead the blade can not be swallowed, causing a subsonic flow downstream the shock with high total pressure losses. Besides, a spillage of massflow appears at the leading edge due to the fact that the flow is subsonic and it can turn around the inlet. Then, a shock-induced blockage effect contributes to the loss of performances.

The best achievable working condition is shown in Fig. 3.22 for a started rotor configuration. In this case, the normal shock is completely swallowed through the vane and only a weak oblique shock is generated at the leading edge. In this way, the flow downstream of the shock wave is always supersonic and the best rotor turbine performances can be obtained.

Given the blade geometry and inlet flow conditions, is quite simple to assess if the row is started or not for a perfect gas, by determining the limit contraction ratio by applying the well-known



**Figure 3.21:** Unstarted configuration for a supersonic rotor blade row.



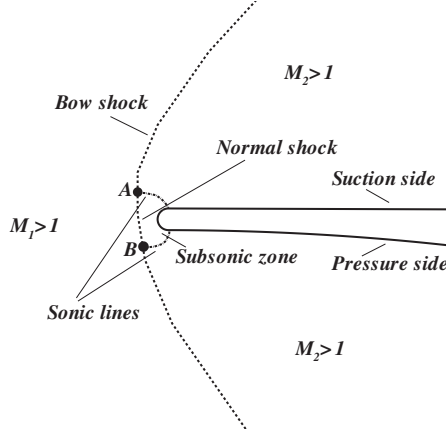
**Figure 3.22:** Started configuration for a supersonic rotor blade row.

isentropic relations upstream and downstream the shock wave (Paniagua et al., 2014; Kantrowitz and Donaldson, 1948). However, for a real gas these relations do not hold anymore and a more general model is required.

Fig. 3.23 shows the bow shock structure close to the leading edge of the rotor. As known, the field downstream the bow shock is characterized by a subsonic zone whose extension is generally restricted to the vicinity of the stagnation point. This zone is necessary in order to transfer at the flow the informations about the presence of the leading edge as a finite body (Landau, 1959). To a first approximation, the central portion  $A - B$  of the detached shock wave can be considered as a normal shock, which decelerates the flow up to a subsonic condition; subsequently, then the flow accelerates again, crossing the sonic lines, and the acceleration continues in the supersonic region by means of Prandtl-Meyer expansion fans. Since this process is isentropic, the total



pressure downstream the normal shock  $A - B$  is conserved across the sonic lines.



**Figure 3.23:** Bow shock schematic representation on the leading edge of a super-sonic rotor.

If the flow conditions upstream of the shock wave are known and an isenthalpic transformation is considered, the steady isentropic conservation equations across the discontinuity  $A - B$  can be written as:

$$\rho_1 u_1 = \rho_2 u_2 \quad (3.26)$$

$$p_1 + \rho_1 u_1^2 = p_2 + \rho_2 u_2^2 \quad (3.27)$$

$$h_1 + u_1^2/2 = h_2 + u_2^2/2 \quad (3.28)$$

where 1 and 2 refers to the thermodynamic states upstream and downstream the shock, respectively. Since usually the rotor inlet Mach number is provided as an input data, the velocity magnitude  $u_1$  and all the static properties in zone 1 are evaluated as follows:

1. Given  $M_1$  and the inlet total conditions, the critical speed of sound  $a_1^*$  and Mach number  $M_1^*$  are evaluated by means of the iterative procedure described in Section 3.3.1;
2. The inlet velocity magnitude is  $u_1 = M_1^* \cdot a_1^*$ , which provides the static enthalpy as  $h_1 = h_0 - u_1^2/2$ ;
3. Pressure and density are then calculated by means of the complex EOS as  $p_1 = p(h_1, s_{0,1})$  and  $\rho_1 = \rho(h_1, s_{0,1})$ .

By defining the contraction factor  $C_R$  as the isentropic area-contraction ratio from a Mach number  $M$  to the local speed of sound, it is possible to re-write the continuity equation as:

$$C_{R,is} = \frac{A^*}{A} = \frac{\rho u}{(\rho u)^*} \quad (3.29)$$

The product  $(\rho u)^*$  is calculated by a similar procedure to steps 1-3, using  $M = 1$ . This allows to evaluate  $C_R$  by means of Eq. (3.29) for the given inlet Mach number. Unfortunately, the contraction factor calculated with the previous equation is an isentropic quantity that does not

take into account the total pressure loss across the shock.

In order to take into account the shock losses and obtain a more realistic value of  $C_R$ , the contraction factor is now defined with respect to the properties downstream of the shock-wave, as follows:

$$C_R = \frac{A_2^*}{A} = \frac{\rho u}{(\rho u)_2^*} = \frac{p_{0,2} (\rho u)_1^*}{p_{0,1} (\rho u)_2} = \frac{p_{0,2}}{p_{0,1}} \frac{1}{C_{R,is}} \quad (3.30)$$

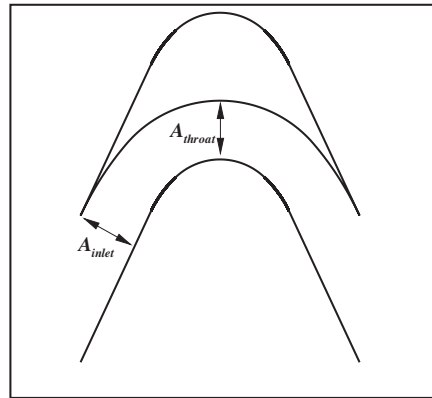
The previous equation is also known as the Kantrowitz contraction factor and usually is given for perfect gases by re-writing the ratios above as explicit function of the Mach number and specific heat ratio  $\gamma$ . For real gases the evaluation of the properties downstream the shock wave is provided by solving iteratively the system of Eqs. (3.26), (3.27) and (3.28):

1. An initial tentative value for the velocity magnitude downstream the shock,  $u_2^i$  with  $i = 0$ , is prescribed in the interval  $(0, u_1)$ ;
2. By knowing the properties upstream the shock, the density  $\rho_2^i$  and enthalpy  $h_2^i$  are calculated from the continuity and energy equations (3.26), (3.28) respectively ;
3. The static pressure downstream the shock is calculated by means of the complex EOS, as  $p_2^i = p(\rho_2^i, h_2^i)$ ;
4. If  $p_2^i$  does not satisfy the momentum equation (Eq. (3.27)), another value for  $u_2$  is guessed by means of a biseption method and the procedure is repeated from point 2 as a  $(i + 1)_{th}$  iteration.

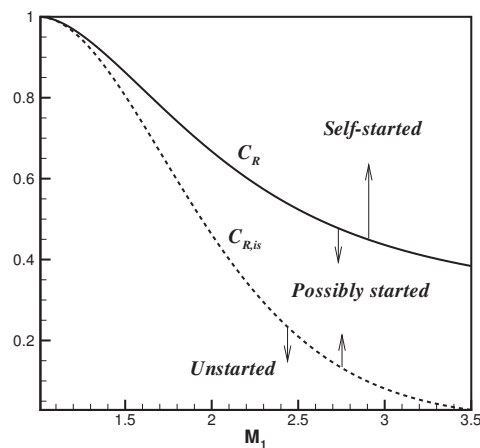
The method converges very quickly and all the static and total properties are calculated across the shock wave. Then, the Kantrowitz contraction factor  $C_R$  can be evaluated. By defining the inlet area of the rotor blade vane  $A_{inlet}$  as shown in Fig. 3.24, the contraction factor is defined as  $C_R = A^*/A_{inlet}$ , where  $A^*$  represents the critical area downstream the bow-shock. As example, the procedure explained above has been applied to compute  $C_R$ , for R245fa fluid at a reduced relative total pressure and temperature  $p_r^0 = 0.1$  and  $T_r^0 = 0.95$  respectively, in order to be in the dense gas region. The results are shown in Fig. 3.25 in terms of both the Kantrowitz and isentropic contraction factor.

Above the  $C_R$  curve the rotor is said *self-started*, which means that the turbine is able to ingest the normal shock that occurs at the inlet of the passage during the start-up. Between the Kantrowitz and isentropic contraction factor lines the turbine could be started, but not spontaneously (a variation of the outlet pressure is required). Below the isentropic limit the turbine can not be started and the normal shock is necessary to adapt the massflow at the downstream conditions. In order to evaluate the influence of the dense gas effects on the Kantrowitz limit, a comparison has been carried out for  $C_R$  in dense ( $p_r^0 = 0.1$ ,  $T_r^0 = 0.95$ ) and dilute ( $p_r^0 = 0.01$ ,  $T_r^0 = 1.18$ ) gas conditions for the R245fa fluid. The results are shown in Fig. 3.26. For a dense gas, the contraction factor curve is lower than the one corresponding to a perfect gas. As a consequence, the dense gas has a larger self-started region than the ideal gas. A rotor designed with a  $C_R$  close to the dense gas Kantrowitz curve would provide a wider range of started configurations for the same inlet Mach number, implying higher inlet-to-throat area ratios, higher turning flows and, then, higher performances.

The RODEC code has been equipped with a verification of self-starting of the designed geometry, by comparing the design throat-to-inlet area ratio (where the throat area for a rotor is defined as in Fig. 3.24) with the corresponding Kantrowitz limit.



**Figure 3.24:** Definition of the area sections for a supersonic rotor.



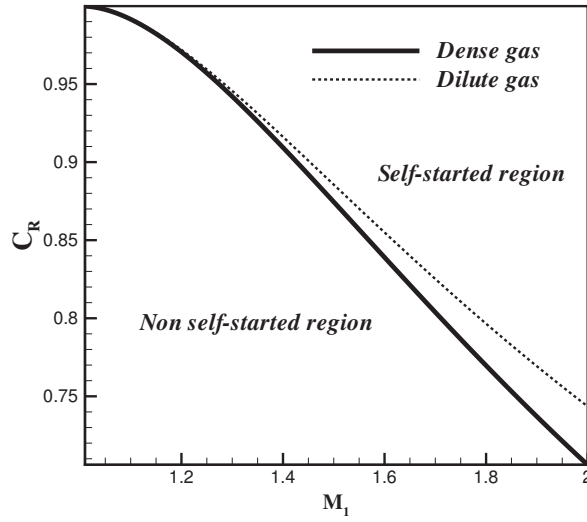
**Figure 3.25:** Kantrowitz contraction factor as function of the inlet Mach number for the R245fa fluid.

### 3.3.4 The unique incidence problem in dense gas regime

Even though a fully supersonic flow and a started rotor are the most desirable working conditions for an impulse turbine, some cautions have to be taken into account due to the more complicated aerodynamic phenomena involved in this case.

From perfect-gas aerodynamics of supersonic blade cascades, it is known that in a started turbine the relative inlet flow angle is not always a free parameter, but for some flow configurations it is a function of the inlet Mach number (Budugur, 1995).

In the case of study of this thesis, the flow pattern is that shown in Fig. 3.19. It is possible to see that the inlet relative flow angle is set by the leg of the bow-shock generated on the adjacent



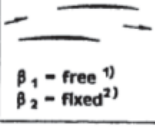
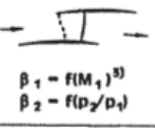
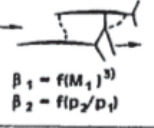
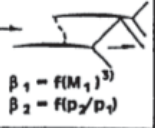
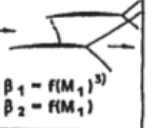
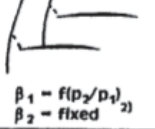
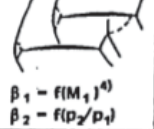
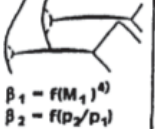
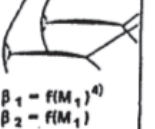
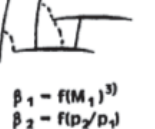
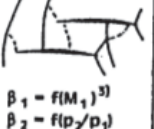
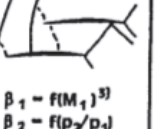
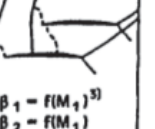
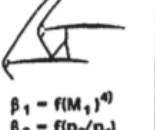
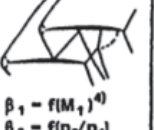
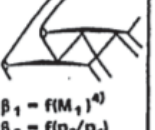
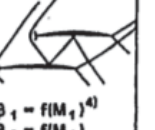



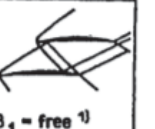
**Figure 3.26:** Comparison of the Kantrowitz contraction factor as function of the inlet Mach number for the R245fa fluid in dense and dilute gas conditions.

blade leading-edge. For sake of completeness, it should be considered that, for an infinite cascade, the inlet flow is indeed influenced by the action of all the bow-shock legs coming from below, however, since the strength of the shock generated by blades farer than the first adjacent blade becomes quickly negligible, this effect is not taken into account.

A complete list of possible flow configurations is provided by Starken (1993) and sketched in Fig. 3.27. Since the rotors are designed in order to have an a subsonic inlet axial relative velocity component, the inlet relative flow angle  $\beta_1$  is always a function of the inlet relative Mach number. This behaviour has consequences on the definition of the inlet boundary condition and is known as the *unique incidence* problem.

This problem can be described (Starken et al., 1984) by studying the pattern of characteristic lines departing from the leading edge of a rotor with an incident supersonic and axial subsonic flow (see Fig. 3.28a). The analysis is carried out by making the hypotheses of *simple wave* characteristic lines, which means that all the characteristics are considered as straight lines. Besides, the bow-shocks are considered to become Mach lines far from the leading edges and only the influence of the first adjacent shock leg is taken into account. In this framework, the supersonic flow is slightly decelerated by the bow-shock, then the deflection imposed by the suction side part of the rounded leading edge leads the flow to expands by means of an expansion fan. The flow, which is subsonic in region close to the leading edge, accelerates again to supersonic conditions after crossing the sonic line  $S - S_{le}$ . Then, it further accelerates on the suction side through a supersonic expansion fan and reaches the Mach number defined by the *limiting characteristic* emanating from point  $E$ . The latter, known also as the *last captured Mach wave*, connects the intersecting point between the detached shock wave  $C$  and the stagnation streamline with point  $E$  on the suction surface of the adjacent blade. Besides, it sets the limit for the maximum massflow allowable for the given flow configuration.

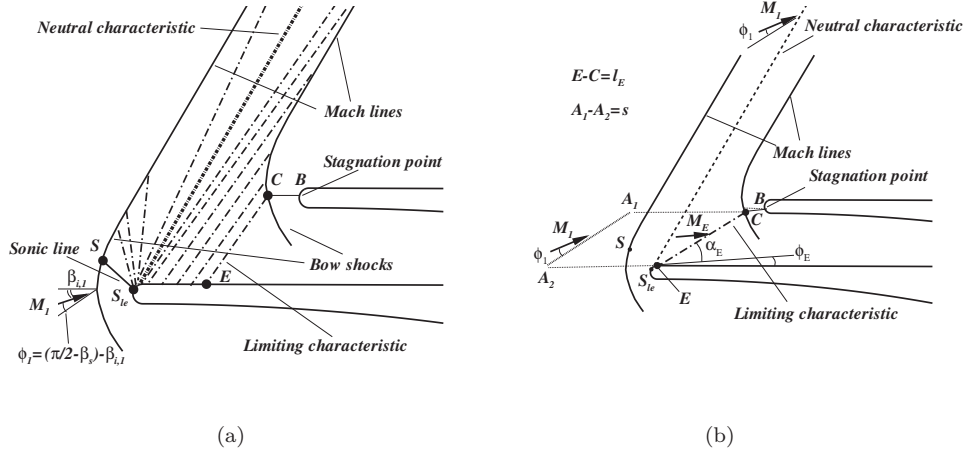
Inside the pattern of characteristic lines it can be shown that only one exists (the "unique") which does not intersect the bow-shocks. Then, this characteristic has the property to meet the

| Exit<br>Inlet                      | Subsonic   | Transonic   | Supersonic<br>axial<br>subsonic  | Supersonic<br>axial<br>supersonic  |
|------------------------------------|--|---|--|--|
| Subsonic                           | <br>$\beta_1 = \text{free}^1)$<br>$\beta_2 = \text{fixed}^2)$ |   |  |  |
| Subsonic<br>choked                 | <br>$\beta_1 = f(M_1)^3)$<br>$\beta_2 = f(p_2/p_1)$           | <br>$\beta_1 = f(M_1)^3)$<br>$\beta_2 = f(p_2/p_1)$        | <br>$\beta_1 = f(M_1)^3)$<br>$\beta_2 = f(p_2/p_1)$        | <br>$\beta_1 = f(M_1)^3)$<br>$\beta_2 = f(M_1)$                 |
| Transonic                          | <br>$\beta_1 = f(p_2/p_1)^2)$<br>$\beta_2 = \text{fixed}^2)$  | <br>$\beta_1 = f(M_1)^4)$<br>$\beta_2 = f(p_2/p_1)$        | <br>$\beta_1 = f(M_1)^4)$<br>$\beta_2 = f(p_2/p_1)$        | <br>$\beta_1 = f(M_1)^4)$<br>$\beta_2 = f(M_1)$                 |
| Transonic/<br>Supersonic<br>choked | <br>$\beta_1 = f(M_1)^3)$<br>$\beta_2 = f(p_2/p_1)$           | <br>$\beta_1 = f(M_1)^3)$<br>$\beta_2 = f(p_2/p_1)$        | <br>$\beta_1 = f(M_1)^3)$<br>$\beta_2 = f(p_2/p_1)$        | <br>$\beta_1 = f(M_1)^3)$<br>$\beta_2 = f(M_1)$                 |
| Supersonic<br>axial<br>subsonic    | <br>$\beta_1 = f(M_1)^4)$<br>$\beta_2 = f(p_2/p_1)$         | <br>$\beta_1 = f(M_1)^4)$<br>$\beta_2 = f(p_2/p_1)$      | <br>$\beta_1 = f(M_1)^4)$<br>$\beta_2 = f(p_2/p_1)$      | <br>$\beta_1 = f(M_1)^4)$<br>$\beta_2 = f(M_1)$               |
| Supersonic<br>axial<br>supersonic  | <br>$\beta_1 = \text{free}^1)$<br>$\beta_2 = f(p_2/p_1)$    | <br>$\beta_1 = \text{free}^1)$<br>$\beta_2 = f(p_2/p_1)$ | <br>$\beta_1 = \text{free}^1)$<br>$\beta_2 = f(p_2/p_1)$ | <br>$\beta_1 = \text{free}^1)$<br>$\beta_2 = f(M_1, \beta_1)$ |

1) free in the meaning of an independent variable parameter between certain limits  
2) fixed due to viscous effects  
3) determined by passage throat  
4) determined by unique incidence

**Figure 3.27:** Flow patterns and related boundary conditions of possible cascade flow configurations, where  $\beta_1$  and  $\beta_2$  are the inlet and outlet relative flow angles, respectively. Figure extracted from (Starken, 1993).

far field without disturbances and all the properties of the homogeneous supersonic inlet flow are conserved along this line, called the neutral characteristic. By considering this feature, the functional dependency of the *unknown* inlet flow angle from the inlet Mach number  $M_1$  can be deduced from the mass conservation across the bow-shock. The control volume, as proposed by (Starken et al., 1984), is chosen as limited far upstream the shock wave by a straight surface of extension equal to the cascade pitch  $s = A_1 - A_2$ , and downstream by the limiting characteristic of length  $l_E = E - C$ , see Fig. 3.28b.



**Figure 3.28:** Characteristics pattern and expansion fan lines for a supersonic rotor (a); definition of the control volume upstream and downstream of the bow-shock (b).

Depending on the Mach number  $M_1$ , the limiting characteristic point  $E$  on the adjacent suction side could be either on the straight part, where the flow is horizontal in the rotated reference frame with flow angle  $\phi_E = 0$  (see Fig. 3.28a) and on the rounded leading edge, with  $\phi_E > 0$  (see Fig. 3.28b). Besides, the position of the stagnation point  $C$  is dependent from the incident flow direction. For the sake of generality, these configurations are taken into account in the following analysis.

By using the notation defined in Figs. 3.28 (here the flow angle is evaluated as  $\phi_1 = (\pi/2 - \beta_s) - \beta_{i,1}$ , where  $\beta_s$  is the stagger angle and  $\beta_{i,1}$  the incidence angle) and applying the mass conservation on the control volume defined previously, the following equation holds:

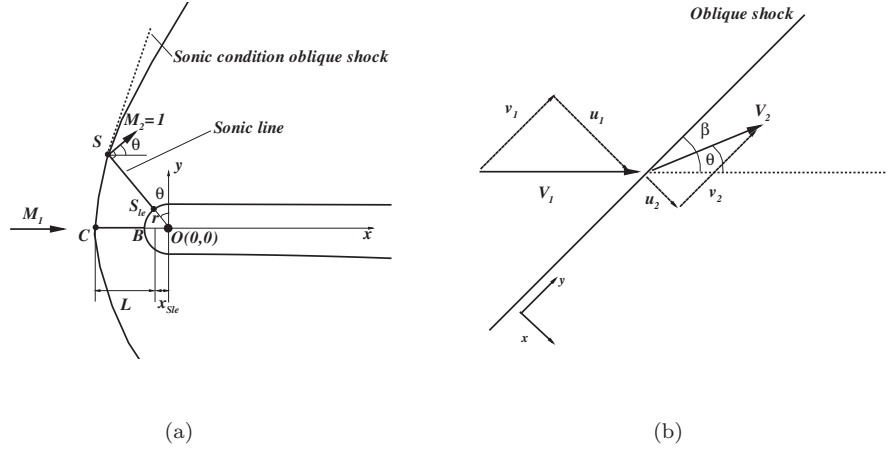
$$\rho_1(V_1 \sin \phi_1)s = \rho_E(V_E \sin \alpha_E)l_E \quad (3.31)$$

In the preceding equation,  $V_1$  and  $V_E$  are the velocity magnitudes of the flow at the control volume surfaces, whereas  $\alpha_E$  is the Mach angle associated to the limiting characteristic. This equation can provide the unknown inlet flow angle  $\phi_1$ , which is the solution to the unique incidence problem, if all the quantities on the right hand side are calculated in advance.

Firstly, the limiting characteristic line length  $l_E$ , defined as the distance between the stagnation point on the bow-shock  $C$  and the point  $E$ , requires the definition of the point  $C$  position. This is a function of the bow-shock stand-off distance from the stagnation point on the leading edge  $B$ ,  $B - C$ , depending on the intensity of the shock (i.e. on  $M_1$ ), and on the leading edge radius. In order to estimate it, the procedure proposed by Moeckel is followed (Moeckel, 1949), with modifications in order to take into account the real gas effects.

This methodology is based on the assumption that the form of the shock between its foremost point and its sonic point is adequately represented by an hyperbola asymptotic to the free-stream Mach lines. Besides, the sonic line, delimiting the sonic region in front of the leading edge, is considered to be a straight one and the flow downstream to be normal to it. The geometrical configuration of the bow-shock and of the oblique shock leading the flow to the sonic condition is depicted in Figs. 3.29a and 3.29b, respectively.

By following this scheme, the first quantity to be evaluated is the position of the sonic point



**Figure 3.29:** Geometric scheme of the bow-shock and sonic line (Moeckel, 1949) (a); oblique shock geometric scheme and reference system (b).

on the leading edge  $S_{le}$ , which depends on the deflection  $\theta$  of the flow due to the sonic oblique shock. In this analysis the inlet flow is considered to be horizontal since the flow angle is supposed to have just a rotation effect on the reference system without affecting the value of the shock stand-off distance from the leading edge.

For real gases the calculation of  $\theta$  can not be carried out by means of analytical functions, as for the perfect gas case, then the following iterative procedure is followed by considering the scheme of Fig. 3.29b as reference system:

1. An initial tentative value for the shock inclination  $\beta$  is assigned in the range  $(0, \pi/2)$ , then the normal component of the inlet velocity  $V_1$  is calculated in terms of Mach number as  $M_{1,n} = M_1 \sin \beta$ ;
2. All the flow properties downstream the normal shock are evaluated by means of the iterative procedure shown in Section 3.3.3, then the normal downstream Mach number is  $M_{2,n} = u_2/a_2$ , with  $a_2$  being the speed of sound;
3. The value of  $\theta$  is calculated by inversion of the general geometric relation  $\tan(\beta - \theta) = u_2/u_1 \tan \beta$ , with  $u_1 = V_1 \sin \beta$ ;
4. The downstream Mach number, at iteration  $i$ , is finally calculated as  $M_2^i = M_{2,n} / \sin(\beta - \theta)$ ;
5. Since the sonic condition is searched, the target Mach number is  $M_2^t = 1$ . If the quantity  $|M_2^i - M_2^t|$  is greater than a prescribed accuracy the iterative procedure is repeated from point 2 by means of the bisection method.

With the previous procedure, the position of point  $S_{le}$  in the reference frame of Fig. 3.29a can be determined as  $x_{S_{le}} = -r \cdot \sin \theta$  and  $y_{S_{le}} = r \cdot \cos \theta$ , where  $r$  is the radius of the leading edge. By following Moeckel, the ordinate of the sonic point on the bow-shock  $y_S$  and the bow-shock stand-off distance from the leading edge  $L$ , as defined in Fig. 3.29, are:

$$y_S = y_{S_{le}} (1 - C_R \cos \theta)^{-1} \quad (3.32)$$

$$L = y_{S_{le}} [y_S / y_{S_{le}} (C_\beta + \tan \theta) - \tan \theta] \quad (3.33)$$

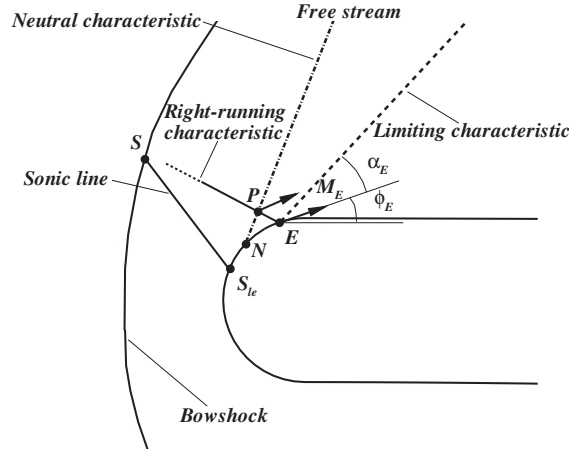
$$C_\beta = \beta_M \left( \beta_M \tan \beta - \sqrt{\beta_M^2 \tan^2 \beta - 1} \right)$$

$$\beta_M = \sqrt{M_1^2 - 1}$$

In Eq. (3.32), the parameter  $C_R$  is the Kantrowitz contraction factor evaluated for real gases at the given free stream conditions, as described in Section 3.3.3.

Once that the coordinates of point  $C$  have been determined (see Fig. 3.28b), it is required to calculate those of point  $E$ , located on the adjacent blade suction side, which gives the length  $l_E$  along the limiting characteristic. However, this problem can not be considered as decoupled from the solution of the unique incidence one, since the position of  $E$  depends on the inlet flow angle. Besides, in Eq. 3.31, the angle  $\phi_1$  is still unknown and another information is required in order to get the solution.

Then, the last equation is provided by considering the properties of the neutral characteristic. By considering the scheme of Fig. 3.30, it exists a right-running characteristic which connects the



**Figure 3.30:** Main characteristic lines on the rotor leading edge.

point  $P$  on the neutral characteristic, where all the inlet free stream informations are transferred, with  $E$ . The equation of this line is the last one required to solve the unique incidence problem. Since no analytical solution for the Prandtl-Meyer function exists in the dense gas case, the discretised form is used, as for Eq. (3.18):

$$(\beta_{i,1} - \phi_E) = \bar{A} (V_E - V_1) \quad (3.34)$$

$$\bar{A} = (A_1 + A_E)/2$$

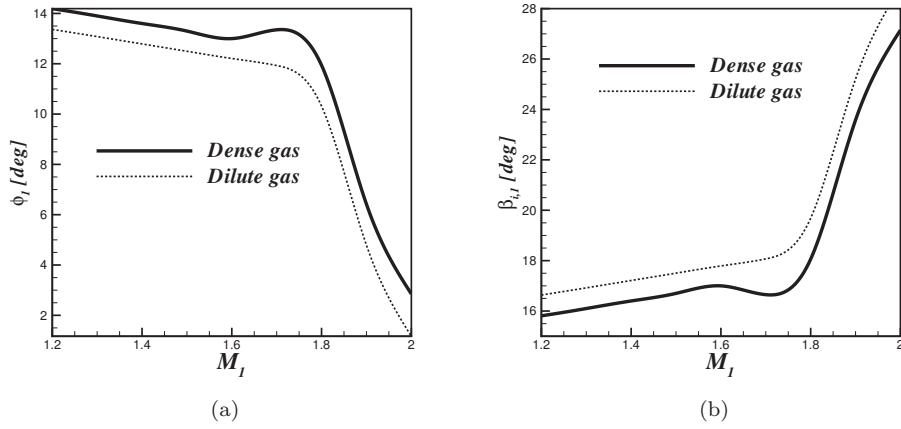
$$A = \sqrt{M^2 - 1}/V$$

By calculating  $\beta_{i,1}$ , the flow angle  $\phi_1$  can be easily evaluated by means of its definition. Eqs. (3.31) and (3.34), along with the unique incidence problem, can now be solved by means of the following iterative procedure:



1. An initial tentative value for the position of the point  $E$ ,  $(x_E, y_E)$ , is assigned between the position of the sonic point  $S_{le}$  and the abscissa of the stagnation point on the adjacent bow-shock,  $C$ . Then,  $\phi_E$  can be calculated by geometrical considerations;
2. By knowing  $\phi_E$ , the actual position of point  $C$  is evaluated (see Fig. 3.28b) and the limiting characteristic length  $l_E$  is calculated, along with the Mach angle on point  $E$ ,  $\alpha_E$ , by means of geometrical considerations. Then,  $M_E = 1/\sin \alpha_E$ ;
3. By means of the complex EOS, the critical Mach number and critical speed of sound downstream the shock,  $M_E^*$  and  $a_2^*$  respectively, are evaluated with the iterative procedure shown in Section 3.3.1. Then,  $V_E = M_E^* \cdot a_2^*$ ;
4. The information on the velocity  $V_E$ , along with the static and total properties downstream the shock previously calculated, provides the density  $\rho_E$  by means of the complex EOS;
5. The flow angle  $\phi_1$  is calculated from the Eq. (3.31) and compared with that provided by the characteristic equation, Eq. (3.34). If the difference is greater than a pre-set accuracy level, the iterative procedure is repeated from point 2 by assigning another value of the abscissa  $x_E$  by means of the bisection method.

The methodology above, also implemented in the RODEC code, converges quickly to a solution which provides the actual inlet relative flow angle, useful to solve the periodicity problem related to the unique incidence of isolated supersonic rotors and the correct definition of the inlet boundary condition.



**Figure 3.31:** Unique incidence solution and comparison of the inlet and incidence flow angles,  $\phi_1$  and  $\beta_{i,1}$  respectively, as functions of the inlet Mach number  $M_1$  for the R245fa fluid in dense ( $p_r^0 = 0.1$ ,  $T_r^0 = 0.95$ ) and dilute ( $p_r^0 = 0.01$ ,  $T_r^0 = 1.18$ ) gas conditions. The solution is evaluated for a  $r/s$  ratio of 0.05 (with  $r$  the leading edge radius and  $s$  the cascade pitch) and a stagger angle  $\beta_s = \pi/3$ .

In Fig. 3.31 a comparison between the inlet and incidence flow angles,  $\phi_1$  and  $\beta_{i,1}$  respectively, calculated with the procedure described above for the R245fa fluid, in dense ( $p_r^0 = 0.1$ ,  $T_r^0 = 0.95$ ) and dilute ( $p_r^0 = 0.01$ ,  $T_r^0 = 1.18$ ) gas conditions, has been carried out for a blade with  $r/s$  0.05 (with  $r$  the leading edge radius and  $s$  the cascade pitch) and a stagger angle  $\beta_s = \pi/3$ . It can

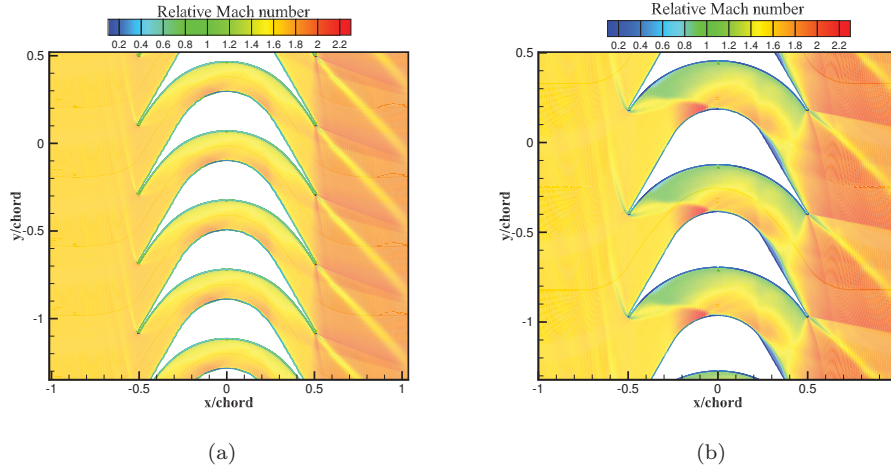
be noticed that the dense gas solution provides higher values of  $\phi_1$  for the same  $M_1$ . Since  $0 < \phi_1 < \beta_s$ , being  $\phi_1 = 0$  and  $\phi_1 = \beta_s$  the limits of the strongest and weakest admissible bow-shock respectively, the dense gas solution provides a less shock-influenced inlet flow angle than the dilute one. This behaviour can be explained by the fact that dense gas effects decrease the strength of the bow-shock.

### 3.3.5 RODEC: code verification

A numerical test of the rotor cascade designed with the RODEC has been carried out in order to verify the advantages of the proposed design methodology with respect to classical designs based on simple geometrical considerations derived from the flow velocity triangles (see [Capetti \(1967\)](#) for further details). These designs are generally based on the concatenation of circular arcs, without any further consideration on thermodynamic or aerodynamic consideration.

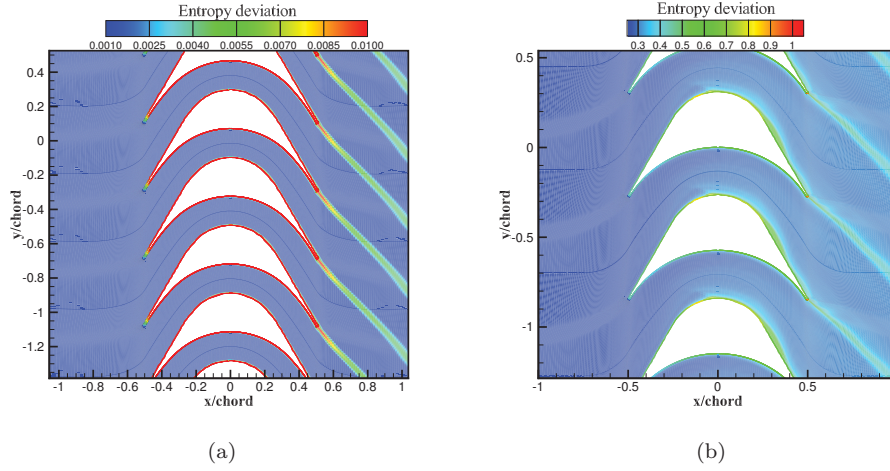
**Table 3.10:** Rotor blade design parameters for R245fa fluid.

| Parameters                               | Values |
|--|--------|
| Inlet total relative reduced pressure    | 1.05   |
| Inlet total relative reduced temperature | 1.05   |
| Inlet relative Mach number               | 1.7    |
| Inlet relative flow angle                | 60     |
| Suction side circular arc Mach number    | 1.9    |
| Pressure side circular arc Mach number   | 1.1    |



**Figure 3.32:** Mach number contour plot for RODEC (a) and circular arcs (b) designs.

Tab. 3.10 provides the main parameters used for the design of the rotor cascade. The thermodynamic conditions are slightly supercritical in order to work in a highly non-ideal thermodynamic region and the working fluid is R245fa. The viscous CFD calculations have been performed by means of the numerical solver described in Section 2.2. Pressure and temperature total conditions at the supersonic inlet along with the inlet relative Mach number ( $M_1 = 1.7$ ) and the flow angle corresponding to the unique incidence condition are prescribed. On the outlet and peripheral



**Figure 3.33:** Entropy deviation  $(S - S_{in})/S_{in}$  (with  $S$  the specific entropy and  $S_{in}$  an inlet entropy reference) contour plot for RODEC (a) and circular arcs (b) designs.

boundaries, a supersonic exit and periodicity conditions have been imposed, respectively. The results are shown in Figs. 3.32 and 3.33 in terms of relative Mach number and entropy deviation, the latter defined as the relative entropy variation  $(S - S_{in})/S_{in}$  with respect to the entropy inlet  $S_{in}$ . In Fig. 3.32a the RODEC design provides a started rotor with a bow-shock on the leading edges that confirms the presence of the unique incidence problem. Inside the rotor vane, the flow pattern characterised by reflections of the bow-shock. Two oblique shocks depart from the trailing edge and interact with the viscous wake.

On the other hand, the classical design based on circular arcs and velocity triangles does not provide satisfactory results (Fig. 3.32b). The solution is characterised by a strong interaction between the lower leg of the bow-shock and the suction side of the adjacent blade, along with a large subsonic region on the pressure side. On the rear part of the blade, the boundary layer separates from the wall. These phenomena affect the performance of the cascade, which can be evaluated in terms of degree of reaction  $\Lambda$  and entropy deviation. The calculation of  $\Lambda$  is based on the average static enthalpies at the rotor inlet and outlet:

$$\Lambda = \frac{\Delta h_{rotor}}{\Delta h_{total}} \quad (3.35)$$

Since the rotor is isolated, a reference constant value has been assigned to  $\Delta h_{total}$  in order to calculate  $\Lambda$ . For the RODEC design  $\Lambda = -0.034$  which is very close to the nominal value (zero reaction degree), whereas for the circular arc design  $\Lambda = -0.12$ . This implies that a re-compression of the supersonic flow happens in both cases, however it is one order of magnitude lower in the first case. The non-zero reaction degree is due to the development of the boundary layer, leading to a non symmetric effective area distribution. The effect is larger for the circular arc design due to boundary layer separation. Boundary layer corrections of the blade geometry are proposed in the next Section.

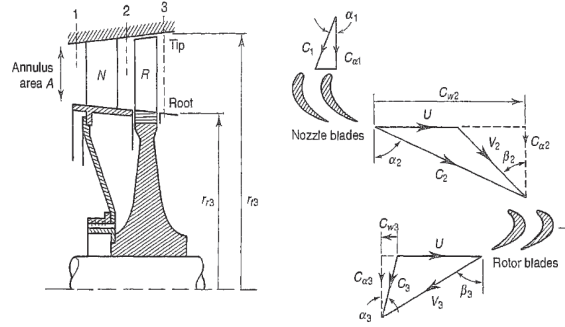
The analysis of the entropy deviation, reported in Figs. 3.33a and 3.33b, shows much higher entropy losses for the circular arc design, especially on the rear suction side part and the viscous wake. For the RODEC design, the losses are localised in the boundary layer and close to the trailing edge.

### 3.4 Full stage design and simulation

#### 3.4.1 ORC turbine stage design methodology

In this section the procedure to design and calculate a full stage (stator and rotor) of the ORC turbine with the in-house utilities NODEC and RODEC, is described.

The following input parameters are known: total plenum conditions (pressure and temperature), massflow rate, shaft angular velocity, interstage pressure ratios. By knowing this data, the design is performed by means of the iterative procedure described below. With subscript 1,2,3 the stator inlet, the stator-rotor interface and the rotor exit conditions are indicated, respectively. The velocity triangles are evaluated by using the convention showed in figure 3.34.



**Figure 3.34:** Typical velocity triangles for an axial turbine stage. Figure extracted from (Cohen et al., 1987).

Design procedure:

1. An initial tentative value for the peripheral velocity of the rotor at the middle blade height,  $U$  [m/s], is chosen
2. Set the desired number of blades for the stator  $n_{bs}$ . In this way the massflow rate across a single stator blade vane will be  $G/n_{bs}$
3. By knowing the conditions at section 1 (total pressure  $p_0$ , total temperature  $T_0$ ), massflow rate  $G$ , pressure ratio  $\beta$  and the organic working fluid, calculations of the nozzle convergent-divergent geometry and thermodynamics/cinematics of the supersonic flow are performed with the NODEC software. In this way  $C_2$ , density  $\rho_2$ , Mach number  $M_2$  and static enthalpy  $h_2$  are known
4. The design is carried out by considering a constant axial velocity component  $C_a$  across the rotor. The value of the flow coefficient  $\phi = \frac{C_a}{U}$  is set to 0.8
5. The Zweifel empirical coefficient (Zweifel, 1945), useful to evaluate an optimal value for the rotor blade solidity  $s/b$  ( $s$  is the blade spacing and  $b$  the axial chord), is set to  $\Psi_T = 2(s/b)\cos^2\alpha_2(\tan\alpha_1 + \tan\alpha_2) = 0.8$
6. The degree of reaction is set to  $\Lambda = 0$ . Calculation of velocity triangles at blade middle height, thermodynamic and cinematic flow properties is provided below:

$$\alpha_2 = \cos^{-1} \left( \frac{C_a}{C_2} \right)$$

$$\begin{aligned}
 \beta_2 &= \tan^{-1} \left( \tan \alpha_2 - \frac{1}{\phi} \right) \\
 W_2 &= \frac{C_a}{\cos \beta_2} \\
 h_{02r} &= h_2 + \frac{W_2^2}{2} \\
 T_{02r} &= f(h_{02r}, S) \\
 p_{02r} &= f(h_{02r}, S) \\
 \beta_3 &= \beta_2 \quad (\Lambda = 0) \\
 \alpha_3 &= \tan^{-1} \left( \tan \beta_3 - \frac{1}{\phi} \right) \\
 M_{2a} &= M_2 \cos \alpha_2 \\
 M_{2r} &= \frac{M_{2a}}{\cos \beta_2} = M_{3r} \quad (\Lambda = 0) \\
 R_m &= U \frac{60}{2\pi N_{RPM}} \quad [m] \\
 A_{annulus} &= \frac{G}{\rho_2 C_a} \quad [m^2] \\
 H &= \frac{A_{annulus}}{2\pi R_m} \quad [m]
 \end{aligned}$$

With subscripts  $r$  and  $a$  the relative and axial properties are indicated, respectively, whereas  $R_m$ ,  $N_{RPM}$ ,  $A_{annulus}$  and  $H$  are the middle blade radius, the design shaft angular velocity in RPM, annulus area (see figure 3.34) and blade height (which is considered to be the same for stator and rotor blades). The function  $f$  used in the previous procedure states the use of complex equation of state to compute the thermodynamic properties.

7. By knowing the relative total reservoir conditions  $(p_{02r}, T_{02r})$ , the inlet-outlet relative flow angles  $\beta_2, \beta_3$  and inlet-outlet relative Mach numbers the rotor geometry can be calculated by means of the RODEC software.
8. The new stator number of blades is evaluated, as:  $n_{bs, new} = 2\pi R_m / s_s$ , where  $s_s$  is the stator blade spacing calculated by NODC. If  $n_{bs, new}$  greatly differs from  $n_{bs}$  then a new value of the peripheral velocity  $U$  has to be set and the procedure is repeated from point 1 until convergence is reached
9. Once get the convergence on  $n_{bs}$ , the rotor solidity is calculated by using the Zweifel formula:  $s_r / b_r = \Psi_T / (2 \cos^2 \alpha_2 (\tan \alpha_1 + \tan \alpha_2))$ , where  $\Psi_T = 0.8$
10. By knowing the geometrical constraints, it is possible to evaluate the desired rotor axial chord  $b_r$  and, from the  $s_r / b_r$  ratio, the rotor blade spacing  $s_r$
11. Finally, the rotor number of blades is evaluated as  $n_{br} = 2\pi R_m / s_r$
12. The stage power output is evaluated as  $P = G \Delta h_{0S}$ , where  $\Delta h_{0S}$  is the ideal total enthalpy drop across the turbine stage, calculated as:  $\Delta h_{0S} = \psi \frac{U^2}{2}$ , where  $\psi$  is the work factor, calculated as (for  $\Lambda = 0$ ):  $\psi = 4\phi(\tan \beta_3)$

### 3.4.2 Full stage numerical simulations

Viscous 2-D numerical simulations have been carried out for a full turbine stage designed using the preceding methodology, without implementation of the boundary layer correction. The subsonic part of the stator blade has been designed in a slightly different way in order to reduce the blade length. The CFD software used is the commercial code Ansys CFX 16.0, due to the possibility to run it in parallel and the easier management of the multiblock grids with respect to the in-house solver. The turbulence model used is k-omega SST (Shear Stress Transport). The thermodynamic properties of the fluids are modelled using the real gas properties (rgp) library.

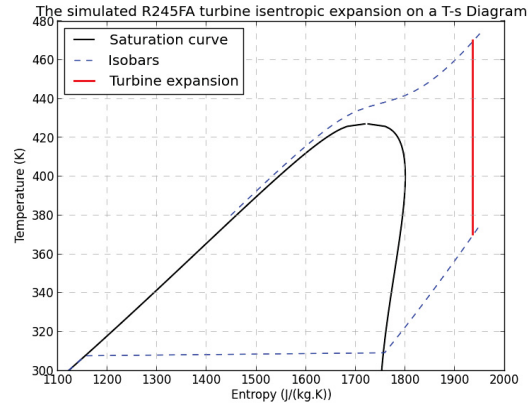
The `rgp` files contain property tables mapped as a function of temperature and pressure along the turbine expansion and allow accurately taking into account dense gas effects.

Tab. 3.11 provides the parameters used to design the blade shapes and to perform the simulations with the R245fa working fluid. In order to assess the presence of dense gas effects it is important

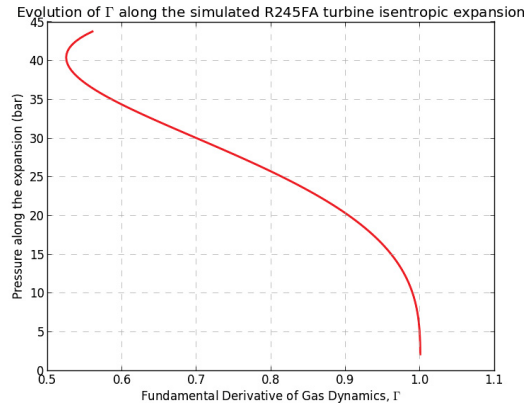
**Table 3.11:** Rotor blade design parameters.

| Parameters                             | Values |
|--|--------|
| Inlet total relative pressure [bar]    | 6      |
| Inlet total relative temperature [K]   | 393.15 |
| Inlet relative Mach number             | 1.5    |
| Inlet relative flow angle              | 60     |
| Suction side circular arc Mach number  | 1.9    |
| Pressure side circular arc Mach number | 1.1    |

to evaluate the position of the operating point on the working fluid state diagram. In Fig. 3.35a the isentropic evolution of the expansion on the T-S diagram is shown. The presence of strong dense gas effects is expected, since fundamental derivative  $\Gamma$  is below 1 throughout the expansion (see Fig. 3.35b). It can be noticed that, for this application, the strongest dense gas effects occur mainly inside the nozzle, where the enthalpy drop is elaborated. This is due to the "dry" nature of R245fa fluid which allows to have the last part of expansion farther from the saturation curve. By using the Zweifel empirical coefficient (Zweifel, 1945), the number of rotor to stator blades ratio is set to 2. The 2-D computational grid for the full stage simulation is composed of C-shaped blocks around the blades and of H-shaped blocks at stage inlet and outlet as shown in Fig. 3.36a. The grid is clustered in order to obtain  $y^+$  values less than 1 at the blade walls. The total number of elements is 330066 total number of elements (121704 overall elements for the rotor row and 208362 elements for the stator row). Simulations for a full turbine stage involving a supersonic rotor blade row and a supersonic stator blade row both designed by the means of the MOC procedures described previously are carried out. The total temperature, the total pressure and the velocity components are imposed at the inlet. Average static pressure is set at the outlet and a mixing-plane boundary condition is set at the stator-rotor interface. Tab. 3.12 presents the main turbine working parameters, taken from a real-world application. In order to maximize the impact of dense gas effects, supercritical turbine inlet conditions (see Fig. 3.35a) have been chosen. Fig. 3.36b presents the relative Mach number distribution for the full turbine stage simulation. The flow is accelerated in the stator vanes up to the design absolute Mach number of 2.4 and, thanks to the accurate design with the MOC algorithm, no normal shocks are formed in the divergent part of the nozzle. However, a set of weak oblique shocks departs outside the stator due the presence of the rounded trailing edge and its non-zero thickness. These shocks interact with the viscous wake. Due to the mixing plane interface, interactions of the latter with the rotor row can not be observed. The flow in the relative reference frame is then deflected by the blade vanes up to a relative Mach number slightly lower than the design one due to the set of oblique shocks departing both from leading and trailing edge. The turbine is found to be in a "started" configuration, so that a normal shock at the inlet is avoided and the flow inside the rotor vanes is supersonic. The calculated total to total isentropic efficiency for this turbine is 92.9%. In order to assess the main source of losses in the turbine stage, the entropy deviation  $(S - S_{in})/S_{in}$  is evaluated. It is shown in Fig. 3.37a for the isolated rotor. Entropy is mainly generated with the viscous boundary layers and wakes, whereas entropy generation across shocks is extremely weak. This demonstrates that the proposed methodology provides blade designs with negligible shock losses. The presence of viscous effects also modifies the design degree of



(a)



(b)

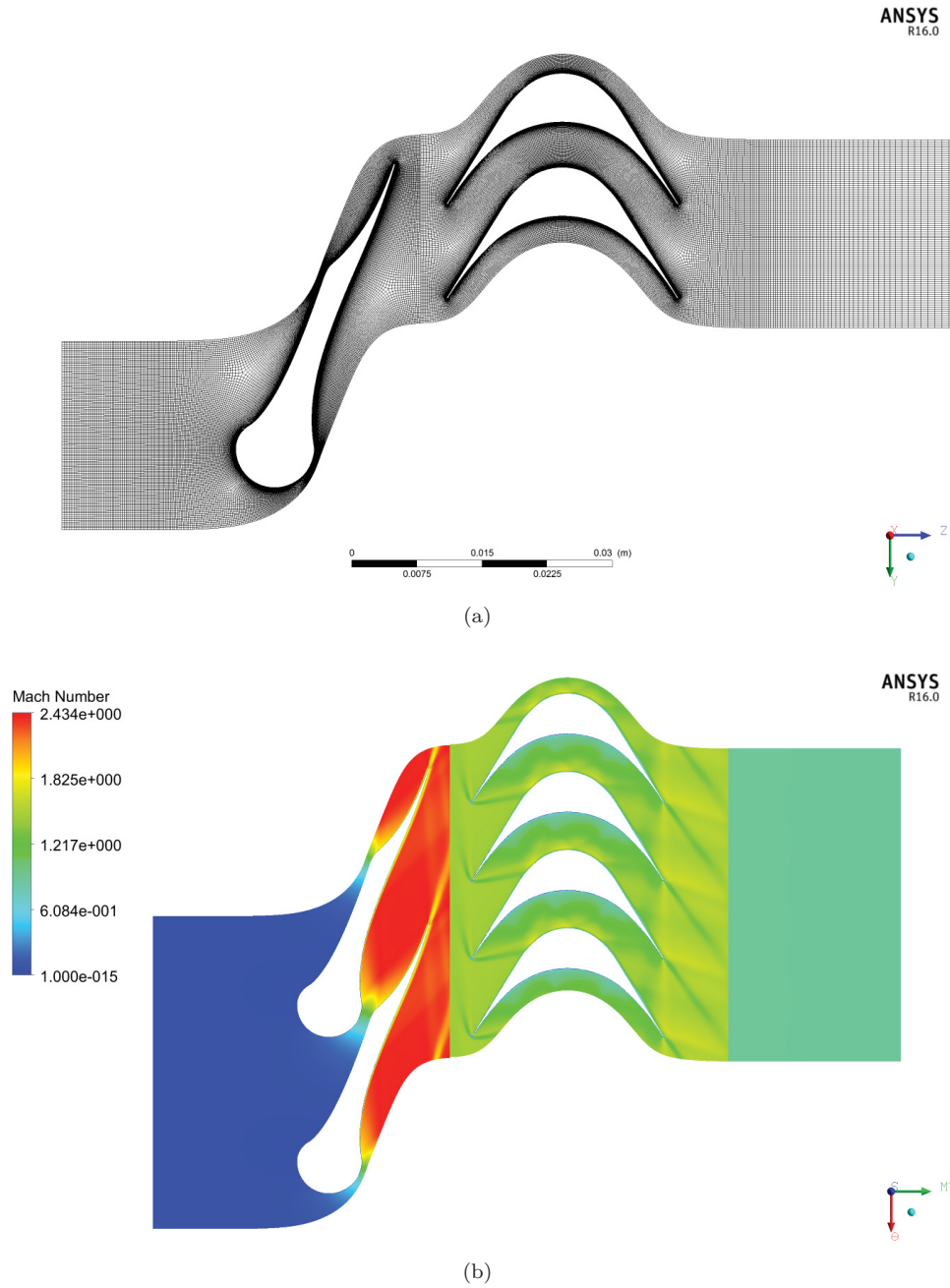
**Figure 3.35:** Isentropic turbine expansion on the R245FA T-S diagram (a); Fundamental Derivative of gas dynamics  $\Gamma$  evaluated along the turbine expansion (b).

reaction, set to zero for the design here proposed. The actual degree of reaction evaluated after simulations is found to be -0.042. This effect can be addressed to the modification of the effective blade vane geometry due to the boundary layer thickness, which leads to lower passage sections going from inlet to outlet.

**Table 3.12:** Main turbine full stage working parameters.

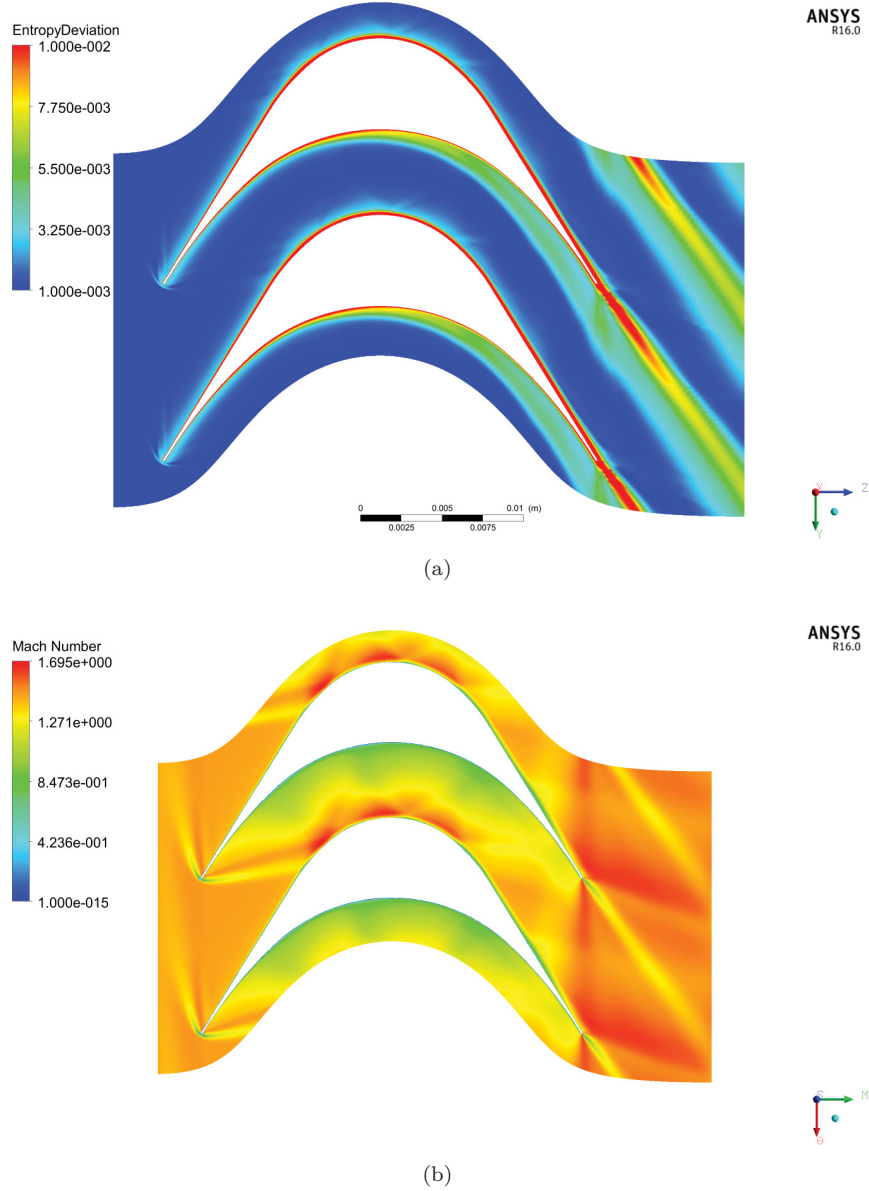
| Parameters                              | Values |
|---|--------|
| Inlet total reduced pressure            | 1.2    |
| Pressure ratio                          | 20.6   |
| Inlet total reduced temperature         | 1.1    |
| Stator nozzle outlet design Mach number | 2.4    |
| Stator stager angle                     | 70     |
| Rotor blade speed [m/s]                 | 141.37 |





**Figure 3.36:** Computational block structured grid for full turbine stage (330066 elements) (a); relative Mach number distribution for R245FA fluid (b).





**Figure 3.37:** Entropy deviation contour plot for the isolated rotor (R245FA fluid) (a); Mach number distribution for the isolated rotor (R245FA fluid) (b).

### 3.5 Boundary layer correction

In the preceding Sections we have seen that viscous effect have a considerable influence on the performance of nozzle guide vanes and rotor blade designed by using the inviscid MOC. Specifically, for nozzle guide vanes, viscous losses reduce the ideal isentropic efficiency by about 10%. Additionally, the boundary layer development reduces the effective exit-to-throat area of the nozzle, leading to an expansion ratio below the target one. For rotor blades, the boundary layer

reduces the degree of reaction and increases losses. To palliate these kind of problems, the presence of boundary layer should be taken into account in the preliminary design. The idea is to use the ideal pressure distribution to evaluate the development of the boundary layer thickness and to correct the inviscid design accordingly.

In order to take into account these effects in a preliminary design stage, an approximate calculation of the compressible turbulent boundary layer subject to an arbitrary pressure gradient is carried out by following the Reshotko-Tucker method (Reshotko and Tucker, 1957). The latter involves the momentum integral and momentum-of-momentum equations as simplified by using the Stewartson-illingworth's transformation. The Ludwig-Tillmann skin-friction relation is used in these equations in a form suitable for compressible flows. A power-law is used for the turbulent velocity profile close to the wall, whereas a quadratic Crocco's law is used for the temperature distribution. The equations above are written such that no hypotheses on the equation of state are done.

### 3.5.1 Boundary layer integral equations

The method is developed under the assumption of a constant turbulent Prandtl number of the order of 1, constant pressure along the direction normal to the wall and flat plane adiabatic surface. In this case it is possible to write the boundary layer integral momentum equation, along with the auxiliary momentum-of-momentum equation in terms of the incompressible form factor  $H_i$ , as follow:

$$\frac{d\Theta_{tr}}{dx} + \frac{\Theta_{tr}}{M_e} \frac{dM_e}{dx} [2 + H_i] = 0.5 \times C_f \quad (3.36)$$

$$\frac{dH_i}{dx} = -\frac{1}{M_e} \frac{dM_e}{dx} \left[ \frac{H_i (H_i + 1)^2 (H_i - 1)}{2} \right] - 0.03 H_i (H_i^2 - 1) 0.5 \times \frac{C_f}{\Theta_{tr}} \quad (3.37)$$

where  $\Theta_{tr}$  is a "transformed" momentum thickness by means of the Stewartson-illingworth transformation (Culick, 2012),  $M_e$  is the external Mach number (obtained from the inviscid MOC calculation) and  $C_f$  is the skin friction.

The coefficient  $-0.03$  in Eq. (3.37) results by introducing the Maskell empirical approximation (Maskell, 1951) for the shear stress integral term in the original momentum-of-momentum equation:

$$\int_0^1 \frac{\tau}{\tau_w} d\left(\frac{Y}{\Delta}\right) = 1.03 \frac{H_i}{H_i + 1} \quad (3.38)$$

where  $\tau$  is the shear stress,  $\tau_w$  the wall shear,  $Y$  and  $\Delta$  are the transformed wall distance and boundary layer thickness, respectively.

The transformed momentum thickness  $\Theta_{tr}$  is related to the compressible one as follows:

$$\Theta = \Theta_{tr} \frac{p_0}{p_e} \frac{a_e}{a_0} \quad (3.39)$$

where  $p_0$  and  $a_0$  are the free stream total pressure and speed of sound, respectively.

In order to close the problem, the skin friction coefficient  $C_f$  needs to be evaluated. For this purpose, the transformed compressible form of the Ludwig-Tillmann equation for turbulent boundary-layer is used. Besides, it is written such that all the thermodynamic variables are explicitly calculated by using a generic EOS. By writing the skin friction in terms of transformed variables and applying the Eckert's (Eckert, 1955) reference enthalpy method the following form is obtained:

$$C_f = \frac{\tau_w}{0.5 \rho_{ref} u_e^2} = 0.246 e^{-1.561 H_i} \left( \frac{M_e a_0 \Theta_{tr}}{\nu_{ref}} \right)^{-0.268} \left( \frac{\rho_e}{\rho_{ref}} \right) \left( \frac{p_e}{p_0} \right)^{-0.268} \quad (3.40)$$

In the above equation the subscript "ref" states a variable calculated at a reference temperature. Here the Eckert method is applied, such that the reference temperature is calculated as:

$$T_{ref} = 0.72T_0 + 0.28T_e \quad (3.41)$$

In this way the variation of viscosity with temperature is taken into account and its value is calculated at the local  $T_{ref}$  with the selected EOS. Finally, the velocity and temperature distribution close to the wall are approximated by a power-law and quadratic Crocco's equation, respectively, leading to the following relations:

$$\frac{u}{u_e} = \left(\frac{y}{\delta}\right)^{\frac{1}{7}} \quad (3.42)$$

$$T = T_0 + (T_e - T_0) \left(\frac{u}{u_e}\right)^2 \quad (3.43)$$

### 3.5.2 Numerical solution of the boundary layer integral equations

Equations (3.36) and (3.37) represents a system of coupled first order ordinary differential equations which can be numerically solved by means of fourth order Runge-Kutta method. The method is carried out starting from the throat section of the inviscid nozzle throat and the leading edge of the inviscid rotor blade. In the first case, it is supposed that the boundary layer thickness is not zero (due to the development of the convergent), but reaches an extremum. This corresponds to imposing the initial condition:

$$\frac{d\Theta_{tr}}{dx}_{throat} = 0 \quad (3.44)$$

From Eqs. (3.44) and (3.36) the initial value for  $\Theta_{tr}$  is then evaluated. For the rotor, the boundary condition  $\Theta_{tr}(x = 0) = 0$  is imposed. For both rotor and nozzle the initial value  $H_i = 1.1$  is selected. Indeed, as explained in (Reshotko and Tucker, 1957), for blunt bodies a good initial guess value for the form factor is between 1.0 and 1.3. The error committed in this choice is inconsequential, since the form factor will tend to reach its proper value in the first few steps of calculation. The integration of equations (3.36)-(3.37) leads to the  $\Theta_{tr}(x)$  distribution along the nozzle/rotor blade wall. By using equation (3.39) the compressible momentum thickness is calculated and, by using its definition, the boundary layer thickness  $\delta$  is evaluated, along with all the integral parameters:

$$\Theta = \int_0^\delta \frac{\rho u}{\rho_e u_e} \left(1 - \frac{u}{u_e}\right) dy \quad (3.45)$$

$$\delta^* = \int_0^\delta \left(1 - \frac{\rho u}{\rho_e u_e}\right) dy \quad (3.46)$$

The above equations for the displacement thickness  $\delta^*$  and momentum thickness  $\Theta$  are solved by numerical integration with a 16 point Gauss-Legendre quadrature method.

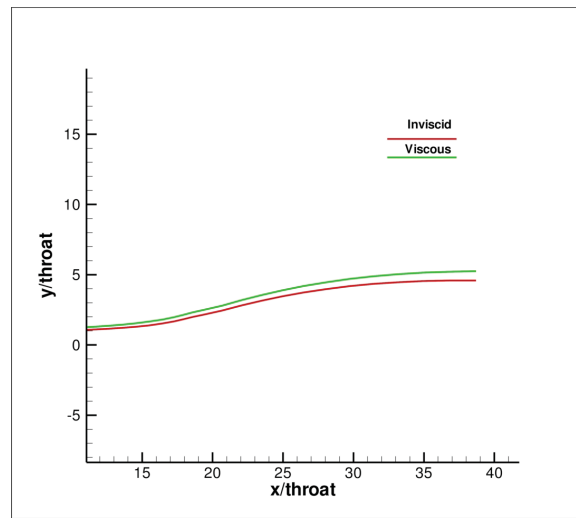
Finally, the inviscid shape  $S(x)_{inviscid}$  calculated with the MOC is corrected as  $[S(x)_{inviscid} + \delta^*]$ . In order to ensure convergence of the numerical methodology, the inviscid shape is used as base for an interpolated curve passing from a high number of point equally spaced. As shown in (Sivells, 1978), the success of the above integration method depends strongly upon the spacing of the shape points.

### 3.5.3 Application to supersonic nozzles

The above methodology is applied to the design of a nozzle guide vane with R245fa. The operating conditions are reported in Tab. 3.13.

**Table 3.13:** Main turbine working parameters.

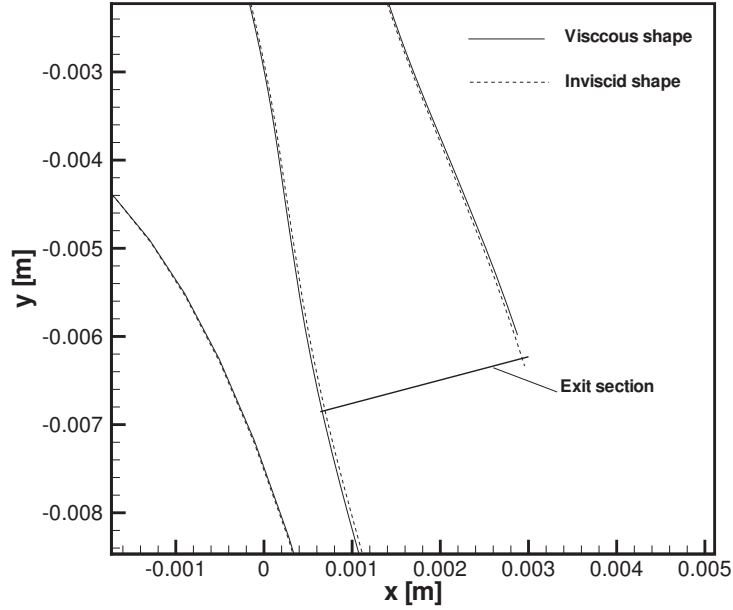
| Parameters                              | Values |
|---|--------|
| Inlet total reduced pressure            | 1.2    |
| Pressure ratio                          | 20.6   |
| Inlet total reduced temperature         | 1.1    |
| Stator nozzle outlet design Mach number | 2.4    |
| Stator stager angle                     | 70     |



**Figure 3.38:** Comparison between inviscid (red) and viscous (green) shape for nozzle calculation with R245FA fluid.

Numerical simulations are carried out by using the in-house CFD solver. As shown in Figs. 3.38-3.39, the viscous shape takes into account the boundary layer thickness which has an influence on the effective flow passage and, then, the enthalpy drop and power output.

Fig. 3.41 shows the results of the Eqs. (3.36)-(3.37) integration in terms of displacement, momentum and boundary layer thickness (Fig. 3.41a) and Ludwig-Tillmann skin friction coefficient (Fig. 3.41b). Fig. 3.42 shows the enthalpy drop across the "inviscid" and "viscous" designs for the guide vane center-line, whereas Fig. 3.40 show a comparison of the Mach number field between the two designs. For the "inviscid" design, the boundary layer reduces the effective flow passage, leading to massflow and exit Mach number to lower than the nominal ones, and consequently to a lower pressure ratio and power output. With the boundary layer correction a significant increase of the enthalpy drop is obtained, as well as improvements in terms of massflow and power output (the latter evaluated as the enthalpy drop times the massflow). The viscous wake and the separation region on the trailing edge are reduced. Performance parameters for the two designs are reported in Tab. 3.14. The isentropic efficiency  $\eta_{is}$  and the power output for the corrected shape are higher than those of the inviscid design and close to those obtained for the latter by using an inviscid flow model.



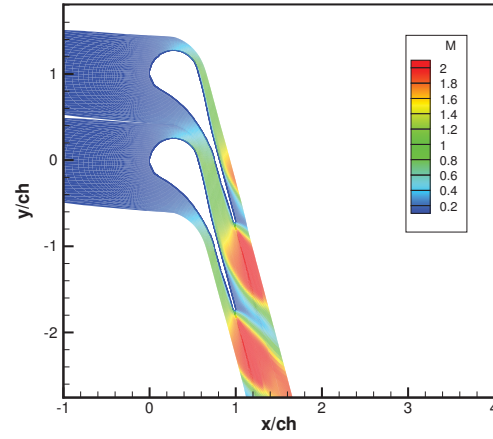
**Figure 3.39:** Comparison between inviscid and viscous nozzle guide vane shapes with view enlargement of the exit section.

**Table 3.14:** Main nozzle performances with and without boundary layer correction.

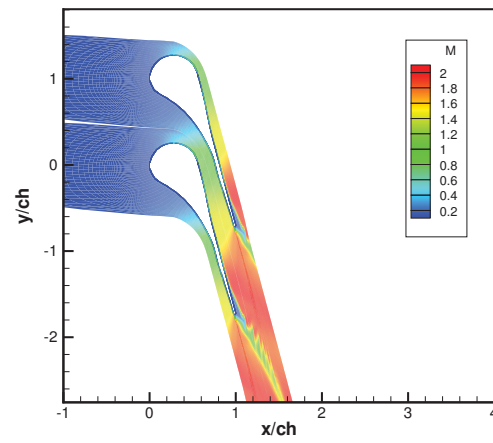
| Parameters        | BL-correction | Without BL-correction |
|-------------------|---------------|-----------------------|
| $\eta_{is}$ [%]   | 91.86         | 88.64                 |
| Power output [kW] | 1.697         | 1.640                 |
| Massflow [kg/s]   | 0.452         | 0.447                 |

### 3.5.4 Application to supersonic rotors

In Fig. 3.43 the boundary layer correction is applied to the design of a rotor blade shape. It can be noticed that after the correction the exit flow angle is slightly different from the design one, thus providing a slightly positive degree of reaction. A viscous CFD simulation has been carried out for the rotor of Section 3.3.5 modified by the boundary layer correction and the results are compared to those previously obtained for a purely inviscid design. The Mach number and entropy deviation distributions for the corrected rotor are reported in Fig. 3.44. The Mach number shows a similar shock pattern with several reflections through the blade vane up to the exit. The rotor is again fully started. We observed that the "viscous" design leads to lower losses, in terms of entropy deviation, since the boundary layer remains thinner (no compression in this case), and so does the wake (Fig. 3.44b). The boundary layer correction has a beneficial effect also on the degree of reaction ( $\Lambda = -0.011$ ), significantly reducing re-compression effects due to the change of the effective flow passage area.

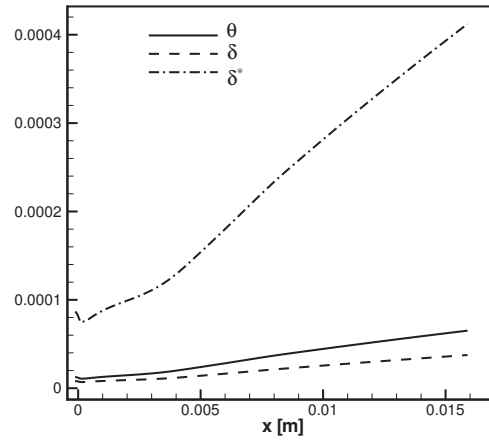


(a)

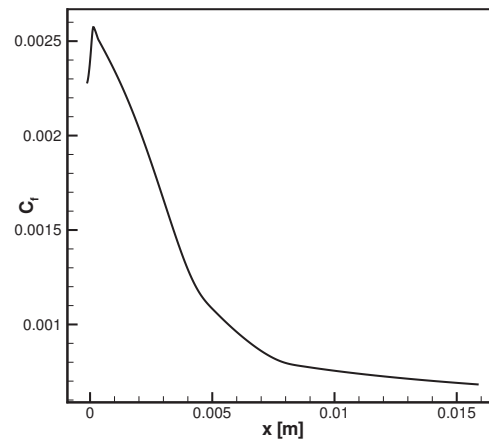


(b)

**Figure 3.40:** Comparison between inviscid (a) and viscous (b) nozzle blade shapes Mach number contour plot.

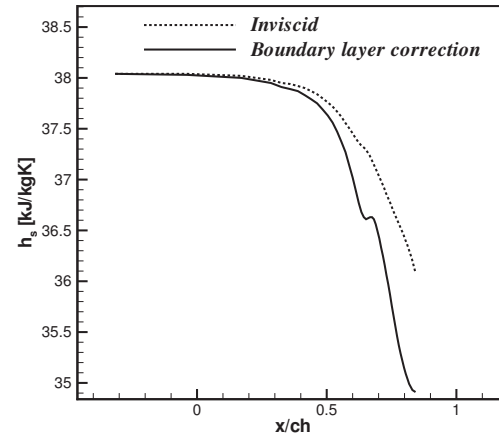


(a)

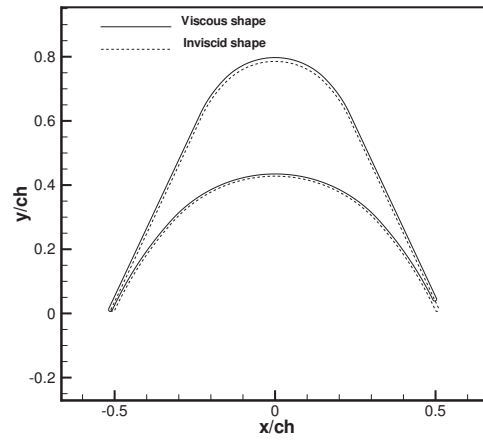


(b)

**Figure 3.41:** Integral boundary layer parameters (a); Compressible Ludwig-Tillmann skin friction coefficient (b).

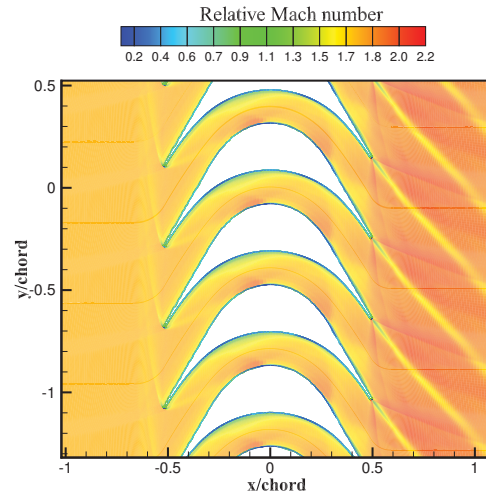


**Figure 3.42:** Comparison between inviscid and viscous nozzle shape of the static enthalpy evolution along the guide vane center-line.

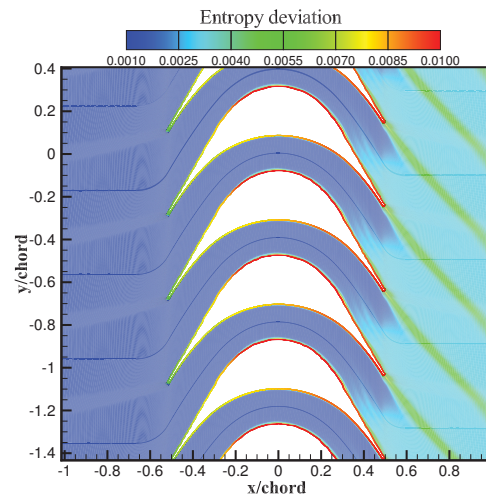


**Figure 3.43:** Comparison between inviscid and viscous impulse rotor blade shapes.





(a)



(b)

**Figure 3.44:** Mach number contour plot (a) and entropy deviation (b) for RODEC rotors with boundary layer correction.

### 3.6 Conclusions

In this Section, a fast design methodology based on the method of characteristics for supersonic ORC nozzle guide vanes and rotors has been developed and tested. The design process, takes into account the complex behaviour of the complex organic working fluids for ORC applications, which show dense gas dynamics effects under the given operating conditions.

Three different gas models, namely the perfect-gas, equivalent- $\gamma$  and multi-parameter EOS models, have been proposed and compared for the nozzle guide vane design. Four fluids of industrial interest for ORC applications (R245fa, Novec649, RE347mcc, R449) have been considered both for stator and rotor designs. The performances have been assessed by means of CFD calculations. In this framework, the R449 provided the best efficiencies and the higher enthalpy drop, assuring the higher power output if coupled with an impeller. It has been investigated the effect of the viscous phenomena, showing that they are responsible of high losses of performances. Indeed, the viscous numerical simulations showed an impact of 10% on the efficiency. The main source of losses are located in the long wake downstream the blade and of in the boundary layer separation zone.

The MOC has been applied also for the rotor design and generalised to complex EOS. The design methodology has been enriched with an investigation of the unique incidence problem, which has been solved in the dense gas regime. Numerical simulations have shown that the MOC design provides a started configuration of the supersonic flow in the blade vane and, subsequently, the rotor performances are improved.

A further improvement in the design approach has been carried out by correcting the "inviscid" nozzle and rotor shapes by means of the boundary layer thickness. It has been showed, with numerical simulations, that the isentropic efficiency and the power output improved by approaching the values provided by the inviscid CFD calculations.

Finally, a full stage calculation has been carried out in order to evaluate the main stage performances.

## Chapter 4

# UNCERTAINTY QUANTIFICATION

### 4.1 Introduction

Uncertainty Quantification (UQ) has been recognized in the last decade as a key component in industrial design and risk management. Indeed, fluid systems may be governed by input parameters, like the operating conditions or the geometry, that are not perfectly known or can be subjected to random fluctuations. These random variations can be modelled by means of probability distribution functions and have to be taken into account. However, introducing the probabilistic nature of the uncertainties in a simulation software system, is a highly challenging undertaking, as the whole process transforms the resolution of deterministic physical conservation laws, to non-deterministic methods, governed by stochastic partial differential equations. As a consequence, predicted quantities, such as loads, lift, drag, efficiencies, temperatures etc., are now represented by a probability density function (pdf), providing a domain of confidence, associated to the considered uncertainties and introducing a new concept of design with respect to classical deterministic methodologies.

In a general way, it exists a distinction between *error* and *uncertainty*. By following the guidelines of the aerospace community ([AIAA-Standards, 1998](#)), the first is "a recognizable deficiency in any phase or activity of the modeling process that is not due to the lack of knowledge" whereas the second is "a potential deficiency in any phase or activity of the modeling process that is due to the lack of knowledge". In this sense, the uncertainty can then be seen as a way to assess the inability to deal *deterministically* with the chaotic, unpredictable working conditions of the real world applications. Two kind of uncertainties can be considered: *aleatory* uncertainties, that are related to the inherent randomness of the system being analyzed, such as variability of operational conditions, geometrical randomness from the manufacturing process, which cannot be reduced by further data and, then, are known also as irreducible; *epistemic* uncertainties, that are globally generated by numerical errors due to discretisation approximations and grid dependences, as well as lack of knowledge associated to the imperfect physical models, such as turbulence, combustion or multiphase models. They are known also as *reducible* uncertainties since can be reduced by improving the knowledge about the system under analysis.

The probabilistic nature of the uncertainties has been taken into account in this thesis work in order to consider the aleatory variability of the operating and geometrical parameters of an ORC system for WHR applications. For this purpose we consider several *non-intrusive* UQ techniques

which require no modification to the existing deterministic models (see e.g. (Hosder and Walters, 2010; Eldred and Burkardt, 2009) for applications based on the Polynomial Chaos). However, the non-intrusiveness property implies an exponential increase of the computational cost for the estimation of the statistics by increasing the number of uncertainties. This problem is known in UQ as *curse of dimensionality* (De Baar et al., 2012; Congedo et al., 2011b) and it needs to be taken into account in order to maintain a feasible computational cost.

The methods selected as candidate UQ methods for the present application are the Probabilistic Collocation Method (PCM), the Simplex Stochastic Collocation (SSC), the mean value Second Order Second Moment (SOSM) and the Bayesian Kriging (BK), which are considered as the state-of-the-art for non-intrusive UQ. Further details are provided below.

## 4.2 UQ methodologies

### 4.2.1 Probabilistic Collocation Method

The stochastic analysis used to determine the system response to input parameter variation by means of the PCM is based on the work of (Loeven et al., 2007). To illustrate the non-intrusive PCM implementation procedure, the following uncertain differential equation system is considered:

$$L(\mathbf{x}, \theta, \phi) = f(\mathbf{x}, \theta) \quad (4.1)$$

where  $L$  is an operator,  $\mathbf{x}$  are the deterministic variables,  $\theta$  the random parameter and  $\phi$  the solution. The latter is decomposed into deterministic:  $\phi_i(\mathbf{x}, t)$ , and stochastic:  $h_i(\boldsymbol{\xi}(\theta))$ , components:

$$\phi(\mathbf{x}, t, \boldsymbol{\xi}(\theta)) = \sum_{i=1}^{P_{PCM}} \phi_i(\mathbf{x}, t) h_i(\boldsymbol{\xi}(\theta)) \quad (4.2)$$

where  $\boldsymbol{\xi}(\theta)$  are the random variables and  $\phi_i(\mathbf{x}, t)$  is the deterministic solution at the collocation point  $\xi_s(\theta_i)$ . The multi-dimensional random space parameters is then discretized in a full-factorial way by means of multiple one-dimensional tensor products.

In the PCM,  $p$  is the order of the quadrature polynomial and the number of collocation points is given by  $P_{PCM} = p^{n_\xi}$ , where  $n_\xi$  represents the total number of random input variables. The term  $h_i$  is the Lagrange interpolated chaos polynomial of order  $N_p = p - 1$  that passes through the  $P_{PCM}$  collocation points:

$$h_i(\boldsymbol{\xi}(\theta)) = \prod_{s=1}^n \left[ \prod_{\substack{k=1 \\ k \neq i}}^{N_p} \frac{\xi_s(\theta) - \xi_s(\theta_k)}{\xi_s(\theta_i) - \xi_s(\theta_k)} \right] \quad (4.3)$$

The collocation points are chosen as the roots of a quadrature polynomial of the same type of chaos polynomials adapted for the solution expansion. The solution has to be integrated in order to obtain for instance the mean or variance. To find the Gaussian quadrature points and weights the Golub-Welsch (Golub and Welsch, 1969) algorithm is followed. In order to perform it, firstly the recurrence coefficients of the polynomials orthogonal to the probability distribution of the weighting function have to be calculated. The exponential convergence property of the PCM is guaranteed if  $w(\xi) = f_\xi(\xi)$ , where  $w(\xi)$  and  $f_\xi(\xi)$  are the orthogonal polynomial weighting functions and the probability distribution associated to the uncertain parameters, respectively. The recurrence coefficients  $\alpha_i$  and  $\beta_i$ , for  $i = 1, \dots, P_{PCM}$ , are computed using the discretized

Stieltjes procedure (Gander and Karp, 2001), which is a stable method for arbitrary distribution functions, and used to construct the matrix  $J$  defined as

$$J = \begin{bmatrix} \alpha_1 & \sqrt{\beta_2} & \dots & 0 & 0 \\ \sqrt{\beta_2} & \alpha_1 & \sqrt{\beta_3} & \dots & 0 \\ & \sqrt{\beta_3} & \alpha_3 & \sqrt{\beta_4} & \\ & \dots & \dots & \dots & \\ 0 & \dots & \sqrt{\beta_{P_{PCM}-1}} & \alpha_{P_{PCM}-1} & \sqrt{\beta_{P_{PCM}}} \\ 0 & 0 & \dots & \sqrt{\beta_{P_{PCM}}} & \alpha_{P_{PCM}} \end{bmatrix}$$

It can be shown that the eigenvalues of  $J$  are the collocation points  $\xi_i$ ,  $i = 1, \dots, P_{PCM}$ , whereas the weights are found by  $w_i = \beta_1 v_{1,i}^2$ , where  $v_{1,i}$  is the first component of the normalized eigenvector corresponding to eigenvalue  $\xi_i$  (Loeven et al., 2007).

A Galerkin projection is performed on each basis polynomial  $h_k(\xi)$ , for  $k = 1, \dots, P_{PCM}$ , by means of the substitution of Eq. (4.2) into Eq. (4.1) and further Gaussian quadrature which provides a fully decoupled system of deterministic equations.

This results in the solution of decoupled deterministic CFD simulations which are carried out at the  $p$  collocation points for each uncertain parameter, permuted by a full factorial design, resulting in  $P_{PCM} = p^n$  independent deterministic simulations. Finally, the statistics can be evaluated with the following formulas derived from the definition of mean  $\mu$  and variance  $\sigma^2$ :

$$\mu_\phi = \sum_{i=1}^{P_{PCM}} \phi_i(\mathbf{x}, t) w_i \quad (4.4)$$

$$\sigma_\phi^2 = \sum_{i=1}^{P_{PCM}} (\phi_i(\mathbf{x}, t))^2 w_i - \left( \sum_{i=1}^{P_{PCM}} \phi_i(\mathbf{x}, t) w_i \right)^2 \quad (4.5)$$

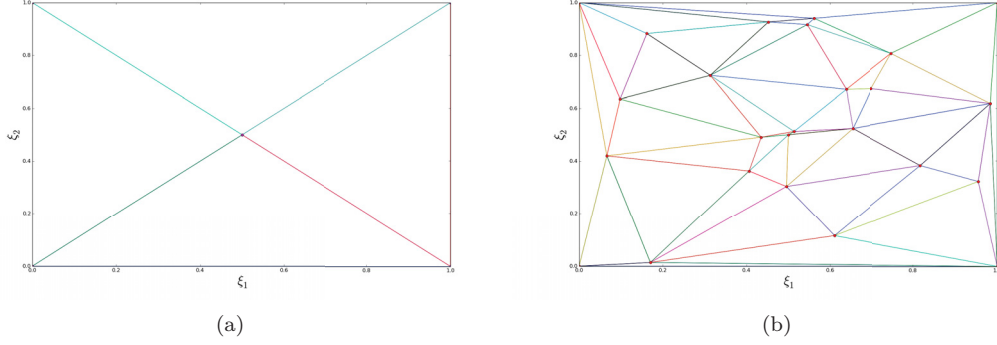
As shown in previous works (Congedo et al., 2011b; Cinnella and Hercus, 2010) a chaos polynomial of order  $N_p = 2$  provides good results for dense gas applications with a reasonable computational cost. Based on that, this value is retained for the further analysis.

#### 4.2.2 Simplex Stochastic Collocation

To alleviate the high computational cost associated to a full-factorial sampling, a more efficient technique has been proposed in (Witteveen and Iaccarino, 2012). The hypercubic parameter space is now discretized in a unstructured way under the form of simplexes by means of an adaptive Delaunay triangulation. A random sampling is performed in order to avoid clustering of points and high order polynomial interpolation allows to reconstruct the random solution for each simplex.

Given the multidimensional uncertain parameter space  $\Xi$ , the Delaunay triangulation on  $n_s$  sampling points divides it into  $n_e$  disjoint simplex sub-domains  $\Xi_j$ , with  $j = 1, \dots, n_e$ . Each sub-simplex is defined by its  $(n_\xi + 1)$  vertices, where  $n_\xi$  is the number of uncertain variables or, alternatively, the cardinality of the parameter space. The initial discretization consists of  $2^{n_\xi}$  sampling points  $\xi_k$ , with  $k = 1, \dots, n_s$ , in the vertexes of a hypercube parameter space  $\Xi$  and one point in the interior of  $\Xi$ .

An example of a initial grid in two dimensions ( $n_\xi = 2$ ) is shown in Fig. 4.1a, with an initial number of simplexes  $n_{e,i} = 4$ . Then, the parameter space discretization is refined by randomly adding new points  $\xi_k$  and the new grid is provided by means of a new Delaunay triangulation (see Fig. 4.1b).



**Figure 4.1:** Delaunay triangulation of randomized sampling points in a two-dimensional parameter space  $\Xi$  with  $n_\xi = 2$  before (a) and after (b) refinement.

The approximation of a generic statistical moment  $\mu$  of order  $i$  is performed as:

$$\mu_{\phi_i}(\mathbf{x}, t) \approx \sum_{j=1}^{n_e} \int_{\Xi_j} w_j(\mathbf{x}, t, \xi)^i f_\xi(\xi) d\xi \quad (4.6)$$

where  $\phi = \phi(\mathbf{x}, t, \xi)$  is the quantity of interest and  $w_j(\mathbf{x}, t, \xi)$  is a piecewise polynomial approximation for  $\xi \in \Xi_j$ .

The triangulation methodology introduces an unstructured discretization and interpolation of the parameter space. The refinement of the SSC grid is carried out based on the introduction of an error measure. By following (Witteveen and Iaccarino, 2012), the error estimates are based on the difference  $\varepsilon(\xi) = w_j(\xi) - v_{k_{j,ref}}$  between the piecewise approximation  $w_j(\xi)$  and the exact value  $v_k$  in the new sampling point  $\xi_{k_{j,ref}}$  at the refinement of simplex  $\Xi_j$ . Then, by defining the approximation of the absolute error  $\tilde{\varepsilon}$  in a simplex  $\Xi_j$  as the absolute value of the error  $\varepsilon_k$  at the most recently added sampling point  $\xi_k$ , with the highest value of  $k$  denoted by  $k^*$ , the following relation between the error before and after refinement,  $\tilde{\varepsilon}$  and  $\hat{\varepsilon}$  respectively, can be written:

$$\hat{\varepsilon}_j \approx \tilde{\varepsilon}_j \left( \frac{|\bar{\Xi}_j|}{|\bar{\Xi}_{k^*_{ref}}|} \right)^{\frac{p_j+1}{n_\xi}} \quad (4.7)$$

where  $|\bar{\Xi}_j|$  represents the volume measure of the current element  $j$ ,  $|\bar{\Xi}_{k^*_{ref}}|$  the volume measure of the old simplex which is refined by adding the last added sample  $\xi_{k^*}$  and  $p_j$  is the local polynomial order of the  $j$ -th simplex. Then, the ratio  $\frac{|\bar{\Xi}_j|}{|\bar{\Xi}_{k^*_{ref}}|}$  is the relative volume variation

of the current refined simplex with respect to the old one before refinement. The preceding equation states that the error estimates after refinement is proportional to the variation of the local element volume between its current size  $\bar{\Xi}_j$  and the size after adding the new sample  $\xi_{k^*}$ . This method is suitable for dealing with discontinuities, such as shocks, thanks to the introduction of a local smoother based on a Local Extremum Conserving (LEC) criterion. A super-linear convergence is reached during the simplex refinement process. The adaptive random sampling of the space parameters is expected to improve the efficiency, leading to a lower overall number of deterministic calculations than the full-factorial sampling.

More advanced versions of the SSC algorithm exists (Edeling et al., 2016), even if they are not applied here, given the relatively low number of uncertain parameters involved in the present study.

### 4.2.3 Bayesian-Kriging

A surface-response method based on the Bayesian-Kriging approach has been implemented in order to evaluate mean and variance of a Quantity of Interest (QoI), (e.g. the isentropic efficiency of the ORC expander), by means of a surrogate model of the output response. The Kriging models are exact interpolation models based on the modelling of the response as the realization of a Gaussian process. In general, the unknown QoI  $\mathbf{y}$  is modelled as a regression function of the form  $\mathbf{y}(\boldsymbol{\xi}) = \sum_i f_i(\boldsymbol{\xi})\beta_i + Z(\boldsymbol{\xi})$ , where  $\boldsymbol{\xi}$  is the vector of coordinates of a generic point in the multi-dimensional parameter space,  $f_i$  the basis functions of the regression model,  $\beta_i$  the regression coefficients to be calculated and  $Z(\boldsymbol{\xi})$  a zero mean Gaussian process. Usually, a zero-order polynomial (constant) is adopted as regression model, defining the so-called *ordinary Kriging model*. The Gaussian process  $Z$  is considered as a multi-variate normal distribution  $Z \sim N(0, \mathbf{P})$ , with mean zero and covariance matrix  $\mathbf{P}$ .

The preceding kriging formulation can be revised in the Bayesian framework. In this case, the kriging surrogate predicts a set of  $M$  values of the QoI  $\mathbf{y}(\boldsymbol{\xi})$ , conditional on  $N$  observed data  $\mathbf{y}^*$ , where the data  $\mathbf{y}^*$  are a subset of  $\mathbf{y}$  selected by the observation matrix  $\mathbf{H}$ . The vector of the unknown QoI  $\mathbf{y}(\boldsymbol{\xi})$  is supposed to follow a prior normal distribution  $p(\mathbf{y})$ ,  $\mathbf{y} \sim N(0, \mathbf{P})$ , where the multi-variate covariance matrix  $\mathbf{P}$  needs to be evaluated. Besides, the conditional probability to observe the  $N$  data  $\mathbf{y}^*$  given the unknowns  $\mathbf{y}$  (known as likelihood probability) is considered to be a normal distribution of the form:

$$\mathbf{y}^*|\mathbf{y} \sim N(\mathbf{H}\mathbf{y}^*, \mathbf{R}) \quad (4.8)$$

where  $H$  is the observation matrix of  $M \cdot N$  dimensions which allows to select the values of  $\mathbf{y}$  among the data  $\mathbf{y}^*$ , by means of the following formulation:

$$H_{ij} = \begin{cases} 1, & \text{if } i = j \\ 0, & \text{otherwise} \end{cases} \quad (4.9)$$

for  $i = 1, \dots, M$  and  $j = 1, \dots, N$ . The observation error covariance matrix  $\mathbf{R}$  is modelled as uniform and uncorrelated, such that:

$$\mathbf{R} = \epsilon^2 \mathbf{I} \quad (4.10)$$

where  $\mathbf{I}$  is the identity matrix and  $\epsilon$  a pre-defined error of the observed variable values.

The posterior distribution of the unknowns, conditional to the observed data, can be inferred by means of the Bayes theorem, such that:

$$p(\mathbf{y}|\mathbf{y}^*) \sim p(\mathbf{y}^*|\mathbf{y})p(\mathbf{y}) \quad (4.11)$$

Given that the product in the preceding equation is performed between two normal distributions, the posterior will be of the same normal form. However, before to define it, the expression of the covariance matrix  $\mathbf{P}$  has to be evaluated.

Assuming that  $\mathbf{y}$  and  $\mathbf{y}^*$  are normalized such that  $\mathbf{y}^*$  has zero mean and unit variance, the covariance matrix  $\mathbf{P}$  of the prior distribution  $p(\mathbf{y})$  is defined such that its elements are generated by the Gaussian function (reported below in the 1-D case, for simplicity):

$$\mathbf{P} = [P_{ij}(\theta)] = \left[ \exp\left(-\frac{h_{ij}^2}{2\theta^2}\right) \right] \quad (4.12)$$

where  $h_{ij} = \xi_i - \xi_j$  is the correlation range,  $\xi_i$  the generic coordinate of the prediction  $\mathbf{y}$  and  $\theta$  an hyperparameter which need to be estimated (for multi-dimensional problems it is a vector whose dimension is the cardinality of the parameter space). By following [Wikle and Berliner \(2007\)](#), the kriging predictor mean and variance are:

$$E(\mathbf{y}|\mathbf{y}^*) = \mathbf{P}\mathbf{H}^T(\mathbf{R} + \mathbf{H}\mathbf{P}\mathbf{H}^T)^{-1}\mathbf{y}^* \quad (4.13)$$

$$var(\mathbf{y}|\mathbf{y}^*) = [\mathbf{I} - \mathbf{P}\mathbf{H}^T(\mathbf{R} + \mathbf{H}\mathbf{P}\mathbf{H}^T)^{-1}]\mathbf{P} \quad (4.14)$$

The advantage of this methodology is to obtain directly an estimation of the surrogate model accuracy by means of the kriging variance. Because we deal with an ordinary kriging model where the hyperparameters need to be estimated, the Maximum Likelihood Estimation (MLE) approach is implemented in order to evaluate the hyperparameter  $\theta$  as the solution of the optimization problem:

$$max_{\theta} \left\{ - \left( \ln |\mathbf{A}| + \mathbf{y}^{*T} \mathbf{A}^{-1} \mathbf{y}^* \right) \right\} \quad (4.15)$$

where  $\mathbf{A} = (\mathbf{R} + \mathbf{H}\mathbf{P}\mathbf{H}^T)$ . Since the problem in Eq. (4.15) is performed over a multidimensional space whose cardinality is given by the number of uncertain variables and the cost varies as  $O(n_s N^3)$ , where  $n_s$  is the number of optimization steps and  $N$  is the number of observed samples, it represents a bottleneck for the above methodology. The MLE problem is classically solved by means of the Nelder-Mead downhill simplex method. Here a global-search algorithm based on a differential genetic evolution approach has been implemented, providing an improvement in term of computation time. Besides, the inversion of the matrix  $\mathbf{A}$  is improved with a Cholesky decomposition.

More efficient methodologies for estimating the hyperparameters could be implemented, such as the fast estimation in the frequency domain proposed by [De Baar et al. \(2013\)](#), who speeded-up the Kriging by solving the MLE by means of a Fourier Transform and reducing the cost to  $O(N^2 + n_s N)$ .

Finally, once the Kriging surrogate has been trained and the hyperparameters estimated, the statistics are calculated by means of a Montecarlo simulation of the model by randomly sampling the uncertain variable distributions.

In order to test the algorithm, a test with the well-known 2-D Rosenbrock function is shown (see Figs. 4.2). The domain is reduced such that  $0 < x_1, x_2 < 0.8$ , where is located the global minimum. It can be seen that by choosing 20 samples uniformly distributed by means of the Latin Hypercube Sampling (LHS), the function reconstruction is acceptable, with a maximum Kriging error of 0.042 located on the domain boundaries.

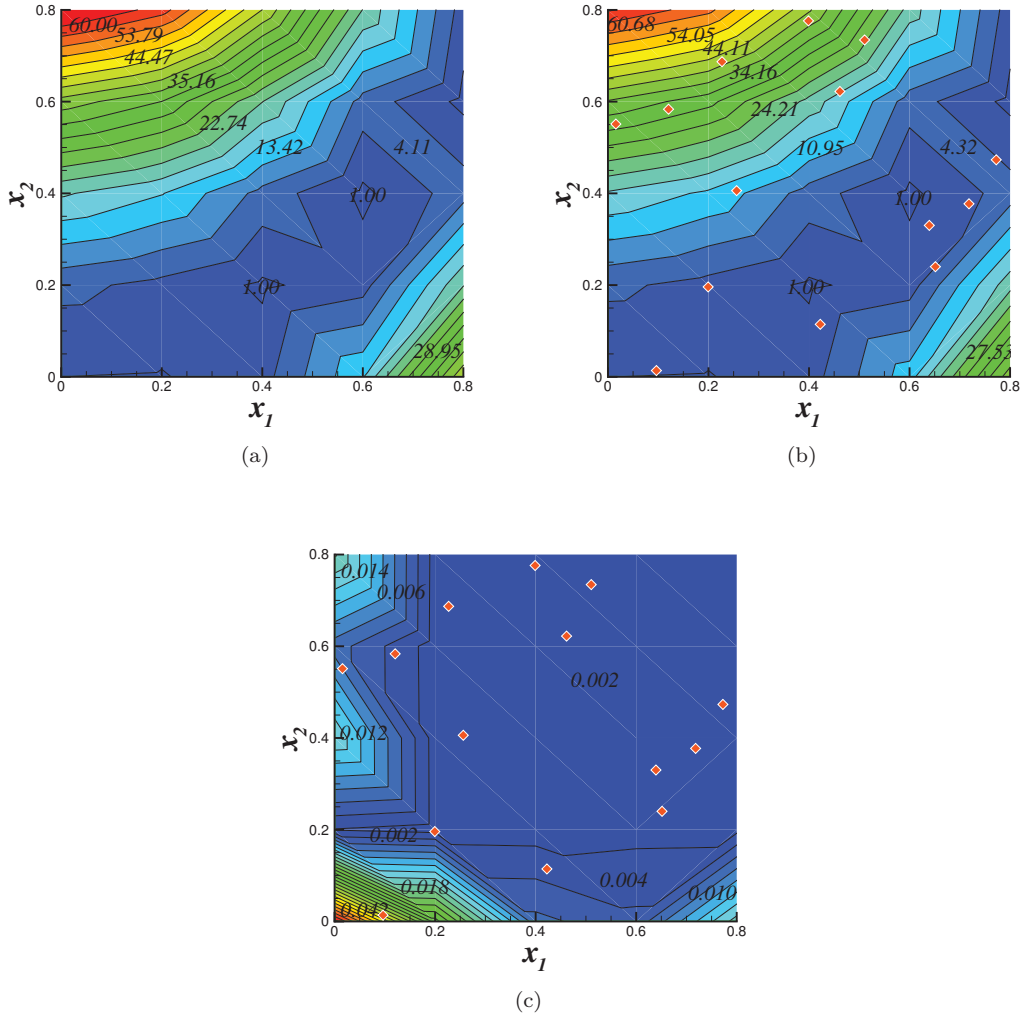
#### 4.2.4 Mean Value Second Order Second Moment

The Mean Value Second Order Second Moment method (MVSOSM or simply SOSM) is a deterministic UQ model which computes the statistics of the random QoI by means of a Taylor expansion around the mean value. In this work the mean and variance are obtained with a second and a first order truncated expansion respectively, according to equations:

$$\mu_{\phi} = \phi(\mu_{\xi}) + \frac{1}{2} \sum_i \frac{\partial^2 \phi(\mu_{\xi})}{\partial \xi_i^2} \sigma_{\xi}^2 \quad (4.16)$$

$$\sigma_{\phi}^2 = \sum_i \left( \frac{\partial \phi(\mu_{\xi})}{\partial \xi_i} \sigma_{\xi} \right)^2 \quad (4.17)$$





**Figure 4.2:** Bayesian-Kriging algorithm test for the 2-D Rosenbrock function. (a) True function; (b) surrogate function with 20 samples; (c) surrogate error in terms of Kriging variance.

where  $\mu_\xi$  and  $\sigma_\xi$  are the mean and standard deviation of the uncertain variable  $\xi$ .

Here a second order variance formulation is adopted in order to avoid the definition of additional parameters of the input distributions, such as skewness and kurtosis.

The cross derivatives are neglected in the Taylor expansion, i.e. the interaction among the random parameters are not considered here, such that a cheap estimation of the statistics can be carried out. If a centred scheme is used for all the derivatives, the number of deterministic calculations  $P_{SOSM}$  varies linearly with the number of random variables  $n_\xi$ , as  $P_{SOSM} = 2n_\xi + 1$ . The increments  $\Delta\xi_i$  for the numerical calculation of the derivatives have been chosen as 1% of the QoI mean value.

The method requires a relatively low number of samples and is expected to be cheap in terms of

computational costs. An additional deterministic calculation is required in order to evaluate the QoI at the mean value of the random inputs.

### 4.3 Sensitivity of supersonic ORC nozzle guide vane designs to fluctuating operating conditions

In this Section, the NODEC algorithm for dense gas nozzle designs previously described has been coupled with the PCM. Here, inviscid calculations are performed, by means of the solver described in Section 2.2, and used to carry out the UQ analysis.

The purpose is to evaluate the sensitiveness of the performances of ORC expanders designed with the new methodology to stochastic variations of the design parameters and quantify the variability of the nozzle shape geometries and performances under variable operating conditions. Also, an UQ analysis has been carried out by coupling the dense gas numerical solver (see Section 2.2) with the PCM algorithm and evaluating the sensitivity of nozzle guide vane performances to variability of operational, geometrical and thermodynamic parameters.

In the following, it is assumed that all of the input random parameters, like the total pressure and temperature upstream of the turbine, are independent. If some of the parameters were to be correlated, the method could be still applied by treating one of the parameters as random and by computing the other ones using the correlation law.

#### 4.3.1 Sensitivity of supersonic convergent-divergent nozzle designs

In this section the nozzle geometries are designed by means of the NODEC. We assume that the inlet total pressure  $p_0$  and inlet total temperature  $T_0$  behave as random functions (then,  $n_\xi = 2$ ). The nozzles are designed such that the mass-flow  $G = 20$  kg/s and the pressure distribution along the nozzle axis  $p(x)$  (such that the exit Mach number is  $M = 2$ ) are kept constant. As first approximation, a uniform continuous distribution has been considered. Then, once defined the input parameters range variability  $(a, b)$ , the main statistics mean  $\mu$  and variance  $\sigma$  have been calculated, as follows:

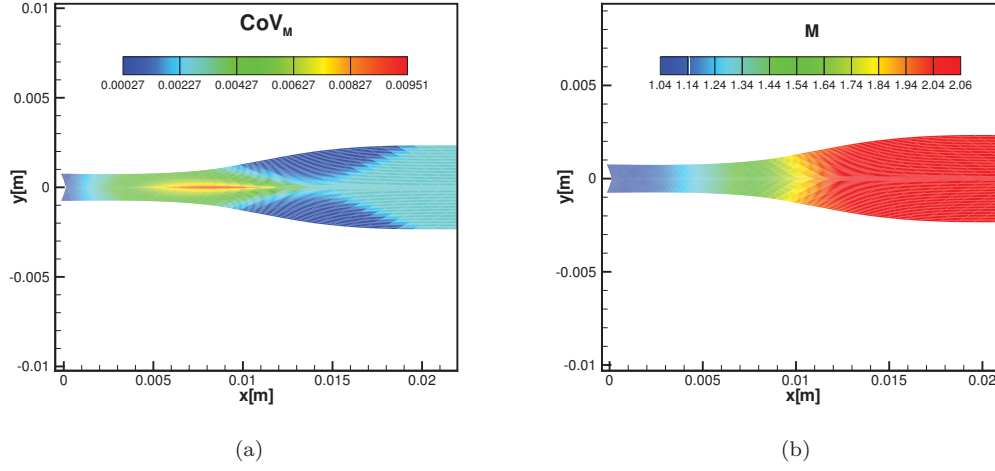
$$\mu = \frac{a + b}{2} \quad (4.18)$$

$$\sigma^2 = \frac{(b - a)^2}{12} \quad (4.19)$$

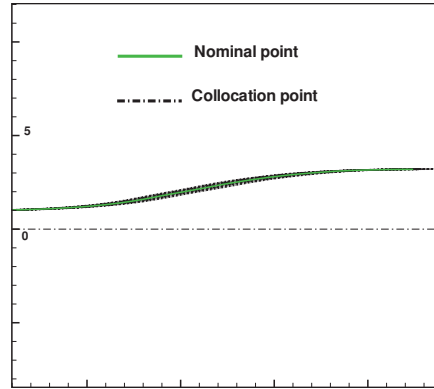
Another quantity of interest for the statistical analysis is the coefficient of variation (CoV), calculated as  $CoV = \frac{\sigma}{\mu}$ .

A variation of  $\pm 3\%$  of the reduced inlet total conditions around the nominal point ( $p_r^0 = 0.98, T_r^0 = 1.13$ ) has been preliminarily considered. This choice allows to avoid the gas-liquid co-existence region of the state diagram during the gas expansion, which could implies issues from the numerical point of view. Indeed, for the ORC application here considered, the nominal operating conditions are close to the saturation curves and their perturbations have to be defined in such a ways as to avoid multi-phase expansions.

By considering a second-order Lagrange interpolated chaos polynomial, the total number of collocation points (and, then, of deterministic simulations) is  $P_{PCM} = 9$ . The results are obtained for the R245fa. Our goal is to investigate the sensitivity of the resulting geometry to the fluctuating inlet conditions. The variability of the operating conditions induces a variability in the output nozzle design. In this case, the prescribed variation of operating condition results only in a slight modification of the nozzle geometry with respect to the one obtained at nominal operating conditions (see Fig. 4.4), with a maximum variation of only 0.01% of the exit-to-throat area



**Figure 4.3:** Coefficient of Variation (a) and mean value (b) of the Mach number for uniformly distributed input parameters ( $\pm 3\%$  of variation around the nominal point).



**Figure 4.4:** Variability of the nozzle shape geometry for uniformly distributed input parameters ( $\pm 3\%$  of variation around the mean value).

ratio with respect to the mean value (nominal point). This shows that the MOC design is not strongly affected by the variability of the reservoir conditions when the mass-flow ratio is kept constant, which was expected for a perfect gas. For real gases, these variations lead essentially to modifications of the nozzle shape in the throat region.

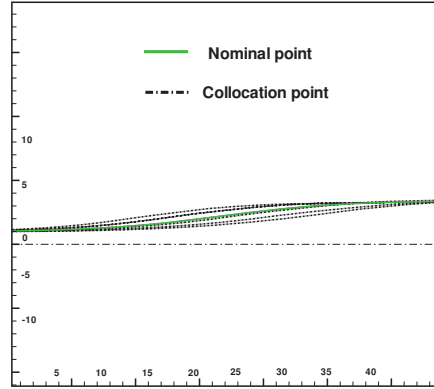
Due to this considerations, we should expect that the sensitivity to variations of the main flow quantities, such as the Mach number, is very low. Indeed, inspection of top Fig. 4.3, displaying the percent coefficient of variation of the Mach number, the peak of variability of the solution, located close to the nozzle center-line, is of about 0.01%, which is negligible.

Bottom Fig. 4.3 shows the mean Mach number field applied to the mean nozzle shape and it is very similar to the one obtained for the nominal operating conditions.

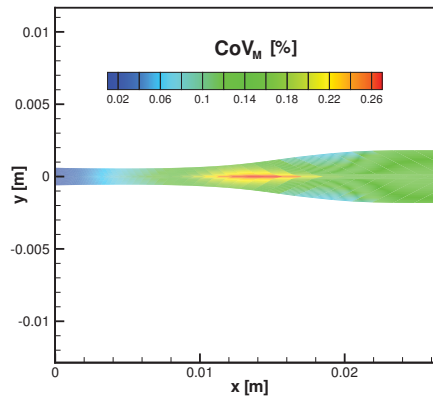
In order to investigate the effect of large perturbations of the inputs conditions while avoiding

to cross two-phase regions during the expansion, the Beta continuous distribution is selected because of its higher versatility. Indeed, by setting up its parameters to generate a non-symmetrical distribution, the Beta pdf can be advantageously used for increasing the inputs variability obtaining collocation points quite far from the saturation curves.

The four Beta parameters  $\hat{\alpha}$ ,  $\hat{\beta}$ ,  $\bar{a}$ ,  $\bar{b}$  (with  $\hat{\alpha}$ ,  $\hat{\beta}$  the pdf shape parameters and  $\bar{a}$ ,  $\bar{b}$  the lower and upper base interval limits) are estimated and fitted on the imposed input mean and variance. Now, a coefficient of variation of 8% respect to the nominal point ( $p_r^0 = 0.98, T_r^0 = 1.13$ ) is considered. In Fig. 4.5 an increase of the geometric variability is shown. However, it remains



**Figure 4.5:** Variability of the nozzle shape geometry for beta distributed input parameters (8% Coefficient of Variation).



**Figure 4.6:** Coefficient of Variation of the nozzle Mach number for beta distributed input parameters (8% Coefficient of Variation).

still quite low with variations of the shape below 1%, even if the percent variation (see Fig. 4.6) is one order higher than before. This effect could be related to a substantial insensitivity of the MOC algorithm to input variations. Besides, the choice to impose a constant design massflow for all the calculations implies to keep the exit-to-throat nozzle area ratio constant. Then, the only variations for real gas applications are due to the thermodynamic model and to the variability

of the specific heats ratio inside the nozzle. This results only in slight variations of the nozzle geometry in the accelerating part.

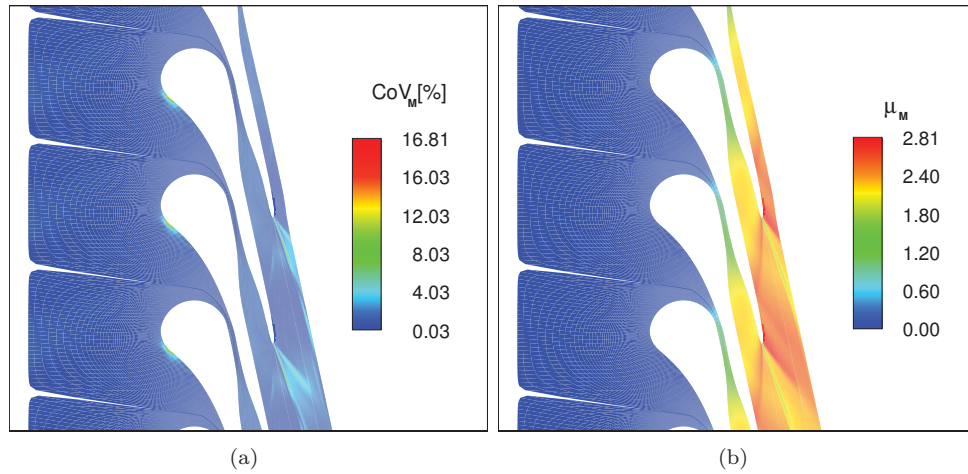
### 4.3.2 Sensitivity of supersonic nozzle guide vane designs

Here an analysis similar to the previous one has been carried out for the stator blade vane geometry, by means of the coupling of the inviscid dense gas solver with the PCM algorithm. The design is provided for the nominal operating conditions shown in Tab. 4.1. The mean flow configuration is very similar to that provided in Section 3.2.4 and the same observations can be addressed. Especially, the flow experiences dense gas effects, has shown in Fig. 3.10c. In

**Table 4.1:** Nominal nozzle operating conditions.

| $p_r^0$ | $T_r^0$ | $G$ [kg/s-m] | $M_e$ | Fluid  |
|---------|---------|--------------|-------|--------|
| 0.98    | 1.13    | 20.0         | 2.06  | R245fa |

this case, the inlet total conditions are varied with a fixed outlet pressure, leading to mass-flow variations. We then expect to observe a stronger impact of input uncertainties on the output



**Figure 4.7:** Coefficient of Variation of Mach number for beta distributed input parameters (8% Coefficient of Variation) for an inviscid stochastic calculation (a); mean Mach number contour plot for beta distributed input parameters ((8% Coefficient of Variation) for an inviscid stochastic calculation.

**Table 4.2:** Means and variations of nozzle guide vane performances (two uncertainties case).

| $\mu_{\eta_{is}}$ | $\mu_P$ [kW/m] | $CoV_{\eta_{is}}$ [%] | $CoV_P$ [%] |
|-------------------|----------------|-----------------------|-------------|
| 0.942             | 195.12         | 0.38                  | 6.88        |

solution. The results are shown in Fig. 4.7a and Fig. 4.7b under the form of percent coefficient of variation and mean Mach number, respectively. Nevertheless, significant variability of the Mach number can be observed by analysing the coefficient of variation. Some zones of high uncertainty are located in correspondence of the oblique shocks and wake departing from the trailing edge, with contributions between 4% and 10%. The highest variability zone is located on the stagnation point at the blade leading edge, with a contribution of about 16%.

Here an Analysis Of Variance (ANOVA) decomposition is proposed in order to carry out a sensitivity analysis. The procedure is applied at the Mach number variance evolution and implements the evaluation of the Sobol' indices for each source of uncertainty (Tang et al., 2010) and aims to identify the main contributors to the total variance estimated with the full-factorial PCM algorithm. Even though the PCM represents a numerically expensive method, it is very accurate (Congedo et al., 2011b) and is here implemented for obtaining a reference solution. Comparisons with other more efficient uncertainty quantification methods are provided in the next Section.

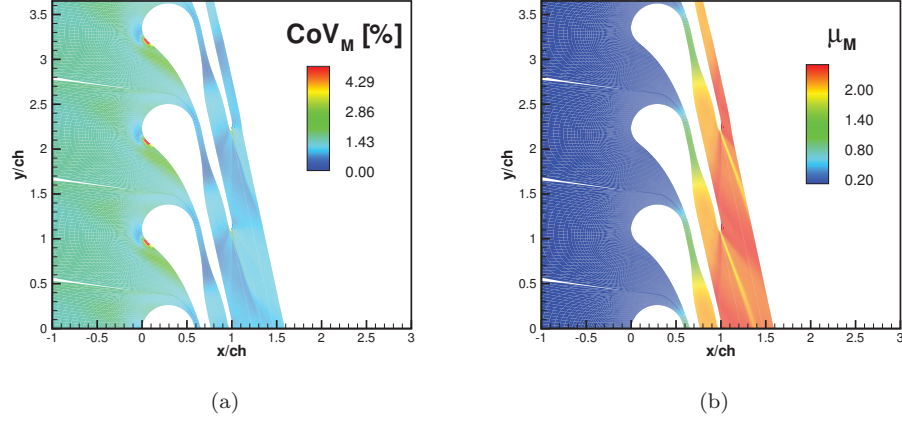
In this problem five uncertain input parameters are taken into account: two operating conditions ( $p_r^0, T_r^0$ ) and three geometric factors (angle of attack  $\beta_a$ , blade stagger angle  $\theta$  and blade thickness  $\epsilon$ ). In this set the thermodynamic parameters have been neglected in order to reduce the parameter space and save computational cost. Indeed, as shown by other authors (Congedo et al., 2011b), the thermodynamic model plays a marginal role in this kind of application. In this way, by considering a second order Lagrange interpolated chaos polynomial, the total number of collocation points (and, then, of deterministic simulations) is  $P_{PCM} = 3^5 = 243$ . The results are obtained in the same hypotheses of the two-parameter calculations: uniformly distributed input parameters; operating conditions variability of 3% respect to the nominal point ( $p_r^0 = 0.98, T_r^0 = 1.13$ ). It has been imposed a variability of 1% around the base nozzle guide vane shape for the geometric parameters. These values agree with the common geometric tolerances for turbomachinery applications.

In Fig. 4.8b the mean Mach number field is shown. It is qualitatively similar to those previously obtained with other simulations and no further considerations will be carried out. More significant informations are provided by Fig. 4.8a, where the Mach number percent coefficient of variation is shown. The average of the amplification factor given by the output-to-input variables  $CoV_M$  ratio, evaluated for the Mach number, is about 0.537 with a maximum value of 5.2. These values state the existence of a global damping effect of the upstream uncertainties provided by the nozzle blade vane system, with spot values higher than unity which, however, remain still low.

Besides, even though the level of uncertainty for the operational input parameters is the same of the uniform two-parameter case, the variability of the output reaches higher level which are comparable with those obtained with the Beta distribution calculation. This behaviour is observed also for the statistics of isentropic efficiency and power output. By comparing the data provided by Tab. 4.3 with Tab. 4.2, it can be noticed that the mean performances are slightly increased, however the percent variation with respect to the mean values is 4% and 10% higher for  $\eta_{is}$  and  $P$ , respectively. These results could be explained by asserting that the introduction of variations of the pressure ratio have increased the global level of uncertainty. To verify this claim the ANOVA analysis can help to evaluate the contribution of the single uncertain parameters to the global variance.

Here only first order Sobol' indices are evaluated and the second order parameter interactions are neglected. In Fig. 4.9a the five Sobol' indices are shown as evaluated along center line. The operating conditions ( $p_r^0, T_r^0$ ), with higher importance of the inlet total pressure, and the geometric parameters ( $\beta_a, \epsilon$ ) give a substantial contribution to the final value of the Mach number variance. On the other hand, the stagger angle  $\theta$  seems to have a negligible action. In Fig. 4.9b the percent contribution to the variability of the nozzle blade performances by means of isen-

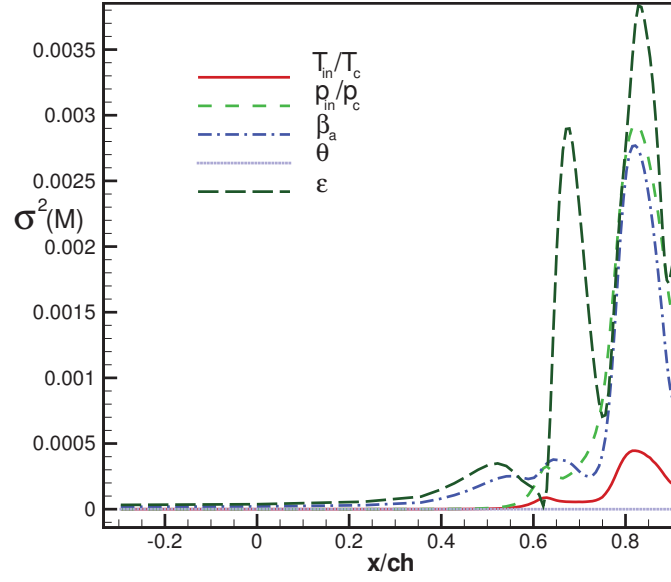
tropic efficiency and power output, in terms of Sobol' indices for each input parameter, is shown. The histogram confirms the importance of the operating conditions on the final results, along with minor contributions given by the blade thickness and the angle of attach.



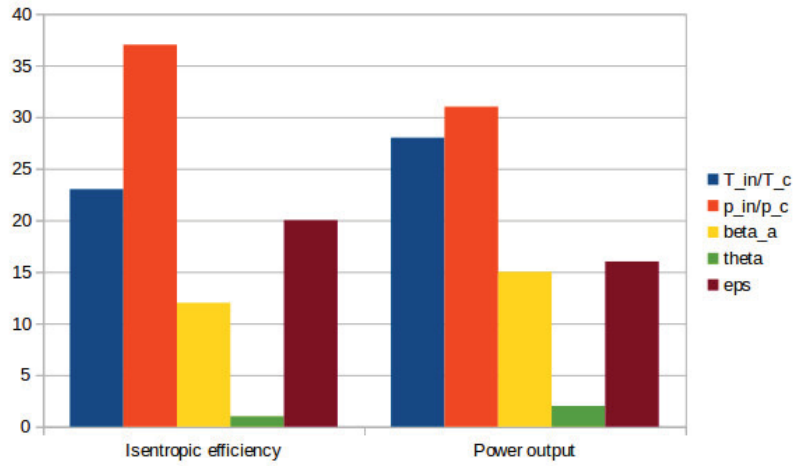
**Figure 4.8:** Coefficient of Variation (a) and mean (b) of Mach number contour plot for five uniformly distributed input parameters for an inviscid stochastic calculation (a).

**Table 4.3:** Means and variations of nozzle guide vane performances (five uncertainties case).

| $\mu_{\eta_{is}}$ | $\mu_P$ [kW/m] | $CoV_{\eta_{is}}$ [%] | $CoV_P$ [%] |
|-------------------|----------------|-----------------------|-------------|
| 0.950             | 196.86         | 4.94                  | 17.54       |



(a)



(b)

**Figure 4.9:** ANOVA of the contribution of the five input parameters to the variance of the Mach number along the vane axis (a) and of the nozzle blade performances in terms of efficiency and power output (b).



## 4.4 Selection of an efficient uncertainty quantification method for ORC applications

In this Section the assessment of different UQ methodologies for the stochastic analysis and robust design of Organic Rankine Cycle (ORC) turbines under multiple uncertainties is carried out. Precisely, the capability of the state-of-the art UQ methods previously described is explored to efficiently and accurately compute the average and standard deviation of the aerodynamic performance of supersonic ORC turbine expanders, whose geometry is preliminarily designed by means of the NODEC algorithm. Stochastic solutions provided by the adaptive SSC, BK, and SOSM are compared to a baseline solution obtained by running a full-factorial PCM analysis. Here, viscous CFD calculations are carried out to evaluate the statistics. The computational cost required to estimate the average adiabatic efficiency, as well as its standard deviation, to stay within a given tolerance level, are compared and conclusions are drawn about the more suitable method for the robust design of ORC turbines.

Indeed, problems involving a high number of uncertain parameters suffer from the "curse of dimensionality" problem, since the number of code runs required to approximate the statistical moments of the probability density functions associated to the output quantities of interest increases exponentially with the number of parameters. Besides, due to the complexity of the geometry and computational cost associated with the ORC geometries and working fluids, no advanced UQ method has been applied so far to these turbines and little work has been done on uncertainty quantification in turbomachinery in general (Zou et al., 2015). A few applications of non-intrusive, sparse grid Generalized Polynomial Chaos methods to simple ORC turbine simulations exist (Hercus and Cinnella, 2011; Congedo et al., 2011b), generally under an inviscid flow assumption. For somewhat more realistic applications such the ORC turbines considered here, the overall computational cost of an UQ calculation becomes prohibitive. Computational cost is especially crucial when the aim is using robust design techniques in an industrial context. To overcome these limitations, the selection of efficient sampling techniques of the parameter space is of vital importance. Then, the aim is to assess and compare very different UQ techniques, in terms of accuracy and efficiency, for a realistic ORC nozzle configuration and to suggest useful guidelines to engineers and designers for selecting an efficient UQ method for this kind of problems.

Firstly, the performances of the supersonic turbulent nozzle guide vane at nominal operating conditions have been evaluated by means of the dense gas solver. By considering the highly deformed computational mesh and the requirement for a low  $CFL$  number ( $\approx 0.4$ ) to get stability and convergence, a deterministic run requires about 10 hours of CPU time on a single processor machine. This high computational cost is required to reach the desired level of convergence of the solution. Indeed, the rate of convergence is affected by the presence of viscous effects coupled with the real-gas EOS and by the development of the supersonic flow along with the shock wave pattern. Besides, the high cell skewness in the suction side region does not allow to use a high  $CFL$  number, which is set to a value of  $\nu_{CFL} = 0.4$ .

The RANS equations are solved on a structured C-shaped mesh with  $384 \cdot 128$  cells (see Appendix for details). The inlet total thermodynamic conditions, periodicity in peripheral direction and a supersonic outlet are imposed as boundary conditions. As usual, the working fluid is R245fa and the operating conditions are chosen close the saturation curves in the supercritical region, characterized by significant dense gas effects. The nozzle guide vane geometry has been preliminarily designed by means of the NODEC, with the inlet total reduced pressure and temperature  $(p_r^0, T_r^0)$ , the target massflow  $G$  and the Mach number  $M_e$  at exit section as input conditions (see Tab. 4.4). Differently from previous viscous calculations, here the effect of the trailing edge thickness is taken into account in order to simulate a feasible stator blade vane. The flow

**Table 4.4:** Nozzle main design parameters.

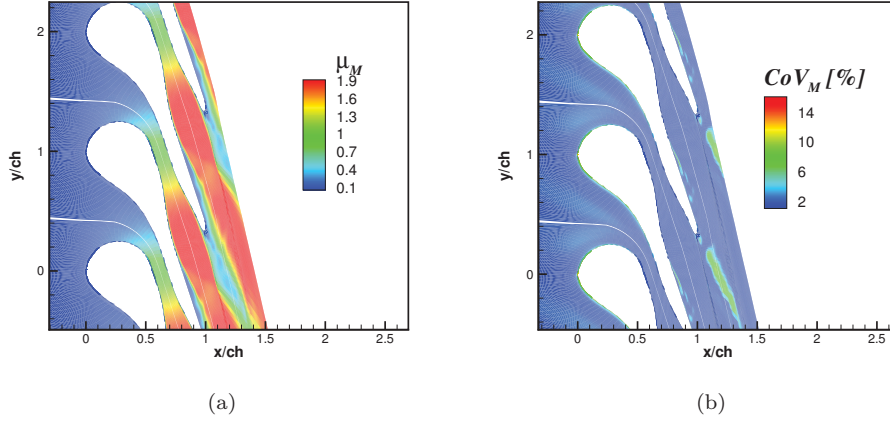
| $T_r^0$ | $p_r^0$ | $G$ | $M_e$ |
|---------|---------|-----|-------|
| 1.28    | 1.15    | 20  | 1.8   |

**Table 4.5:** Input uncertain parameters and their distributions.

|           | $\mathbf{T}_r^0$ | $\mathbf{p}_r^0$ | $\epsilon$ | $\beta$ | $\theta$ |
|-----------|------------------|------------------|------------|---------|----------|
| $CoV[\%]$ | 5                | 5                | 2          | 2       | 2        |
| $\mu$     | 1.15             | 1.28             | 1          | 0       | 0        |
| $pdf$     | beta             | beta             | uniform    | uniform | uniform  |

is expected to accelerate guided by the suction side wall and then decelerated by a weak oblique shock departing from the trailing edge. Besides, the viscous wake at the exit should be a source of high uncertainty.

In order to perform the UQ analysis, five uncertain input parameters, such as the total pressure and temperature, the nozzle thickness  $\epsilon$  and stagger angle  $\theta$ , and the flow angle  $\beta$ , are taken into account with their probability distributions, mean and variances (see Tab. 4.5). A full-factorial



**Figure 4.10:** Mean (a) and Coefficient of Variation (b) of the Mach number for a viscous supersonic nozzle blade vane evaluated by means of the full-factorial PCM with five uncertainties. The wake is visible at the vane exit, which is source of high levels of uncertainty.

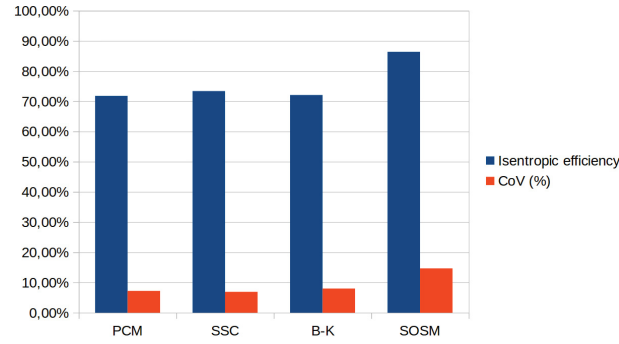
analysis via PCM has been preliminarily carried out and the results are shown in Fig.4.10. By considering a second order polynomial chaos expansion and the five uncertain parameters, the number of deterministic calculations is  $P_{PCM} = 243$ , requiring 3000 hours of total calculation time. Second-order polynomial chaos was found to provide a good compromise between accuracy and computational cost (Hercus and Cinnella, 2011). In Fig. 4.10a and 4.10b the distribution of mean and percent  $CoV$  of the Mach number are shown. The  $CoV$  shows the presence of regions

with high uncertainty close to the wall of the divergent part and to the trailing edge, which can be addressed to the viscous effects and to the wake, with  $CoV \approx 15\%$ .

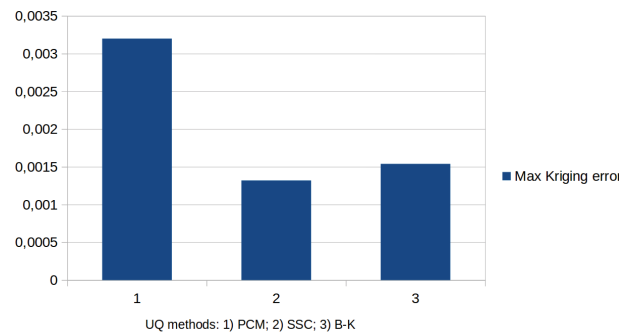
In a second step the random space parameters cardinality has been lowered by means of the ANOVA in order to take into account only the most influential random parameters. The uncertain parameter space is then reduced by retaining only the total conditions and blade thickness as uncertain variables. The four candidate UQ models are applied to the reduced space in order to compare their performances in terms of accuracy and calculation time requirements. By taking

**Table 4.6:** Performance analysis of the UQ models.

| UQ model | $N_{CFD}$ | Polynomial order | Time [h]              | Time/ $N_{CFD}$ [h] |
|----------|-----------|------------------|-----------------------|---------------------|
| PCM      | 27        | 2                | 264                   | 9.78                |
| SSC      | 25        | 83%=3,17%=2      | 270 (2.1% due to LEC) | 10.8                |
| BK       | 30        | -                | 296                   | 9.87                |
| SOSM     | 7         | -                | 73                    | 10.42               |



**Figure 4.11:** Mean and Coefficient of Variation of the blade vane isentropic efficiency for the four UQ models.



**Figure 4.12:** Comparison of the different UQ models sampling strategy in terms of maximum Kriging error.

into account the full-factorial PCM reduced to three uncertainties as the baseline solution, the

comparison among the different models is provided in Fig. 4.11 under the form of mean (along the blade wall) and variance (on the nozzle blade axis) of the isentropic efficiency. The mean values provided by the SSC and B-K models show similar results, with variations below 2% with respect to the PCM, whereas the SOSM provides an over-estimation of almost 15%. Also the SOSM variance of the isentropic efficiency, which is affected by the first order approximation and neglecting cross interactions, results in a value which differs of 7 – 8% from the other models.

An analysis of the UQ models performances (see Tab. 4.6) in terms of calculation time/computational costs is carried out. The comparison is provided by means of the CPU time normalised by means of the number of samples for each UQ model. In this way, the additional time required by the SSC and B-K models, for the LEC and MLE procedures respectively, can be distributed among the samples and a more direct comparison with the PCM and SOSM can be performed. The B-K provides a calculation time of 9.87 hours for each sample, which is slightly higher than that required by the PCM. Both the SSC and SOSM provide higher computational time. The SSC is affected by the computation of the LEC procedure, which is a bottleneck of the present algorithm that required 2.1% of the total computational cost to be performed. On the other hand, the SSC provides higher accuracy than the PCM, by means of a third order polynomial reconstruction of the solution which is obtained on 83% of the total simplexes after refinement, against the 2th global order of PCM. The SOSM has required an additional cost due to the automatic recalculation of one sample which did not reach convergence.

By considering only the UQ models based on a polynomial reconstruction of the QoI, a comparison has been performed with the BK surrogate model in terms of the sampling strategy. For PCM and SSC, the full-factorial and adaptive unstructured refined grids (in the three-dimensional parameter space  $(p_0, T_0, \epsilon)$ ) have been used as training set of two new BK surrogates, respectively. Besides, a classic Latin Hypercube Sampling strategy has been used to train a third surrogate. The resulting Kriging variance as error criterion (see Eq. (4.14)) has been used as metric to compare the three different sampling strategies.

The results have been compared in terms of maximum Kriging variance, as shown in Fig. 4.12. The SSC provides the lower error, with a value slightly below the BK one. This analysis shows that the random adaptive unstructured grid refinement is very accurate for this application, even though the number of samples is the lower. This behaviour can be addressed to the accurate discretisation of the parameter space by means of the adaptive Delaunay triangulation.

By discarding the SOSM method without cross derivatives and first order variance, which is suitable only for fast preliminary analyses, the BK model results to be a good compromise between computational costs and accuracy, even if it results to be slightly expensive than the PCM.

Besides, the higher is the cardinality of the parameter space the higher is the advantage to use the BK with respect to the PCM or SSC. For example, for  $n_\xi = 8$  uncertain variables, the PCM would require 6561 deterministic calculations against 80-100 samples for the BK.

## 4.5 Conclusions

In this Section, the uncertainty quantification framework has been presented with a focus on the ORC turbines. Especially, the MOC design methodology for nozzle guide vanes, presented in the preceding Sections, has been coupled with a full-factorial collocation method (PCM) which has allowed to perform a sensitivity analysis of 2-D ORC supersonic nozzles to fluctuating operating conditions. It has been shown that the design is quite insensitive to variation of 8% of the operational parameters as pressure and temperature in the plenum. A more accurate UQ analysis has been carried out for the design of the nozzle guide vanes, where also geometrical parameter as blade thickness, stagger angle and flow incidence angle, have been taken into account. A vari-

ability of 8% and 1% for the operating conditions and geometrical parameters, respectively, has provided a good robustness of the baseline to the fluctuations of the design parameters, showing a dumping effect of the output variance with respect to inlet values. An ANOVA analysis has shown that the plenum conditions and the blade thickness, give the highest contribution to the global variance. In this way, it has been possible to reduce the parameter space cardinality from 5 to 3, with advantages in terms of computational costs.

As second analysis, the MOC design has been tested with other three different UQ algorithm, namely SSC, BK and SOSM, in order to carry out a comparison in terms of integral parameters, such as the isentropic efficiency, and computational performances. As results, the surrogate-based BK model has provided a compromise between accuracy and computational costs, if compared with the PCM and SSC methods. The SOSM method, developed in a cheap form without consideration of higher order terms in the variance calculation, has provided results very different from the other three methods, thus resulting as a good approach only for preliminary considerations.

## Chapter 5

# ROBUST OPTIMIZATION OF SUPERSONIC ORC NOZZLE GUIDE VANES

### 5.1 Introduction

The seek for high quality with minimum costs for the manufacture of industrial products is a desirable requirement which is not always easily achievable. Typically, this problem is treated as the engineer's task to evaluate different designs by changing some parameters and to choose the best solution depending on some production requirements. The process of finding the "right" design parameters according to one or more predefined criteria, is usually referred to as *optimization* (Beyer and Sendhoff, 2007). The optimization process needs the definition of one or multiple requirements (the objectives) to be minimized or maximized on a set of design variables (the design parameters). An important aspect to take into account is that the choice of the objectives implies the approximation of the real-world application by means of mathematical models. Then, by considering the modelling errors, the search for the optimum could lead the user to find a solution very different from the true one. Besides, even in the case of a perfect model prediction, the realization of the predicted optimum design would be affected by manufacturing and operative uncertainties (geometric tolerances, environmental conditions etc.), thus providing very different performances during the prototype tests with respect to the predicted ones. In this framework, by considering that a classical optimization design would be too sensitive to small changes of the model inputs, the concept of *robustness* has to be introduced.

*Robust optimization* (RO) is a relatively recent idea developed by Taguchi on 1960s, with the introduction of a new paradigm for the design of an industrial product. By citing Marczyk (Marczyk, 2000), "*optimization is actually just the opposite of robustness*". This statement means that classical and robust optimizations lead to different solutions which are sensitive or insensitive to uncertain conditions, respectively. By following Taguchi (Taguchi, 1986), the "father" of RO, a design process can be divided into three stages:

- **System design:** determines the basic performance parameters of the product and its general structure;
- **Parameter design:** optimizes the design parameters in order to meet the quality requirements;

- **Tolerance design:** fine-tuning of the design parameters obtained in the second stage.

For the first time, Taguchi introduced the notion of *noisy parameters* in the second design stage. In this way, a general quantity of interest  $y$ , classically defined as a function of the design vector parameters  $\mathbf{x}$  only, became also function of some noise factors  $\xi_i$ , representing the presence of uncertainties,  $y = y(\mathbf{x}, \xi)$ . For the optimization process, a new objective function was defined, the *signal-to-noise* measure. By minimising the latter, defined as a function of the variance with respect to the true value of the quantity of interest, and maximising the quality function in the design parameter space, the robust design was achieved. Taguchi implemented a statistical data analysis based on a full-factorial exploration of the parameter space by means of a Design Of Experiment (DOE) plan, which provided a set of vectors  $\mathbf{x}$ . For each of these designs, a new set of noise variables  $\xi_{i=1,\dots,k}$  was selected, thus generating at least  $k \cdot 2^N$  experiments (or numerical simulations), if the minimum number of 2 points for each design space dimension is considered and  $N$  elements for the vector  $\mathbf{x}$  are taken into account.

Despite the successful implementation of this methodology for real world applications (Hwang et al., 2001), it lacks of numerical feasibility for large dimension parameter spaces and moderate number of uncertainties because of the curse of dimensionality due to the full-factorial approach. To circumvent this problem, other methodologies have been developed during the years.

Two main classes of RO approaches can be distinguished:

- **Deterministic approach** : the robustness measures are calculated by means of direct and explicit numerical techniques (see e.g. (Sundaresan et al., 1995));
- **Randomized approach** : the optimization process is applied directly to the noisy functions and constraints by taking into account the probabilistic nature of the design inputs and their uncertainties.

This thesis work relies with the second class of RO method and no further discussions are provided about the first one. Especially, a subclass of the randomized approaches, namely the *meta-model approach*, is here followed. Indeed, a surrogate model is constructed using a set of design points  $\mathbf{x}$  carefully chosen. The optimization of this model is then used as an estimate of the real robust design.

In the framework of the RO without meta-model approach, Congedo et al. (2009) investigated optimal shapes for dense gas turbines with BZT effects by using the NSGA genetic algorithm. Cinnella and Hercus (2010) performed RO of airfoils subject to transonic dense gas flows by coupling a PCM UQ method and the NSGA algorithm. Congedo et al. (2011a) also optimized airfoils in dense gas flows by performing ANOVA analysis, whereas Hercus and Cinnella (2011) carried out for the first time RO of a transonic turbine blade in the dense gas regime, by coupling PCM and NSGA. Massive parallelisation was used to partly alleviate the curse of dimensionality. Congedo et al. (2011b) compared RO based on full-factorial PCM and sparse grid methods, showing that the latter may partly alleviate the computational cost problems while keeping almost the same accuracy.

Recently, the randomized approach has gained interest with respect to other techniques, such as the adjoint methods (see e.g. Pini et al. (2014) for application to supersonic turbomachinery cascades, Papoutsis-Kiachagias et al. (2011) for the adjoint formulation of the solution of robust design problems in aerodynamic shape optimization), thanks to its versatility and the possibility to use the same algorithm for several applications.

Park and Lee (2005) performed robust optimizations on mathematical models by training a Kriging surrogate of the real function and searching for the global optimum (in the Taguchi sense) by means of the simulated annealing algorithm. In the turbomachinery optimization framework, Harinck et al. (2005) proposed a global optimization approach by means of the



Multiobjective Genetic Algorithm (MOGA-II) developed by Poloni et al. (1998) coupled with an Artificial Neural Network used as the inexpensive predictive method for the optimization of a radial turbine. Congedo et al. (2013) developed a surrogate-based multi-objective robust optimization technique by reconstructing response surfaces for sensitivity indexes in the design variables plan. The methodology was applied to an ORC cascade with the VKI LS-59 as baseline. The seek for more efficient and accurate ways to get higher fidelity surrogate models has led some authors to propose adaptive surrogate training methodologies. Recently, in the global optimization framework, Rodriguez-Fernandez and Persico (2015) proposed an automatic design of ORC supersonic turbines by means of a Kriging-based genetic optimization with surrogate improvement during iterations. The enlargement of the surrogate training set with the best individual of each generation, recomputed with the high fidelity model, led the solution very close to the true optimum. This approach, however, breaks the scalability of the algorithm. Persico (2016) performed optimization of centrifugal nozzles for ORC applications, by means of a genetic algorithm coupled with a Kriging surrogate-based strategy. To improve the reliability of the surrogate model, a Surrogate-Based Global Optimization approach was applied.

In general, the cost of RO increases quickly with the number of uncertain parameters and design variables. This is particularly problematic for ORC applications, due to the high computational cost of the CFD simulations (especially, if accurate EOS are used, and the number of uncertain parameters to be accounted for (thermodynamic parameters, operating conditions, geometrical tolerances etc) is high).

In this Section, a RO of a supersonic ORC nozzle guide vane is performed with the aim to minimize the variance and maximize the mean value of the isentropic efficiency. An original global optimization methodology has been developed in order to overcome the numerical issues typical of CFD dense gas calculations, which affect convergence and time calculation. A Non-dominated Sorted Genetic Algorithm (NSGA) (Deb et al., 2002) is coupled with a non-intrusive Uncertainty Quantification (UQ) model which provides the statistics (mean and variance). The UQ subloop is based on the Bayesian-Kriging surrogate trained with the system response to the uncertain variables. As shown in the previous Section, for ORC applications it is possible to consider only operational (total pressure and temperature) and geometrical (blade thickness) parameters as the main contributors to the total variance of the system output and, then, to reduce the dimensions of the parameter space to 3. The nozzle guide vane baseline is designed by means of the NODEC software and a Free Form Deformation (FFD) approach, which allows to easily handle any kind of shape independently from the geometrical complexity, is applied to generate a variety of nozzle designs. The resulting parametrization of the nozzle guide vane shape depends on a relatively low number of parameters. The evaluation of the isentropic efficiency is carried out by means of 2D RANS simulations. Given the computational cost of viscous CFD simulations, an original approach to speed-up the RO by training a second surrogate Kriging model for the multi-objective fitness function is here developed and tested. To do so, an adaptive sample infill strategy based on the Multi Objective Expected Improvement (MOEI) is implemented in order to improve the surrogate accuracy during the genetic optimization, with a minimal additional cost.

## 5.2 Shape parametrization: FFD method

The FFD methods are widely used in computer graphics to model 3D objects. The term "free-form" designates: *"whatever the object is, whatever its description and topology, we are able to deform it"* (Raffin, 2013). In this sense, these methods are useful when the geometrical complexity is high and a low number of control parameters are required to deform the object. Besides, the



use of a combination of Bernstein polynomials allows to take easily into account geometrical singularities, control smoothness and represent the baseline exactly. This approach has been successfully applied in the past to airfoil optimization in external Aerodynamics (Duvigneau, 2007). The FFD is performed by parametrizing the space surrounding the object of interest (the blade, in our case). A lattice is created, whose node coordinates represent the control points and a deformation space is defined by means of a trivariate (bivariate for 2D case) tensor product Bernstein polynomial. For the 2D case, a baseline point  $\mathbf{X}$  can be described in the lattice reference system as (Sederberg and Parry, 1986):

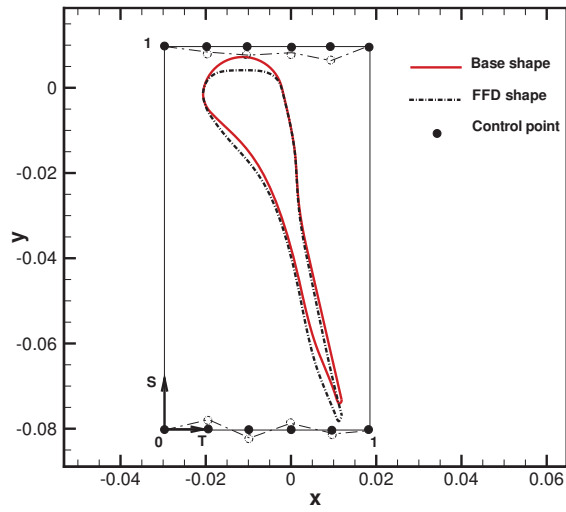
$$\mathbf{X} = \mathbf{X}_0 + s\mathbf{S} + t\mathbf{T} \quad (5.1)$$

where the  $(s, t)$  lattice coordinates are limited in the  $[0, 1]$  intervals and can be related to the baseline reference system as  $s = \frac{\mathbf{T} \times \mathbf{U} (\mathbf{X} - \mathbf{X}_0)}{\mathbf{T} \times \mathbf{U} \mathbf{S}}$ ,  $t = \frac{\mathbf{S} \times \mathbf{U} (\mathbf{X} - \mathbf{X}_0)}{\mathbf{S} \times \mathbf{U} \mathbf{T}}$ , where  $\mathbf{U}$  is the direction normal to the object plane. Given a  $(l \times m)$  lattice (where  $l$  and  $m$  are the number of interval along the horizontal and vertical direction, respectively) the node locations (i.e. the control points) are calculated as  $\mathbf{P}_{ij} = \mathbf{X}_0 + \frac{i}{l}\mathbf{S} + \frac{j}{m}\mathbf{T}$ . Then, once the  $(s, t)$  coordinates are calculated and the deformation specified by the new  $\mathbf{P}_{ij}$  position, the deformed location of a point  $\mathbf{X}$  will be given by:

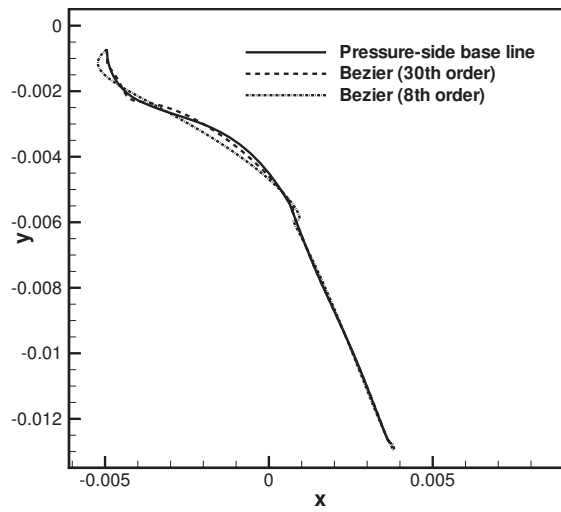
$$\mathbf{X}_{\text{FFD}} = \sum_{i=0}^l \binom{l}{i} (1-s)^{l-i} s^i \left[ \sum_{j=0}^m \binom{m}{j} (1-t)^{m-j} t^j \mathbf{P}_{ij} \right] \quad (5.2)$$

An application of the above method to the parametrization of an ORC nozzle guide vane is illustrated in Fig. 5.1a for a lattice with 12 nodes. The four corners are fixed and only vertical shifts are allowed, leading 8 control parameters, which are the design variables of the subsequent optimization step.

If compared to a classical parametrization by means of Bezier's curves, the FFD method shows its great advantages. In Fig. 5.1b the nozzle blade pressure side is used as base-line and parametrized by means of a 8th and 30th order Bezier's curves. The control point coordinates have been calculated by solving a minimum squares problem which minimize the error between the approximated curve and the base shape. It can be seen that, in order to have an adequate approximation of the pressure side, a high order polynomial curve is required with 30 control points. Besides, during the optimization the Bezier's curves could provide highly deformed shapes which would result in an unfeasible CFD calculation with loss of convergence time of the process. Differently, the FFD avoids all these issues thanks to its intrinsic properties described above.



(a)



(b)

**Figure 5.1:** Application of FFD to a supersonic nozzle blade for a  $l \times m$  lattice ( $l = 6, m = 1$ ) with 8 control parameters. (a); classical parametrization by means of Bezier's curves of the nozzle blade pressure side (b).

### 5.3 Robust Optimization strategy

The RO is carried out by coupling the NSGA with the Kriging-based UQ method. The objective functions are the statistical expectancy and variance of a QoI, here the isentropic efficiency. The NSGA is then used to construct a Pareto front of optimal solutions to the problem *"find a shape for which the expectation of the QoI is maximal and its variance is minimal"*. A straightforward coupling of the NSGA with UQ solver is overly costly for the present application, due to the high number of function evaluations, each one involving a CFD simulation. If we consider a Kriging surrogate trained with  $10n_{dim}$  samples, where  $n_{dim}$  is the number of uncertain variables, and a population of 30 individuals in each genetic generation, it results that  $300n_{dim}$  CFD calculations have to be performed for a single genetic step. To reduce the computational cost, a second Kriging surrogate has been developed to predict the response of the multi-objective fitness function, i.e. the mean and variance of the QoI, to the design variables. Since a single output Kriging model is used, the multi-output response is obtained by training two independent surrogates, one for each fitness component. Fig. 5.2 presents a flow chart of the RO algorithm. The first step consists of a Design Of Experiments (DOE) plan based on Latin Hypercube Sam-

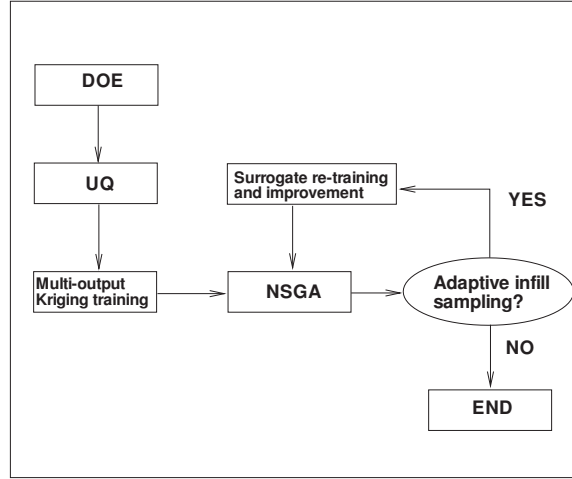
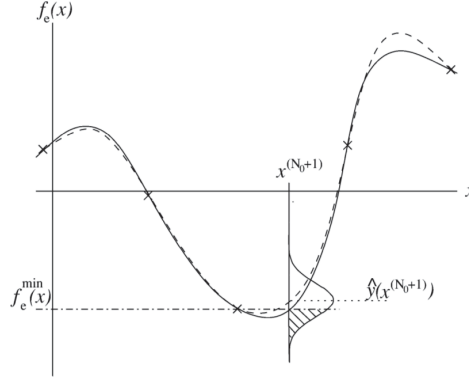


Figure 5.2: Flow chart of the RO algorithm.

pling (LHS) of the design space. A large training set is sampled with  $N > 10n_{dim}$  samples and, after the evaluation of mean and variance through the UQ, the multi-output Kriging surrogate is trained. This is then used in the genetic algorithm to evaluate the bi-objective fitness function. A convergence criterion is used by comparing the fitness average of the current individuals with that of the best individuals and stopping the optimization process if a tolerance of 0.001 is reached. Also a maximum number of generation is imposed in order to avoid waste of calculation time if convergence is not reached. The cost of the surrogate RO is reduced to  $10n_{par}10n_{dim}$  CFD calculations, with respect to the  $(n_{gen}n_{individuals}10n_{dim})$  required by the straightforward RO, where  $n_{gen}$ ,  $n_{individuals}$  and  $n_{par}$  are the number of genetic generations, individuals and design parameters, respectively. Since the Kriging surrogate automatically provides a surrogate accuracy criterion through the Kriging error estimate, a sample infill strategy can be used to improve the model during the NSGA loop. However, an approach based only on the mean value of the Kriging error can mislead the improvement procedure. This is avoided through a more sophisticated method, described in the next Section.

### 5.3.1 Adaptive sample infill strategy

The adaptive infill sampling consists of adding to the initial DOE new samples selected during the NSGA iteration, and to retrain the Kriging model in order to improve its accuracy (see Fig. 5.2). A possible approach consists in selecting some individuals from the Pareto front according to performances criteria. Unfortunately, this method does not ensure to explore the design parameter space in such a way that the direction of the optimization process is preserved. Besides, the number of samples chosen among the individuals of the Pareto front influences the Kriging accuracy. To overcome these issues, a more efficient approach is to exploit the probabilistic nature of the surrogate error estimate to adapt it in regions where the *expected improvement* (EI) of the global minimum is maximised (Dwight et al., 2012; Keane, 2006). The EI quantifies the probability to improve the surrogate on the design space parameters and, then, a global optimization process of the EI function provides the most suitable location for the new surrogate training. The analytic approach followed by Keane (2006) has been implemented in the RO presented in this thesis and it is described below.



**Figure 5.3:** Probability of improvement and expected improvement for one-dimensional test function: solid line, true function  $f_e(x)$ ;  $x$ , sample points; dashed line, Kriging surrogate. Figure extracted from (Keane, 2006).

In order to visualize the effect of the EI optimization, it is useful to consider a one-dimensional function  $f_e(x)$  which is reconstructed by means of the Kriging surrogate, based on an initial training set of  $N_0$  samples (see Fig. 5.3). In the optimization framework, the aim is to minimize the prediction  $\hat{y}(x)$  which, since the Kriging model is a Gaussian process, is described by a normal distribution. Then, by defining the *probability of improvement*  $P[I]$  as the probability that a new sample  $x^{(N_0+1)}$  provides a lower function response  $y(x^{(N_0+1)})$  with respect to the current best value  $f_e^{\min}(x)$ , the following formulation holds:

$$P[I] = \Phi \left[ \frac{f_e^{\min}(x) - \mu(x^{N_0+1})}{\sigma(x^{N_0+1})} \right] \quad (5.3)$$

where  $\Phi$  is the normalized Gaussian cumulate function,  $I$  the magnitude of improvement,  $\mu$  and  $\sigma$  the mean and variance of the Kriging prediction, respectively. The value of  $P[I]$  is represented by the hatched area in Fig. 5.3 and can be interpreted as an indicator of how far from the true optimum is the current surrogate model. Then, by supposing to carry out a global maximization of this area in the design space, it should be possible to find the point with the higher probability to improve the surrogate. However,  $P[I]$  has just the properties of a probability distribution and,

in order to have a quantity to maximise, it is convenient to evaluate its expectancy  $E[I(x^{N_0+1})]$  (where  $I(x^{(N_0+1)}) = \max[f_e^{min}(x) - y(x^{(N_0+1)}), 0]$ ), as:

$$E[I(x^{(N_0+1)})] = [f_e^{min}(x) - \hat{y}(x^{(N_0+1)})] \cdot \Phi \left[ \frac{f_e^{min}(x) - \hat{y}(x^{(N_0+1)})}{\sigma(x^{(N_0+1)})} \right] + \sigma(x^{(N_0+1)}) \phi \left[ \frac{f_e^{min}(x) - \hat{y}(x^{(N_0+1)})}{\sigma(x^{(N_0+1)})} \right] \quad (5.4)$$

where  $\phi$  is the normalized Gaussian density function. The preceding quantity is the first moment of the hatched area of Fig. 5.3 and is referred-to as *expected improvement*. It gives a measure of how large an improvement will be achieved and, then, can be used to perform a global optimization in order to evaluate the best point for updating the surrogate.

Since the RO is a multi-objective optimization process, the EI function will be a surface on a hyper-dimensional parameter space, and a more complicated formulation is implemented with respect to Eq. (5.4). A Multi Objective Expected Improvement (MOEI) approach is here carried out and the main features of this approach are explained below.

In the first step of the optimization process, a DOE is carried out in order to construct the surrogate, which now provides two outputs,  $\hat{y}_1(\mathbf{x})$  and  $\hat{y}_2(\mathbf{x})$  (mean and variance in the RO case), where  $\mathbf{x}$  is the design variable on a  $n_{dim}$ -dimensional space. In the first iteration of the optimizer, the first set of  $M_0$  non-dominated individuals  $f_{1,2}^*(x^{(i)})_{i=1,\dots,M_0}$  can be detected on the true Pareto front. In Fig. 5.4a this step is depicted and the hatched area represents the set of possible improvement individuals which could dominate the members of the current Pareto front.

Given the initial training set, a two-output Kriging surrogate is built on the values of the two objective functions (mean and variance of the QoI). These values are considered as uncorrelated and, then, the model prediction is constructed as a 2-D Gaussian pdf of the form:

$$\phi(\hat{y}_1, \hat{y}_2) = \frac{1}{\sigma_1(x)\sqrt{2\pi}} \exp \left\{ -\frac{1}{2} \frac{[\hat{y}_1 - \mu_1(x)]^2}{\sigma_1^2(x)} \right\} \cdot \frac{1}{\sigma_2(x)\sqrt{2\pi}} \exp \left\{ -\frac{1}{2} \frac{[\hat{y}_2 - \mu_2(x)]^2}{\sigma_2^2(x)} \right\} \quad (5.5)$$

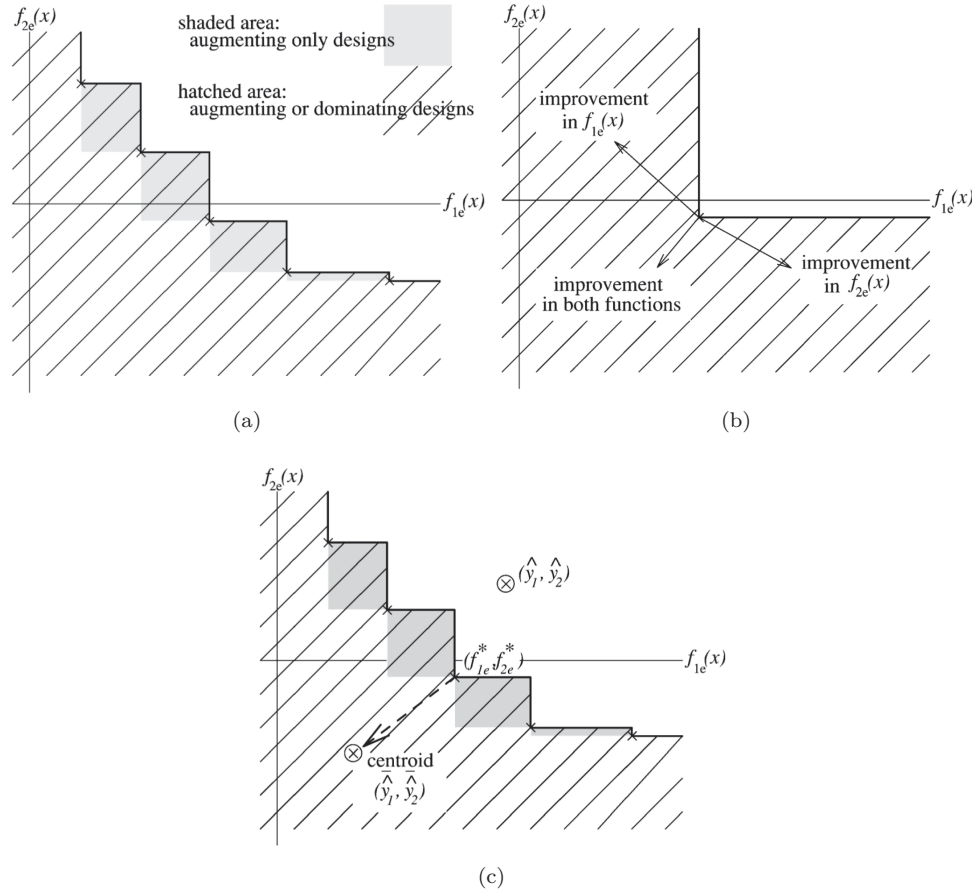
where  $\hat{y}_{i=1,2}$  are the predictions of the QoI, whereas  $\mu_{i=1,2}$  and  $\sigma_{i=1,2}$  are the Kriging-surrogate mean and variance.

Given a new design point to add at the existing training set, for a two-objective optimization it can improve the surrogate in the direction of the first fitness, the second fitness or both (see Fig. 5.4b). In terms of probability measure, the probability of improvement of a new sample  $x^{N_0+1}$  with respect to the Pareto front individuals is:

$$P[I] = P[\hat{y}_1(x^{(N_0+1)}) \leq f_{1e}^*(x) \cup \hat{y}_2(x^{(N_0+1)}) \leq f_{2e}^*(x)] \quad (5.6)$$

which can be calculated by integrating the volume under the joint pdf of Eq. (5.5), i.e. integrating over the hatched area of Fig. 5.4a. By dividing this area in the contributions of the left, center and right part with respect to the Pareto front, the integral is written as:

$$P[I] = \int_{-\infty}^{f_{1e}^{*(1)}} \int_{-\infty}^{\infty} \phi(\hat{y}_2, \hat{y}_1) d\hat{y}_2 d\hat{y}_1 + \sum_{i=1}^{M_0-1} \int_{f_{1e}^{*(i)}}^{f_{1e}^{*(i+1)}} \int_{-\infty}^{f_{2e}^{*(i)}} \phi(\hat{y}_2, \hat{y}_1) d\hat{y}_2 d\hat{y}_1 + \int_{f_{1e}^{*(M_0)}}^{\infty} \int_{-\infty}^{f_{2e}^{*(M_0)}} \phi(\hat{y}_2, \hat{y}_1) d\hat{y}_2 d\hat{y}_1 \quad (5.7)$$



**Figure 5.4:** Example of Pareto fronts of a two-objective optimization process. (a) Pareto front with augmenting (shaded area) and dominating (hatched area) designs; (b) possibilities of improvement during optimization; (c) centroid of probability integral and moment arm used for calculating the multi-objective expected improvement. Figures extracted from (Keane, 2006).

In order to get an improvement metric, as for the one-dimension function cited above, the first moment of the previous pdf integral, called *Multi-Objective Expected Improvement*  $moE[I]$ , is evaluated. The arm of this moment can be calculated as the shortest euclidean distance of the front members from the centroid of the volume integral, Eq. (5.7), as  $d_{MOEI} = moE[I]/P[I]$ . Then, by evaluating  $d_{MOEI}$ , the improvement metric  $moE[I]$  can be determined. By following the scheme of Fig. 5.4c, the centroid coordinates  $(\hat{y}_1(x^{(N_0+1)}), \hat{y}_2(x^{(N_0+1)}))$  of the

current integral volume after adding a new sample  $x^{(N_0+1)}$  at the training set, are calculated as:

$$\begin{aligned} \bar{y}_j(x^{(N_0+1)}) = & \left[ \int_{-\infty}^{f_{1e}^{*(1)}} \int_{-\infty}^{\infty} \hat{y}_j \phi(\hat{y}_1, \hat{y}_2) d\hat{y}_1 d\hat{y}_2 + \right. \\ & \sum_{i=1}^{M_0-1} \int_{f_{1e}^{(i)}}^{f_{1e}^{*(i+1)}} \int_{-\infty}^{f_{2e}^{*(i)}} \hat{y}_j \phi(\hat{y}_1, \hat{y}_2) d\hat{y}_1 d\hat{y}_2 + \\ & \left. \int_{f_{1e}^{*(M_0)}}^{\infty} \int_{-\infty}^{f_{2e}^{*(M_0)}} \hat{y}_j \phi(\hat{y}_1, \hat{y}_2) d\hat{y}_1 d\hat{y}_2 \right] / P[I] \end{aligned} \quad (5.8)$$

with  $j = 1, 2$ . The integrals of Eq. (5.7) and Eq. (5.8) can be analytically calculated (see [Keane \(2006\)](#) for details).

The distance of a Pareto front member from the centroid is the euclidean distance  $d_{MOEI} = \sqrt{[\bar{y}_1(x^{(N_0+1)}) - f_{1e}^*(x^*)]^2 + [\bar{y}_2(x^{(N_0+1)}) - f_{2e}^*(x^*)]^2}$ , where  $x^*$  is the design which provides the front member closest to the centroid. Finally, the expected improvement for a multi-objective optimization is given by:

$$moE[I] = P[I] \cdot d_{MOEI} \quad (5.9)$$

If a global optimization is performed by maximisation of the functional above in the design parameter space, the sample which would provide the best improvement for the multi-output surrogate can be evaluated. This step is performed by means of the stochastic differential evolution algorithm ([Storn and Price, 1997](#)). Once the best MOEI is found in the design space, its fitness is calculated using the UQ solver and added to the training set. The accuracy of the surrogate is rapidly improved with a few MOEI evaluations, then it is possible to have accurate predictions of the Pareto fronts by using a number of MOEI (i.e. UQ) evaluations  $n_{MOEI} \ll n_{gen}$ , as shown in the next Section. The cost of the RO based on the adaptive infill strategy is of  $(10n_{par} + n_{MOEI})10n_{dim}$  CFD calculations.

### 5.3.2 Parallelisation of the RO on cluster

The RO calculations have been performed by means of parallelisation on the high-performance supercomputer OCCIGEN, the CINES machine equipped with 50544 cores, divided into 2106 nodes, each one composed by 2 processors Intel 12-Cores (E5-2690 at 2.6 GHz). The algorithm is characterised by two parallelisation steps for one NSGA generation: a first step for the calculation of the individuals and a second step for the UQ samples of each individual. The parallelisation of the RO algorithm has been performed by means of the ParallelPython utility.

A disadvantage of the RO with surrogate equipped with MOEI sampling is that the global optimization step for the MOEI maximisation is performed on a single core of the machine and the global parallelisation process is temporary blocked. Then, the MOEI procedure can not be applied at each generation of the genetic algorithm, but only for a pre-defined number of genetic iterations.

## 5.4 Numerical verifications

In this Section the MOEI procedure is first tested on the analytic multi-dimensional Kursawe function in order to show the feasibility and accuracy of the adaptive infill strategy. Then, the surrogate-based RO algorithm is applied to a supersonic 1D inviscid nozzle with real gas flow, for which it is possible to carry out a reference CFD-based RO.

#### 5.4.1 Surrogate-based optimization of the multi-dimensional Kursawe function

The adaptive sampling strategy through MOEI is validated against the analytic Kursawe function, of the form  $F = (f_1(\mathbf{x}), f_2(\mathbf{x}))$ , where  $f_1$  and  $f_2$  are expressed as:

$$f_1(\mathbf{x}) = \sum_{i=1}^{n_{dim}-1} -10e^{-0.2\sqrt{x_i^2+x_{i+1}^2}}$$

$$f_2(\mathbf{x}) = \sum_{i=1}^{n_{dim}} (|x_i|^{0.8} + 5\sin(x_i^3))$$

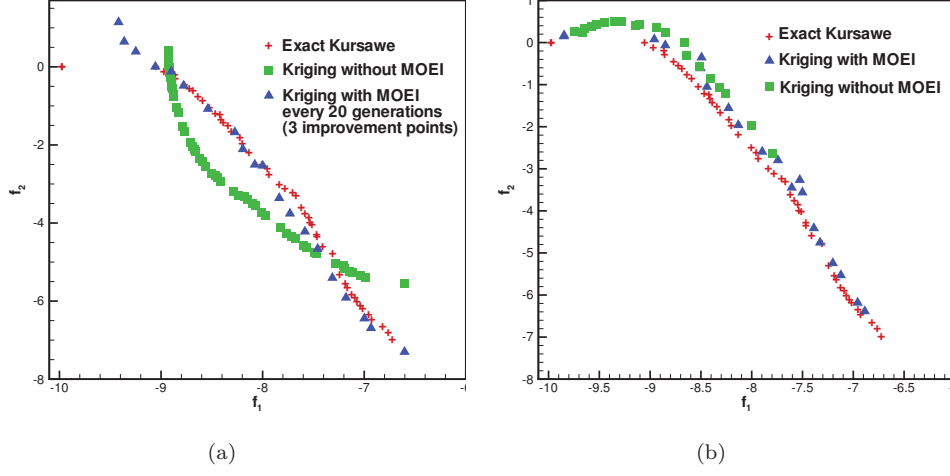
where  $-5 < x_i < 5$  for  $i = 1, \dots, n_{dim}$ .

This is a multi-dimensional function with two outputs, widely used for global optimization tests in the form of multi-objective minimization problem. Here the two-dimensional form is used to perform the cycle shown in Fig. 5.2, without the UQ loop. The Kriging surrogate is trained on an initial LHS training set of 20 samples and used to perform the NSGA. Two calculations, with and without the activation of the MOEI, are carried-out and compared with the exact Pareto front. The maximum number of individuals and generations are set to 50 and 60, respectively, and the MOEI is activated every 20 generations. As a consequence, the Kriging surrogate is updated with only 3 new samples during the genetic loop. Figure 5.5a compares the exact Pareto front with those provided by the Kriging surrogates with and without MOEI. In the first case the discrepancy is high, whereas the MOEI front is well predicted. To verify the exact position of the two Kriging surrogates respect to the exact Pareto front, the fitness of individuals laying on the approximate Pareto fronts is recalculated with the Kursawe function. Fig. 5.5b shows that the MOEI strategy greatly improves accuracy compared to Kriging without adaptive sampling. Other tests have been performed by increasing the space parameter up to 8 dimensions, showing that the MOEI suffers of a curse of dimensionality problem. Indeed the higher is the cardinality, the higher are the number of MOEI calculations required to reach good results by providing more samples to the updated training set. Despite of these issues, the total cost of the algorithm in terms of function evaluations remains much lower than a high-fidelity RO. The results for the 8-D Kursawe function are shown in Fig. 5.6, where the exact Pareto front is compared with the predicted one by means of the MOEI. The best individuals have been recalculated with the exact function. To reach these results, 9 MOEI evaluations have been performed and 9 additional points have been added to the surrogate training set.

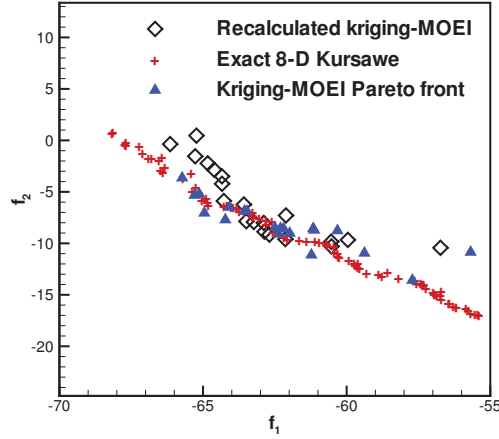
#### 5.4.2 RO of a quasi-1D supersonic nozzle

The RO methodology described in the previous section is first applied to a supersonic quasi-1D inviscid nozzle. The flow is modelled by the Euler equations supplemented by the PRSV EOS. More details about the solver can be found in (Pini and Cinnella, 2012). The working fluid is MDM and the uncertain parameters in terms of mean, percent coefficient of variation (CoV) and probability density function (pdf) are shown in Tab. 5.1. Three uncertainties are taken into account: two operational (total pressure and temperature  $p_0, T_0$ ) and one geometrical (wall nozzle displacement  $\varepsilon$ ) parameters. The nominal operating conditions are normalized with the critical values and are chosen such that a normal shock is set in the nozzle divergent. The chosen CoV ensures that a shock is always present in the divergent, while allowing a significant variation of the shock position. The latter is treated a random QoI, whose mean and variance are estimated through UQ. The RO problem is defined as follows:





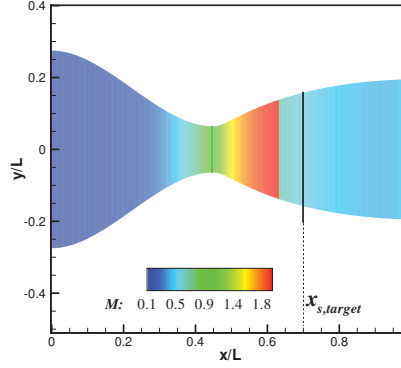
**Figure 5.5:** Pareto fronts comparison among exact 2-D Kursawe function and Kriging surrogates with and without MOEI (a); exact Pareto front and comparison with the Kriging surrogate best individuals recalculated with the exact 2-D Kursawe function (b).



**Figure 5.6:** Exact Pareto front and comparison with the Kriging surrogate best individuals recalculated with the exact 8-D Kursawe function.

$$\min_{\alpha} |\mu(x_s) - \mu(x_s)_{target}|, \min_{\alpha} |\sigma(x_s)^2 - \sigma(x_s)_{target}^2| \quad (5.10)$$

where  $\alpha$  is the vector of design parameters,  $x_s$  the shock position normalised with the nozzle length,  $\mu_{target} = 0.7$  and  $\sigma_{target}^2 = 1.0 \times 10^{-4}$  two target values to which to converge during the optimization (see Fig. 5.7). The nozzle geometry is deformed by means of the FFD and  $n_{par} = 8$  control parameters are defined by a  $6 \times 1$  lattice around the nozzle with the four corners blocked and only vertical shifts are allowed. The accuracy of the Kriging-based UQ solver is first assessed by means of a convergence study. The QoI is the shock location and the maximum Kriging error

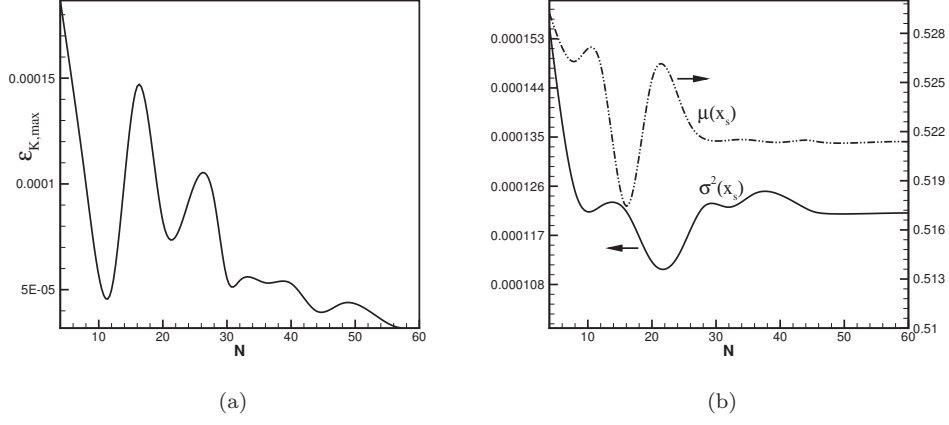


**Figure 5.7:** Scheme of the quasi-1D nozzle optimization problem.

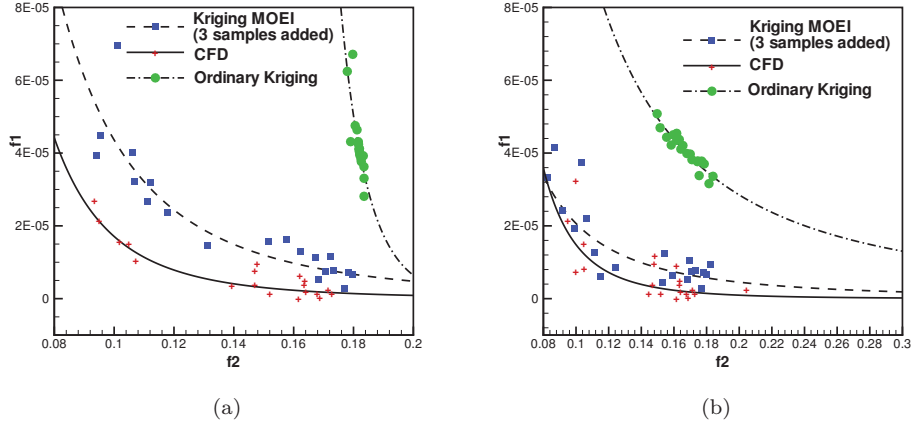
**Table 5.1:** Uncertain variables for the 1D supersonic nozzle. Total pressure and temperature are normalised respect to the critical values,  $\varepsilon$  is the wall nozzle displacement.

| Parameter     | Mean   | CoV% | pdf     |
|---------------|--------|------|---------|
| $p_0$         | 0.212  | 15%  | UNIFORM |
| $T_0$         | 0.0709 | 15%  | UNIFORM |
| $\varepsilon$ | 1      | 1%   | UNIFORM |

estimate  $\varepsilon_{K,max}$  is computed as a function of the number of samples  $N$ . The results, displayed in Figs. 5.8a,5.8b, show that after 30 samples the Kriging error is below  $6 \times 10^{-5}$  and small variations of mean and variance are observed. Then, the UQ-Kriging with  $N = 30$  is coupled to the NSGA. The results are compared with those of a surrogate-based optimization, with and without MOEI. The initial surrogate is based on a LHS training set of  $10n_{par} = 80$  samples. The results of the RO are shown in Figs. 5.9a,5.9b, where  $f1 = |\sigma(x_s)^2 - \sigma(x_s)_{target}^2|$  and  $f2 = |\mu(x_s) - \mu(x_s)_{target}|$ . The first figure compares CFD-based and surrogate-based Pareto fronts. The ordinary Kriging surrogate, without MOEI, fails to predict adequately the high-fidelity Pareto front. On the other hand, by adaptively adding only 3 samples with MOEI (i.e. one every 5 generations of the NSGA), the prediction is more accurate. To verify if the individuals of the surrogate-based Pareto front with MOEI lie on the high-fidelity one, the fitness function of the non-dominated individuals is recalculated with the CFD solver. Fig. 5.9b shows an even better agreement between the two fronts, which proves the accuracy and efficiency of the MOEI strategy for the present test case.



**Figure 5.8:** Maximum Kriging error estimate convergence plot as function of the number of samples. (a); Variance and mean convergence plot as function of the number of samples (b).



**Figure 5.9:** Pareto fronts comparison between high-fidelity CFD RO and Kriging surrogate (with and without MOEI) RO. (a); Pareto individuals recalculation for the Kriging surrogate with MOEI and comparison with CFD (b).

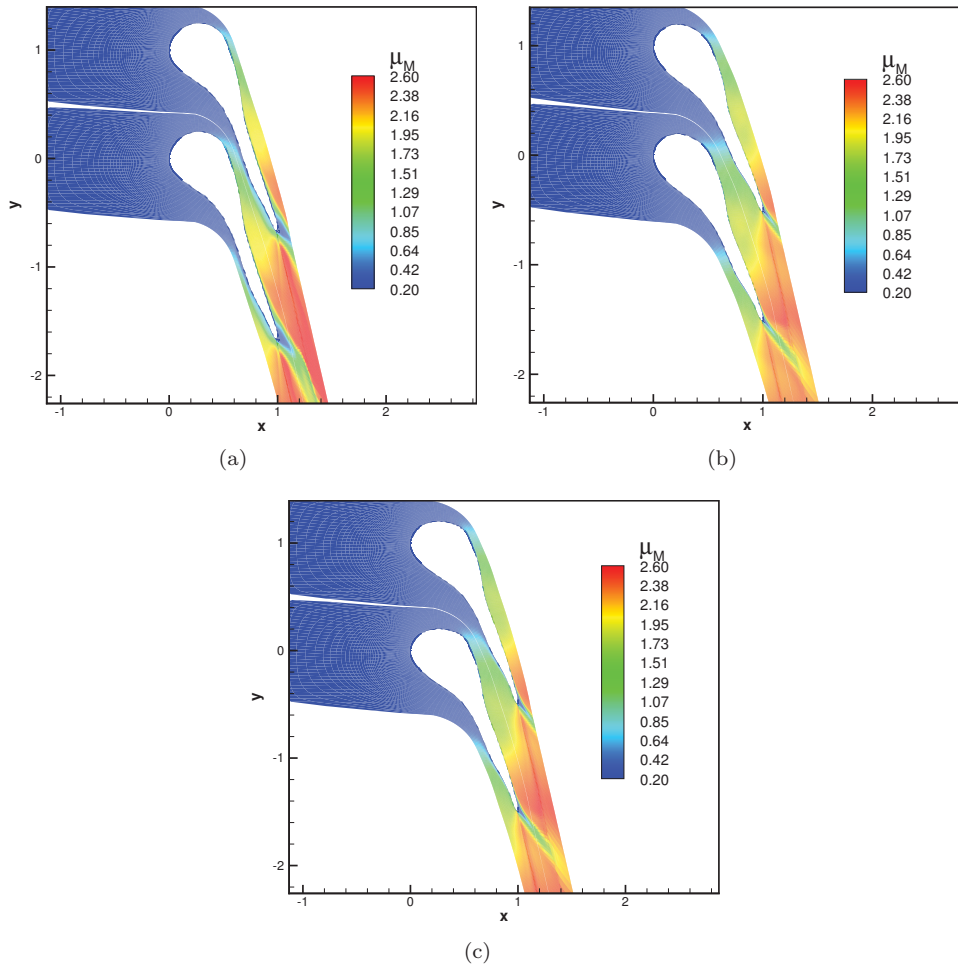
## 5.5 Application: RO of ORC nozzle guide vanes

A deterministic optimization is first performed for the baseline geometry of Fig. 5.1, obtained by applying the accurate MOC based methodology developed in this thesis work. The viscous CFD calculations are carried out on a structured  $384 \times 128$  mesh, for which  $y^+ < 1$ . Grid convergence is checked for the wall pressure distribution (see the grid check analysis in the Appendix for further details). The maximum deformations allowed with the FFD are set to 20% in the lattice reference system, and 8 control points are taken into account, as shown in Fig. 5.1. In this way the axial chord is kept constant whereas the shape can change freely. The number of control

points has been chosen as compromise between the variety of nozzle guide vane geometries provided by the parametrization, and the computational cost of the optimization loop. In Tab. 5.2 the nominal design parameters are shown.

**Table 5.2:** Nominal nozzle parameters. Total pressure and temperature are normalised with respect to the critical values whereas  $\beta$  is the throat-to-exit static pressure ratio.

| Fluid  | $p_r^0$ | $T_r^0$ | $\beta$ |
|--------|---------|---------|---------|
| R245FA | 1.1     | 0.98    | 5       |



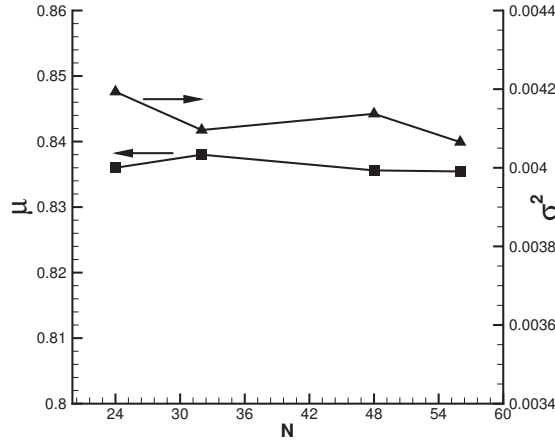
**Figure 5.10:** Mach contour plots for the baseline design (a); the deterministically optimized blade (b); and the robustly optimized blade (individual #A, from Fig. 5.12) (c).

In Figs. 5.10a, 5.10b the Mach contour plots are shown for baseline and optimized geometry, respectively. In the first case, the presence of a weak oblique shock at the trailing edge leads

the Mach number from 2.37 to 2.31. The optimized blade is narrower and exhibits significantly different shapes at the leading edge. This shows that the MOC procedure provides already a satisfactory design for the divergent part, whereas the convergent benefits from CFD optimization. The throat area per unit depth is 9% higher, leading to a slightly higher massflow rate. The expansion pressure ratio through the nozzle is unchanged, and the exit Mach number is 2.1 for both cases. The optimized shape still exhibits oblique shocks on the trailing edge, but with lower upstream Mach number, so that shocks are weaker. The stagger angle is slightly changed from  $72^\circ$  to  $71.4^\circ$  and the viscous wake and the separation zone on the suction side, are reduced. These improves the isentropic efficiency from 0.879 to 0.962 (8%).

Afterwards, a RO of the baseline blade is also carried out by maximizing mean  $\mu_{\eta_{is}}$  and minimizing variance  $\sigma_{\eta_{is}}^2$  of the isentropic efficiency and using the multi-objective Kriging surrogate with MOEI adaptive sampling. Total inlet conditions ( $p_r^0, T_r^0$ ) and blade thickness  $\varepsilon$  are set as uncertain variables, with the distribution shown in Tab. 5.3. The choice of beta pdfs, with a proper calculation of the shape parameters based on the known mean and standard deviation, allows to avoid expansions in the liquid-vapor region.

To evaluate the objective function, the UQ Kriging with 24 samples is used. This choice is related to the need for exploiting in an efficient way the parallelisation of the OCCIGEN machine, which is characterised by 24 cores for each node. In order to assess the accuracy of the Kriging trained with 24 samples (instead of 30), an UQ resolution analysis has been carried out for the nozzle guide vane baseline, by increasing the number of samples. In Fig. 5.11, the hystory of convergence for the statistics of the QoI (isentropic efficiency) shows that with 24 samples the mean is almost already converged, whereas the variance shows a difference of 4.6% with respect to calculation with 58 samples.



**Figure 5.11:** Convergence of the UQ Kriging surrogate statistics for the nozzle guide vane baseline.

The optimization converges after 60 generations with 3 samples adaptively added each 20 generations. Fig. 5.12a shows the Pareto front. The results are compared with stochastic solutions obtained for the baseline design and the deterministically optimized blade by running UQ with the BK (30 samples).

In Fig. 5.12c a comparison between the full CFD RO and the Kriging-based MOEI optimization is shown, in terms of Pareto fronts, after 60 generations. The predicted front shows good

agreement with the high fidelity calculations. Slight differences can be noticed in the region of the higher mean values, where some additional individuals are computed by the full-CFD RO. The lack of prediction of these design points by the surrogate can be addressed to the different convergence rate of the two methods and the consequent evaluation of further non-dominated individuals by the high fidelity model. Indeed, the latter needs 10 generations less than the surrogate model to reach convergence and further iterations of the optimizer have generated new non-dominated individuals which, however, are localised close to the predicted front. Besides, the recalculated samples of the Pareto front computed by the NSGA-Kriging with MOEI surface method are in good agreement with those calculated by using CFD only (no Kriging surrogate for the optimization).

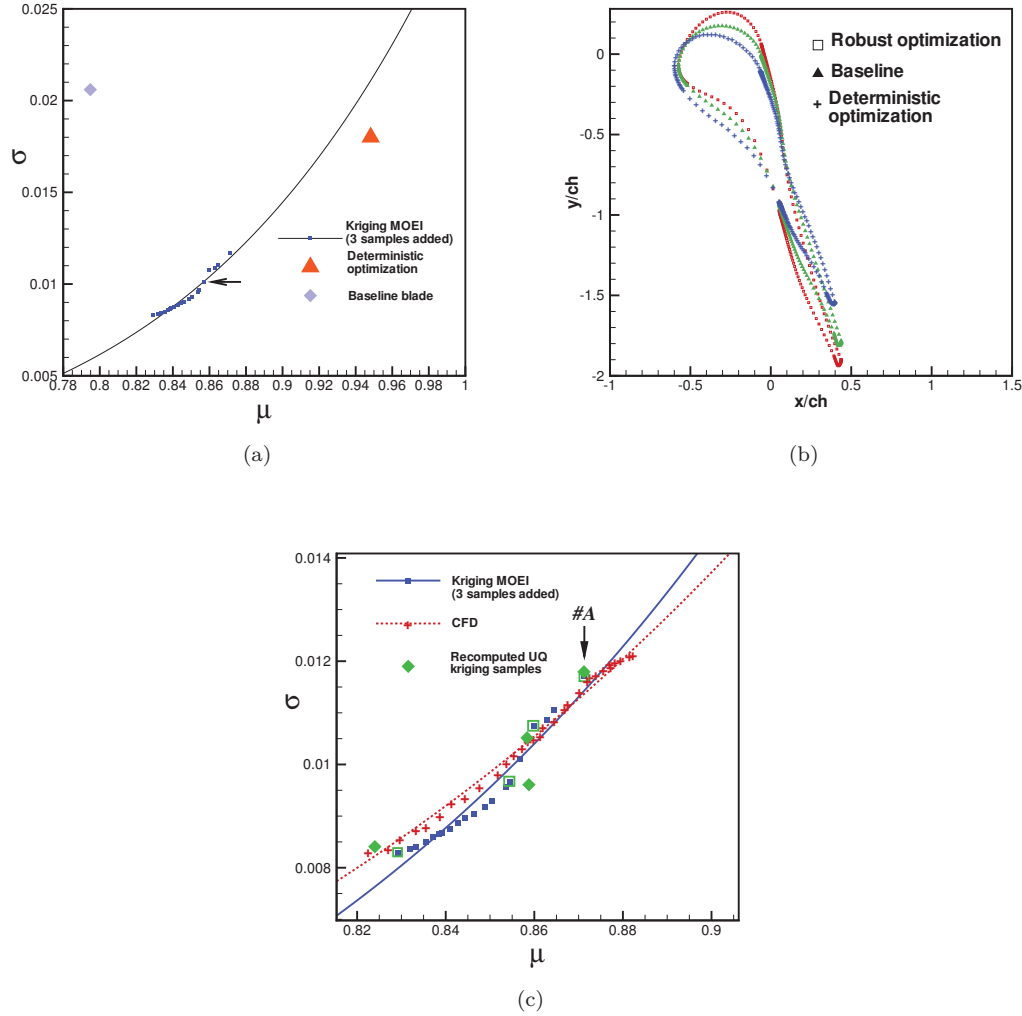
In Fig. 5.10c the contour plot of the mean Mach number distribution is shown for the individual #A, selected from the Pareto front, which shows the higher mean efficiency of the front  $\mu_{\eta_{is}, \#A} = 0.872$ . If compared to the baseline it can be noticed again the reduction of the viscous wake and of the oblique shocks strength, however these improvements are less effective on the mean isentropic efficiency with respect to the deterministic optimization, because of the conflict between mean and variance to be maximised and minimised, respectively. In order to evaluate the effect of the robust optimization, the variation of performances with respect to the mean values needs to be analysed and compared with the other designs. In Fig. 5.13 the coefficient of variation (in percent) of the Mach number is shown for the baseline (5.13a), deterministically (5.13b) and robustly (5.13c) optimized blade shapes. The baseline provides high levels of uncertainty localised within the turbulent boundary layer and the viscous wake, with maximum variations of 8%. The deterministic optimization provides a shape with high mean performance, due to the minimisation of the viscous layers, but the design results in low robustness with high variance close to the trailing edge, corresponding to a maximum variation of 7.4%. The robust design is able to reduce this level of uncertainty by lowering the maximum variation of Mach number by 2%.

The stochastic performances of the different designs are also represented for comparison in Tab. 5.5 and Fig. 5.12a. The deterministic optimization provides a mean value of the isentropic efficiency  $\mu_{\eta_{is}, det} = 0.946$ , i.e. slightly lower than the deterministic value  $\eta_{is, det} = 0.962$  with a variation of 1.5%. The higher variance compared to the robust individuals confirms that the deterministic optimization provides a less robust blade, in spite of the high performances. The stochastic performance of the baseline blade shows that the RO provides a 6% average increase of the isentropic efficiency and a 1% decrease of the standard deviation. Also for the other parameters, as the Carnot factor  $\Theta_C$  and the specific power output, is observed an improvement with both the deterministic and robust optimization in terms of mean values, whereas the robust design provides a reduction by 2% and 1.3% in terms of variation of the Carnot factor and power output with respect to the baseline. The increased  $\Theta_C$  indicates a better exploitation of the energy source thanks to the optimization. The massflow shows an increase of the mean value through the optimization due to the throat area variation, whereas the coefficient of variation is not changed significantly.

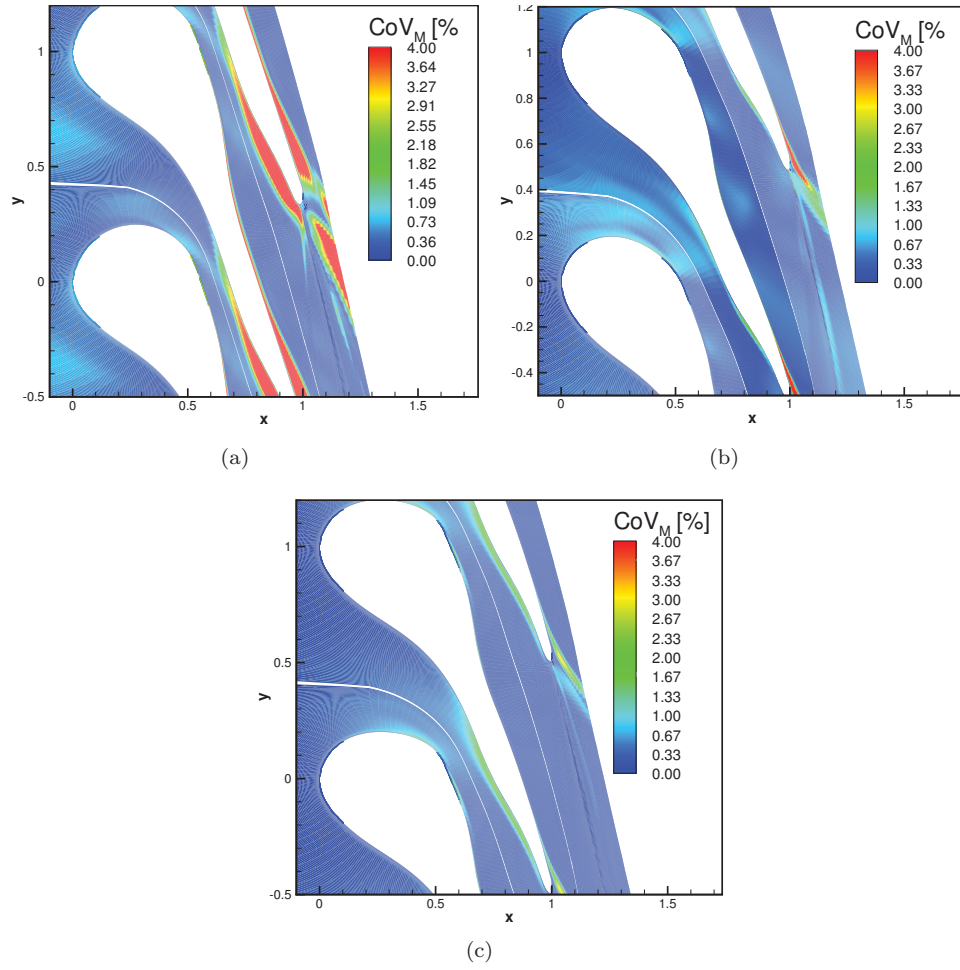
In Fig. 5.12b the robustly optimized shape, selected on the Pareto front (horizontal black arrow in Fig. 5.12a), is compared with the baseline and deterministic optimized ones. Once again, the more significant geometrical variations are observed in the subsonic zone.

As described in Section 5.3.2, the calculations have been performed in parallel on the OCCIGEN (CINES) cluster by exploiting the parallel nature of the NSGA algorithm. At the current generation of the genetic algorithm, each individual is a UQ computation by means of the BK with 24 samples, thus implying a new set of parallel processes (20 for the present application). In order to improve the convergence rate of the CFD solver, the converged solution of the baseline has been used as starting solution for each individual, thus reducing the CPU time for one sample to

3 hours. By considering the number of generations (60), of individuals (20) and of UQ samples (24), the number of function evaluations and the related wall-clock time for the computation is that reported in Tab. 5.5. By comparing the full-CFD with the surrogate-based RO in terms of computational costs, for the present application the second approach allowed to reduce by 14 times the wall-clock time required to perform a complete RO up to convergence, and by 1 order magnitude the number of functional evaluations.



**Figure 5.12:** Pareto front of the ORC nozzle RO. Horizontal arrow: design compared with the deterministic optimization. (a); Comparison among baseline and deterministically and robustly optimized shapes. The robust shape is selected from the center zone of the Pareto front (horizontal arrow in (a)) (b); Pareto front comparison between full CFD (red points) and Kriging-surrogate with MOEI (blue squares) RO. The green diamonds corresponds to the Kriging-MOEI Pareto individuals (marked with green square) recomputed with Kriging UQ. The individual marked with #A is used for further comparisons with the other designs (c).



**Figure 5.13:** Mach percent variation contour plots of: Baseline (a); Deterministically optimized shape (b); Robustly optimized shape (individual #A, see Fig. 5.12) (c).

**Table 5.3:** Uncertain variables for the ORC supersonic nozzle. Total pressure and temperature are normalised respect to the critical values,  $\varepsilon$  is the blade thickness.

| Parameter     | Mean | CoV% | pdf     |
|---------------|------|------|---------|
| $p_0$         | 0.98 | 8%   | BETA    |
| $T_0$         | 1.13 | 8%   | BETA    |
| $\varepsilon$ | 1    | 1%   | UNIFORM |



**Table 5.4:** Computational costs comparison between the full CFD-based and the surrogate-based with MOEI RO.

|                     | Full CFD-based RO | Krig./MOEI RO |
|---------------------|-------------------|---------------|
| No. function eval.  | 28800             | 1992          |
| Wall-clock time [h] | 86400             | 6000          |

**Table 5.5:** Summary of means and variances for the blade vane performances, Carnot factor  $\Theta_C$ , specific power per depth unit and massflow per depth unit for the three nozzle guide vane shapes: baseline, deterministically optimized and robustly optimized (individual #A of Fig. 5.12).

| OPT. CASE        | $\eta_{is}$ | $\Theta_C$ | P [ $kW/(kg \cdot m)$ ] | G [ $kg/(s \cdot m)$ ] |
|------------------|-------------|------------|-------------------------|------------------------|
| <b>BASELINE</b>  |             |            |                         |                        |
| $\mu$            | 0.796       | 0.376      | 1.6505                  | 0.365                  |
| CoV[%]           | 2.6         | 5.3        | 7.14                    | 4.9                    |
| <b>DET. OPT.</b> |             |            |                         |                        |
| $\mu$            | 0.942       | 0.398      | 1.8452                  | 0.419                  |
| CoV[%]           | 1.9         | 4.7        | 6.42                    | 4.8                    |
| <b>RO #A</b>     |             |            |                         |                        |
| $\mu$            | 0.88        | 0.387      | 1.808                   | 0.397                  |
| CoV[%]           | 1.3         | 3.2        | 5.84                    | 4.8                    |

## 5.6 Conclusions

A RO has been carried out for an ORC supersonic nozzle with isentropic efficiency as QoI. The efficiency of the optimization procedure with the NSGA has been improved by means of a Kriging surrogate model coupled with the MOEI technique for an adaptive sampling strategy. The accuracy of the algorithm has been assessed by comparing the Pareto front with the high fidelity calculation provided by an expensive full CFD RO process, showing good approximation of the predicted best individuals. The results have been also compared with those obtained from a deterministic optimization, showing that the deterministic shape provides a less robust shape. Indeed, the deterministic design exhibits a not negligible sensitivity to the operational and geometrical uncertain variable variations. The RO provides a good compromise between average performance and stability. Besides, the calculation performances of the RO methodology are promising and able to handle the intrinsic high computational cost of dense gas calculations by reducing the number of CFD simulations. Finally, results show that the initial design of the nozzle divergent, based on MOC along with boundary layer corrections, is little modified by both the robust and deterministic optimization, which affect essentially the design of subsonic part.

# CONCLUSIONS AND PERSPECTIVES

In this thesis, a numerical analysis of supersonic organic Rankine cycle (ORC) turbines has been carried out. The development of a small-scale turbine with a high aerodynamic load and a low number of stages, is a solution nowadays followed by several enterprises which would provide a feasible and efficient ORC turbine for public transportation purposes. In the framework of the project TRENERGY, the attention has been focused on the design of a robust expander which could manage the high variability of the heat source without too high performance drops with respect to the nominal point. Thus, a robust optimization (RO) methodology has been developed along with an accurate turbine baseline design procedure, which provides the starting point for the optimization process.

In the first part of the work, a thorough methodology has been developed for the fast mean-line design of 2-D turbine stages. The molecular complexity of the working fluids typically used in ORC applications, introduces non-classical real gas effects which are as stronger as the dense gas region is approached during the expansion. As investigated in the first Section, these effects have an influence on the geometry of the expander.

In order to develop an accurate design methodology which could allow to perform the analysis of these phenomena, the method of characteristic (MOC) has been selected as the inverse design tool. The MOC has been generalised to any equations of state (EOS) and several analysis with different fluids have been carried out.

Three thermodynamic models have been implemented in the nozzle design tool, namely the perfect-gas, the equivalent- $\gamma$  and the multi-parameter EOS. It has been shown that the perfect-gas model fails to provide the correct nozzle shape for the given target parameter as massflow and expansion pressure ratio. This behaviour can be addressed to the inadequate thermodynamic modelling of the organic fluids close to the dense gas region, where the molecular interactions are not negligible. An improvement is provided by the efficient equivalent- $\gamma$  method, which allows to use the same isentropic relations of the perfect-gas case. The real gas behaviour is, in this case, modelled by means of a polytropic exponent for the expansion whose value, fitted on accurate multi-parameter EOS and being less than 1, allows to take into account typical dense gas effects such as the increase of the speed of sound during the expansion. However, by performing CFD inviscid calculations of the nozzle guide vanes designed with the three thermodynamic models and comparing the results obtained with the Peng-Robinson-Stryjek-Vera EOS, it has been shown that the equivalent- $\gamma$  model is not so accurate as the multi-parameter equations. Indeed, differences up to 2% on the isentropic efficiency (with respect to the fluid reference EOS) and 5% on the design expansion ratio, have shown that the multi-parameter EOS provide the most accurate nozzle design with a negligible additional computational cost.

The comparison among the four organic fluids has shown that the R449 provides the best performances in terms of isentropic efficiency. Even though these results have to be considered limited at the present application, i.e. 2-D steady inviscid calculations, the general trend of higher performances provided by the more engineered fluids, as Novec649, RE347mcc and R449, with respect to the R245fa, has shown an improvement in the development of an advanced heat transfer fluid suitable for ORC applications, without neglecting the safety and environmental requirements.

The introduction of the viscous effects in the computational simulations, has provided a dramatic abatement of the isentropic efficiency up to 10% for all the organic fluids. The presence of a turbulent boundary layer, a bubble separation on the rear part of the nozzle guide vane suction side and the viscous wake, have produced losses with an effect on the expected design operating parameters. Especially, the boundary layer provided a change of the effective nozzle passage area with reduction of the massflow (with respect to the target value), of the expansion pressure ratio and, thus, of the enthalpy drop and power output.

In order to design a complete ORC turbine stage, the MOC has been adapted for the design of supersonic, isolated, axial and low reaction-grade rotors. The methodology, already known for perfect-gas designs, has been extended to any EOS, with focus on the multi-parameter EOS. The four organic fluids used for the nozzle guide vanes, have been tested in the rotor design procedure in thermodynamic conditions close to the dense gas region. The comparisons with a perfect-gas design have provided important differences in terms of geometry parameters. Especially, the blade solidity, defined as the chord-to-pitch ratio, resulted overestimated up to 10% with respect to the accurate multi-parameter EOS design. These differences have an impact on the blade performances. Indeed, if the flow in the blade vane is not properly guided, i.e. the compatibility with the thermodynamic behaviour of the working fluid is not respected, the shock/expansion wave pattern, along with the high flow deflections in the vane, provides high losses and flow separations close to the wall.

Another feature has been deduced by investigating the effect of the molecular complexity on the rotor geometry, by selecting the four working fluids of interest. It has been seen that the higher is the molecular complexity (an index of the low-ideal behaviour of the fluid), the lower is the blade solidity.

The rotor design procedure has required a verification of the goodness of the methodology by means of CFD calculations. In this step, an investigation of the correct boundary conditions to impose at the rotor inlet domain has been conducted. Indeed, by dealing with rotors characterised by a relative supersonic incident flow with a subsonic axial component, the unique incidence problem has been taken into account in order to evaluate the correct inlet flow angle and solve the periodicity problem typical of infinite linear cascades.

The unique incidence problem, related to the effect of the bow-shocks on the incident flow, has been solved in the dense gas framework and the results have been compared with those obtained in dilute gas conditions. A decrease of the unique incidence angle in the dense gas region, with respect to the dilute condition for the same inlet Mach number, has been observed. Such a result is coherent with the damping effect of the dense gases on the bow-shock intensity.

Besides, the proper blade vane design has been shown to have an impact also on the rotor capability to ingest the initial normal shock-wave and, thus, to provide a self-started configuration. In dense gas conditions, the results have provided a wider range of self-started designs with respect to the dilute-gas, showing that the rotor performances could be improved by taking into account the dense gas effects, for the same operating conditions.

The CFD results for isolated rotor designs with the MOC methodology, have been compared with those obtained for a typical circular arcs rotor shape. With the new design methodology, a substantial improvement in terms of losses (entropy deviation decreased of one order magnitude)

and degree of reaction (still negative but closer to zero) has been assessed.

The stator and rotor designs have been coupled in order to provide a full ORC axial stage. By performing a 2-D steady calculation with mixing plane as stator-rotor interface, the viscous results have shown good performances for R245fa, with an isentropic efficiency of 92.9%. However, a more accurate analysis should be carried out by means of unsteady simulations, in order to take into account the stator-rotor interactions, which are a supplemental source of not-negligible losses.

The influence of viscous effects on the global performances of both stator and rotor, has motivated the authors to develop an extension of the design methodology, in order to take them into account in a preliminary design stage. The attention has been focused on the correction of the inviscid baseline provided by the MOC design by means of a calculation of the turbulent boundary layer thickness, which affect the effective flow passage area and, then, the vane performances. The solution of the momentum equation, along with an auxiliary equation for the shape-factor, has been evaluated with generalisation to any EOS. The stator and rotor shapes with viscous correction have been compared with the inviscid ones by means of CFD calculations. A reduction of the viscous wake and an improvement of the enthalpy drop, along with an increase of massflow and power output, has been observed for the stator, whereas the viscous rotor design has provided a recuperation of the flow re-compression due to the lower flow passage area.

The turbine design tool has been developed with the aim to provide an accurate baseline design for optimization purposes. In this way, a starting point not too far from the true optimum, for the present design configuration, should be achieved with a beneficial effect on the convergence of the optimization process. By dealing with highly variable heat sources, as typical for ORC applications, a robust optimization strategy has been adopted in order to perform a multi-objective optimization by means of maximisation and minimization of mean and variance of the isentropic efficiency, respectively. In this framework, a preliminary analysis of the sensitivity of the MOC design for nozzle guide vanes has been carried out by means of an uncertainty quantification (UQ) model. With this approach, the aleatory variability of design conditions, such as operating and geometrical parameters, has been modelled by means of suitable probability distributions and included in the analysis.

In a first step, a UQ analysis with a probabilistic collocation method (PCM) has been carried out for the nozzle guide vane design. Given a variability of 8% for the plenum operating conditions and 1% for some geometrical parameters (as model of the manufacturing tolerances), the MOC design has shown a slight dumping effect on the outputs variance, with a positive influence on the robustness of the nozzle vane design. The decomposition of the global variance of the output quantity of interest, provided by the analysis of variance (ANOVA), has allowed to choose the plenum operating conditions (pressure and temperature), and the blade thickness as the uncertain parameters with the highest influence on the output variability. In this way, a reduction of the parameter space cardinality has been obtained along with a mitigation of the curse of dimensionality problem due to the full-factorial sampling of the PCM.

In a second step, the UQ analysis has been extended to other state-of-the-art methods, namely Simplex Stochastic Collocation (SSC), Second Order Second Moment (SOSM) and Bayesian-Kriging (BK), with the aim to identify the most suitable to use for ORC nozzle guide vanes (with limitation to the assumptions considered in the present work). The comparison has been carried out on the base of accuracy and computational cost considerations. By considering the isentropic efficiency as integral QoI to investigate, the BK and PCM have provided very similar results in terms of mean values and slight differences for the variances. The SSC has resulted an accurate model, with a third order polynomial reconstruction of the QoI for the greatest part of the parameter space sub-domains and an efficient parameter space discretisation by means of the adaptive unstructured grid. By using 25 samples, the SSC has provided variation of 2% and

1% for mean and variance, respectively, with respect to the BK, and slightly lower differences if compared to the PCM. In terms of computational cost, evaluated as the CPU time spent for a single sample calculation, the BK has provided a good compromise with respect to the other models, by resulting, thus, the chosen UQ approach for the further analysis. The SOSM has not provided very reliable data, in comparison with the other methods, mainly due to the first order variance formulation. For a more accurate comparison with the SOSM, a second order variance approach should be used in the future.

After the choice of the BK as UQ model, the robust optimization strategy has been defined. In the last Section, a promising RO methodology, based on the meta-model approach coupled with a genetic algorithm, has been described and tested. The choice of the BK as meta-model to reconstruct the two objectives of the optimization, namely mean and variance of the QoI, has been evaluated in terms of reliability of the response by comparing the Pareto fronts of the true solution with that provided by the approximated model. This analysis has been carried out preliminarily for an analytic function test and a simple quasi-1D CFD problem. The results have shown that the initial design of experiment (DOE) plan, especially its cardinality, has a fundamental role on the accuracy of the model predictions. However, during the robust optimization process, it is not straightforward to reach the true optimum, even though the initial model shows good performances. In order to help the meta-model to follow the correct direction towards the robust optimum, the genetic algorithm with Kriging has been equipped with a multi-objective expected improvement (MOEI) model. In this way, an adaptive improvement strategy has been set up for the Kriging response, showing promising results during the tests. One of the disadvantages of this methodology is the temporary block of the parallelisation of the genetic optimizer due to the CPU time required to find the maximum of the MOEI functional by means of a global optimization process. On the other hand, the results have shown good agreement between the predicted and the true Pareto front with a small number of additional samples, added during the optimization through the MOEI procedure.

The RO strategy has been finally adopted with the nozzle guide vane, with baseline designed by means of the MOC algorithm. The results have been compared in terms of mean and variances of the isentropic efficiency as QoI with those provided by a deterministic optimization and baseline UQ. The RO has provided a 6% average increase of the isentropic efficiency and a 1% decrease of the standard deviation with respect to the stochastic performances of the baseline blade, whereas the deterministic optimization has showed high improvements for the mean but also high variability of the isentropic efficiency. In terms of computational costs, the genetic optimization with MOEI has shown a wall-clock time 14 times lower than a full-CFD RO, thus becoming a promising solution for expensive RO with non-intrusive UQ methods. A further mitigation of the number of dimensions to deal with the optimization has been achieved by using a free form deformation approach, instead of more classical methods as Bezier curves, for the parametrization of the baseline, by resulting an efficient way to parametrize complex shapes with the minimum number of design parameters.

The development of the relatively cheap RO strategy, in terms of computational costs, developed in this thesis, along with the fast methodology to design accurately the mean-line of ORC supersonic impulse turbine stages, is of interest when the time-to-market is a variable to minimise for the realization of a product such as a ORC turbine expander. During the thesis period, several collaborations have been settled between the DynFluid and enterprises, namely ENOGIA, ENERTIME and MAHLE, interested into the fast MOC algorithm to design full ORC turbine stages for public transportation purposes, without considering the shape optimization.

As future perspectives, further analysis need to be carried out in order to improve the knowledge of the behaviour of the system under consideration. Especially, in the ORC stage design step, URANS simulations should be carried out for the mean-line shape in order to assess the influ-

ence of the stator-rotor interactions on the global performances, such as isentropic efficiency and power output. In a second step, 3-D CFD simulations could provide an insight on the viscous phenomena involved into the blade vanes and the effect of the vicinity to the dense gas region on the secondary flows.

In the UQ framework, more efficient UQ models could be implemented, as the SSC improved with an High-Dimensional Model-Reduction approach, or the BK with a more efficient maximum likelihood estimation step by means of an analysis in the Fourier space, as proposed by other authors.

Finally, the RO methodology proposed in this work will be used for a more thorough analysis extended to rotors, full ORC turbine stages and 3-D shape designs.

# I

## Appendix

### I.1 Spatial grid convergence study

The study performed in this thesis work is based on the elaboration of inviscid and viscous CFD results. The numerical solution of the problem implies the use of a spatial grid with a pre-defined refinement level which can be more or less accurate depending on the needs. One of the most important issues about the choice of the grid refinement is to obtain a grid-independent solution, which is equivalent to say that the *asymptotic solution* is approached. In this way, the uncertainties due to the discretization errors are minimized.

An efficient methodology to check the grid convergence is the Roache's one, based on the Richardson's extrapolation (Roache, 1998). In general, a CFD code uses a numerical algorithm that will provide a theoretical *order of convergence*. However, the boundary conditions, numerical models, and grid will reduce this order so that the observed order of convergence will be lower. Then, by considering three functional evaluations  $f_1, f_2, f_3$  on decreasingly refined grids with a given constant grid refinement ratio  $r$ , the actual *order of convergence*  $p$  can be directly calculated as:

$$p = \ln \left( \frac{f_3 - f_2}{f_2 - f_1} \right) / \ln(r) \quad (\text{I.1})$$

The previous equation would provide an order of convergence slightly lower than the theoretical one and it could be used to evaluate the convergence level of the solution. To do so, given two functional evaluations on a coarse and finer grid, the *grid convergence index* (GCI) for the latter is:

$$\text{GCI}_{fine} = \frac{1.25 |\varepsilon|}{(r^p - 1)} \quad (\text{I.2})$$

where  $\varepsilon = (f_2 - f_1)/f_1$  represents the relative error and 1.25 is a safety factor suitable for a convergence study based on three functional evaluations.

The GCI for the medium grid will be then:

$$\text{GCI}_{medium} = \frac{1.25 |\varepsilon| r^p}{(r^p - 1)} \quad (\text{I.3})$$

where, now,  $\varepsilon = (f_3 - f_2)/f_2$ .

To check if the computed solutions are in the asymptotic range of convergence, the above two GCI values can be compared as evaluated on three differently refined grids:

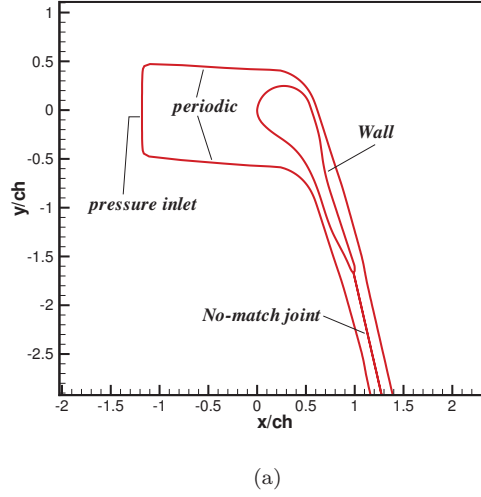
$$\text{GCI}_{23} = r^p \text{GCI}_{12} \quad (\text{I.4})$$

If Eq. (I.4) is satisfied, the asymptotic range is reached and the solution can be considered grid-independent.

In this work, the functional of main interest is the isentropic efficiency  $\mu_{is}$ , then in the following will be  $f = \mu_{is}$ , whereas the theoretical order of convergence will be set to  $p_{inviscid} = 3$  and  $p_{viscous} = 2$ , for inviscid and viscous calculations, respectively.

### I.1.1 Nozzle guide vane

All the computational grids of the nozzle guide vanes analysed in this thesis work, have been generated as single-block C-grid by means of an automatic grid generator. The flow domain is sketched in Fig. I.1 along with the boundary conditions. The convergence study has been carried out for the operating conditions listed in Tab. 3.5.



**Figure I.1:** Computational domain of the nozzle guide vane and boundary conditions.

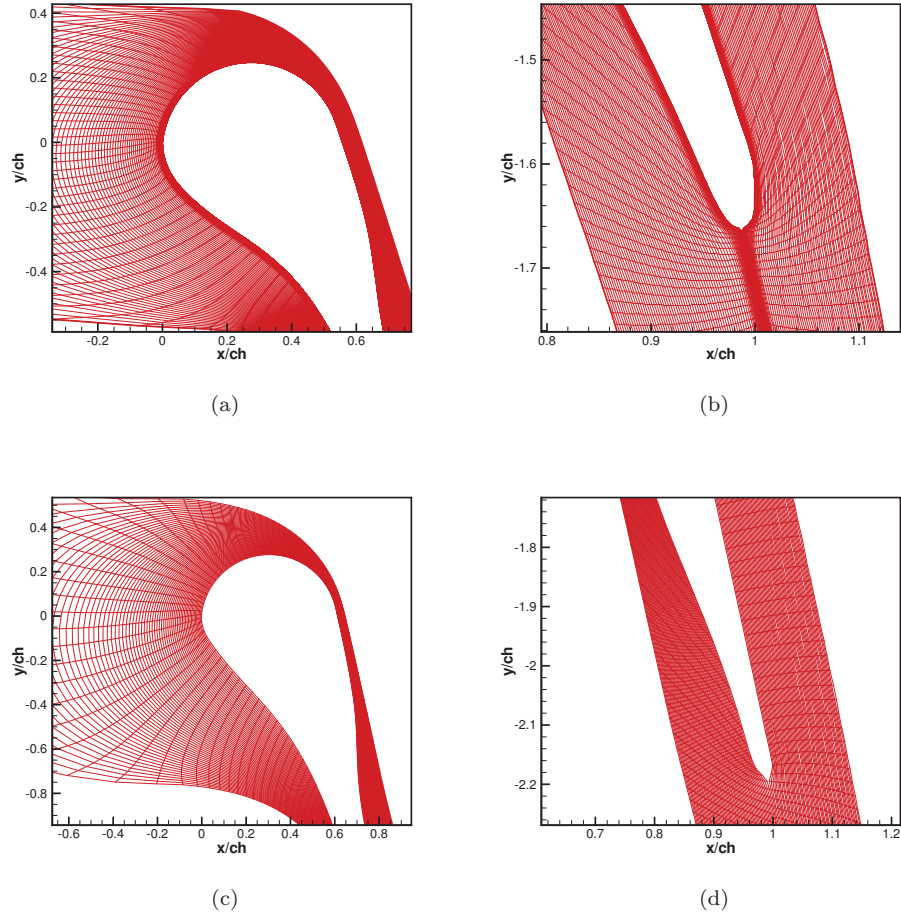
By doubling the number of elements ( $r = 2$ ) along the two directions, three grids of increasing refinement level (coarse, medium and fine) have been designed by means of structured blocks with 192·64, 384·128, 768·256 cells for the viscous case (see Fig. I.2a,b for the medium viscous mesh), and 192·32, 384·64, 768·128 cells for the inviscid case (see Fig. I.2c,d for the medium inviscid mesh). For the viscous mesh, the height of the first cell close to the wall is  $2 \cdot 10^{-5}$ ,  $5 \cdot 10^{-6}$ ,  $2 \cdot 10^{-6}$  times the axial chord for the coarse, medium and finer grids, respectively.

By using Eq. (I.1) and considering the isentropic efficiency as the functional of interest, the actual order of convergence for the inviscid case is  $p = 2.2$ . The grid convergence indexes for the finer and medium grids are 0.12 and 0.52, respectively, showing that the solution can be considered in the asymptotic range in both the cases.

For the viscous grid, an actual order of convergence  $p = 1.9$  has been computed. By using this value, the finer and medium grid convergence indexes are 0.09 and 0.34, respectively. Also in this case, the asymptotic convergence is approached for the medium grid. Then, both for the inviscid and viscous case, the medium grid is used for the CFD calculations. In Fig. I.3, the comparison in terms of nozzle guide vane wall static pressure distribution is carried out. It can



be noticed that, between the finer and medium grids, there are differences below 2%.

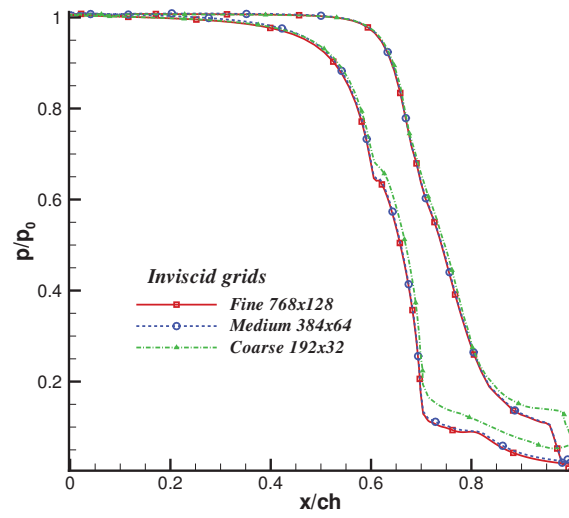


**Figure I.2:** Computational mesh details of the nozzle guide vane leading and trailing edge, for viscous ((a)-(b), medium mesh with 384· 128 cells), and inviscid ((c)-(d), medium mesh with 384· 64 cells) calculations.

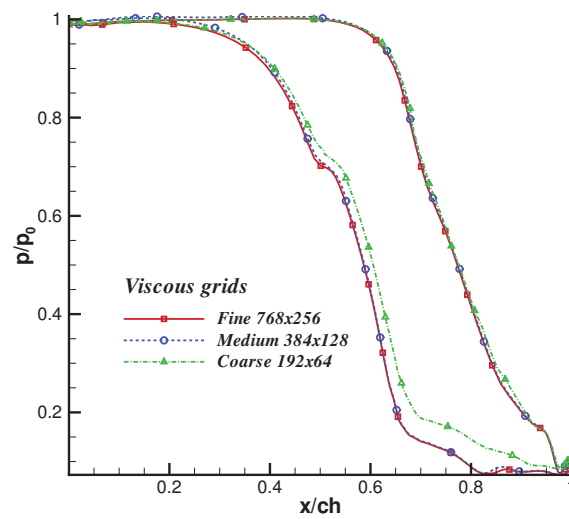
### I.1.2 Isolated rotor

The isolated rotor flow domain is sketched in Fig. I.4a. It has been split into 9 structured blocks by using H-shaped blocks at the inlet and outlet of the domain and one O-shaped block around the blade for the clustering of cells on the wall, in order to take into account the development of the boundary layer. Three grids have been generated by doubling the number of elements of the blocks, thus obtaining a coarse (49152 cells), a medium (98304 cells) and a fine (196604 cells) grid. The height of the first cell close to the wall has been set equal to  $8 \cdot 10^{-6}$ ,  $5 \cdot 10^{-6}$ ,  $1 \cdot 10^{-6}$  times the axial chord for the coarse, medium and finer grids, respectively. In Fig. I.4b a detail of the rotor leading edge is shown for the medium grid.

The grid convergence has been checked for the viscous grid, with the operating conditions listed



(a)

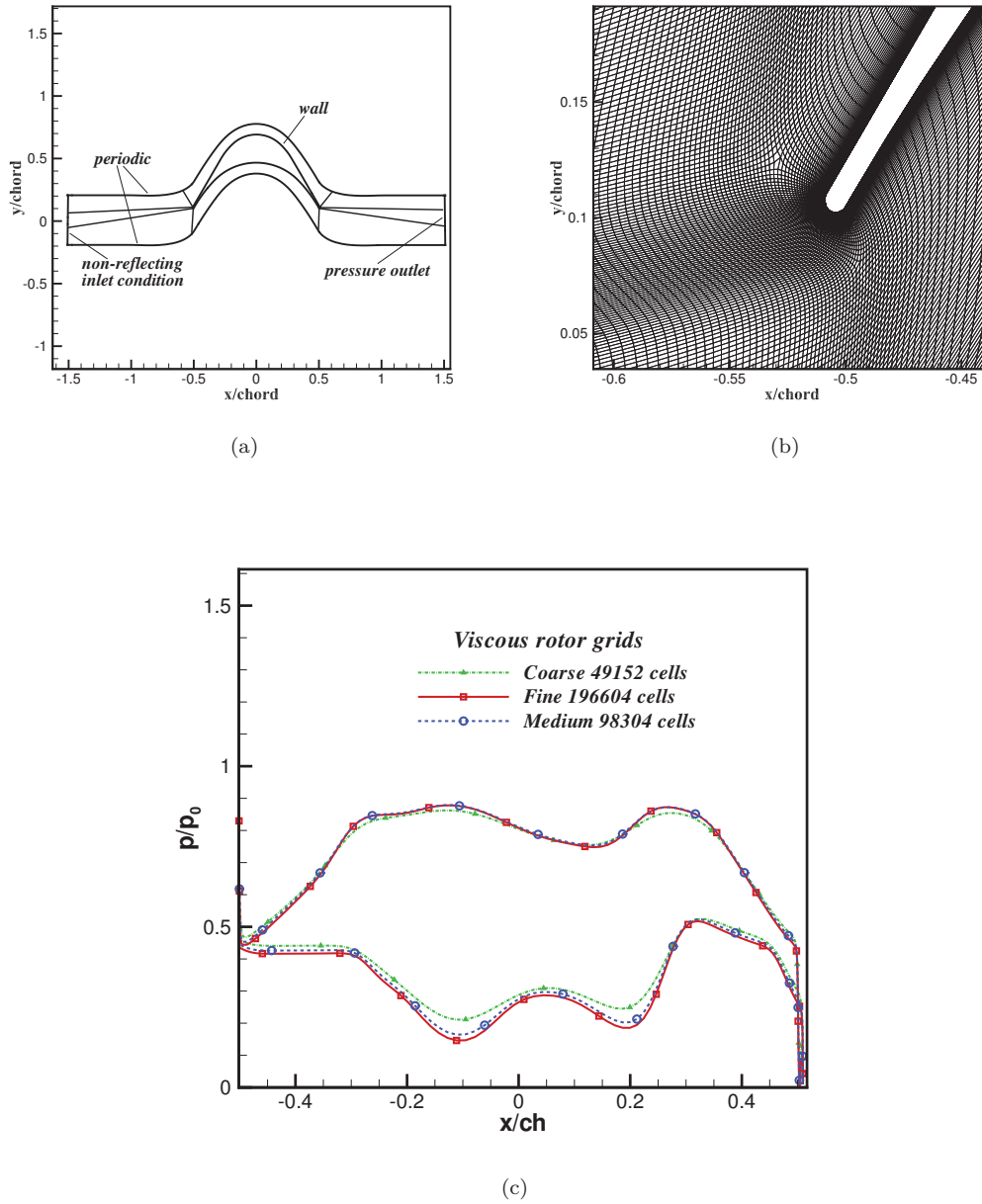


(b)

**Figure I.3:** Nozzle guide vane wall pressure distributions for the inviscid (a) and viscous (b) grids.

in Tab. 3.13, by considering a computed order of convergence  $p = 1.95$ . The grid convergence indexes for the finer and medium grids have been found to be 0.21 and 0.58, thus confirming that the medium grid has approached the asymptotic range. This result is confirmed by the

comparison of the rotor wall pressure distributions , showed in Fig. I.4.



**Figure I.4:** Computational domain of the isolated rotor and multi-block split strategy (a); leading edge detail of the medium computational viscous mesh of the rotor (98304 cells) (b); wall rotor pressure distributions for the three computational grids (c).

# Bibliography

- AIAA-Standards, C. (1998). AIAA guide for the verification and validation of computational fluid dynamics simulations (g-077-1998).
- Aldo, A. and Argrow, B. (1995). Dense gas flow in minimum length nozzles. *Journal of fluids engineering*, 117(2):270–276.
- Aldo, A. C. and Argrow, B. M. (1993). Supersonic minimum length nozzle design for dense gases.
- Ali, M., Mashud, M., Al Bari, A., and Islam, M. M.-U. (2006). Numerical solution for the design of minimum length supersonic nozzle.
- Bethe, H. (1998). On the theory of shock waves for an arbitrary equation of state. In *Classic Papers in Shock Compression Science*, pages 421–495. Springer.
- Beyer, H.-G. and Sendhoff, B. (2007). Robust optimization—a comprehensive survey. *Computer methods in applied mechanics and engineering*, 196(33):3190–3218.
- Borsukiewicz-Gozdur, A. and Nowak, W. (2007). Maximising the working fluid flow as a way of increasing power output of geothermal power plant. *Applied thermal engineering*, 27(11):2074–2078.
- Brown, B. P. and Argrow, B. M. (2000). Application of bethe-zel’dovich-thompson fluids in organic rankine cycle engines. *Journal of Propulsion and Power*, 16(6):1118–1124.
- Budugur, L. (1995). Fluid dynamics and heat transfer of turbomachinery.
- Bufl, E. A., Cinnella, P., and Merle, X. (2015). Sensitivity of supersonic orc turbine injector designs to fluctuating operating conditions. *Proceedings of the ASME 2015 Turbo Expo Turbine Technical Conference, ASME TURBO EXPO 2015 June 15-19, 2015, Montreal, Canada*.
- Capetti, A. (1967). *Motori termici*. Unione tipografico-editrice torinese.
- Casati, E., Vitale, S., Pini, M., Persico, G., and Colonna, P. (2014). Centrifugal turbines for mini-organic rankine cycle power systems. *Journal of Engineering for Gas Turbines and Power*, 136(12):122607.
- Chen, H., Goswami, D. Y., and Stefanakos, E. K. (2010). A review of thermodynamic cycles and working fluids for the conversion of low-grade heat. *Renewable and Sustainable Energy Reviews*, 14(9):3059–3067.
- Chung, T. H., Lee, L. L., and Starling, K. E. (1984). Applications of kinetic gas theories and multiparameter correlation for prediction of dilute gas viscosity and thermal conductivity. *Industrial & engineering chemistry fundamentals*, 23(1):8–13.

- Cinnella, P. and Congedo, P. (2004). A numerical method for dense gas flows. *AIAA Paper*, 2137:2004.
- Cinnella, P. and Congedo, P. (2005a). Aerodynamic performance of transonic Bethe-Zel'dovich-Thompson flows past an airfoil. 43:370–378.
- Cinnella, P. and Congedo, P. M. (2005b). Numerical solver for dense gas flows. *AIAA journal*, 43(11):2458–2461.
- Cinnella, P. and Congedo, P. M. (2007). Inviscid and viscous aerodynamics of dense gases. *Journal of Fluid Mechanics*, 580:179–217.
- Cinnella, P. and Hercus, S. (2010). Robust optimization of dense gas flows under uncertain operating conditions. *Computers & Fluids*, 39(10):1893–1908.
- Cohen, H., Rogers, G. F. C., Saravanamuttoo, H. I. H., and (r.) Saravanamuttoo, H. (1987). Gas turbine theory.
- Collercandy, R. (1998). Multigrid strategy for euler and navier-stokes computations for flows around complex aerospace configurations. *Tiré à part- Office national d'études et de recherches aérospatiales*.
- Colonna, P., Casati, E., Trapp, C., Mathijssen, T., Larjola, J., Turunen-Saaresti, T., and Uusitalo, A. (2015). Organic rankine cycle power systems: from the concept to current technology, applications, and an outlook to the future. *Journal of Engineering for Gas Turbines and Power*, 137(10):100801.
- Congedo, P., Corre, C., and Martinez, J.-M. (2011a). Shape optimization of an airfoil in a BZT flow with multiple-source uncertainties. 200(1-4):216 – 232.
- Congedo, P. M., Cinnella, P., and Corre, C. (2009). Shape optimization for dense gas flows in turbine cascades. In *Computational Fluid Dynamics 2006*, pages 555–560. Springer.
- Congedo, P. M., Cinnella, P., Hercus, S., Corre, C., et al. (2011b). Efficient robust optimization techniques for uncertain dense gas flows. In *CFD & Optimization-ECCOMAS Thematic Conference*.
- Congedo, P. M., Geraci, G., Abgrall, R., Pediroda, V., and Parussini, L. (2013). Tsi metamodels-based multi-objective robust optimization. *Engineering Computations*, 30(8):1032–1053.
- Cramer, M. and Crickenberger, A. (1992). Prandtl-meyer function for dense gases. *AIAA journal*, 30(2):561–564.
- Cramer, M. and Fry, R. (1993). Nozzle flows of dense gases. *Physics of Fluids A: Fluid Dynamics (1989-1993)*, 5(5):1246–1259.
- Cramer, M. and Tarkenton, G. (1992). Transonic flows of bethe-zel'dovich-thompson fluids. *Journal of Fluid Mechanics*, 240:197–228.
- Culick, F. E. (2012). A turbulent analog of the stewartson-illingworth transformation. *Journal of the Aerospace Sciences*.
- Dai, Y., Wang, J., and Gao, L. (2009). Parametric optimization and comparative study of organic rankine cycle (orc) for low grade waste heat recovery. *Energy Conversion and Management*, 50(3):576–582.

- De Baar, J., Dwight, R. P., and Bijl, H. (2013). Speeding up kriging through fast estimation of the hyperparameters in the frequency-domain. *Computers and Geosciences*, 54:99–106.
- De Baar, J., Scholcz, T. P., Verhoosel, C. V., Dwight, R. P., van Zuijlen, A. H., and Bijl, H. (2012). Efficient uncertainty quantification with gradient-enhanced kriging: Applications in fsi. *Eccomas Vienna*.
- Deb, K., Pratap, A., Agarwal, S., and Meyarivan, T. (2002). A fast and elitist multiobjective genetic algorithm: Nsga-ii. *IEEE transactions on evolutionary computation*, 6(2):182–197.
- Délery, J. (2010). *Handbook of compressible aerodynamics*. ISTE.
- Doyle, E., Dinanno, L., and Kramer, S. (1979). Installation of a diesel-organic rankine compound engine in a class 8 truck for a single-vehicle test. Technical report, SAE Technical Paper.
- Duvigneau, R. (2007). Aerodynamic shape optimization with uncertain operating conditions using metamodels.
- Dwight, R., De Baar, J., and Azijli, I. (2012). A tutorial on adaptive surrogate modeling.
- Eckert, E. (1955). Engineering relations for friction and heat transfer to surfaces in high velocity flow.
- Edeling, W., Dwight, R., and Cinnella, P. (2016). Simplex-stochastic collocation method with improved scalability. *Journal of Computational Physics*, 310:301–328.
- El Chammas, R. and Clodic, D. (2005). Combined cycle for hybrid vehicles. Technical report, SAE Technical Paper.
- Eldred, M. and Burkardt, J. (2009). Comparison of non-intrusive polynomial chaos and stochastic collocation methods for uncertainty quantification. *AIAA paper*, 976(2009):1–20.
- Endo, T., Kawajiri, S., Kojima, Y., Takahashi, K., Baba, T., Ibaraki, S., Takahashi, T., and Shinohara, M. (2007). Study on maximizing exergy in automotive engines. Technical report, SAE Technical Paper.
- Fowlkes, W. Y. and Creveling, C. M. (1995). *Engineering methods for robust product design*. Addison-Wesley.
- Gander, M. J. and Karp, A. H. (2001). Stable computation of high order gauss quadrature rules using discretization for measures in radiation transfer. *Journal of Quantitative Spectroscopy and Radiative Transfer*, 68(2):213–223.
- Glover, S., Douglas, R., Glover, L., McCullough, G., and McKenna, S. (2015). Automotive waste heat recovery: Working fluid selection and related boundary conditions. *International Journal of Automotive Technology*, 16(3):399–409.
- Goldman, L. J. (1968). Analytical investigation of supersonic turbomachinery blading. 1/2-analysis of impulse turbine-blade sections.
- Golub, G. H. and Welsch, J. H. (1969). Calculation of gauss quadrature rules. *Mathematics of computation*, 23(106):221–230.
- Gu, W., Weng, Y., Wang, Y., and Zheng, B. (2009). Theoretical and experimental investigation of an organic rankine cycle for a waste heat recovery system. *Proceedings of the Institution of Mechanical Engineers, Part A: Journal of Power and Energy*, 223(5):523–533.

- Guardone, A. (2010). Real-gas effects in supercritical carbon dioxide gasdynamic nozzles. *HEFAT 2010*.
- Guardone, A., Spinelli, A., and Dossena, V. (2013). Influence of molecular complexity on nozzle design for an organic vapor wind tunnel. *Journal of Engineering for Gas Turbines and Power*, 135(4):042307.
- Guardone, A., Vigeveno, L., and Argrow, B. (2004). Assessment of thermodynamic models for dense gas dynamics. *Physics of Fluids (1994-present)*, 16(11):3878–3887.
- Guardone, A. and Vimercati, D. (2016). Exact solutions to non-classical steady nozzle flows of bethe–zel’dovich–thompson fluids. *Journal of Fluid Mechanics*, 800:278–306.
- Hall, I. (1962). Transonic flow in two-dimensional and axially-symmetric nozzles. *The Quarterly Journal of Mechanics and Applied Mathematics*, 15(4):487–508.
- Harinck, J., Alsalihi, Z., Van Buijtenen, J., and Van den Braembussche, R. (2005). Optimization of a 3d radial turbine by means of an improved genetic algorithm. In *Proceedings of the Fifth European Conference on Turbomachinery*, pages 1033–1042.
- Hercus, S. J. and Cinnella, P. (2011). Robust shape optimization of uncertain dense gas flows through a plane turbine cascade. In *ASME-JSME-KSME 2011 Joint Fluids Engineering Conference*, pages 1739–1749. American Society of Mechanical Engineers.
- Hosder, S. and Walters, R. W. (2010). Non-intrusive polynomial chaos methods for uncertainty quantification in fluid dynamics. In *48th AIAA Aerospace Sciences Meeting, Jan*, pages 4–7.
- Huang, Y., Cinnella, P., and Lerat, A. (1998). A third-order accurate centered scheme for turbulent compressible flow calculations in aerodynamics. *Numer. Meth. Fluid Dynamics*, 6:355–361.
- Hung, T., Wang, S., Kuo, C., Pei, B., and Tsai, K. (2010). A study of organic working fluids on system efficiency of an orc using low-grade energy sources. *Energy*, 35(3):1403–1411.
- Hwang, K.-H., Lee, K.-W., and Park, G.-J. (2001). Robust optimization of an automobile rearview mirror for vibration reduction. *Structural and Multidisciplinary Optimization*, 21(4):300–308.
- Ibaraki, S., Endo, T., Kojima, Y., Takahashi, K., Baba, T., and Kawajiri, S. (2007). Study of efficient on-board waste heat recovery system using rankine cycle. *Review of automotive engineering*, 28(3):307–313.
- Jameson, A. and Baker, T. (1983). Solution of the euler equations for complex configurations. In *6th Computational Fluid Dynamics Conference Danvers*, page 1929.
- Jameson, A., Schmidt, W., Turkel, E., et al. (1981). Numerical solutions of the euler equations by finite volume methods using runge-kutta time-stepping schemes. *AIAA paper*, 1259:1981.
- Jing, L., Gang, P., and Jie, J. (2010). Optimization of low temperature solar thermal electric generation with organic rankine cycle in different areas. *Applied Energy*, 87(11):3355–3365.
- Kandathil, A. K. (2015). A guide to working fluid selection for organic rankine cycle orc generators.



- Kantrowitz, A. and Donaldson, P. (1948). Preliminary investigation of supersonic diffusers. *NACA technical report*.
- Karellas, S. and Schuster, A. (2008). Supercritical fluid parameters in organic rankine cycle applications. *International Journal of Thermodynamics*, 11(3):101–108.
- Keane, A. J. (2006). Statistical improvement criteria for use in multiobjective design optimization. *AIAA journal*, 44(4):879–891.
- Kliegel, J. and Levine, J. (1969). Transonic flow in small throat radius of curvature nozzles. *AIAA Journal*, 7(7):1375–1378.
- Kluwick, A. (2004). Internal flows of dense gases. *Acta mechanica*, 169(1-4):123–143.
- Kumar, A., Nair, P. B., Keane, A. J., and Shahpar, S. (2008). Robust design using bayesian monte carlo. *International Journal for Numerical Methods in Engineering*, 73(11):1497–1517.
- Kunte, H. and Seume, J. (2015). Experimental setup of a small supersonic turbine for an automotive orc application running with ethanol. In *3 International Seminar on ORC Power Systems, October 12-14, 2015, Brussels, Belgium*.
- Landau, L. (1959). Em lifshitz fluid mechanics. *Course of Theoretical Physics*, 6.
- Lemmon, E. W. and Span, R. (2006). Short fundamental equations of state for 20 industrial fluids. *Journal of Chemical & Engineering Data*, 51(3):785–850.
- Lemort, V., Declaye, S., and Quoilin, S. (2012). Experimental characterization of a hermetic scroll expander for use in a micro-scale rankine cycle. *Proceedings of the Institution of Mechanical Engineers, Part A: Journal of Power and Energy*, 226(1):126–136.
- Lerat, A., Sidès, J., and Daru, V. (1982). An implicit finite-volume method for solving the euler equations. In *Eighth International Conference on Numerical Methods in Fluid Dynamics*, pages 343–349. Springer.
- Loeven, A., Witteveen, J., and Bijl, H. (2007). Probabilistic collocation: An efficient non-intrusive approach for arbitrarily distributed parametric uncertainties. In *45th AIAA Aerospace Sciences Meeting and Exhibit*, number AAIA Paper 2007-317, Reno, Nevada, USA.
- Mago, P., Chamra, L., and Somayaji, C. (2007). Performance analysis of different working fluids for use in organic rankine cycles. *Proceedings of the Institution of Mechanical Engineers, Part A: Journal of Power and Energy*, 221(3):255–263.
- Maizza, V. and Maizza, A. (1996). Working fluids in non-steady flows for waste energy recovery systems. *Applied Thermal Engineering*, 16(7):579–590.
- Maizza, V. and Maizza, A. (2001). Unconventional working fluids in organic rankine-cycles for waste energy recovery systems. *Applied Thermal Engineering*, 21(3):381–390.
- Marczyk, J. (2000). Stochastic multidisciplinary improvement: beyond optimization. In *Proceedings of 8th AIAA/USAF/NASA/ISSMO symposium on multidisciplinary analysis and optimization, Long Beach*.
- Maskell, E. (1951). Approximate calculation of the turbulent boundary layer in two-dimensional incompressible flow. *Royal Aircraft Est., Farnborough, Gt. Britain, Report Aero*, 2443.



- McLinden, M. O., Perkins, R. A., Lemmon, E. W., and Fortin, T. J. (2015). Thermodynamic properties of 1, 1, 1, 2, 2, 4, 5, 5, 5-nonafluoro-4-(trifluoromethyl)-3-pentanone: Vapor pressure, ( $p$ ,  $\rho$ ,  $t$ ) behavior, and speed of sound measurements, and an equation of state. *Journal of Chemical & Engineering Data*, 60(12):3646–3659.
- Moeckel, W. (1949). Of detached shock waves ahead of plane or.
- Monaco, J. F., Cramer, M. S., and Watson, L. T. (1997). Supersonic flows of dense gases in cascade configurations. *Journal of Fluid Mechanics*, 330:31–59.
- Napolitano, M., Bonfiglioli, A., Cinnella, P., De Palma, P., and Pascazio, G. (2002). Future directions for computing compressible flows: higher-order centering vs multidimensional upwinding. *Frontiers of Computational Fluid Dynamics 2002*, page 113.
- Nelson, C. (2008). Waste heat recovery. In *DEER Conference*.
- Paniagua, G., Iorio, M., Vinha, N., and Sousa, J. (2014). Design and analysis of pioneering high supersonic axial turbines. *International Journal of Mechanical Sciences*, 89:65–77.
- Papoutsis-Kiachagias, E. M., Papadimitriou, D. I., and Giannakoglou, K. C. (2011). Discrete and continuous adjoint methods in aerodynamic robust design problems. *CFD and Optimization*, pages 23–25.
- Park, G.-J. and Lee, K.-H. (2005). A global robust optimization using the kriging based approximation model. *Transactions of the Korean Society of Mechanical Engineers A*, 29(9):1243–1252.
- Park, G. J., Lee, T. H., and Hwang, K. H. L. K. H. (2004). A review of robust design methodologies. *Transactions of the KSME A (in Korean)*, (28(9)):1368–1383.
- Patel, P. S. and Doyle, E. F. (1976). Compounding the truck diesel engine with an organic rankine-cycle system. Technical report, SAE Technical Paper.
- Peng, D.-Y. and Robinson, D. B. (1976). A new two-constant equation of state. *Industrial & Engineering Chemistry Fundamentals*, 15(1):59–64.
- Persico, G. (2016). Evolutionary optimization of centrifugal nozzles for organic vapours.
- Persico, G., Pini, M., Dossena, V., and Gaetani, P. (2015). Aerodynamics of centrifugal turbine cascades. *Journal of Engineering for Gas Turbines and Power*, 137(11):112602.
- Pini, M. and Cinnella, P. (2012). Hybrid adjoint-based robust optimization approach for fluid-dynamics problems. In *15th AIAA Non-Deterministic Approaches Conference*, page 16.
- Pini, M., Persico, G., Casati, E., and Dossena, V. (2013). Preliminary design of a centrifugal turbine for organic rankine cycle applications. *Journal of Engineering for Gas turbines and power*, 135(4):042312.
- Pini, M., Persico, G., and Dossena, V. (2014). Robust adjoint-based shape optimization of supersonic turbomachinery cascades. In *ASME Turbo Expo 2014: Turbine Technical Conference and Exposition*, pages V02BT39A043–V02BT39A043. American Society of Mechanical Engineers.
- Platell, O. B. (1976). Progress of Saab Scania’s steam power project. Technical Report 10.4271/760344, SAE Technical Paper.

- Poloni, C., Quagliarella, D., Periaux, J., and Winter, G. (1998). *Genetic algorithms and evolution strategy in engineering and computer science: recent advances and industrial applications*. John Wiley & Son Ltd.
- Potenza, M., Naccarato, F., Stigliano, G., and de Risi, A. (2014). Numerical optimization of an organic rankine cycle scheme for co-generation. *International Journal of Renewable Energy Research (IJRER)*, 4(2):508–518.
- Quoilin, S., Van Den Broek, M., Declaye, S., Dewallef, P., and Lemort, V. (2013). Techno-economic survey of organic rankine cycle (orc) systems. *Renewable and Sustainable Energy Reviews*, 22:168–186.
- Raffin, R. (2013). Free form deformations or deformations non-constrained by geometries or topologies. In *Deformation Models*, pages 49–74. Springer.
- Rayegan, R. and Tao, Y. (2011). A procedure to select working fluids for solar organic rankine cycles (orcs). *Renewable Energy*, 36(2):659–670.
- Redlich, O. and Kwong, J. N. (1949). On the thermodynamics of solutions. v. an equation of state. fugacities of gaseous solutions. *Chemical reviews*, 44(1):233–244.
- Reshotko, E. and Tucker, M. (1957). Approximate calculation of the compressible turbulent boundary layer with heat transfer and arbitrary pressure gradient.
- Rezgui, A., Cinnella, P., and Lerat, A. (2001). Third-order accurate finite volume schemes for euler computations on curvilinear meshes. *Computers & fluids*, 30(7):875–901.
- Rinaldi, E., Pecnik, R., and Colonna di Paliano, P. (2015). Unsteady rans simulation of the off-design operation of a high expansion ratio orc radial turbine. In *3rd International Seminar on ORC Power Systems, Brussels, Belgium, 12-14 October 2015*. ASME.
- Roache, P. J. (1998). *Verification and validation in computational science and engineering*. Hermosa.
- Rodriguez-Fernandez, P. and Persico, G. (2015). Automatic design of orc turbine profiles using evolutionary algorithms.
- Saleh, B., Koglbauer, G., Wendland, M., and Fischer, J. (2007). Working fluids for low-temperature organic rankine cycles. *Energy*, 32(7):1210–1221.
- Sauer, R. (1947). General characteristics of the flow through nozzles at near critical speeds.
- Schuster, A., Karellas, S., and Aumann, R. (2010). Efficiency optimization potential in supercritical organic rankine cycles. *Energy*, 35(2):1033–1039.
- Sederberg, T. W. and Parry, S. R. (1986). Free-form deformation of solid geometric models. *ACM SIGGRAPH computer graphics*, 20(4):151–160.
- Setzmann, U. and Wagner, W. (1989). A new method for optimizing the structure of thermodynamic correlation equations. *International Journal of Thermophysics*, 10(6):1103–1126.
- Sivells, J. C. (1978). A computer program for the aerodynamic design of axisymmetric and planar nozzles for supersonic and hypersonic wind tunnels. Technical report, DTIC Document.
- Soave, G. (1972). Equilibrium constants from a modified redlich-kwong equation of state. *Chemical Engineering Science*, 27(6):1197–1203.

- Song, P., Wei, M., Shi, L., Danish, S. N., and Ma, C. (2015). A review of scroll expanders for organic rankine cycle systems. *Applied Thermal Engineering*, 75:54–64.
- Starken, H. (1993). Basic fluid dynamic boundary conditions of cascade wind tunnels. *Chapter*, 2:11.
- Starken, H., Yongxing, Z., and Schreiber, H.-A. (1984). Mass flow limitation of supersonic blade rows due to leading edge blockage. In *ASME 1984 International Gas Turbine Conference and Exhibit*, pages V001T01A064–V001T01A064. American Society of Mechanical Engineers.
- Storn, R. and Price, K. (1997). Differential evolution—a simple and efficient heuristic for global optimization over continuous spaces. *Journal of global optimization*, 11(4):341–359.
- Strobl, D.-I. W. et al. (2008). The turbosteamer: A system introducing the principle of cogeneration in automotive applications. *MTZ worldwide*, 69(5):20–27.
- Stryjek, R. and Vera, J. (1986). Prsv: An improved peng–robinson equation of state for pure compounds and mixtures. *The canadian journal of chemical engineering*, 64(2):323–333.
- Sundaresan, S., Ishii, K., and Houser, D. R. (1995). A robust optimization procedure with variations on design variables and constraints. *Engineering Optimization+ A35*, 24(2):101–117.
- Taguchi, G. (1986). *Introduction to quality engineering: designing quality into products and processes*.
- Tang, G., Eldred, M., and Swiler, L. P. (2010). Global sensitivity analysis for stochastic collocation expansion. *CSRI Summer Proceedings*, 2009:100.
- Tang, Z. and PÉriaux, J. (2012). Uncertainty based robust optimization method for drag minimization problems in aerodynamics. *Computer Methods in Applied Mechanics and Engineering*, 217:12–24.
- Teng, H. and Regner, G. (2009). Improving fuel economy for hd diesel engines with whr rankine cycle driven by egr cooler heat rejection. Technical report, SAE Technical Paper.
- Thompson, P. A. (1971). A fundamental derivative in gasdynamics. *Physics of Fluids (1958-1988)*, 14(9):1843–1849.
- Uusitalo, A., Turunen-Saaresti, T., Guardone, A., and Grönman, A. (2014). Design and flow analysis of a supersonic small scale orc turbine stator with high molecular complexity working fluid. In *ASME Turbo Expo 2014: Turbine Technical Conference and Exposition*, pages V03BT26A004–V03BT26A004. American Society of Mechanical Engineers.
- Van der Waals, J. D. (1873). *Over de Continuïteit van den Gas-en Vloeistofoestand*, volume 1. Sijthoff.
- Wheeler, A. P. and Ong, J. (2013). The role of dense gas dynamics on orc turbine performance. In *ASME Turbo Expo 2013: Turbine Technical Conference and Exposition*, pages V002T07A030–V002T07A030. American Society of Mechanical Engineers.
- Wikle, C. K. and Berliner, L. M. (2007). A bayesian tutorial for data assimilation. *Physica D: Nonlinear Phenomena*, 230(1):1–16.

- Witteveen, J. A. and Iaccarino, G. (2012). Simplex stochastic collocation with random sampling and extrapolation for nonhypercube probability spaces. *SIAM Journal on Scientific Computing*, 34(2):A814–A838.
- Yamamoto, T., Furuhashi, T., Arai, N., and Mori, K. (2001). Design and testing of the organic rankine cycle. *Energy*, 26(3):239–251.
- Zou, A., Sauret, E., Chassaing, J.-C., Saha, S. C., and Gu, Y. (2015). Stochastic analysis of a radial-inflow turbine in the presence of parametric uncertainties. In *Proceedings of the 6th International Conference on Computational Methods*, volume 2. ScienTech.
- Zucrow, M. J. and Hoffman, J. D. (1976). Gas dynamics. *New York: Wiley, 1976*, 1–2.
- Zweifel, O. (1945). The spacing of turbo-machine blading, especially with large angular deflection. *Brown Boveri Rev.*, 32(12):436–444.

## Optimisation robuste de turbines pour les cycle organique de Rankine (ORC)

### RESUME :

Au cours des dernières années, le cycles organique de Rankine (ORC) ont reçu un grand intérêt par la communauté scientifique et technique en raison de sa capacité à récupérer de l'énergie à partir de sources de chaleur faible. L'optimisation numérique sous incertitudes est appelé Optimisation robuste (RO) et il surmonte la limitation de l'optimisation déterministe qui néglige l'effet des incertitudes dans les variables de design et / ou des paramètres de design. Pour mesurer la robustesse d'un nouveau design, les statistiques (la moyenne et la variance, ou écart-type) d'une réponse sont calculées dans le processus RO. Dans ce travail, la méthode des caractéristiques (MOC) pour le design des aubes ORC supersoniques est utilisé pour créer une profil de référence. Cela est optimisé grâce à une boucle RO. L'optimiseur stochastique est basée sur un modèle de krigeage bayésien de la réponse du système aux paramètres incertains, utilisé pour l'approximation des statistiques de la sortie du système, couplé à une algorithme génétique multi-objectif (NSGA). Une forme optimale qui maximise la moyenne et minimise la variance de l'efficacité isentropique est recherché. L'efficacité isentropique est évaluée au moyen de simulations RANS (Reynolds Average Navier-Stokes) de l'aube. Le comportement thermodynamique du fluide de travail est modélisée au moyen de l'équation d'état de Peng-Robinson-stryjek-Vera. La forme de l'aube est paramétrée au moyen d'une approche Free Form Deformation. Pour accélérer le RO processus, un modèle de krigeage supplémentaire est construit pour la fonction multi-objectifs et une stratégie adaptif de remplissage basée sur le Multi Objective Expected Improvement es prise en compte afin d'améliorer la précision de krigeage à chaque génération de la NSGA. La forme robuste optimisé d'aube ORC est comparé aux résultats fournis par le MOC et l'optimiseur déterministe.

**Mots clés :** (gaz dense, ORC, turbine, optimisation, incertitudes)

## Robust optimization of ORC turbine expander

### ABSTRACT :

In recent years, the Organic Rankine Cycle (ORC) technology has received great interest from the scientific and technical community because of its capability to recover energy from low-grade heat sources. In some applications, as the Waste Heat Recovery (WHR), ORC plants need to be as compact as possible because of geometrical and weight constraints. Recently, these issues have been studied in order to promote the ORC technology for Internal Combustion Engine (ICE) applications. Since proposed heat sources for ORC turbines typically include variable energy sources such as WHR from industrial processes or automotive applications, as a result, to improve the feasibility of this technology, the resistance to variable input conditions is taken into account. The numerical optimization under uncertainties is called Robust Optimization (RO) and it overcomes the limitation of deterministic optimization that neglects the effect of uncertainties in design variables and/or design parameters. To measure the robustness of a new design, statistics such as mean and variance (or standard deviation) of a response are calculated in the RO process. In this work, the method of characteristics (MOC) design of supersonic ORC nozzle blade vanes is used to create a baseline injector shape. Subsequently, this is optimized through a RO loop. The stochastic optimizer is based on a Bayesian Kriging model of the system response to the uncertain parameters, used to approximate statistics of the uncertain system output, coupled to a multi-objective non-dominated sorting genetic algorithm (NSGA). An optimal shape that maximizes the mean and minimizes the variance of the expander isentropic efficiency is searched. The isentropic efficiency is evaluated by means of RANS (Reynolds Average Navier-Stokes) simulations of the injector. The fluid thermodynamic behavior is modelled by means of the well-known Peng-Robinson-Stryjek-Vera equation of state. The blade shape is parametrized by means of a Free Form Deformation approach. In order to speed-up the RO process, an additional Kriging model is built to approximate the multi-objective fitness function and an adaptive infill strategy based on the Multi Objective Expected Improvement for the individuals is proposed in order to improve the surrogate accuracy at each generation of the NSGA. The robustly optimized ORC expander shape is compared to the results provided by the MOC baseline shape and the injector designed by means of a standard deterministic optimizer.

**Keywords :** (dense gas, ORC, turbine, optimization, uncertainty)

